EIC Yellow Report

November 16, 2020

Editor:
LALAL

Contributors:
X. XYZ[1],

[1]Brookhaven National Laboratory, USA

Contents

Part I

Executive Summary

Chapter 1

The Electron-Ion Collider

Chapter 2

Physics Measurements and Requirements

Chapter 3

Detector Concepts

Chapter 4

Opportunities for Detector Technology and Computing

Part II

Physics

Chapter 5

Introduction

Chapter 6

The EIC Physics Case

Chapter 7

The EIC Measurements and Studies

Chapter 8

Detector Requirements

https://www.overleaf.com/project/5f7b4be817a43a0001f2f714

Part III

Detectors

Chapter 9

Introduction

Chapter 10

Detector Challenges and Performance Requirements

10.1 Beam Energies, Polarization, Versatility, Luminosities

10.2 Rate and Multiplicities

10.3 Integrated Detector and Interaction Region

10.4 Backgrounds

10.5 Systematics and Ancillary Detectors

10.5.1 Luminosity

10.5.2 Polarimetry

10.6 Physics Requirements

Chapter 11

Detector Aspects

11.1 Magnet

The EIC detector is built around a central solenoid magnet with optional correction trim coils required to meet the solenoid field specification. Tracking resolutions in the central pseudo-rapidity range suggest the nominal field of 1.5 T, but a range between 1.5 T and 3 T makes physics measurements accessible. A central field as high as 3 T is needed to maximize the effective $|B|\cdot$dl integral for particles scattered at small polar angles, both in forward and backward directions. High magnetic fields come at the cost of reducing the low-pT acceptance of charged tracks. The acceptance for low-pT particles down to the momenta ~100 MeV/c requires that a fraction of physics data are taken at a substantially lower field. Field polarity flip is a standard measure to address systematic effects due to a different acceptance for the positively and negatively charged particles, hence a bipolar magnet operation with a polarity switch is one of the magnet requirements.

Physics studies available to date suggest a solenoid with a bore diameter 2.5-3.5 m in a traditional composition of an EIC detector. Specifications on coil length, presently assumed to be able to provide a ~3.0 m magnetic length as a reference figure, cryostat radial space, and coil configuration require an optimization integrated with the overall detector design. The solenoid design is characterized by three regions, the barrel and backward endcap with the field parallel to the magnet axis and the RICH detector in the forward direction, which extends from +100 cm to +240 cm with respect to the magnet centre, where the field lines should be projective with respect to the nominal IP location. A flux return path could be provided through the hadronic calorimeter assemblies in the forward and backward directions. Correction coils in the hadron end-cap may be required to meet the RICH detector readout on field projectivity. The need for these coils should be avoided as they will adversely affect the hadron calorimeter performance, but if needed, should be allowed to occupy a maximum of 10 cm of the available linear space.

Alternative detector integrated designs, where a dipole or toroidal field are superimposed with the solenoid field in the central region of the detector, have been considered to improve the $|B|\cdot$dl integral at small scattering angles. These integrated designs could be an option if an acceptance that meets the physics requirements can be demonstrated.

Re-use of the existing BABAR/sPHENIX magnet is an alternative to the realization of a new solenoid with optimized design. Whereas the new solenoid main specifications are an up-to 3T magnetic field, a 2.5-3.5 m diameter bore, and a magnetic length of ~3 m, the BABAR/sPHENIX magnet provides an up-to 1.5 T field,

a 2.8 m diameter bore, and similar magnetic length. The magnet for the BABAR experiment at PEP-II at SLAC, CA was manufactured by Ansaldo, Italy in 1997 and was commissioned in 1998. It was then transferred to BNL, NY in 2015 for use in the sPHENIX experiment where it still resides today. It received a high-field test (up to 1.3 T) in 2018. The prolonged use of the BABAR/sPHENIX magnet requires the implementation of several maintenance and improvement modifications, including new protection circuits such as voltage taps, inspection of and as needed reinforcement of the internal mechanical support, including new strain gauges, and replacement of control instrumentation sensors. Several of these implementations involve the delicate operation of disassembly of the magnet. To repair an existing small leak in the valve box for the cryogenic cooling system requires a replacement of the valve box or disassembly to inspect cooling pipework and to repair leaks. Moreover, additional changes are required for re-using the magnet, for example those needed to match the requirements of projective field lines in the RICH region.

The main parameters of both a new superconducting solenoid magnet, at the present stage of magnet optimization integrated with the overall detector design, and the existing BABAR/sPHENIX magnet are shown in Table 11.1. For a new magnet, a slightly larger bore of 3.2 meter is chosen as compromise between, on one hand, magnet complexity and mechanical Hall space considerations, and on the other hand providing some much-needed space in the bore to ensure more detector technology choices to ensure functionality of tracking, hermetic electromagnetic calorimetry and particle identification (both e/π and π/K/p) over a large range of particle momenta. The choice of NbTi conductor in a Cu matrix for the new magnet is driven by that for EIC no detection beyond hadronic calorimetry is foreseen beyond the bore, alleviating a material requirement on small radiation lengths and allowing use of Cu facilitating the magnet mechanical design.

The coil length is driven by the present definition of the barrel region as between pseudo-rapidity of -1 and 1. This corresponds to an angle of ~40 degrees. This means that for a certain bore size, the space for the mechanical length of the magnet cryostat is roughly 20% larger, or 3.84 meter for a 3.2-meter bore. Folding in an approximate need of 12 cm additional need on each side of the magnet coil for inner vacuum and helium vessels, and multi-layer isolation, determines the coil length requirement to be 3.6 meter. A somewhat larger coil length of 3.8 meter would not be a major issue, but likely not much more as the edge of the cryostat is one of the regions where detector infrastructure (support, cabling, etc.) will reside, and deliberations between the need for equal coverage of tracking and electromagnetic calorimeter as trade-off with particle identification detector readout will occur.

Parameter	New Magnet	BABAR/sPHENIX Magnet
Maximum Central Field (T)	3	1.5
Coil length (mm)	3600	3512
Warm bore diameter (m)	3.2	2.8
Uniformity in tracking region (z = 0, r < 80 cm) (%)	3	3
Conductor	NbTi in Cu Matrix	Al stabilized NbTi
Operating Temperature (K)	4.5	4.5

Table 11.1: Summary of some of the main requirements of the EIC detector solenoid magnet.

The main advantage of accessibility of low central solenoid fields (down to ~0.5 T) is towards the low-PT acceptance of charged-particle tracks. A central field of 0.5 T roughly equates to a detection capability of charged particles down to transverse momenta of below ~ 0.1 GeV/c. This is for example relevant for

mapping the decay products of heavy-flavor mesons. The main advantage of a 3 T versus a 1.5 T central solenoid field is for the momentum resolution of charged particles as function of pseudo-rapidity. Doubling the magnetic field can lead to a reduction of the momentum resolution by a factor of ≈2 from a leading order $\sim 1/B$ dependence. This is relevant in the central region, but even more so in the forward pseudo-rapidity regions, $\eta > 2$, where the momentum resolutions rapidly worsen. For example, for $\eta \sim 3$, a momentum resolution of ∼2-3% is achievable for pions with momenta up to about 30 GeV/c with a 3 T central field, and only double that resolution for a 1.5 T central field.

11.2 Tracking

11.2.1 Introduction

This section represents an attempt to combine the requirements from the physics working groups and tracking technologies and detector design into viable detector concepts that can meet these requirements. These concepts contain assessments of the current state of the art in both the technologies, services, mechanical support and other components to deliver a design that is deemed to be consistent with what can reasonably be expected to be deployed at the EIC in the needed timescales. In order to reduce risk and ensure that the needed development proceeds apace with the construction schedule, a set of areas of targeted R&D have also been generated and are presented in Chapter 14.

11.2.2 Main requirements and acceptance coverage

η	θ	Nomenclature			Tracking					
					Resolution	Relative Momentum	Allowed X/X_0	Minimum-pT	Transverse Pointing Res.	Longitudinal Pointing Res.
< -4.6		↓ p/A	Far Backward Detectors	low-Q2 tagger						
-4.6 to -4.0										
-4.0 to -3.5										R
-3.5 to -3.0			Central Detector	Backward Detector		σ_p/p ~0.2%×p⊕5%	~5% or less X	70-150 MeV/c (B=1.5 T)		
-3.0 to -2.5										
-2.5 to -2.0						σ_p/p~ 0.04%×p⊕2%				
-2.0 to -1.5									dca(xy) ~ 40/pT μm ⊕ 10 μm	dca(z) ~ 100/pT μm ⊕ 20 μm
-1.5 to -1.0										
-1.0 to -0.5				Barrel		σ_p/p ~0.04%×p⊕1%		200 MeV/c	dca(xy) ~ 30/pT μm ⊕ 5 μm	dca(z) ~ 30/pT μm ⊕ 5 μm
-0.5 to 0.0										
0.0 to 0.5										
0.5 to 1.0										
1.0 to 1.5				Forward Detectors		σ_p/p ~0.04%×p⊕2%		70 - 150 MeV/c (B = 1.5 T)	dca(xy) ~ 40/pT μm ⊕ 10 μm	dca(z) ~ 100/pT μm ⊕ 20 μm
1.5 to 2.0										
2.0 to 2.5										
2.5 to 3.0						σ_p/p ~0.2%×p⊕5%				
3.0 to 3.5										
3.5 to 4.0		↑ e		Instrumentation to separate charged particles from photons						R
4.0 to 4.5										Not
> 4.6			Far Forward Detectors	Proton Spectrometer						
				Zero Degree Neutral Detection						

Figure 11.1: Requirements Table

The requirements for the tracking in an EIC detector are derived from the physics simulations and are represented by the detector requirements table. This is shown in table 11.1: The ranges in pseudorapidity are accompanied with requirements for momentum resolution, allowed radiation length, minimum pT cutoff and transverse and longitudinal pointing resolution. These requirements form the basis of the designs that are presented.

11.2.3 Technology survey

11.2.3.1 Silicon Detector Technologies for EIC

[TEXT BY LAURA GONELLA - 16 NOVEMBER 2020]

To satisfy the requirements detailed above, the EIC silicon vertex and tracking (SVT) detector needs ot have high granularity and very low material budget. Performance simulations of the detector concepts presented in 11.2.5.4.1, 11.2.5.2 highlight the need for: - a spatial resolution $\leq 5\mu m$ in tracking layers and disks, and around 3 μm in the vertex layers; - a material budget $\leq 0.1\% X_0$ in the vertex layers, $\leq 0.8\% X_0$ in the tracking layers and $\leq 0.3\% X_0$ in the disks.

The stringent requirements for the vertex layers are driven by the rather large beam pipe radius and are necessary to obtain the required vertex reconstruction performance. This is shown in Figure 11.2. Pre-CD0 simulations assumed a beam pipe radius of 18 mm and an ALICE ITS2 derived SVT detector where vertexing layers and disks had a material budget of 0.3% X/X_0 per layer, and the tracking layers had a material budget of 0.8% X/X_0 per layer. The pixel size was 20×20 μm^2. This configuration gives the transverse pointing resolution described by the green curve in Figure 11.2. With the updated beam pipe radius of 31 mm, this configuration would lead to a severe decrease in tracking performance (blue curve). The transverse pointing resolution can be recovered, and even improved, with higher granularity and lower material budget. The result in the red curve assumes a configuration based on the ALICE ITS3 technology explained below, where the vertexing layers have a material budget of 0.05% X/X_0 per layer, the tracking layers 0.55% X/X_0 per layer, and the disks each have a material budget of 0.24% X/X_0. The pixel size is 10×10 μm^2.

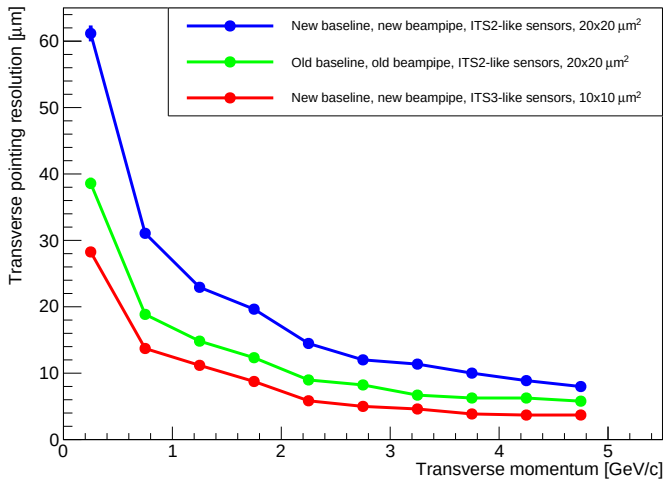

Figure 11.2: Transverse pointing resolution versus transverse momentum, comparing the ALICE ITS2 based detector configuration with old (green) and new (blue) beam pipe, and the ALICE ITS3 based detector configuration with new beam pipe (red).

In addition to these requirements, an EIC SVT detector needs to be designed with an integration time below to 2 μs to cope with the interaction frequency expected at the highest luminosity, i.e. 500 kHz at 10^{34} cm^{-2} s^{-1}. These requirements drive the choice of the silicon detector technology.

A broad survey of silicon detector technologies has been presented and discussed at the first EIC Yellow Report Workshop in March 2020 [1] covering hybrid pixel detectors, strip detectors, Low Gain Avalanche Detectors (LGAD), the DEPFET sensor, and Monolithic Active Pixel Sensors (MAPS). The survey has considered existing examples of these detectors as well as the silicon technologies used for their development to understand their potential for application at the EIC. MAPS have been identified as the best detector technology to satisfy the requirements of the EIC SVT and are discussed below. These detectors provide the highest granularity, lower power consumption and consequently lower material budget, as well as the required readout speed in one device. Recent development of these devices are the only option to satisfy the requirements of the EIC vertex layers 11.2.3.1.2. The integration of charge collection and readout capabilities into one silicon substrate is well suited for the required level of integration and acceptance coverage of the EIC SVT. Silicon technologies such as LGAD and SOI whose developments in the next few year could produce a viable alternative for the EIC SVT are presented in [reference to chapter 14].

11.2.3.1.1 MAPS

[TEXT BY LAURA GONELLA - 16 NOVEMBER 2020]

MAPS are currently used as vertex detectors in the STAR Heavy Flavour Tracker [2] and in the upgraded ALICE Inner Tracker (ITS2) [3]. The latter deploys the ALPIDE sensor [4]. This sensor represents a breakthrough with respect to traditional MAPS such as the MIMOSA used by the STAR experiment. ALPIDE is fabricated in a commercial 180 nm CMOS imaging process provided by Tower Jazz (TJ). The main novelty of this device is the possibility to partially deplete the substrate and thus collect part of the charge by drift, and to integrate both PMOS and NMOS transistors. These features have improved MAPS charge collection properties, radiation hardness, and signal processing capabilities. Figure 11.3 shows the cross-section of an ALPIDE pixel. This design retains as in previous MAPS generations a small collection electrode and thus a small sensor capacitance of a few fF that is key to low power, low noise, fast sensor readout, and compact front-end electronics design for small pixel pitch.

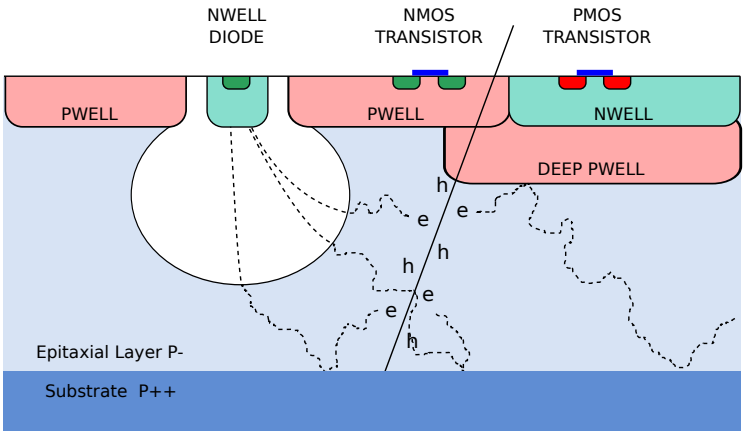

Figure 11.3: Cross-section of an ALPIDE pixel, showing the small n-type collection electrode and the p-wells containing the electronics in a p-type epitaxial layer. A small depletion region develops around the collection electrode for an applied reverse bias voltage of a few volts [3].

Following on from the ALPIDE, a new generation of MAPS sensors has been developed in the past ten years with the goal of reaching the rate and radiation tolerance capability typically required by high luminosity

particle physics experiments. These so-called Depleted MAPS (DMAPS) are fabricated in High Voltage or High Resistivity commercial 150/180 nm CMOS imaging technologies and can be fully depleted. A number of prototypes have been fabricated targeting the upgrades of the ATLAS pixel detector for the HL-LHC in different CMOS technologies. The ATLASPix sensor in the AMS/TSI technology [5] and the LF-MONOPIX in the LFoudry technology [6] feature a large collection electrode that contains the electronics. This results in a uniform electric field in the sensor substrate needed to achieve the required speed and radiation hardness but comes at the price of high sensor capacitance. The MALTA and TJ-MONOPIX prototypes in the TJ 180 nm technology [6–8] keep the small collection electrode and achieve full depletion with a modification of the process by adding a deep n-implant so that the depletion region grows from below the collection electrode and electronics implant [9, 10]. These sensors have demonstrated to fulfil the requirements of operation at the HL-LHC, but use at the EIC SVT would have to be demonstrated as they have been designed to match very different requirements. An application of the MALTA sensor for tracking at large z is described in 11.2.5.3.

It is however important to note that the CMOS imaging technologies in which existing DMAPS prototypes have been fabricated could be used to design a dedicated MAPS sensor for the EIC SVT. In particular, the TJ 180 nm modified CMOS imaging process is very interesting because of the benefit of the small sensor capacitance towards low power and fine pitch. This technology has been positively evaluated for use at the EIC by the eRD18 project, a collaboration between the University of Birmingham and the RAL CMOS Sensor Design group (CSDG), in the framework of the EIC Generic Detector R&D programme [11].

Recently, an effort is emerging to develop a third generation MAPS in a 65 nm CMOS imaging technology. A large community is gathering to develop this process for future experiments through the ALICE ITS3 project and the CERN EP R&D programme. This path is more attractive for the development of an EIC MAPS as the 65 nm technology offers improved performance in terms of granularity and power consumption that are key for precision measurements at the EIC, as well as process availability on the EIC project timescale. The drawbacks with respect to older technology nodes are higher non recurring engineering (NRE) costs and complexity.

A joint EIC SVT sensor development has started with the ALICE ITS3 group [12]. The ALICE ITS3 project aims at developing a new generation MAPS sensor at the 65 nm node to build an extremely low mass detector for the HL-LHC. The ITS3 sensor specifications and development timescale are largely compatible with those of the EIC. Furthermore, non-ALICE members are welcome to contribute to the R&D to develop and use the technology for other applications. Having joined the ITS3 collaboration, the EIC can leverage on a large effort at CERN, sharing development costs, to design an innovative sensor solution at the 65 nm node, suited for an experiment starting in approximately 10 years and demonstrating the capabilities of this technology for future proposed collider experiments.

11.2.3.1.2 65 nm MAPS SVT detector

[TEXT BY LAURA GONELLA - 16 NOVEMBER 2020]

An EIC SVT concept is being developed based on the proposed 65 nm MAPS sensor and ITS3 detector concept [13]. Both baseline configurations presented under investigation (11.2.5.2, 11.2.5.4.1) assume the use of this technology to define pixel pitch and realistic estimates of material budget for services and support structure [14], and configuration of the vertex layers. In addition to the advantages discussed in 11.2.3.1.1, joining the ITS3 development has additional benefits.

Figure 11.4 compares the specifications for the proposed ITS3 sensor to the ones of the existing ALPIDE. Figure 11.5 shows preliminary specifications for an EIC sensor. From these it is clear that the ITS3 fully satisfies and even exceeds the requirements of the EIC SVT with higher granularity, lower power consumption, shorter integration time and lower fake hit rate. In particular, the 10 μm pixel pitch is key to the design of the vertex layers (Figure 11.2).

ALICE

Specifications

Parameter	ALPIDE (existing)	Wafer-scale sensor (this proposal)
Technology node	180 nm	65 nm
Silicon thickness	50 µm	20-40 µm
Pixel size	27 x 29 µm	O(10 x 10 µm)
Chip dimensions	1.5 x 3.0 cm	scalable up to 28 x 10 cm
Front-end pulse duration	~ 5 µs	~ 200 ns
Time resolution	~ 1 µs	< 100 ns (option: <10ns)
Max particle fluence	100 MHz/cm^2	100 MHz/cm^2
Max particle readout rate	10 MHz/cm^2	100 MHz/cm^2
Power Consumption	40 mW/cm^2	< 20 mW/cm^2 (pixel matrix)
Detection efficiency	> 99%	> 99%
Fake hit rate	< 10^{-7} event/pixel	< 10^{-7} event/pixel
NIEL radiation tolerance	~3 x 10^{13} 1 MeV n_{eq}/cm^2	10^{14} 1 MeV n_{eq}/cm^2
TID radiation tolerance	3 MRad	10 MRad

M. Mager | ITS3 kickoff | 04.12.2019 | 5

Figure 11.4: Specifications for the ALICE ITS2 ALPIDE sensor and the proposed sensor for the ITS3 upgrade.

Parameter	EIC Vertex and Tracking MAPS
Technology	65 nm (Backup: 180 nm)
Substrate Resistivity [kohm cm]	≥ 1
Collection Electrode	Small
Detector Capacitance [fF]	< 5
Chip size [cm x cm]	Full reticule or stitched
Spatial resolution [µm]	≤ 5 3 for vertex layers
Integration Time [µs]	≤ 2
Timing Resolution [ns]	< 9 (optional)
Particle Rate [kHz/mm^2]	**TBD**
Readout Architecture	Asynchronous
Power [mW/cm^2]	< 20
NIEL [1MeV neq/cm^2]	10^{10}
TID [Mrad]	< 10
Noise [electrons]	< 50
Fake Hit Rate [hits/s]	< 10^{-5}/evt/pix
Interface Requirements	**TBD**

Figure 11.5: Preliminary specifications for an EIC SVT MAPS sensor based on simulations by the eRD18 (Birmingham/RAL CSDG) and eRD16 (LBNL) projects of the EIC Generic Detector R&D programme.

The ITS3 project is taking an integrated approach where design and post-processing techniques are com-

bined to develop a three-layer vertex detector with an extremely low material budget (Figure 11.6). The use of low power design techniques, large area, 2D stitched sensors thinned below 50 μm and bent around the beam pipe minimises cooling, support structure and services in active area allowing to reach a material budget of only 0.05% X_0. Such detector concept is a very attractive solution for the EIC vertex layers where extremely low material budget coupled with the sensor's high granularity will deliver the required vertex resolution (Figure 11.2). The implementation of the ITS3 detector concept into the EIC vertex layers is currently being worked out by the EIC Silicon Consortium.

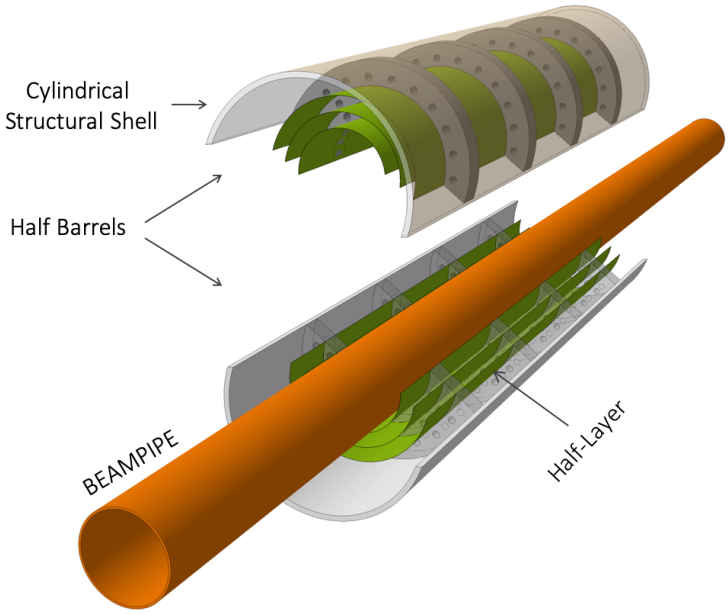

Figure 11.6: Layout of the ITS3 Inner Barrel. The figure shows the two half-barrels mounted around the beampipe [12].

Despite the large overlap, the EIC and ITS3 detectors have some significant differences, most notably the size. The ITS3 is a 0.12 m^2, three layers vertex detector. The EIC SVT baseline configurations presented in (11.2.5.2, 11.2.5.4.1) have an area of approximately 12 m^2 and 15 m^2, for hybrid and all-silicon respectively. Cost and yield of stitched wafer-scale sensors will not be compatible with use in the EIC detector outside the vertex layers. For the tracking layers and disks the EIC sensor development will fork off the ITS3 sensor design path to develop a reticule-size version of the ITS3 sensor (no changes in other aspects of the sensor design are foreseen a part from its size) as well as a more conventional design of support structures (classical staves and disks), where dedicated engineering solutions will be deployed to meet the material budget constraints [14].

11.2.3.2 Alternative Silicon Sensors

[Edited by Xuan Li on behalf of the LANL EIC team, on Nov. 3rd]

[COMMENT BY LAURA: as discussed at the last YR working group meeting, MAPS are covered above including the ones mentioned here. I have added explicitly now that MALTA is proposed for the LANL detector concept and put a reference to 15.3. The LGAD, as well as SOI, will be discussed in the write-up

that Leo prepared and circulated to us for review, and will be in chapter 14. I would suggest the following, if Xuan and Leo agree: remove this section as part of the information is covered elsewhere, but add in 15.3 explicitly why you choose MALTA for the disks at high Z. I suppose you might do anyway to justify why MALTA and not MPGDs for instance. I also do not understand the comment on needing ASIC development. MAPS do not need a separate ASIC, the readout is fully integrated in the same substrate which is the attractiveness of this solution. The production line will also not be the same for MALTA and ITS3 sensor. The technology is from TJ for both but one is 180 nm and the other 65nm. These are very different production lines and imaging processes.]

The proposed silicon vertex/tracking detector will be built around the beam pipe and is close to the beam interaction region of the EIC. High beam background such as synchrotron radiation generated by keV electrons and MeV neutron gas could generate dead areas in the silicon detector which significantly impacts on its vertex/tracking capability. To achieve precise measurements in Semi-Inclusive Deeply Inelastic Scattering (SIDIS) processes, event separation from different collisions is required. A radiation hard and fast timing silicon detector, which can survive the accidental beam injection onto the detector and is capable to separate the 1-10ns EIC bunch crossings, will enhance the physics measurement precision and could reduce the correlated systematical uncertainties.

To meet these requirements, various silicon technology options have been considered, which are 1) High-Voltage Monolithic Active Pixel Sensor (HV-MAPS) and 2) the Low Gain Avalanche Detector (LGAD). The HV-MAPS technology process fully depleted charged particle propagation inside the active silicon region. This technology can reach relatively low material budgets (< 0.5%X per layer), fine spatial resolution (< 10 μm) and fast timing (< 5 ns). The ongoing R&D will further improve the performance for the next-generation sensor production. Meanwhile, we also consider the LGAD [15–18] or AC-LGAD [19] technology to be placed in the most forward planes, which can provide fast time stamping to separate different bunch crossings. The HV-MAPS technology such as MALTA [20–22], ATLASPIX3 [23] or Mupix [23] could be implemented for the EIC day-1 detector. The LGAD or AC-LGAD technology could be used for EIC detector upgrade depends its R&D progresses. The performance of the LGAD (AC-LGAD) and MALTA technology has been summarized in Table 11.27.

Parameter	LGAD or AC-LGAD	MALTA
Technique	Low Gain Avalanche Diode	180 nm Tower Jazz DMAPS
Pixel size	current 1.3mm × 1.3mm towards 100 μm × 100 μm, ~ 10 μm spatial resolution is achieved with the new design.	36.4 μm × 36.4 μm, ~ 7 μm spatial resolution.
Integration time	300-500 ps	< 5 ns
Thickness per layer	$< 1\%X_0$	$< 0.5\%X_0$
Power consumption	under R&D	80 mW/cm^2
Noise level	under R&D	10^{-5} with low threshold
Radiation tolerance	$\sim 1.5 \times 10^{15}$ n_{eq}/cm^2	$> 10^{15}$ n_{eq}/cm^2

Table 11.2: Comparison of the LGAD and MALTA sensor performance

The advantages of the MALTA technology are: 1) prototype sensor and front-end readout electronics exist; 2) its spatial and temporal resolutions have been demonstrated by previous/ongoing bench/beam tests; 3) this technology with further developments could be in production stage in around 2 to 3 year time scale. The power consumption of the MALTA sensor is relatively higher than the ALPIDE sensor. Although it is in a reasonable scale, additional R&D for the next generation sensor developments and dedicated mechanical structure design are needed. The advantages of the LGAD technology are: 1) prototype sensor and front-end readout electronics exist; 2) fast timing (20ps) provided by the LGAD technology can not only be used for time stamping but also for PID purpose. This technology is in early R&D stage, and the full readout chain needs to be defined.

The required R&D path includes back-end electronics and the readout full chain developments. The most critical (urgent) item is ASIC design and readout developments. The HV-MAPS technology (e.g. MALTA) can use the same production line as the ITS-3 technology. We could share the R&D on sensor developments, readout integration and EIC silicon/vertex detector conceptual design. The approximated timeline for the relevant R&D is: Ongoing detector R&D work which includes the silicon sensor characterization and down selection supported by the LANL LDRD project from 2020 to 2022. Continued R&D efforts which focus on the readout chain developments for the EIC day-1 detector from 2022 to 2025 depend on additional funding availability. This is a rough estimate and may change depends on the schedule.

11.2.3.3 Gaseous Tracking Detector Technologies

11.2.3.3.1 Time Projection Chambers (TPC)

A TPC is an option for the central detector in an EIC detector. It will provide required momentum resolution for the physics program at an EIC and is also a detector that can deliver PID by means of dE/dx.
A TPC is presently under construction for the sPHENIX experiment which is expected to start taking data in IP8 of RHIC, in 2023. The sPHENIX-TPC is a compact detector with a minimum material budget in the central region. It has been also designed with an eye toward the use in an EIC detector. This concerns the minimization of the material budget in the forward region which takes into account not only the front-end electronics but also necessary infrastructure, like mounting structure and cooling.
The TPC design follows the classical cylindrical double-sided TPC layout, with a cathode located at the middle of the interaction region dividing the TPC into two mirror-symmetric volumes. The end-caps of the TPC accommodate gas-amplification modules in a subdivided arrangement; 12 sectors in azimuth and 3 sectors in radial extension. This results in a total of 72 readout modules for both end-caps. An illustration can be seen in Fig. 11.7. The physics program with the sPHENIX detector requires excellent pattern recognition as well as excellent momentum resolution. One of the performance parameters to be fulfilled for the sPHENIX program is the separation of the Y-states which requires a momentum resolution from the TPC in the order of $\Delta p/p \approx 1.2\% \times p(GeV/c)$. This translates to a required position resolution $\sigma_{r\phi} \lesssim 300\mu m$ with 40 track points in the sPHENIX TPC. This requirement is relaxing with more space points. A test-beam campaign with a TPC prototype verified that this resolution goal more than achievable, see Fig. 11.8,
The TPC has to be operated in a gate-less configuration such that the readout is not limited due a severe dead-time. This requires in turn the use of Micro Pattern Gas Detectors (MPGDs). For the sPHENIX TPC the choice was made to use a quadruple-GEM avalanche structure, similar to the solution that has been implemented in the ALICE-TPC at the LHC. The operating point of the GEM-stack has been adapted to the sPHENIX environment.

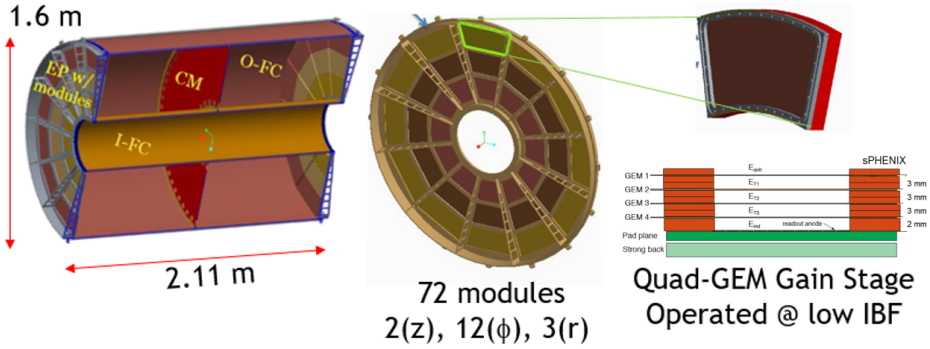

Figure 11.7: Pictorial diagram of the sPHENIX TPC. The gas volume and thus the active registration volume for charged particle tracks is between the inner field-cage (I-FC) and the outer field-cage (O-FC). The cathode consist of a thin metallized membrane.

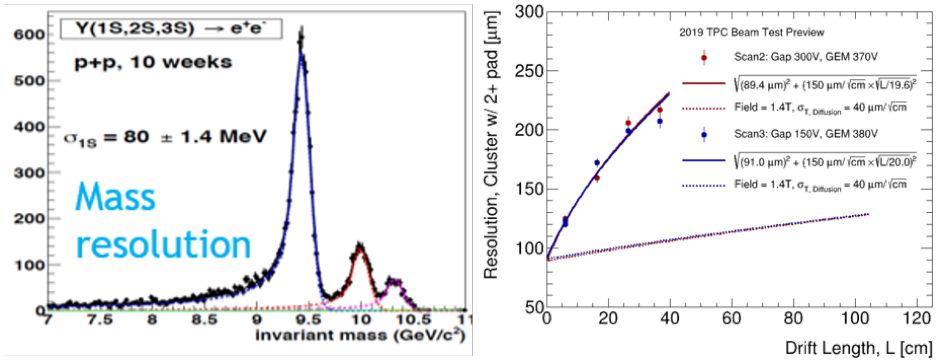

Figure 11.8: Left: simulation for the mass resolution sufficient to separate Upsilon states. Right: test-beam results extrapolated to sPHENIX conditions.

Gas Amplification The goal to limit space charge effects requires a low ion-back flow from the amplification device into the main tracker gas volume. A vast R&D program to this extent has been performed by the ALICE collaboration and the experience gained there directly affected the design choices for the sPHENIX TPC. One of the R&D results can be seen in Fig. 11.9, left. For the sPHENIX program the energy resolution does not play a role, hence the operating point for the readout has been chosen around the minimum IBF ($\sim 0.3\%$). For the EIC program this choice can be modified to gain back good energy resolution: the space charge effects in an EIC TPC might be less severe. Studies on the effect of space are ongoing. In principle, there are already solutions in the prototype stage if it turns out that IBF will play a similar role in an EIC environment (see next paragraph). The gas choice for the sPHENIX TPC is based on Ne-CF_4 because of its advantageous properties: 1) high drift velocity, 2) low transverse diffusion and 3) comparatively fast ion drift velocity. The Neon component could be exchanged with Argon which provides a higher ionization yield and therefore improves dE/dx performance. Other gas components can be added to the gas mixture which is under consideration for optimizing the TPC for EIC purposes. It is worth the mentioning that the sPHENIX configuration has been investigated in a test-beam environment with a modified operating point and promising dE/dx performance has been measured.An alternative to the quadruple GEM readout option is the MM2G option. It consists of a double-GEM layer on top of a MicroMegas as the main amplification device, hence the term MM2G. The double-GEM structure provides the necessary field ratios to maintain a

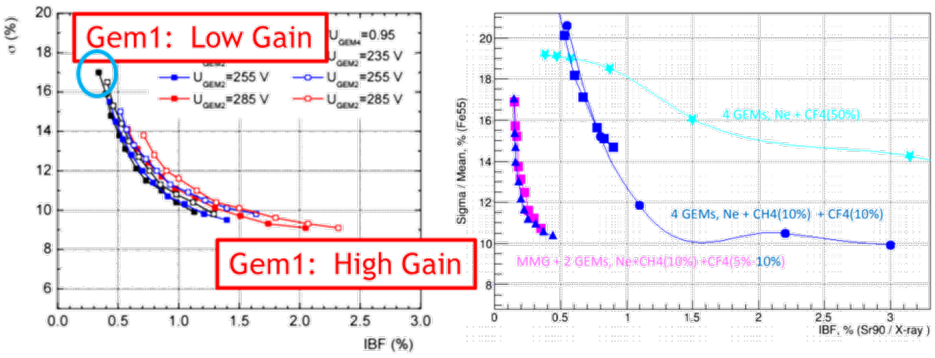

Figure 11.9: Left: Operation regime for a quadruple-GEM amplification for a Ne-CO_2 gas mixture. The trend for the behavior of energy resolution vs. IBF can be attributed to the gain of the first GEM. Right: comparison of the operation regime between a MM2G and quadruple-GEM amplification with various gas mixtures.

low IBF and act as pre-amplifier. It has been shown that it is possible to obtain a low IBF while maintaining an energy resolution of better than 12% (Fig. 11.9, right).

Modifications to the sPHENIX TPC A major modification of the TPC presently under construction for sPHENIX will be the recovery of about 10 cm vertical track length. The design for sPHENIX was chosen such that the first 10 cm in radial extension will not be read out electronically. This choice has its origin in that space charge distortions, i.e., deflections from the ideal electron trajectory are largest in the vicinity of the field cage. Therefore, the space charge distortions will be still real within the vicinity of the field-cage, however, the track information from this part will not be considered and therefore not electronically read out. This can be easily reverted in the EIC era.
A modified readout pad-geometry with perhaps a modified readout electronics might improve the performance for the TPC in the EIC era. However, these are topics which are discussed in the Section **??**.

11.2.3.3.2 Micro Pattern Gaseous Detectors (MPGDs)

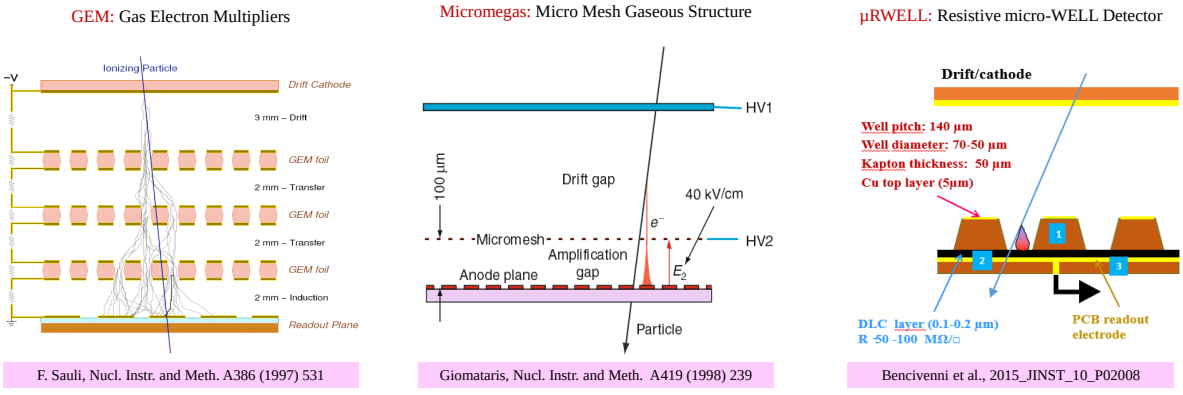

Figure 11.10: Cross sectional view of mature MPGD Technologies for tracking: Triple-GEM detector [24], *(left)*; Micromegas [25], *(center)*; µRWELL detector [26], *(right)*.

MPGD technologies such as Gas Electron Multiplier (GEM) [24], Micro Mesh Gaseous Structures (Micromegas) [25], Resistive Micro Well (μRWELL) [26] are widely used for tracking in various particle physics experiment across the world such as the COMPASS [27], LHC main detectors upgrade (ATLAS, CMS ALICE & LHCB) at CERN, SBS [28], CLAS12 [29], PRad [30], MOLLER [31] and SoLID [32] at Jefferson Lab, STAR FGT and PHENIX HDB at BNL. These technologies typically combine a gaseous device for electron amplification with high granularity strips or pads anode readout PCB to provide a combined excellent 2D space point resolution ($\approx 50\,\mu m$), fast signal ($\approx$ 5ns), high rate capabilities ($\approx MHz/cm^2$), low material budget ($\approx 0.5\%X_0$) per layer, radiation hardness and large area capabilities at a significantly lower cost compared to silicon trackers.
An extensive R&D program conducted by the eRD6 Consortium [33] within the EIC Generic Detector R&D program is dedicated to the development and optimization of MPGD technologies as main tracker in the central region of an baseline EIC hybrid tracker as descried in section 11.2.5.4. In this hybrid configuration, two options, both of them involving MPGD detectors, are under study for the barrel tracker. The first option has a TPC detector (see section 11.2.3.3.1) for the main tracker with a MPGD device or a combination of two MPGD devices for electron amplification and readout in the TPC end cap. The alternative to the TPC in barrel region explores large cylindrical Micromegas or μRWELL layers for the main tracker. Both TPC and and cylindrical MPGDs options are complemented in the hadron end electron end caps by planar MPGD discs. Performances studies for various geometrical configurations of the planar MPGD layers in the end cap regions are reported in section 11.2.5.4.3

11.2.3.3.3 Drift Chambers & Straw Tubes (DCs)

Grancagnolo...

11.2.3.3.4 Small-strip Thin Gap Chambers (sTGCs)

Small-strip thin gap chambers (sTGC) detector technology was developed for the ATLAS new small wheel upgrade [34]. A modified version of the sTGC tracker, based on the ATLAS design, is being used for the STAR forward rapidity upgrade [35]. The small-strip thin gap chamber detector technology offers a reasonably good space-point resolution ($\approx 100\mu$m) and low material budget $\sim 0.5X_0$ per layer, for a relatively low cost compared to various other technologies. The sTGC as designed by ATLAS for the new small wheel upgrade consists of a grid of 50μm diameter gold-plated tungsten wires with a 1.8mm pitch sandwiched between two cathode planes 1.4mm from the wire plane. The sTGC wires operate at 2.9 kV in a gas mixture of 55% CO_2 and 45% n-pentane. The sTGC modules feature both strip and pad readout. Copper strips with a pitch of 3.2 mm are located on one of the anode planes and run perpendicular to the wires. Large rectangular readout pads, useful for fast triggering, are located on the other anode plane. An illustration of the basic design of an sTGC is shown in Fig. 11.11.

While position resolution better than 50μm has been achieved in test beam studies [36], in practice, the sTGC strip readout is expected to provide position resolution on the order of $100 - 150\mu$m, depending on the charged track's incident angle. The ATLAS new small wheel setup employs sTGC modules with strips aligned to provide precise position measurement in the bending coordinate, with measurement of the azimuthal information provided by wire readout. The STAR forward upgrade application employs sandwiches of two layers of sTGC modules with one layer providing precise x-position measurements and the other layer providing precise y-position measurements [35, 37]. In addition, the design used by STAR replaces

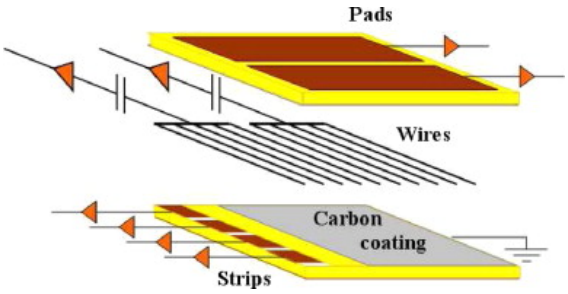

Figure 11.11: Schematic diagram of the basic sTGC structure reproduced from [36].

pads on one of the two layers with diagonal strips to help improve space point reconstruction.

Since the sTGC detectors are highly cost-effective with a low material budget and robust up to single hit rates of 100 kHz/cm^2, they are a suitable technology choice for large area planar regions of tracking. Specifically, sTGC layers could be employed for tracking in the hadron-going (forward) direction at a $z \approx 300$ cm beyond the Ring Imaging Cherenkov (RICH) detector. The sTGC may be a good choice for tracking in this region, beyond the central tracking and PID detectors, where the magnitude of the multiple scattering effects will be larger rendering precise space point resolution less important. Similarly, sTGC planes may be a viable cost-effective option for the regions that require large area trackers in the electron-going (backward) direction.

11.2.4 Comparison of Technology Choices

Domenico, Kondo, Leo ...

11.2.5 Detector concepts and performance studies

In this section we present two baseline detector concepts. The first is an all-silicon set of tracking layers and discs. The second concept is a hybrid design that contains silicon tracking layers and discs with a gaseous tracking detector surrounding the silicon based barrel layers. Each of these designs has particular strengths. In the all-silicon case, the full tracking detector can be realized in a comparatively compact form while retaining excellent tracking capabilities. In the hybrid case, the gaseous detector can provide dE/dx measurements that can add to the PID capabilities while maintaining tracking that meets the EIC requirements. It is hoped that the inclusion of two simulated baseline configurations will aid in the selection of a detector that will contain optimizations based on the full set of overall detector requirements. In addition, these options may aid in the formulation of complimentary detector configurations for the second interaction point. The detector performance for each detector baseline in comparison to the physics derived requirements can be found in summary tables in the concluding Summary section of the tracking chapter.

11.2.5.1 All-Silicon Tracking Option

11.2.5.2 Baseline All-Silicon Tracking Option (Barrel & End Caps)

A pixelated all-silicon tracker prototype for the EIC is shown in Fig. 11.12 (left). The detector is cylindrically symmetric and has three main regions: a 6-layer barrel in the mid-rapidity region, 5 disks in the forward

Table 11.3: Main barrel-layer characteristics.

Barrel layer	radius [cm]	length along z [cm]
1	3.30	30
2	5.70	30
3	21.00	54
4	22.68	60
5	39.30	105
6	43.23	114

Table 11.4: Main disk characteristics.

Disk number	z position [cm]	outer radius [cm]	inner radius [cm]
-5	-121	43.23	4.41
-4	-97	43.23	3.70
-3	-73	43.23	3.18
-2	-49	36.26	3.18
-1	-25	18.50	3.18
1	25	18.50	3.18
2	49	36.26	3.18
3	73	43.23	3.50
4	97	43.23	4.70
5	121	43.23	5.91

region, and 5 disks in the backward region. The extent of the tracker along the beam axis is identical in both directions, a constraint consistent with the current choice to have the nominal beam collision point coincide with the geometric center of the overall general purpose detector concepts. In the barrel region, the trade-off from pairing layers to gain momentum-resolution performance is primarily with the momentum measurement threshold, $2p_T \simeq 0.3B \cdot r$ (about 0.2 GeV for a representative $B = 3$ T and $r \simeq 0.4$ m). Pairing of layers also reduces the number of stave designs and associated tooling. In the all-silicon concept under consideration, the layers that constitute the barrel are thus paired with the outermost pair at $\simeq 0.4$ m and the intermediate pair near the mid-point to the beam axes to best capture the sagitta. The transition between the outer barrel layers and the disks is near $|\eta| \simeq 1.1$ to minimize the amount of traversed material. Further details on the barrel and disk geometries are presented in tables 11.3 and 11.4, respectively. In this concept, the innermost barrel layers drive the vertexing performance. Their length (well) exceeds the extent of the $\simeq 8$ cm beam-collision region and is chosen to accept (displaced) tracks for $|\eta| \lesssim 2$ without relying on track-pointing with the disks, which will near-inevitably involve tracking across inactive material from services and supports in this region of the detector. The dominant parts of the services and supports are thought to be guided out in a projective way along the transition angle between the barrel and the disks. This is modeled in a simplified form as an effective 5-mm-thick aluminum cone in the performance simulations thus far; engineering evaluations remain to be done. This geometry is wrapped around the EIC beam pipe, which in the region $-79.8 < z < 66.8$ cm corresponds to a 3.17-cm-radius beryllium cylinder of thickness of 760 μm.

In this configuration, the detector is made up of ALICE-ITS3-like staves, each having an average material budget of $X/X_0 = 0.3\%$. These staves, assembled into the detector geometry, contribute the amount of material shown in Fig. 11.12 (right). Since the staves form a periodic but changing material budget, the azimuth (ϕ) is swept for each pseudorapidity ($\eta \equiv -\ln(\tan\theta/2)$, where θ is the polar angle) direction, and the minimum and maximum found X/X_0 define the width of the uncertainty band. Overall, the active areas of the detector provide a material budget of $X/X_0 < 5\%$. The support structure adds a significant amount of material. The projective design of this structure ensures that most of this material is concentrated in a small pseudorapidity range, at $|\eta| \approx 1.1$.

This configuration was studied and optimized using the Geant-4-based Fun4All framework [38–40]. Mo-

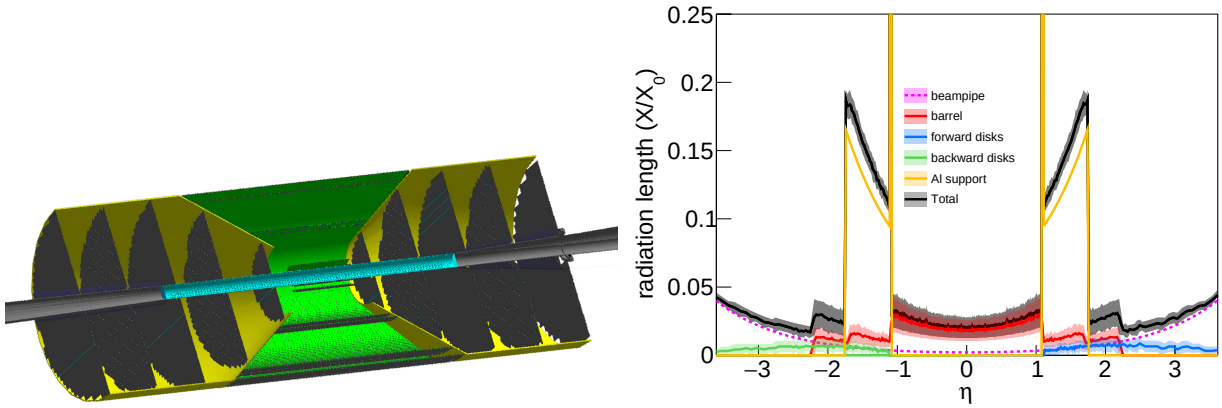

Figure 11.12: All-silicon tracker geometry. Left: Geant-4 schematic of the tracker cross section. The barrel, disks, and support structure correspond to the green, dark-gray, and yellow components, respectively. The beryllium section of the beam pipe is shown in cyan. The rest of the beam pipe, which takes into account the expected electron-hadron-beam crossing angle is shown in light-gray. Right: Detector material scan. The dashed line describes the baseline material budget from the beam pipe. The red, blue, and green curves correspond to the barrel, forward, and backward components of the detector, respectively. The uncertainty band defines the minimum and maximum amounts of material found in a given η as the material is scanned around ϕ. The yellow curve describes the aluminum support structure. See text for details.

mentum, pointing, and angular resolutions at the vertex were studied by bombarding the detector over the entire acceptance with single particles (charged pions, electrons, and protons) generated in the momentum range of $0 < p < 30$ GeV$/c$ with a fixed vertex at $(x, y, z) = (0, 0, 0)$, and reconstructing their tracks with the detector. The simulated silicon-pixel size corresponds to 10 μm (point resolution $= 10/\sqrt{12}$ μm). The studies were carried out with magnetic-field maps describing the BaBar (1.4 T) [41] and Beast (3.0 T) [42, 43] solenoids.

The fractional momentum resolution is determined as the standard deviation of a normal function fitted to the $\Delta p/p \equiv (p_{truth} - p_{reco})/p_{truth}$ distribution. Here, the labels 'truth' and 'reco' represent generated and reconstructed variables, respectively. Momentum-resolution results for pions are shown as a function of pseudorapidity in Fig. 11.13 (left). As expected from the leading-order $\sim 1/B$ dependence of the momentum resolution, doubling the magnetic field reduces the momentum resolution by a factor of ≈2. The resulting distributions were characterized via fits with the functional form

$$dp/p = Ap \oplus B, \tag{11.1}$$

where $\oplus$ is shorthand notation for sum in quadrature. The A and B fit parameters are presented in Table 11.5.

The Distance of Closest Approach (DCA) is defined as the spatial separation between the primary vertex and the reconstructed track projected back to the z axis (DCA_z) or to the $x-y$ plane (DCA_T). The DCA resolutions were determined as the standard deviation of normal functions fitted to the DCA_z and DCA_T distributions. DCA-resolution results as a function of transverse momentum (p_T) for pions are shown in Fig. 11.13 (center and right). The resulting distributions were characterized via fits with the functional form

$$\sigma(\mathrm{DCA}) = A/p_T \oplus B. \tag{11.2}$$

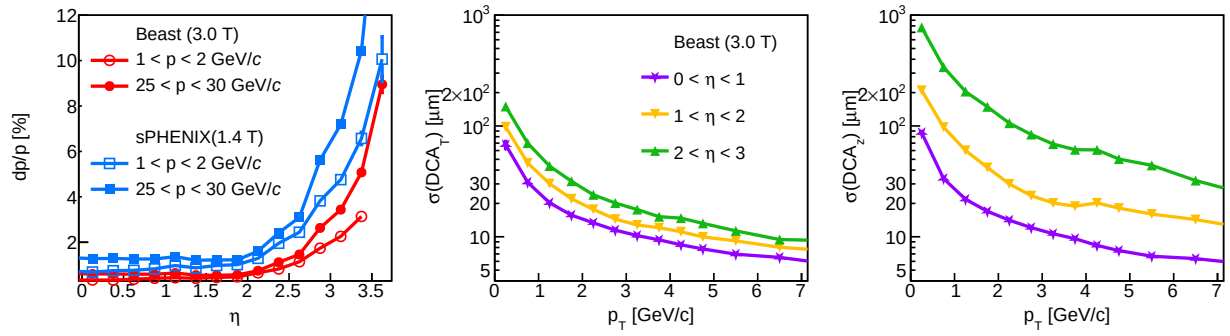

Figure 11.13: Detector resolutions. Left: Momentum resolution as a function of pseudorapidity for pions for two magnetic-field configurations for representative momentum bins. Center: Transverse Distance-of-Closest-Approach (DCA_T) resolution as a function of transverse momentum for several pseudorapidity bins. Right: Longitudinal Distance-of-Closest-Approach (DCA_z) resolution as a function of transverse momentum for several pseudorapidity bins.

Table 11.5: All-silicon tracker momentum and pointing resolution parametrizations.

		$\delta p/p = Ap \oplus B$		$\mathrm{DCA}_z = A/p_T \oplus B$		$\mathrm{DCA}_T = A/p_T \oplus B$	
		A [%/GeV]	B [%]	A [μm GeV]	B [μm]	A [μm GeV]	B [μm]
$0.0 < \lvert\eta\rvert < 0.5$	B = 3.0T	0.018	0.382	27	3.2	25	4.9
	B = 1.4T	0.041	0.773	27	3.3	26	3.9
$0.5 < \lvert\eta\rvert < 1.0$	B = 3.0T	0.016	0.431	37	3.8	28	4.5
	B = 1.4T	0.034	0.906	35	3.8	31	4.0
$1.0 < \lvert\eta\rvert < 1.5$	B = 3.0T	0.016	0.424	56	5.9	33	5.5
	B = 1.4T	0.034	0.922	56	5.4	35	5.1
$1.5 < \lvert\eta\rvert < 2.0$	B = 3.0T	0.012	0.462	111	7.0	40	5.1
	B = 1.4T	0.026	1.000	112	7.1	41	4.9
$2.0 < \lvert\eta\rvert < 2.5$	B = 3.0T	0.018	0.721	213	13.8	47	7.1
	B = 1.4T	0.041	1.551	212	16.0	48	7.7
$2.5 < \lvert\eta\rvert < 3.0$	B = 3.0T	0.039	1.331	347	40.5	52	11.9
	B = 1.4T	0.085	2.853	373	37.9	59	11.2
$3.0 < \lvert\eta\rvert < 3.5$	B = 3.0T	0.103	2.441	719	87.6	59	26.0
	B = 1.4T	0.215	5.254	732	87.7	66	25.3
$3.5 < \lvert\eta\rvert < 4.0$	B = 3.0T	0.281	4.716	1182	206	69	65.9
	B = 1.4T	0.642	9.657	1057	221	69	72.1

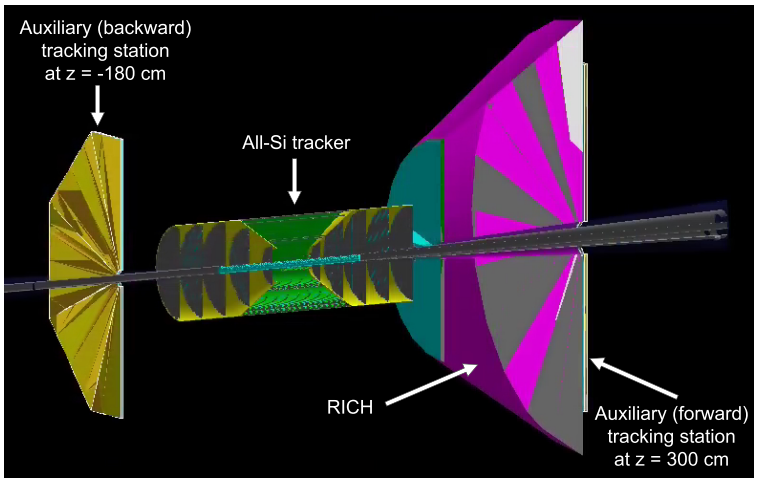

Figure 11.14: Event display showing the all-silicon tracker complemented with additional tracking stations in the available space [44]. In the backward region, the tracking station is installed at $z = -180$ cm with no significant amount of material expected between the all-silicon tracker and the complementary tracking station. In the forward region, the auxiliary tracking station is installed at $z = 300$ cm, behind the Ring Imaging Cherenkov (RICH) detector. The RICH material parameters were provided by the PID detector working group [45].

The A and B fit parameters are presented in Table 11.5.

As seen in Fig. 11.13 (left), the momentum resolution is overall constant as a function of pseudorapidity up to $\eta \sim 2$, and then rapidly worsens. We studied the possibility of recovering the quickly-worsening momentum resolution at forward and backward pseudorapidities by complementing the all-silicon tracker with auxiliary tracking stations, including Gas Electron Multiplier (GEM) detectors with 50-μm resolution in the radial and azimuthal directions and additional 10-μm-pixel silicon disks in the available space away from the interaction point [44]. The available space for such additional detectors is different in the forward and backward directions, as shown in Fig. 11.14. In the electron-going (backward) direction, a complementary tracking station can be installed at $z \sim -180$ cm, and no significant amount of material is projected to be placed between said detector and the all-silicon tracker. In the hadron-going (forward) direction, the additional station can be installed at $z \sim 300$ cm, behind the Ring Imaging Cherenkov (RICH) detector.

The effect of complementing the all-silicon tracker in the electron-going direction is shown in Figs. 11.15 and 11.16 for a 10 μm and 20 μm all-silicon-tracker pixel sizes, respectively. In the backward region, where the available space is closer to the all-silicon tracker, an auxiliary 10-μm-pixel detector provides a significantly better momentum resolution, mainly in the higher momentum region.

Results in the forward region are shown in Figs. 11.17 and 11.18 for a 10 μm and 20 μm all-silicon-tracker pixel sizes, respectively. The auxiliary station is placed behind the Ring Imaging Cherenkov (RICH) detector. The RICH material parameters were provided by the PID detector working group [45]. Since in the forward region the available space is farther away from the all-silicon tracker, the path traversed by a charged particle through the magnetic field in the tracking region ($\int \mathbf{B} \cdot d\mathbf{l}$) is larger. As a result, the resolution is less sensitive to the complementary detector resolution, and while the silicon disk provides the best performance, the GEM detectors considered provide a comparable enhancement to the momentum resolution. The effect of these auxiliary tracking stations depends on the EIC magnetic-field details. In these simulations, solenoidal fields were used. Likely, the magnetic field lines will be shaped to minimize bending inside the

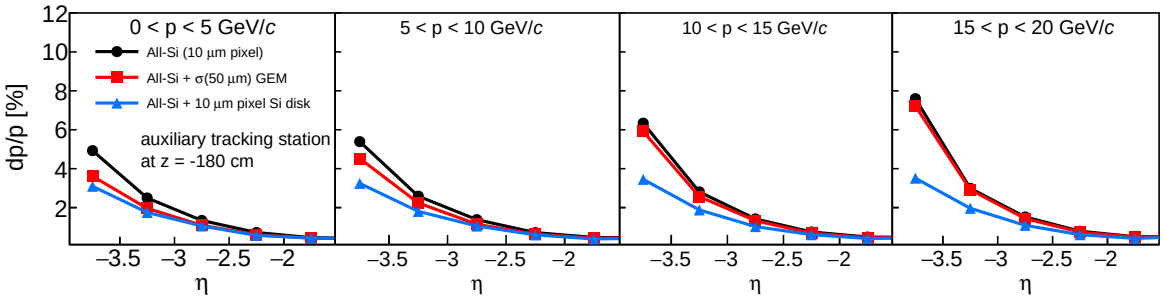

Figure 11.15: Momentum resolution as a function of pseudorapidity demonstrating the effect of complementing the all-silicon tracker in the electron-going (backward) direction. Each panel corresponds to a different momentum bin, from 0 to 20 GeV/c. The black circles correspond to the standalone all-silicon tracker (for a 10 μm × 10 μm pixel size). The red squares and blue triangles correspond to the all-silicon tracker complemented with a 50-μm-resolution GEM detector and a 10-μm-pixel silicon disk, respectively.

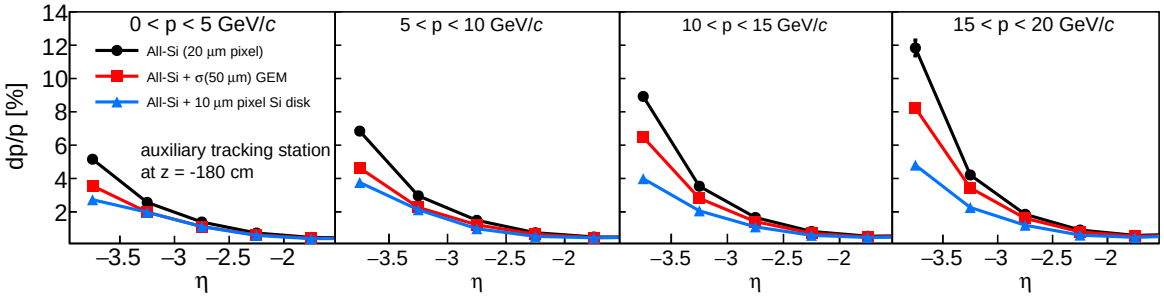

Figure 11.16: Same as Fig. 11.15, but for a 20 μm × 20 μm all-silicon-tracker pixel size.

RICH detector, which will lower the $\int \mathbf{B} \cdot d\mathbf{l}$.

While the auxiliary tracking stations in these simulations cover pseudorapidities $|\eta| > 1.2$, they have a larger impact at higher pseudorapidities ($|\eta| \gtrsim 2.5$). Consequently, smaller tracking stations can be used to complement the all-silicon tracker.

In closing, we have discussed several of the considerations for an instrument-performance driven integration of barrel tracking and vertexing layers with backward and forward disk arrays into an all-silicon tracking concept based on MAPS technology [46]. This all-silicon concept offers similar or better momentum and angular performance than the hybrid TPC-silicon concept of BeAST [47] with identical vertexing performance. It is radially more compact, $r = 43.23\,\text{cm}$ versus $r = 80.0\,\text{cm}$, thereby freeing 36.77 cm that could be used for alternate purposes such as PID and offering opportunities for complementary baseline EIC general purpose central detector concepts.

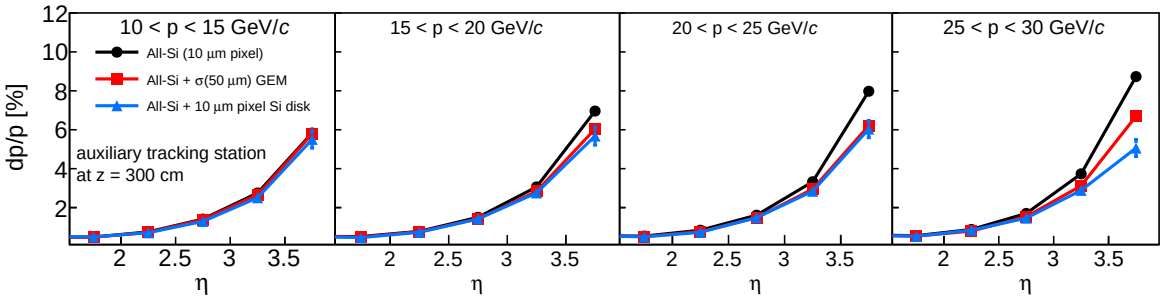

Figure 11.17: Momentum resolution as a function of pseudorapidity demonstrating the effect of complementing the all-silicon tracker in the hadron-going (forward) direction. Each panel corresponds to a different momentum bin, from 10 to 30 GeV/c. The black circles correspond to the standalone all-silicon tracker (for a 10 μm × 10 μm pixel size). The red squares and blue triangles correspond to the all-silicon tracker complemented with a 50-μm-resolution GEM detector and a 10-μm-pixel silicon disk, respectively.

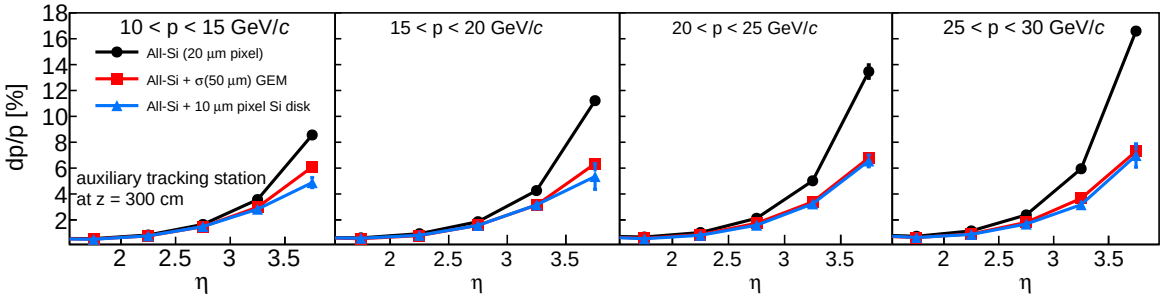

Figure 11.18: Same as Fig. 11.17, but for a 20 μm × 20 μm all-silicon-tracker pixel size.

11.2.5.3 Alternative Forward Tracking Option: Hadron End Cap with Si disk + MPGDs

[UPDATED BY CHEUK-PING WONG ON 11/15/2020]

A forward silicon tracker (FST) is designed for heavy flavor and jet measurements in EIC [48, 49]. The proposed FST covers pseudorapidity between 1–3.5 and momentum up to 30 GeV. An integrated detector design with the use of both FST and GEM tracker, which will be a cost effective option, are also studied in detector simulation.

Detector Design The FST, which is implemented in Fun4All simulation, consists of six planes of silicon sensor as shown in Figure 11.19. The FST detector design parameters are listed in Table 11.6. The FST is placed between 35 cm and 300 cm along the z axis. The inner radius of each plane changes with the z position to fit the ion beam pipe geometry. Effects on detector performance from different pixel pitch size and thickness of silicon thickness are studied and documented in ref [49]. In the latest FST detector design, the first three planes (plane 0-2) use a pixel pitch of 20 μm and a silicon thickness of 50 μm that are close to the ALICE ITS-3 type sensor [12, 50] while the last three planes (plane 3-5) apply MALTA sensor properties [20,22,51]. With both sensor technologies, the FST can provide excellent spatial and timing resolutions.

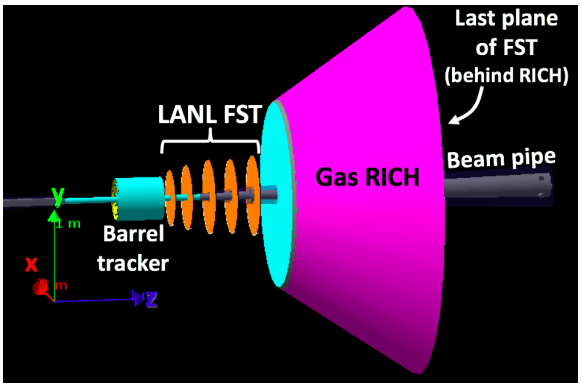

Figure 11.19: FST setup in Fun4All simulation.

Plane	z (cm)	r_{in} (cm)	r_{out} (cm)	pixel Pitch (μm)	silicon thickness (μm)
0	35	4	25	20	50
1	62.3	4.5	42	20	50
2	90	5.2	43	20	50
3	115	6	44	36.4	100
4	125	6.5	45	36.4	100
5	300	15	45	36.4	100

Table 11.6: FST geometry parameters

Detector Integration Integrated detector setups are also implemented in the simulation. The first integrated setup, which is shown in Figure 11.19, includes an additional gas RICH with aerogel and C_2F_6 gas as radiator. The second integrated setup is similar to the first integrated setup, but replaces the last plane (plane 5) of FST with a mock up GEM tracker. The GEM tracker, which consists of three planes filled with methane, covers $1.5 < \eta < 3.5$. The material budgets of the integrated setups are shown in Figure 11.20. The material budgets of the first and the second integrated setup are $< 8\%$ X_0 and $< 10\%$ X_0 at $\eta < 3.3$, respectively.

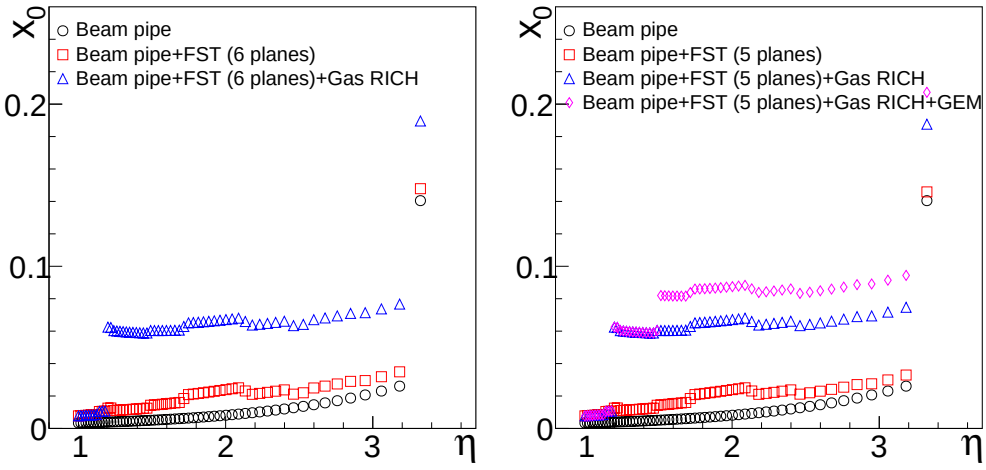

Figure 11.20: Material budgets of different integrated detector setups.

Detector performance The momentum resolutions of the integrated detector setup with the GEM track are shown in Figure 11.21. The results are fitted using Equation (11.1). The fitting results of different detector setups are listed in Table 11.7. The momentum resolutions of the integrated detector setups with the 3 T (1.5 T) magnet are $< 10\%$ (18%) and $< 4\%$ (8%) at $\eta < 1$ and $\eta > 1$, respectively. Comparing results of different detector setups as shown in Table 11.7, the additional gas RICH worsens the momentum resolutions by about 1% at $\eta > 2.5$. Furthermore, Table 11.7 shows that replacing the last plane of FST with

a GEM tracker does not gives significant changes in momentum resolution. The DCA_T resolutions of the integrated detector setups with the GEM tracker are shown in Figure 11.22. The DCA_T resolutions are fitted using Equation (11.2). The fitting results of different detector setups with the use of the 3 T magnetic field are listed in Table 11.8. The fitting results of DCA_T resolutions with the use of the 1.5 T magnetic fields are not shown in Table 11.8 as the DCA_T resolutions shows a weak dependence on the magnetic fields. Table 11.8 shows that the DCA_T resolutions are < 50 μm and < 110 μm at $\eta < 2$ and $\eta > 2$, respectively. Furthermore, Table 11.8 shows that the replacement of the last plane of FST with the GEM tracker gives no significant differences in DCA_T resolution. The results of momentum and DCA_T resolutions, which show that replacing the last plane of FST by the GEM tracker does not give significant differences in detector performance, make the integrated detector setup with the GEM tracker an attractive option considering the lower cost of a GEM tracker compared to a silicon detector.

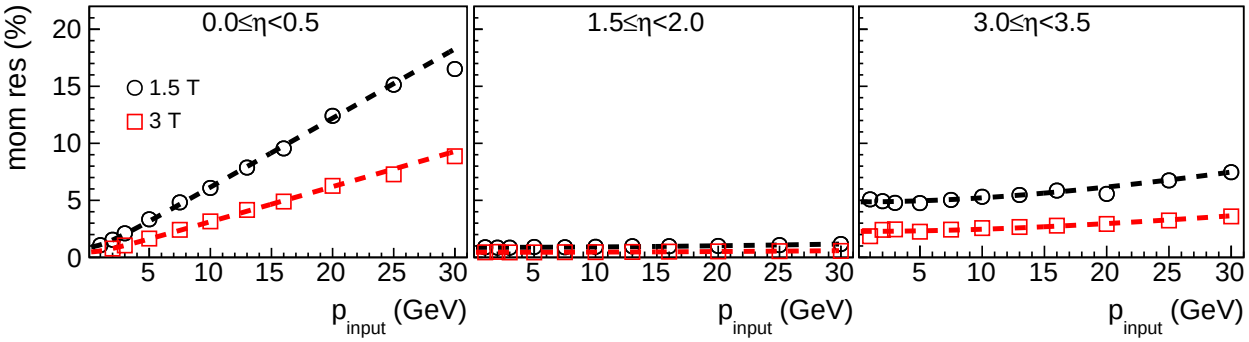

Figure 11.21: Momentum resolutions as a function of input momentum of the integrated detector setup with the beam pipe, the barrel tracker, the five-plane FST, the gas RICH and the GEM tracker. The dash lines are the fits using Equation (**??**). The fitting results are shown in Table 11.7.

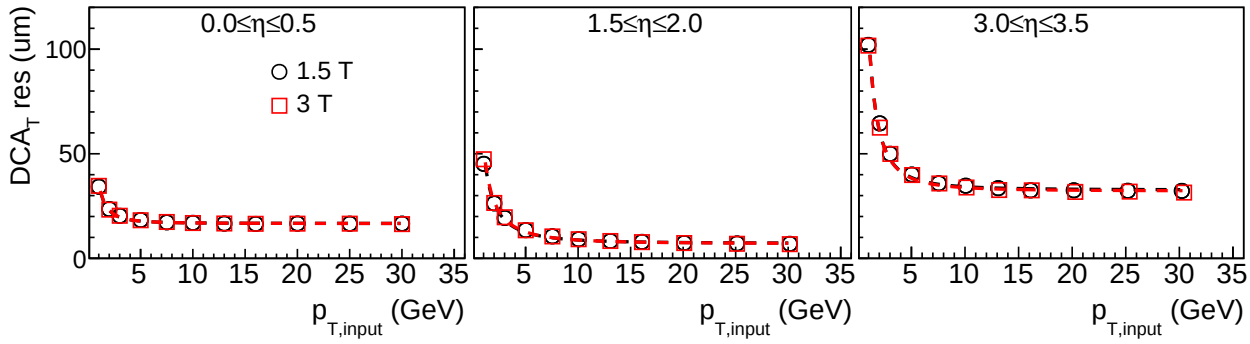

Figure 11.22: DCA_T resolutions of the integrated detector setup with the beam pipe, the barrel tracker, the five-plane FST, the gas RICH and the GEM tracker. The dash lines are the fits using Equation (**??**). The fitting results are shown in Table 11.8.

Table 11.7: Fitting parameters of the momentum resolutions of different detector integration setups.

η	B field	FST (6 planes)		FST (6 planes) + RICH		FST (5 planes) + RICH + GEM	
		A (%/GeV)	B (%)	A (%/GeV)	B (%)	A (%/GeV)	B (%)
0.0–0.5	3 T	0.313	0.440	0.310	0.457	0.309	0.475
	1.5 T	0.608	0.880	0.605	0.892	0.608	0.915
0.5–1.0	3 T	0.267	0.510	0.259	0.494	0.263	0.494
	1.5 T	0.520	0.971	0.513	1.035	0.513	1.010
1.0–1.5	3 T	0.039	0.568	0.040	0.551	0.032	0.597
	1.5 T	0.076	1.039	0.077	1.120	0.070	1.088
1.5–2.0	3 T	0.019	0.454	0.018	0.448	0.013	0.445
	1.5 T	0.039	0.839	0.039	0.882	0.026	0.876
2.0–2.5	3 T	0.032	0.687	0.035	0.682	0.028	0.704
	1.5 T	0.068	1.346	0.070	1.374	0.051	1.402
2.5–3.0	3 T	0.037	1.190	0.062	1.306	0.062	1.336
	1.5 T	0.086	2.362	0.127	2.607	0.123	2.629
3.0–3.5	3 T	0.063	1.746	0.095	2.069	0.095	2.278
	1.5 T	0.124	3.378	0.189	4.305	0.189	4.868

Table 11.8: Fitting parameters of the DCA_T resolutions of different detector setup with the use of the 3 T magnetic field.

η	FST (6 planes)		FST (6 planes) + RICH		FST (5 planes) + RICH + GEM	
	A (μm ·GeV)	B (μm)	A (μm ·GeV)	B (μm)	A (μm ·GeV)	B (μm)
0.0–0.5	30.73	16.71	30.17	16.86	30.84	16.78
0.5–1.0	32.80	17.22	32.14	17.37	32.83	17.28
1.0–1.5	41.54	14.19	39.47	14.39	40.73	14.06
1.5–2.0	49.57	8.24	48.49	8.43	51.56	7.36
2.0–2.5	57.87	13.73	54.79	14.16	59.58	11.48
2.5–3.0	76.78	20.42	81.63	21.13	83.90	20.35
3.0–3.5	77.79	29.71	95.90	30.01	104.95	31.55

11.2.5.4 Hybrid Tracking System

11.2.5.4.1 Barrel: Silicon Vertex + TPC

Figure 11.23 shows the simulated layout of this hybrid configuration. The silicon part is made of three layers close to the beampipe (vertexing layers) and two layers at larger radii (tracking layers) in the central region, and seven disks in the forward and backward regions. A TPC surrounds the central region and two TPC

endcaps are placed after the silicon disks in both forward and backward regions.

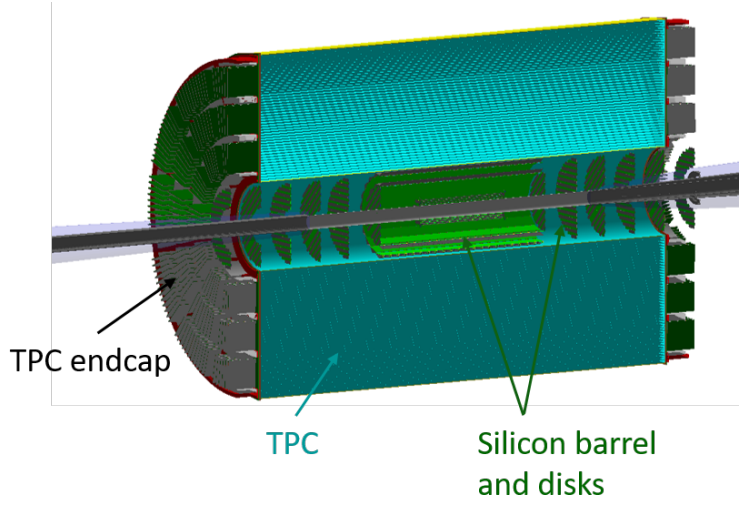

Figure 11.23: New hybrid baseline layout. The silicon layers and disks are shown in green, and the TPC in light blue.

The silicon detector parameters are based on the ALICE ITS3 technology. The vertexing layers have a material budget of 0.05% X/X_0 each, the tracking layers 0.55% X/X_0, and the disks each have a material budget of 0.24% X/X_0. The pixel size is $10 \times 10\ \mu m^2$.

The placements and parameters of barrel layers and disks are described in detail in Tables 11.9a and 11.9b. The table for the disks only shows the forward region, since this detector layout is symmetric in z. The radial

Layer	**Length**	**Radial position**
Layer 1	420 mm	36.4 mm
Layer 2	420 mm	44.5 mm
Layer 3	420 mm	52.6 mm
Layer 4	840 mm	133.8 mm
Layer 5	840 mm	180.0 mm
TPC start	2110 mm	200.0 mm
TPC end	2110 mm	780.0 mm

(a) Barrel region

Disk	**z position**	**Inner radius**	**Outer radius**
Disk 1	220 mm	36.4 mm	71.3 mm
Disk 2	430 mm	36.4 mm	139.4 mm
Disk 3	586 mm	36.4 mm	190.0 mm
Disk 4	742 mm	49.9 mm	190.0 mm
Disk 5	898 mm	66.7 mm	190.0 mm
Disk 6	1054 mm	83.5 mm	190.0 mm
Disk 7	1210 mm	99.3 mm	190.0 mm

(b) Disk region

Table 11.9: Positions and lengths of detector parts in the barrel region and the disk region. In the disk region, the seven disks in the forward region are shown, but this layout is symmetric so it is the same with reversed sign on the z position in the backward region.

positions for the barrel layers are based on the minimum distance between layers used in the ALICE ITS2 system [52]. While it may be possible to put layers closer together, using these distances give a detector that is plausible to build with currently existing technologies and structure solutions. Each detector layer is built up of overlapping staves, consisting of several chips along with material representing cables, cooling pipes,

and simple support structures.

Momentum and pointing resolutions; Studies for the resolutions are made in the following parameter space:

- Transverse momentum range: 0 to 30 GeV/c
- Pseudorapidity: $-1.0 \leq \eta \leq 1.0$, $1.0 \leq \eta \leq 2.5$, $2.5 \leq \eta \leq 3.5$
- Magnetic field: 1.5 T and 3.0 T

Since this detector layout is symmetric, negative pseudorapidities will have the same resolutions as the positive ones. Positive pions are used, with 1 000 000 events in each pseudorapidity range.

The formulae for resolution parameterisation are given in Equation 11.3, where A and B indicate constants.

$$\frac{\sigma_p}{p} = A \cdot p \oplus B = \sqrt{(A \cdot p)^2 + B^2}, \qquad \frac{\sigma_{xy}}{p_{\mathrm{T}}} = \frac{A}{p_{\mathrm{T}}} \oplus B = \sqrt{\left(\frac{A}{p_{\mathrm{T}}}\right)^2 + B^2} \tag{11.3}$$

This parametrisation works well for the pointing resolution, but it has limitations for the relative transverse momentum resolution when using a gas TPC. In this case, as can be seen from Figure 11.24, the parametrisation works well for p_{T} between 0 and 4 GeV/c, but the resolution value goes into a less steep linear increase after this point. The figure shows the relative transverse momentum resolution versus transverse momentum for both a 1.5 T field and a 3.0 T field, and the dashed line shown is the parametrisation provided by the Physics Working Group. Fits to these data will be split up in momentum intervals to characterise the two clear regions (above and below 4 GeV/c) separately. The pseudorapidity interval $1 \leq \eta \leq 2.5$ receives similar treatment. The final results from the relative momentum fits, with parameters taken from Equation 11.3 can be seen in Table 11.10 for a 1.5 T field and a 3.0 T field.

Table 11.11 shows a comparison between the currently listed parameters provided by the Physics Working Group for the transverse pointing resolution, and the fit values for the data from simulations using the silicon plus TPC hybrid baseline detector. Table 11.12 shows the same for the longitudinal pointing resolution.

These results show that the requirements on pointing resolutions can be met with this layout and the ITS3-like technology, in all regions. The relative momentum resolution does not meet the requirements however, especially with a 1.5 T magnetic field. With a 3.0 T magnetic field the requirements are met apart from at $|\eta| \geq 2.5$.

Minimum-p_{T} limit; The minimum reconstructable p_{T} is investigated in the full pseudorapidity range, by sending out low-momentum (0 to 0.5 GeV/c in p_{T}) kaons and pions from the vertex, and seeing what fraction of total tracks in a region can be reconstructed, using a simple fast Kalman filter reconstruction algorithm. Improved reconstruction methods may fare better, but as an approximation of the highest limit of the minimum-p_{T} that can be reconstructed, this method is deemed feasible. Table 11.13 contains minimum reconstructable p_{T} values for different pseudorapidity regions. Results for pions and kaons are similar, and thus only one value is presented, representing the cutoff point where 90% of events are reconstructed. This cutoff point is important to keep in mind; lower p_{T} tracks can also be reconstructed up to a point, but less efficiently.

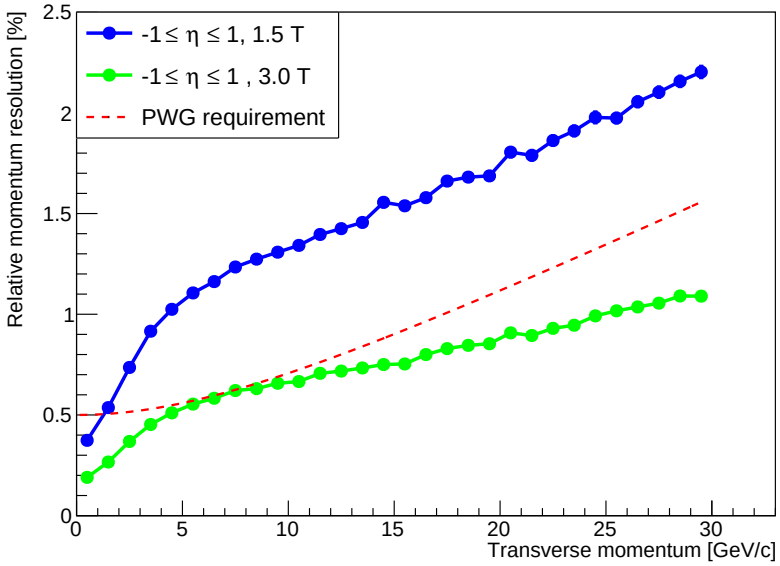

Figure 11.24: Relative transverse momentum resolution versus transverse momentum, for the baseline hybrid silicon plus TPC layout. The data are for the central region ($-1 \leq \eta \leq 1$). The blue curve shows the resolution for a 1.5 T field, and the green curve shows the resolution for a 3.0 T field. The red line shows the relative momentum resolution parametrisation requirement as given by the Physics Working Group (see Equation 11.3).

11.2.5.4.2 Barrel: Silicon Vertex + Cylindrical MPGDs

In the barrel, the silicon vertex tracker can be complemented by several layers of MPGDs. Each cylindrical layer of the MPGD tracker consists of curved detector elements of about 50cm width and long enough to cover the range $|\eta| < 1$. The spatial resolution both in the z and the $r \cdot \varphi$ directions is assumed to be of 150 μm. The implementation of each tile in simulation is based of the technology developed for the CLAS12 barrel Micromegas tracker [29]: the material budget in the active area per each detector is about 0.3% X/X_0.

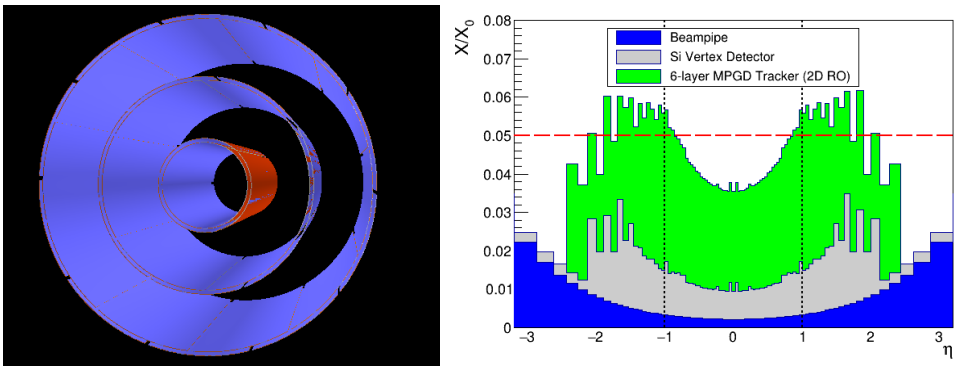

Figure 11.25: (left) A possible configuration of the cylindrical MPGD tracker with three pairs of layers. (right) The stack plot of the material budget for the hybrid detector with a six layer MPGD tracker: in blue the contribution of the beam pipe, in gray the silicon vertex detector and in green the MPGD tracker contribution.

Interval	p_T **interval**	**PWG values [%]**	**Fit 1.5 T [%]**
$-3.5 \leq \eta \leq -2.5$	0 to 30 GeV/c	$A = 0.1$, $B = 0.5$	$A = 0.6 \pm 0.01$, $B = 4.2 \pm 0.03$
$-2.5 \leq \eta \leq -1.0$	0 to 4 GeV/c	$A = 0.1$, $B = 0.5$	$A = 0.5 \pm 0.01$, $B = 0.9 \pm 0.01$
	4 to 30 GeV/c	$A = 0.1$, $B = 0.5$	$A = 0.1 \pm 0.01$, $B = 2.2 \pm 0.01$
$-1.0 \leq \eta \leq 1.0$	0 to 4 GeV/c	$A = 0.05$, $B = 0.5$	$A = 0.2 \pm 0.01$, $B = 0.4 \pm 0.01$
	4 to 30 GeV/c	$A = 0.05$, $B = 0.5$	$A = 0.07 \pm 0.001$, $B = 1.1 \pm 0.01$
$1.0 \leq \eta \leq 2.5$	0 to 4 GeV/c	$A = 0.05$, $B = 0.5$	$A = 0.5 \pm 0.01$, $B = 0.9 \pm 0.01$
	4 to 30 GeV/c	$A = 0.05$, $B = 0.5$	$A = 0.1 \pm 0.01$, $B = 2.2 \pm 0.01$
$2.5 \leq \eta \leq 3.5$	0 to 30 GeV/c	$A = 0.05$, $B = 1.0$	$A = 0.6 \pm 0.01$, $B = 4.2 \pm 0.03$
Interval	p_T **interval**	**PWG values [%]**	**Fit 3.0 T [%]**
$-3.5 \leq \eta \leq -2.5$	0 to 30 GeV/c	$A = 0.1$, $B = 0.5$	$A = 0.3 \pm 0.01$, $B = 2.1 \pm 0.01$
$-2.5 \leq \eta \leq -1.0$	0 to 4 GeV/c	$A = 0.1$, $B = 0.5$	$A = 0.2 \pm 0.01$, $B = 0.5 \pm 0.01$
	4 to 30 GeV/c	$A = 0.1$, $B = 0.5$	$A = 0.06 \pm 0.001$, $B = 1.1 \pm 0.01$
$-1.0 \leq \eta \leq 1.0$	0 to 4 GeV/c	$A = 0.05$, $B = 0.5$	$A = 0.1 \pm 0.01$, $B = 0.2 \pm 0.01$
	4 to 30 GeV/c	$A = 0.05$, $B = 0.5$	$A = 0.03 \pm 0.001$, $B = 0.5 \pm 0.01$
$1.0 \leq \eta \leq 2.5$	0 to 4 GeV/c	$A = 0.05$, $B = 0.5$	$A = 0.2 \pm 0.01$, $B = 0.5 \pm 0.01$
	4 to 30 GeV/c	$A = 0.05$, $B = 0.5$	$A = 0.06 \pm 0.001$, $B = 1.1 \pm 0.01$
$2.5 \leq \eta \leq 3.5$	0 to 30 GeV/c	$A = 0.05$, $B = 1.0$	$A = 0.3 \pm 0.01$, $B = 2.1 \pm 0.01$

Table 11.10: Relative transverse momentum resolution fit parameters for a 1.5 T magnetic field and a 3.0 T magnetic field, using the fit presented in Equation 11.3, and how they compare to the Physics Working Group values provided for the detector matrix.

Interval	**PWG values [μm]**	**Fit 1.5 T [μm]**	**Fit 3.0 T [μm]**
$-3.5 \leq \eta \leq -2.5$	N/A	$A = 49.3 \pm 0.2$, $B = 9.64 \pm 0.02$	$A = 48.5 \pm 0.2$, $B = 9.58 \pm 0.02$
$-2.5 \leq \eta \leq -1.0$	$A = 40$, $B = 10$	$A = 23.3 \pm 0.1$, $B = 3.32 \pm 0.01$	$A = 23.1 \pm 0.1$, $B = 3.31 \pm 0.01$
$-1.0 \leq \eta \leq 1.0$	$A = 30$, $B = 5$	$A = 14.1 \pm 0.1$, $B = 2.11 \pm 0.01$	$A = 13.7 \pm 0.1$, $B = 2.14 \pm 0.01$
$1.0 \leq \eta \leq 2.5$	$A = 40$, $B = 10$	$A = 23.3 \pm 0.1$, $B = 3.32 \pm 0.01$	$A = 23.1 \pm 0.1$, $B = 3.31 \pm 0.01$
$2.5 \leq \eta \leq 3.5$	N/A	$A = 49.3 \pm 0.2$, $B = 9.64 \pm 0.02$	$A = 48.5 \pm 0.2$, $B = 9.58 \pm 0.02$

Table 11.11: Transverse pointing resolution fit parameters, using the fit presented in Equation 11.3, and how they compare to the Physics Working Group values provided for the detector matrix.

Figure 11.25 shows a possible configuration of the MPGD tracker where six layers have been grouped in three pairs. Several configurations have been investigated: one configuration with six layers equally spaced at regular radial intervals, one with three pairs of layers (inner, middle and outer pairs) and a configuration with two layers in the middle and four layers in the outer part of the barrel. Table 11.14 shows the radial position of the layers for the last two configurations.

Studies of relative momentum resolution have been performed by simulating ten thousand π^- per momentum bin at an angle of 66^o with a magnetic field of 1.5 T. The polar and azimuthal angular resolutions have been evaluated at a radius of 81.5 cm, where PID detectors will be placed. The results shown in Figure 11.26

Interval	PWG values [μm]	Fit 1.5 T [μm]	Fit 3.0 T [μm]
$-3.5 \leq \eta \leq -2.5$	N/A	$A = 596.9 \pm 1.5$, $B = 41.05 \pm 0.12$	$A = 596.5 \pm 1.5$, $B = 40.79 \pm 0.12$
$-2.5 \leq \eta \leq -1.0$	$A = 100$, $B = 20$	$A = 78.3 \pm 0.2$, $B = 3.11 \pm 0.02$	$A = 78.1 \pm 0.2$, $B = 3.12 \pm 0.02$
$-1.0 \leq \eta \leq 1.0$	$A = 30$, $B = 5$	$A = 23.2 \pm 0.1$, $B = 2.64 \pm 0.01$	$A = 22.9 \pm 0.1$, $B = 2.64 \pm 0.01$
$1.0 \leq \eta \leq 2.5$	$A = 100$, $B = 20$	$A = 78.3 \pm 0.2$, $B = 3.11 \pm 0.02$	$A = 78.1 \pm 0.2$, $B = 3.12 \pm 0.02$
$2.5 \leq \eta \leq 3.5$	N/A	$A = 596.9 \pm 1.5$, $B = 41.05 \pm 0.12$	$A = 596.5 \pm 1.5$, $B = 40.79 \pm 0.12$

Table 11.12: Longitudinal pointing resolution fit parameters, using the fit presented in Equation 11.3, and how they compare to the Physics Working Group values provided for the detector matrix.

η interval	Min-p_T, 1.5 T	Min-p_T, 3.0 T
$-3.0 \leq \eta \leq -2.5$	100 MeV/c	150 MeV/c
$-2.5 \leq \eta \leq -2.0$	130 MeV/c	220 MeV/c
$-2.0 \leq \eta \leq -1.5$	70 MeV/c	160 MeV/c
$-1.5 \leq \eta \leq -1.0$	150 MeV/c	300 MeV/c
$-1.0 \leq \eta \leq 1.0$	200 MeV/c	400 MeV/c
$1.0 \leq \eta \leq 1.5$	150 MeV/c	300 MeV/c
$1.5 \leq \eta \leq 2.0$	70 MeV/c	160 MeV/c
$2.0 \leq \eta \leq 2.5$	130 MeV/c	220 MeV/c
$2.5 \leq \eta \leq 3.0$	100 MeV/c	150 MeV/c

Table 11.13: Minimum reconstructable p_T, using simple Kalman filter reconstruction algorithm, for different pseudorapidity intervals. This study is done using the silicon plus TPC baseline layout.

Layer	Radial position
0 inner	198 mm
1 inner	217 mm
2 middle	477 mm
3 middle	496 mm
4 outer	719 mm
5 outer	736 mm
6 outer	756 mm
7 outer	775 mm

Table 11.14: Radial position of MPGD tracker layers.

are compared with resolutions obtained with the ideal TPC hybrid detector. Given the equivalent reduced number of measuring position of the MPGD tracker with respect to the TPC, the relative momentum resolution of the former is higher than latter. It is interesting to note, that the configuration "2-middle 4-outer" shows a better momentum resolution likely due to the bigger lever arm relative to the silicon detector and with the reduced material budget closer to the silicon detector. The angular resolutions results show similar

behaviors for all the tested configurations.

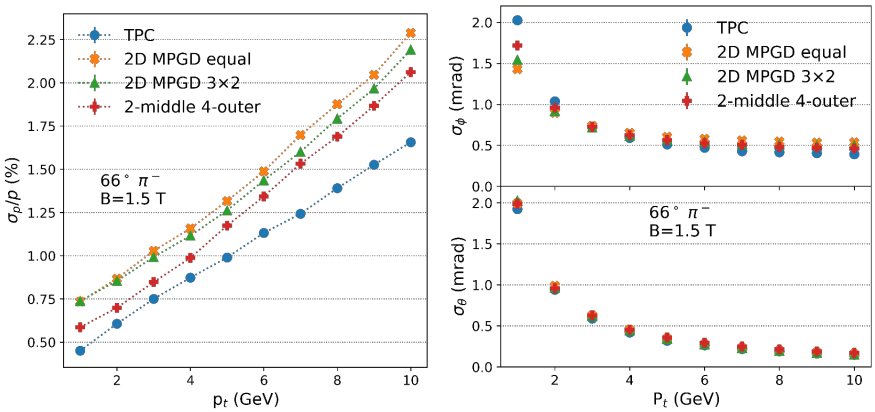

Figure 11.26: (left) Relative transverse momentum resolution. (right) Angular resolution at 81.5 cm.

A study has been made combining the baseline hybrid silicon vertex tracker (as described in Section 11.2.5.4.1) with a "three pair" MPGD layer layout, as shown in Figure 11.25. The study is made in the central region ($-1 \leq \eta \leq 1$) with a 1.5 T field, in a transverse momentum range of 0 to 30 GeV/c. Fitting the resulting resolutions with the equations shown in Equation 11.3, the following results are obtained;

- Relative momentum resolution: $A = 0.1 \pm 0.01$, $B = 0.92 \pm 0.02$
- Transverse pointing resolution: $A = 18.5 \pm 0.2$, $B = 2.5 \pm 0.01$
- Longitudinal pointing resolution: $A = 26.5 \pm 0.2$, $B = 2.8 \pm 0.02$

When compared to the PWG requirements, these results echo those presented in Section 11.2.5.4.1; the pointing resolutions exceed the requirements, but the relative momentum resolution does not meet the requirements over most of the momentum interval. It does however exceed them at $p_{\mathrm{T}} \leq 3$ GeV/c.

11.2.5.4.3 Hadron & Electron End Cap: MPGDs

The tracking in the forward region of the hybrid configuration is composed of two large–area GEM stations, the inner forward GEMs and the outer forward GEMs, with each station made of three disks of triple-GEM detectors as shown in a standard BEAST detector geometry in Fig. 11.27 (left). Using the EicRoot simulation framework, we have studied the impact of inner and outer GEMs on the momentum resolution and the number of hits available for track fitting as a function of particle scattering angle and particle momentum. The simulated detector components include the beam pipe, the vertex and forward silicon trackers, the time projection chamber (TPC), the inner forward GEM station, the ring imaging Cerenkov (RICH) detector gas volume, and the outer forward GEM station behind the RICH. Specifically, the impact of the outer GEM detector on the tracking performance is studied by comparing the performance of the BeAST detector in the standard configuration with only the inner GEMs against the configuration including the outer GEMs while varying the particle parameters (scattering angle and momentum). Here, it is assumed that the detector would operate with a 1.5 T B-field. The scattering angle θ is varied from 5° to 75°. The outer GEMs impact

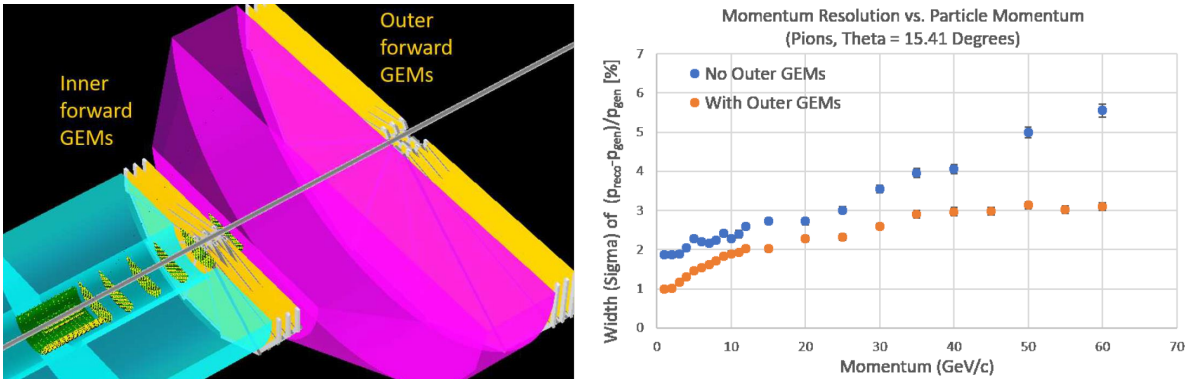

Figure 11.27: *Left:* Simulated BeAST geometry with outer forward GEM detectors. *Right:* Momentum resolution vs. momentum for pions at fixed scattering angle $\theta = 15.41°$ ($\eta = 2.0$) with (orange) and without (blue) outer forward GEMs.

performance within their angular acceptance of $5° < \theta < 35°$ ($3.1 > \eta > 1.15$). The dimensions of the outer GEMs in these simulations are chosen to closely match the acceptance of the inner GEMs.

Fig. 11.27 (right) shows the momentum resolution as a function of momentum while keeping the scattering angle fixed at $\theta = 15.41°$ ($\eta = 2.00$). It demonstrates that the significant improvement from outer GEMs holds over a large momentum range from 1 - 60 GeV/c. From the results shown in Fig. 11.28 (left), it is clear that the outer GEMs significantly improve the momentum resolution, particularly for small scattering angles where the improvement reaches a factor of two. The particular structure of the graph is presumably due to the varying number of hits on the individual detectors. In order to verify this, we plot the average number of hits in each tracking subdetector as a function of θ in Fig. 11.28 (right). Over the full $5° < \theta < 35°$ acceptance region of the outer forward GEM, both inner and outer GEM subdetectors provide a constant number of hits while the number of TPC hits drops rapidly below $\theta = 15°$ and the number of vertex hits is down to one hit below $\theta = 18°$. In this angular range, the number of forward Si hits is comparable to the number of hits in each GEM subdetector. The design of the two GEM subdetector is very similar, so adding the outer forward GEM doubles the total number of GEM hits in this region. The forward Si detector, inner GEMs, and outer GEMs each contribute roughly a third to the total number of track hits in this region. This explains the significant impact of the outer forward GEM in the angular range below $\theta = 15°$ ($\eta > 2$).

11.2.5.5 Fast tracking Layers & Additional PID detectors

11.2.5.5.1 Fast Signal & High Resolution MPGDs for DIRC in the Barrel Region

For the scenario where a TPC is chosen as the central tracker option for the EIC detector and MAPS technology is adopted as the vertex tracker, we have identified three strong motivations for the need of a high-precision and fast-signal tracking detector to complement the inherent limitations of the TPC + MAPS as main tracking detectors in the barrel region.

High angular resolution tracking layer for the barrel PID detector: Particle identification at an EIC is going to be critical. High angular tracking resolution will improve the effectiveness of the PID detectors,

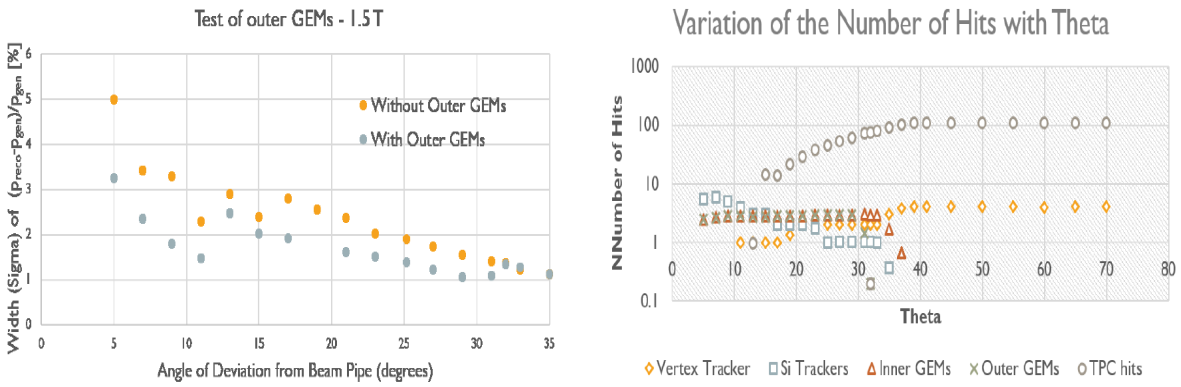

Figure 11.28: *Left*: Momentum resolution vs. scattering angle θ for 10 GeV/c pion tracks from simulation of the standard BeAST detector with (gray) and without (orange) outer forward GEMs added. *Right*: Average number of hits in each tracking subdetector vs. scattering angle Theta.

in particular the DIRC and RICH detectors. We have studied the impact that our fast cylindrical μRWELL trackers would have on the angular tracking resolution in the central region.

We simulated a detector setup within the EicRoot framework, which implemented a silicon vertex tracker, TPC, and cylindrical μRWELL trackers [53]. The study was performed with π^- particles in a 1.5 T magnetic field for scattering angles of $43^o, 66^o$, and 89^o over a momentum range of 1 to 7 GeV. We find an improvement in the angular resolution of tracks entering and exiting the DIRC when cylindrical μRWELL layers are located in front and behind the DIRC [53]. The simulation studies demonstrate that the two layers configuration surrounding the DIRC detector will improve the PID detector performances, and help aid in achieving the required 3σ π/K separation at 6 GeV.

High space point resolution tracking layer for TPC field distortions correction/calibration: In addition to providing the angular resolution information to the DIRC detector, cylindrical μRWELL layers will also provide precision tracking to calibrate the TPC tracks and help correct for well known "scale distortions" of TPC tracks. For this case, the optimal configuration will be two cylindrical μRWELL layers, the first inside the TPC inner field cage and the second outside. We are performing simulation studies for the two-layers configurations to evaluate the performances.

Fast tracking layer to complement slow TPC and MAPS detector Both TPC and MAPS technologies are slow detectors and having an additional fast tracker with a timing resolution of a few ns will be required to provide the bunch crossing timing information to the reconstructed vertex as well as central tracks. μRWELL detector technologies provides the timing resolution needed to satisfy these requirements

11.2.5.5.2 MPGD-based-TRDs for Electron PID and Tracking in the End Caps

Identification of secondary electrons plays a very important role for physics at the Electron-Ion Collider (EIC). J/ψ has a significant branching ratio for decays into leptons (the branching ratio into electrons (e^+e^- pair) is 6%). The branching ratio of D-mesons is Br($D^+ \rightarrow e + X$) $\sim$ 16% and the branching ratio of B-mesons is Br($B^\pm \rightarrow e + \nu + X_c$) $\sim$ 10%. Electron identification is also important for many other physics

topics, such as spectroscopy, beyond the standard model physics, etc. By using more sophisticated electron identification an efficiency of those channels could be increased. A high granularity tracker combined with a transition radiation option for particle identification could provide additional information necessary for electron identification or hadron suppression. Due to asymmetric beam energies and boosted kinematics, it is important to provide such additional instrumentation in the hadron endcap. The basic concept of GEM-

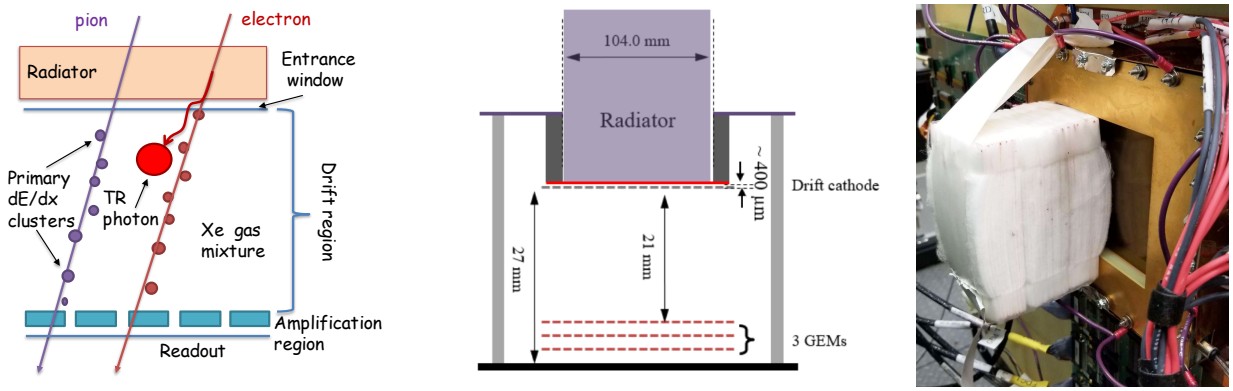

Figure 11.29: The concept of GEM-based TRD (left), the prototype scheme (middle), prototype in testbeam setup (right)

based TRD is shown on the Fig. 11.61. A standard triple-GEM detector [24] with high granularity strip pitch (400 μm) capable of providing high resolution space point position information was converted into a transition radiation detector and tracker (GEM-TRD/T) [54]. This was achieved by making several modifications to the standard GEM tracker. First, since heavy gases are required for efficient absorption of X-rays, the operational gas mixture has been changed from an Argon based mixture to a Xenon based mixture. Secondly, the drift region also needed to be increased from ~3 mm to 20-30 mm in order to detect more energetic TR photons. Then to produce the TR photons, a TR radiator was installed in front of the GEM entrance window. Finally, the standard APV25 GEM readout electronics was replaced with faster electronics based on flash ADC (FADC) [55] and developed for JLab HallD GlueX Drift Chambers. A GEANT4 simulation and optimized the radiator and detector thicknesses for a single chamber (Fig. 11.61) has been performed. G4XTRGammaRadModel model was used for a fleece radiator, which could be simulated in GEANT4 as an irregular type of radiator with a certain density and two parameters (α_1, α_2), which define a spread of materials and air-gaps within a radiator. Due to the self-absorbing property of the radiator, soft photons (3-6 kEv) generated within first few centimeters of the TR-radiator will be absorbed, leading to an increase in the hard X-ray photon spectrum at the exit from a radiator. A thin layer of gas in Xe-based detector will not be effective at detecting hard X-ray photons. As one could see in Fig. 11.63 (left), rejection power is saturated after 22cm of radiator for our GEM detector with 21mm gas thickness, including 400μm of dead gas layer in front. Experimental data points (stars) shows a good agreement with MC projections. A TRD needs information about the ionization along the track, to discriminate TR photons from the ionization of the charged particle. The GEM-TRD/T prototype used a precise (125 MHz, 12 bit) FADC [55] coupled with fast shaper pre-amplifiers, developed at JLAB, with a VME-based readout. The FADCs have a pipeline readout window of up to 8 μs, which covers the entire drift time (500ns) of the GEM-TRD/T prototype and gives a room for HV scan. The pre-amplifiers used GAS-II ASIC chips to provide 2.6 mV/fC amplification with a peaking time of 10 ns. For the e/π rejection factor the amplitude and arrival time of each individual cluster along the drift time were analyzed. All this information (up to 20 variables) was used as input for

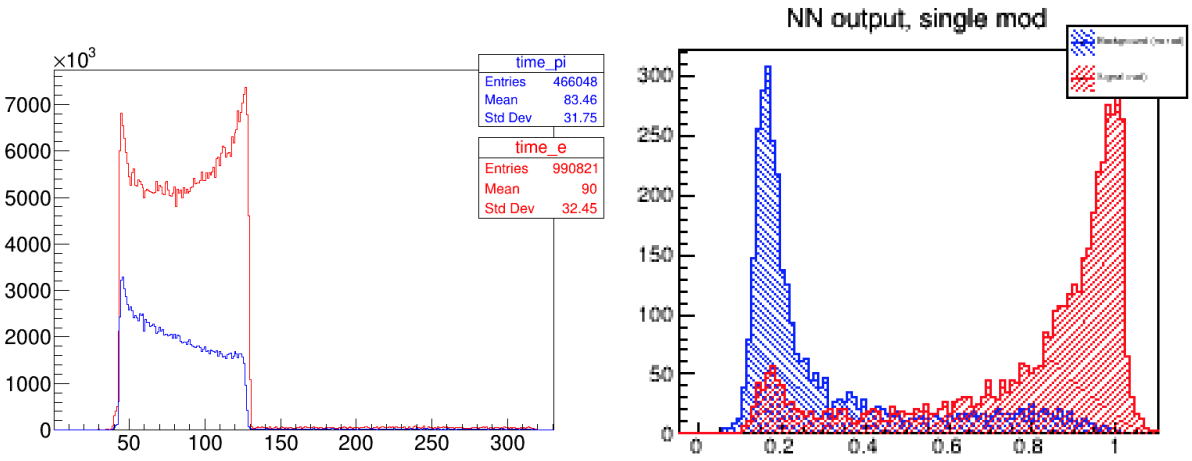

Figure 11.30: Left plot shows average energy deposition along the drift time (x-axis in fADC time-bins). Right plot is output from Neural Network, showing the separation between electrons and pions.

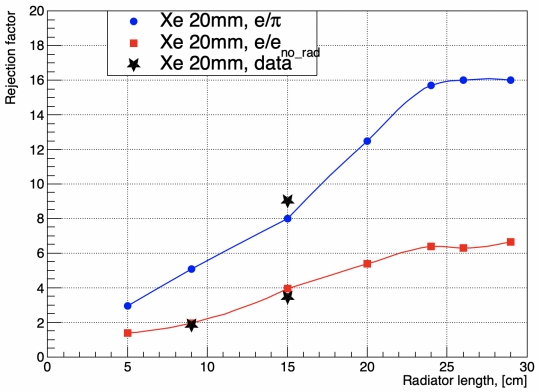

Figure 11.31: Rejection vs. TR-radiator thickness.

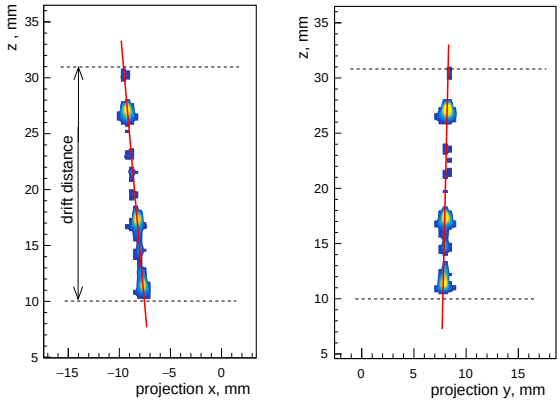

Figure 11.32: Single track reconstruction.

likelihood and artificial neural network (ANN) programs, such as JETNET or ROOT-based (Multi-layer Perceptron). The ANN system was trained with MC or data samples of incident electron and pions. Then an independent sample was used to evaluate the performance. An example of such a training procedure is shown in Fig. 11.62. A 90% efficiency for our electron identification was required. The neural network output for e/π rejection is shown Fig 11.63. As one could see, with a 15cm radiator rejection factor ca. 9 could be achieved.

As for tracking aspects, a standard GEM plane can only provide the 2D X-Y position of a track, while the GEM-TRD/T with increased drift volume and with Flash ADC readout allows for 3D track segments to be reconstructed as in µTPC configuration. In the hadron end cap region, in addition to the e/π rejection capabilities, GEM-TRD track segment behind dRICH could be used to:

- measure a track angular resolution and therefore help to improve dRICH performance;

- correct for a multiple scattering before EMCAL and improve tracking performance for charged particles.
- improve pointing track resolution and cluster-seed position measurements for EMCAL
- could be used as a seed-element for a track finding algorithms.

Figure 11.64 shows projections of a typical 3D reconstructed track from the GEM-TRD/T prototype. The left panel shows the track projection in XZ plane with Z the drift time as a function of the cluster position in the X direction. The right panel shows corresponding projection in YZ plane.

11.2.5.5.3 Readout structures for MPGDs

Zigzag Shaped Charge Collection Anodes

The segmentation of the readout plane for MPGDs can play a critical role for the detector performance, especially for the spatial and angular resolution and should be seriously considered for future experiments. To improve the resolution, a typical strategy is to simply reduce the pitch of the anodes, but this comes at the cost of greater instrumentation. As an alternative, highly interleaved anode patterns, such as zigzags offer relatively coarse segmentation, while preserving performance [56] [57]. By optimizing the three main operant geometric parameters of the zigzag (including the pitch, the periodicity of the zigzag, and the degree of interleaving, here referred to as the "stretch" parameter), charge sharing among neighboring pads or strips may be finely tuned for specific avalanche schemes. The left panel of Fig. 11.33 compares the resolution

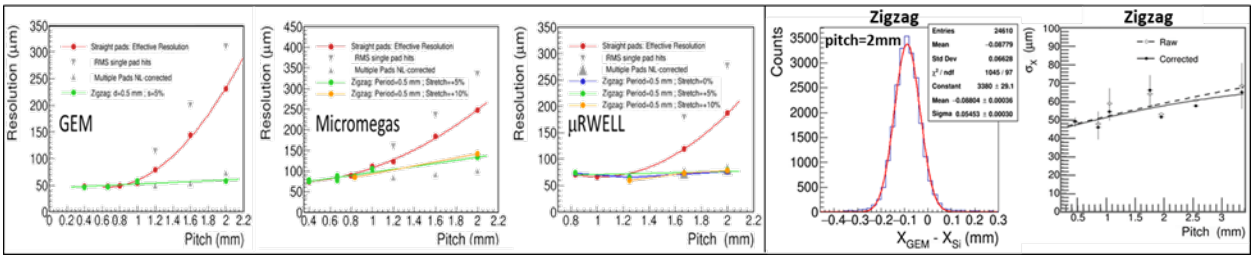

Figure 11.33: Left panel: Position resolution vs. pitch for straight strip and zigzag shaped anodes in GEM, Micromegas and μRWELL detectors respectively. The resolution for straight strips is corrected using pad response functions, however the raw resolutions are quoted for the zigzags. The resolution for the straight strips is broken down into regions of the readout dominated by single and multi-pad clusters (grey points), where the red points denote the weighted average. Right panel: Residual distribution for zigzag anodes with pitch = 2 mm, period = 0.4 mm, and stretch = 0 % and a plot of the position resolution vs. pitch in the case of a 4-GEM detector, respectively.

as a function of the pitch for standard straight strips and various zigzag parameters for GEM, Micromegas, and μRWELL detectors. In all cases, the position resolution is comparable below a pitch of 1mm, but the resolution quickly degrades for straight strips at larger pitch. This is mainly due to poor charge sharing, where the majority of charge is collected by a single pad. An equally beneficial feature of zigzags is the ability to maintain a highly uniform and linear response across the full detector acceptance. The "out of the box" detector response of optimized zigzag anodes is shown in the right panel of the figure, which includes a purely Gaussian raw residual distribution, without the need for pad response functions, as in the case of straight strips. Ultimately, in situations where the detector occupancy is fairly low and a relatively coarse

readout segmentation is acceptable, zigzag shaped charge collection anodes provide a very efficient means of encoding high resolution positional information, with values remaining below 65 μm for a pitch as large as 3.3 mm as indicated in the right-hand plot.

11.2.6 Integration issues

11.2.7 Material Budget Considerations

As is clear from the requirements, the silicon tracking layers require a very low material budget per layer/disc and this need for low mass material budget in the acceptance extends to the surrounding detectors. In order to assess the balance of mass that contributes to the overall load, one needs to make an estimate of the additional material in the fiducial volume that is associated with the tracking detectors. The material budget for the tracking detector is dependent on the parameters of the silicon sensors used, the architecture of the services (powering, readout, cooling, monitoring, safety interlocks, etc.) employed in the deployed detector design and the design and composition of the mechanical support structures used for precisely locating the tracking detector in the main detector volume. A reasonable starting point for estimating the services load is to start with existing technology and powering/readout architectures and project what could be expected should we adopt what has been accomplished. The current state of the art tracking detector of similar characteristics (MAPS sensors, $10/m^2$ of silicon area) is the recently upgraded ALICE ITS. As part of the EIC User Group Yellow Report activities, the service loads have been estimated and parameterized [14]. These estimates have been scaled for what can be expected for a detector system based on the ITS3 sensor which is currently under development [12]. These parameterizations are currently being added to the simulation efforts for the EIC silicon detector baseline detector configurations so that the effects of these mass loads on the physics measurements can be assessed. The largest mass in the services, by far, is the power supply and return cabling. This can be addressed in multiple ways. The most obvious avenue to explore is reducing the power required by the sensors. This is under investigation. An EIC sensor based on the ITS3 type development is expected to reduce the power needed by half to a dissipation of 20 mW/cm^2. This helps, but as the voltage supplied to the sensors is also reduced from 1.8V to 1.2V, to maintain the cable voltage drops to manageable levels, a significant fraction of the conductor is still required. It is possible to reduce the radiation length of the power cabling by moving to copper clad aluminum conductors. This can help significantly since the X_0 of copper is a factor of $\tilde{6}$ lower than the X_0 of aluminum. Using aluminum conductors unfortunately comes at a cost in space required by the services since the conductivity of aluminum is 65% that of copper. Other options would include significantly reducing the number of required conductors to power the detector. This could be addressed by either serial powering of detector staves, or the integration of radiation tolerant DC-DC converters at the stave ends [58]. Both of these options require exploration and R&D to become viable. The readout cabling is also a significant load. It could be possible to combine stave outputs and multiplex the data from multiple staves on detector for readout over high speed fiber optical connections. The multiplexing circuitry and fiber optic drivers would need to be radiation tolerant. In addition, this reduction in the readout granularity would lead to larger portions of the detector becoming inactive in the case of single point failures in the multiplexing and fiber circuits. Clearly an optimization using these factors will need to be carried out. This is also an area for targeted R&D. The reduction in the sensor power dissipation using ITS3 like sensors would significantly help the cooling requirements so smaller and possibly fewer lines could be used. Air cooling is also a possibility, but the envisioned detector is very compact and arranging proper flow and ducting would require careful study. For the detector safety system sensors and environmental monitors, it is likely that the level of services would be similar to what is seen in the ALICE ITS.

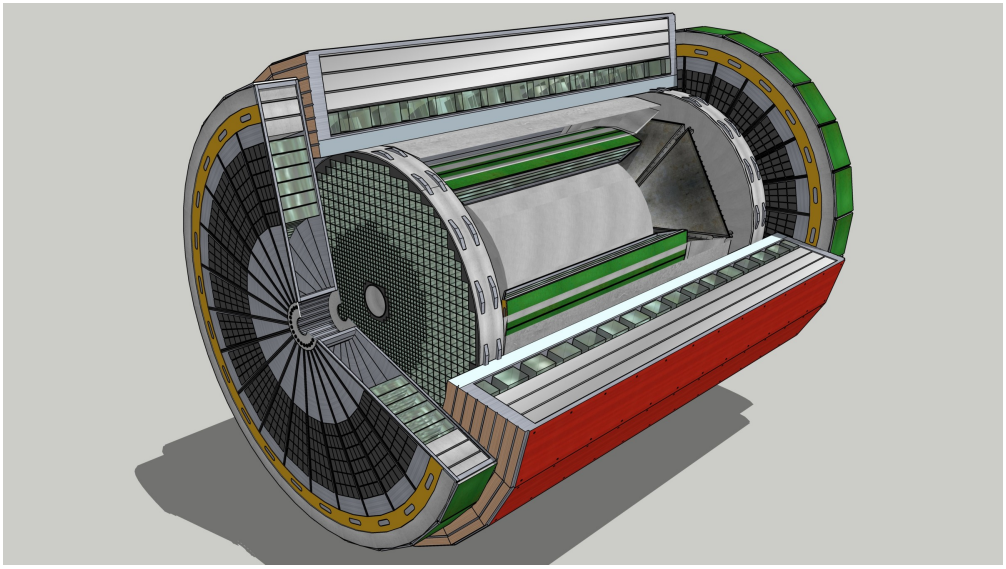

Figure 11.34: Conceptual detector cutaway figure.

11.3 Particle Identification

All multi-purpose detectors, for example as illustrated in Figure 11.34, contain systems that work symbiotically toward achieving the physics goals. Among these detector systems is the subset that identifies the species of collision ejectiles commonly known as Particle Identification Detectors or PID. Typically, the tracking systems provide a momentum measurement ($\vec{p} = m\gamma\vec{\beta}$) which when combined with information on velocity ($\vec{\beta}$) is sufficient to distinguish the various particle species. Most often "PID" refers to the separation of π, K, and *proton* whereas eID refers to the identification of electrons. This section discusses each of these two topics, the requirements for EIC, and possible technological implementations necessary to achieve the physics goals.

The two basic approaches to PID are the direct measurement of the particle's velocity (known as Time-of-Flight or "TOF") and the measurement of velocity dependent interactions of the particle with the detector. Four common velocity-dependent detector interactions are:

- Specific Ionization (aka $\frac{dE}{dx}$), wherein the rate of energy deposit (typically left in a gasseous medium) is measured precisely.
- Cerenkov Radiation, wherein the angle of Cerenkov photon production depends upon velocity as $\cos(\theta_C) = \frac{1}{n\beta}$.
- Bremsstrahlung, wherein the power dissipated to braking radiation goes as $P = \frac{q^2\gamma^4}{6\pi\epsilon_0 c}\left(\dot{\beta} + \frac{\left(\vec{\beta}\cdot\dot{\vec{\beta}}\right)^2}{1-\beta^2}\right)$
- Transition Radiation (TR), wherein the intensity of transition radiation goes as $I = \frac{Z^2 e^2 \gamma \omega_p}{3c}$.

Bremsstrahlung is the effect by which eID is accomplished in an electromagnetic calorimeter. The calorimetry requirements for EIC are discussed in Section 11.4 and will not be additionally discussed here. The ve-

locity necessary to produce sufficient transition radiation is high enough that at EIC a Transition Radiation Detector (TRD) should be considered specifically as an eID device. The velocity dependence of $\frac{dE}{dx}$ and the Cerenkov Effect are highlighted in Figure 11.35 are suitable for PID and eID applications.

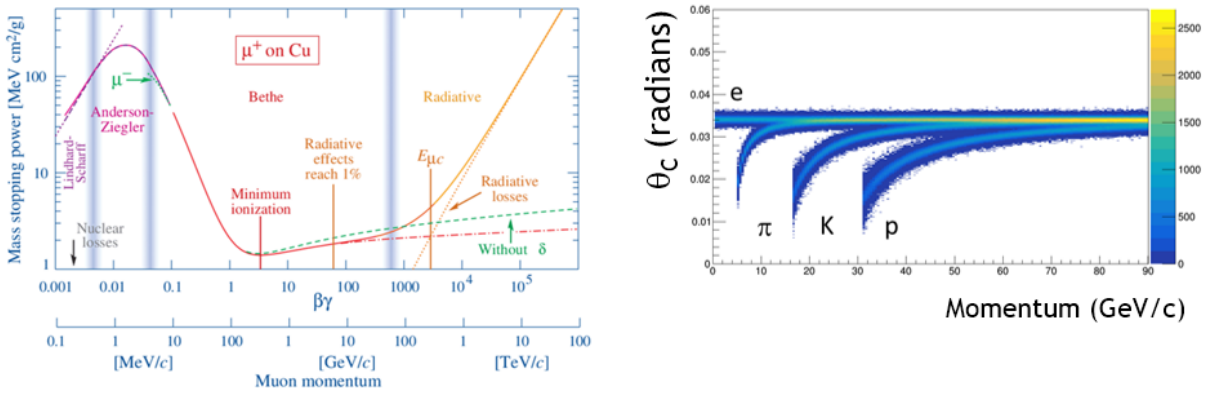

Figure 11.35: Physics of PID devices.

11.3.1 Physics Requirements

As described in part 2 in this report, simulations of collisions for an extensive list of physics processes, each spanning the $\sqrt{s}$ anticipated at EIC have been performed. As an example, Figure 11.36 displays an overview of electron and hadron production as a function of particle lab momentum and polar production angle. The full suite of such calculations were considered and used to formulate the so-called "Requirements Matrix" that specifies relevant detector performance parameters as a function of η. A successful detector design is any that satisfies the detector performance requirements. The PID-relevant subset of the detector matrix is shown in Figure 11.37.

In the following sections we discuss the performance characteristics of multiple suitable detector technologies for the final EIC detector. Following that we discuss how these technologies can be arrayed to best address the requirements matrix.

11.3.2 $\frac{dE}{dx}$

Although many tracking detector configurations are possible (as described in section 11.2), Figure 11.38 captures well two of the leading options. The left panel "hybrid" option includes a Time Projection Chamber (TPC) as its outer layer, which may provide PID information via $\frac{dE}{dx}$. It is thus important to understand the limits of such devices.

At EIC, available space is at a premium, partly due to the longitudinal limit of ± 4.5 meters in Zed. This limit propagates naturally into a radial restriction in the barrel if one chooses the most natural interface between barrel and endcap devices at roughly 45^o or $\eta \sim \pm 1.0$. Given available space, tracking is generally limited to a radiul extend of roughly 1 meter, which is significantly smaller than common TPCs such as STAR (2m) and ALICE (2.5m). It is thus, important to work to achieve excellent $\frac{dE}{dx}$ performance in a small distance.

The primary challenge in any $\frac{dE}{dx}$ measurement comes from the process of energy loss being two steps.

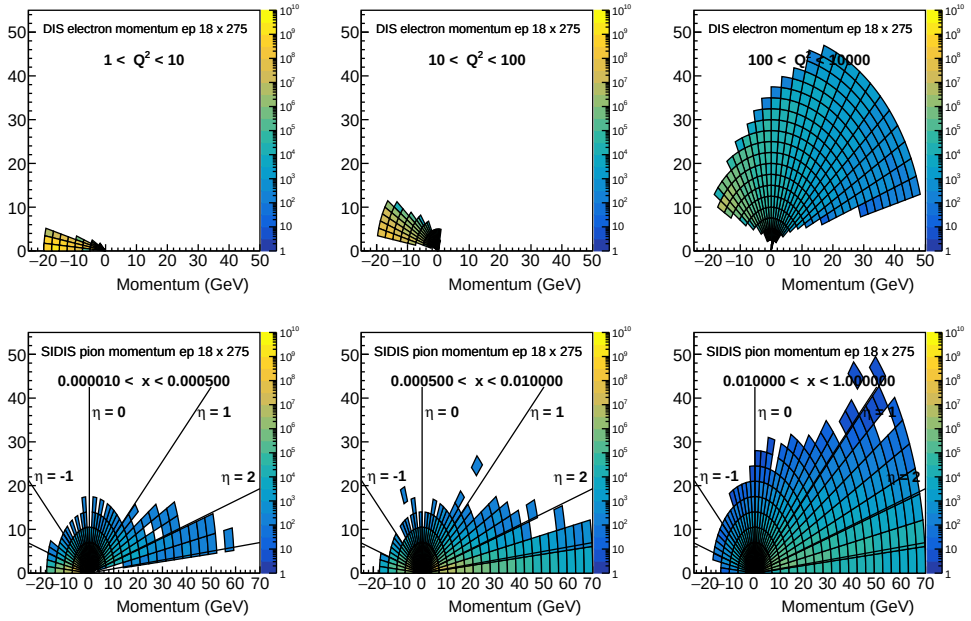

Figure 11.36: SIDIS electron and pion kinematics. This calculation and others were used to establish the detector requirements.

η	θ (mrad)	Nomenclature			Electrons and Photons: Resolution σ_E/E	Electrons and Photons: PID	Electrons and Photons: min E photon	π/K/p: p-Range (GeV/c)	π/K/p: Separation
-4.0 to -3.5					not accessible				
-3.5 to -3.0				Backward Detector	1%/E⊕2.5%/√E⊕1% (for 40 cm space)	π suppression up to 1:1E-4	20 MeV	≤ 10 GeV/c	≥ 3 σ
-3.0 to -2.5									
-2.5 to -2.0									
-2.0 to -1.5					2%/E⊕(4-8)%/√E⊕2% (Upper limit achievable with 50 cm space *Better resolution requires ~65 cm space allocated)	π suppression up to 1:(1E-3 - 1E-2)	50 MeV		
-1.5 to -1.0									
-1.0 to -0.5					2%/E⊕(12-14)%/√E⊕(2-3)% for 30 cm space A better stochastic term can be achieved with more space: 2.5% with crystals 35cm 10% sampling 40cm 4% SciGlass 65cm *Better resolution requires ~65 cm space allocated)	π suppression up to 1:1E-2	100 MeV (50 MeV if higher resolution)	≤ 6 GeV/c	
-0.5 to 0.0			Central Detector						
0.0 to 0.5									
0.5 to 1.0				Barrel				≤ 6 GeV/c	
1.0 to 1.5					2%/E⊕(4*-12)%/√E⊕2% Upper limit achievable with 40cm space *Better resolution requires ~65 cm space allocated	3σ e/π up to 15 GeV/c	50 MeV	≤ 50 GeV/c (worse approaching 3.5)	
1.5 to 2.0				Forward Detectors					
2.0 to 2.5									
2.5 to 3.0									
3.0 to 3.5									

Figure 11.37: Detector performance matrix only for PID.

Each locus of ionization is independent of its neighbors and therefore the rate of primary ionization follows Poisson statistics. This rate is typically captured by the parameter N_p which counts the primary ionization sites per unit length (usually expressed as $\frac{primary}{cm}$. Unfortunately, primary electrons are often released with

sufficient energy to generate several secondaries making a so-called "cluster" of ionization. The total ionization is characterized by $N_t \frac{total}{cm}$ and follows a probability distribution with a long "Landau tail". Battling the resolution loss due to the Landau tail is the primary challenge for any PID detector.

The traditional method of addressing the Landau is to make many independent samples of the ionization and perform either a fit to the $\frac{dE}{dx}$ probability distribution or via a so-called "truncated mean" calculation. An improvement recently suggested and tested by sPHENIX for EIC applications is to use a gas that has an intrinsically small ratio of $\frac{N_t}{N_p}$ so that the fundamental ionization statistics are closer to Poisson. The left panel of Figure 11.39 shows a comparison of STAR $\frac{dE}{dx}$ (72 samples, 150 cm, $\frac{N_t}{N_p} = 3.9$) to a small sPHENIX prototype (48 samples, 60 cm, $\frac{N_t}{N_p} = 2.3$) as measured in test beam. By clever gas choice, similar performance is indeed achieved in a much smaller device. The right panel shows a simulation of performance assuming that one can count explicitly the individual clusters of ionization and thereby approach the limit of Poisson statistics. Such a device might be rather attractive for EIC, but requires further R&D to demonstrate its efficacy in sort length applications such as required for EIC.

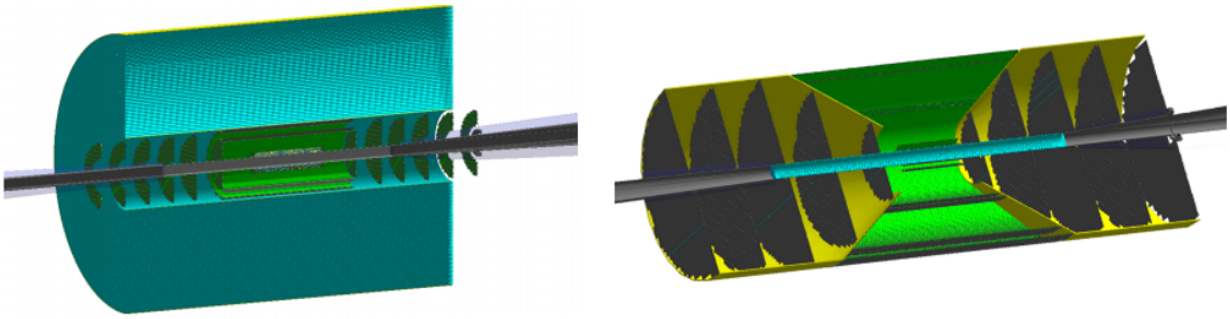

Figure 11.38: Two tracking options. The left panel denotes the "hybrid" option of a silicon tracker to small radius with accompanying TPC, while the right panel denotes an all-silicon tracking option.

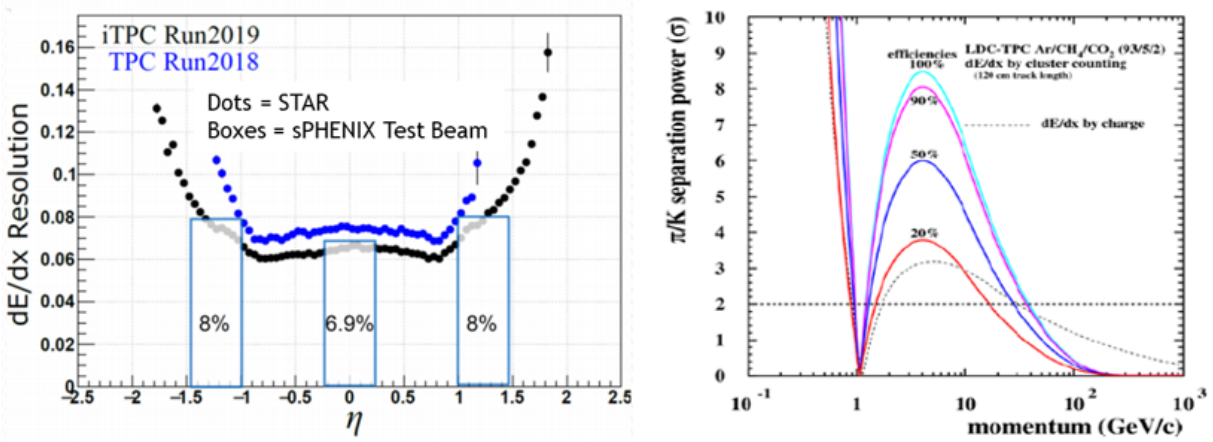

Figure 11.39: Comparison if STAR $\frac{dE}{dx}$ resolution with sPHENIX Test Beam and simulation of a "cluster-counting" detector.

11.3.3 Cerenkov

The measurement of the emission angle of Cerenkov photons is a powerful PID technique with a tunable dynamic range. Because the Cerenkov angle depends upon velocity as $\cos(\theta_C) = \frac{1}{n\beta}$, one is able to accomplish PID at the highest momentum using the lowest index of refraction, n. There are two penalties for choosing low n. First, with lower index, the Cerenkov threshold $\beta > \frac{1}{n}$ goes up, resulting in non-detection of low momentum particles. Second, with lower index, the photon yield per unit length $\frac{dN_\gamma}{dL} = 2\pi\alpha \sin^2(\theta_c) \int \frac{d\lambda}{\lambda^2}$, goes down resulting in long radiators. As a result, Cerenkov detectors must be carefully tuned to the required physics. Because the momentum range needs at EIC (Figure 11.37) vary significantly with η it is necessary to tune the radiator index differently in three regions called "electron endcap", "barrel", and "hadron endcap".

A subtle coupling between Cerenkov measurement and tracking resolution is illustrated in Figure 11.40. Because a Cerenkov detector rarely measures the trajectory of the track it is reliant upon the tracker to provide a direction vector of the track itself underscore while the track passes through the radiator. The effect of a mistake is demonstrated by a simple Monte Carlo that assumes a certain track direction error α as well as a certain photon yield. This simple calculation demonstrates that there is an effect of mismeasurement on the apparent Cerenkov angle and also that the magnitude of the effect depends upon the photon yield of the detector. It is therefore difficult to understand the requirements imposed by the PID device upon the tracker without a detailed Monte Carlo simulation. Detailed simulations have been performed for a number of configurations under consideration and are discussed below.

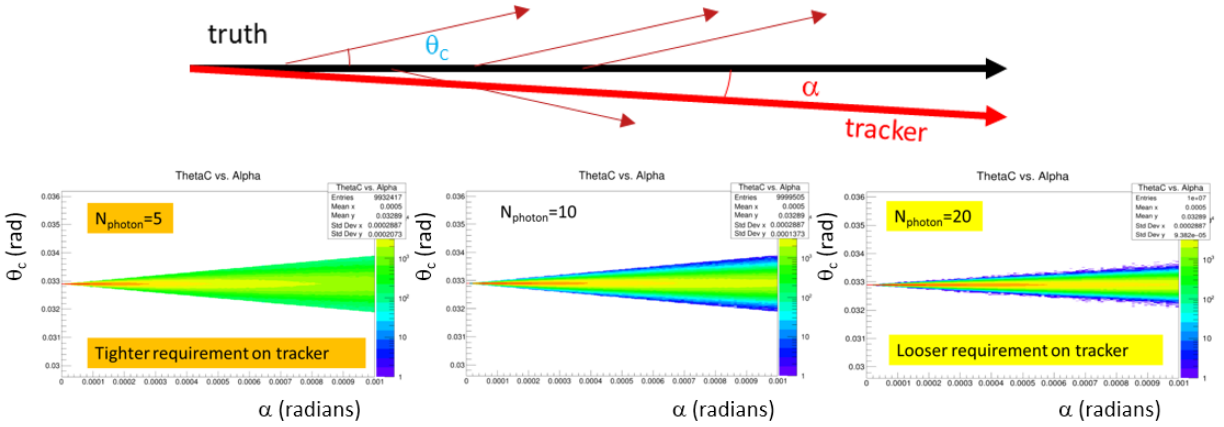

Figure 11.40: Affect of tracking resolution on apparent Cerenkov angle.

A variety of effects limit the precision of measurement of Cerenkov angle in any realistic device. These are listed and discussed here:

- **Chromaticity**
  All materials suffer from an index of refraction that varies with wavelength $(n(\lambda))$ thereby creating a photon-by-photon chromatic smearing of the Cerenkov angle. This effect is particularly acute near the transmission cutoff of the radiating medium.

- **Optical Aberration (aka "Emission Point Error")**
  Even at normal particle-to-mirror incidence, a spherical mirror is just an approximation to a parabolic

reflector. Furthermore, as the angle of incidence strays from the normal, optical aberrations increase. This effectively means that the location at which a photon is detected picks up a dependence on the place within the radiator at which the photon was emitted. It is therefore most often termed as an "Emission Point" Error.

- **Pixelation**
  Cerenkov photons are detected individually and the finite pixel density of the focal plane readout detector thereby generates an uncertainty in the initial emission angle.

- **Magnetic Field**
  Ideally the radiator medium for a Cerenkov radiator is free of magnetic field so that the particle direction is not changing as it propagates through the radiator medium. In a compact application like EIC this is often difficult to arrange and is sometimes approximated by attempting to minimize $\vec{v} \times \vec{B}$ through careful adjustment of the magnetic field orientation. Imperfections necessarily generate uncertainty in the Cerenkov angle.

- **Tracking**
  Finally, the Cerenkov angle resolution can be limited by the knowledge if of the track direction as it traverses the radiator medium.

In the following sections, we'll discuss in detail several options for Cerenkov detector configurations that have been studied in the EIC context.

11.3.3.1 Hadron Blind Detector (HBD)

An HBD device collects unfocused Cerenkov light and makes no attempt to focus the light so as to determine the Cerenkov angle. It is instead operated in a "Threshold Mode" wherein the fastest particles will radiate, making it suitable only for eID and not for PID. The PHENIX experiment was the first implementation of such a device. That implementation is shown in Figure 11.41. Pure CF_4 gas (n=1.00056) is used as a radiator. The transparency at low wavelength is leveraged to take advantage of the $\frac{1}{\lambda^2}$ photon yield. As measured by the "N_0" parameter (325), this is the brightest Cerenkov detector ever built.

A CsI photocathode is evaporated onto Gas Electron Multipliers (GEMs) and provides sensitivity to $\lambda < 200nm$ and has a yield of 20 photon-electrons in 50 cm. In PHENIX, the device was optimized for distinguishing closed Dalitz pairs (40 p.e.) from isolated electrons (20 p.e.). It was not optimized for e/π separation and suffers from an ionization signal generated by any charged particle passing through the focal plane.

Simulations have been done on an alternative HBD implementation (HBD++) as is shown in Figure 11.42. Here the later GEM gain stages are replaced by μMEGAS detector(s) thereby minimizing the ionization signal from the charged particles. This results in a near doubling of the pion rejection provided by the device, but has never been proven in an actual implementation.

11.3.3.2 CsI RICH

A corollary to the HBD design can be achieved by focusing the Cerenkov light into the focal plane and thereby enabling a measurement of the Cerenkov angle. This configuration mostly retains the brightness of

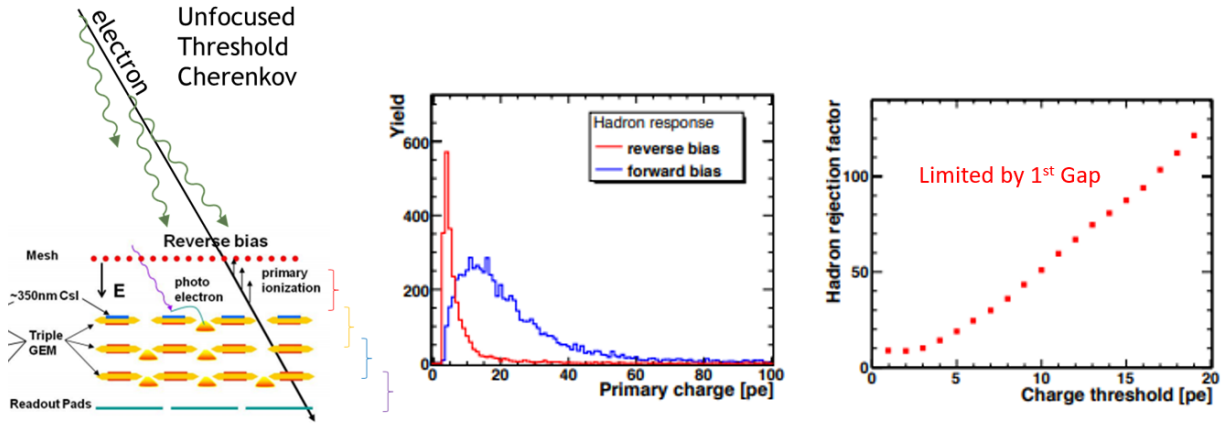

Figure 11.41: Configuration and performance of an HBD Detector in PHENIX.

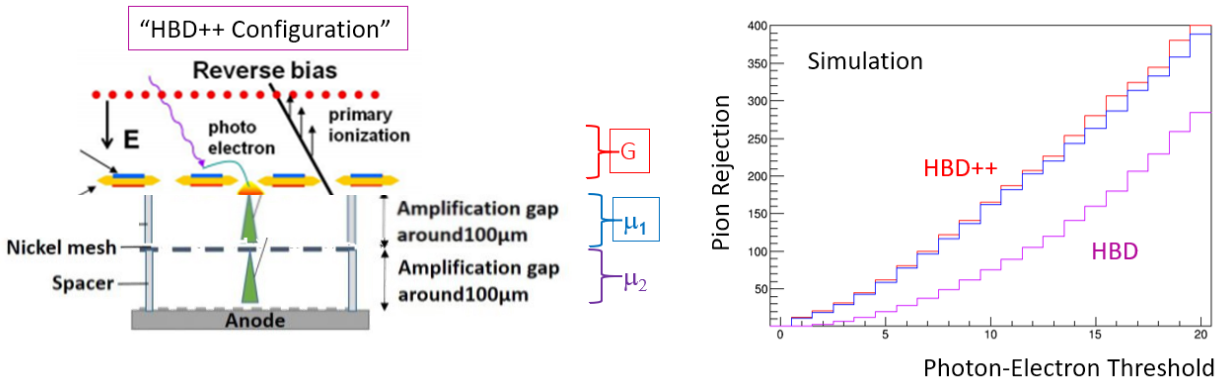

Figure 11.42: Simulated performance of a new HBD Configuration (HBD++).

the original HBD although there is additional light loss due to both the increased gas path length (round trip including the mirror). The concept benefits from the fact that the low material budget of the photon detector (GEMs) can be placed directly in the path of the particles at the entrance of the device. The design suffers, in two critical aspects:

- The low index results in a rather high threshold for pion and Kaon radiation. It must therefore be supplemented by an additional PID device to match the physics requirements.
- Use of the radiation gas down to the transparency cutoff results in a high distortion due to chromaticity.

A detector concept called "ePHENIX" (Figure 11.43) is what results from maximal reuse of sPHENIX detectors and accompanying devices placed in both end caps. The default configuration of this device uses a Cerenkov radiator with CF_4 gas as described above. A prototype of this device was tested at Fermilab (Figure 11.44) with excellent π-K separation measured at 32 GeV/c and extrapolated 3-σ performance to 60 GeV/c.

Figure 11.45 shows the result of a simulation in which the measured detector performance is parameterized and subjected to varying errors in track direction. Because the device is severely limited by "chromatic-

ity" (wavelength-dependent index), this device has comparatively lax requirements on the tracking and is unaffected by track pointing errors of roughly 2 mrad or less.

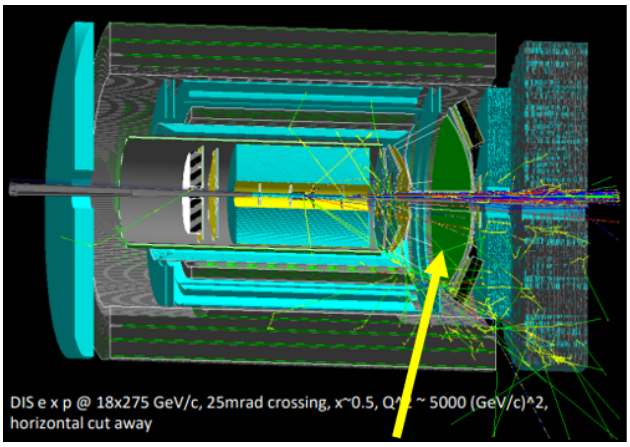

Figure 11.43: ePHENIX configuration of a gas Cerenkov.

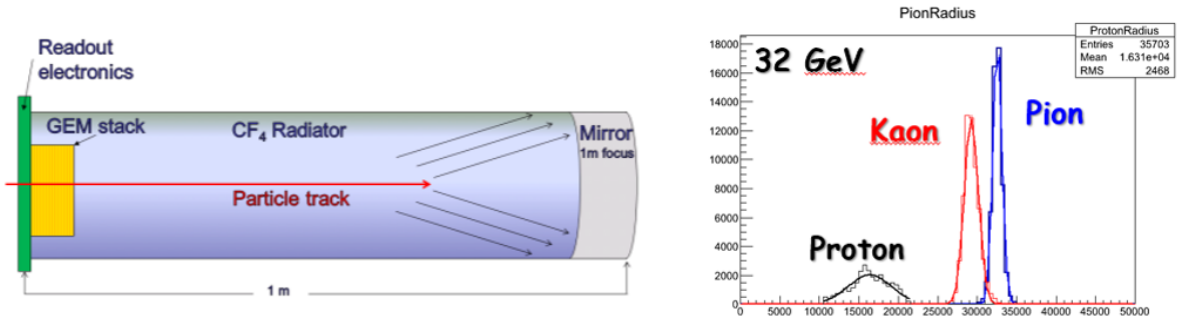

Figure 11.44: Test beam results for the GEM RICH.

In the ePHENIX implementation, the CsI RICH is complemented by mRICH detectors (see below) that compensate for the high Cerenkov threshold over some of the aperture. While somewhat effective, this design is not the most optimal for EIC at the highest momenta.

An alternative to the GEM-based photon detector, is represented by the hybrid MPGD photon detector in use since 2016 in COMPASS RICH []: two THick GEM (THGEM) multiplication layers, the first one coated with a CsI film and acting as photocathode are followed by a resistive MICROMEGAS stage (Fig. 11.46). A reduced pad size is needed to match the compact configuration at EIC, where the gaseous RICH focal length is of the order of 1 m. A prototype with reduced pad-size from 8 mm to 3 mm has been designed, built and successfully beam tested (Fig. 11.47). Its operation in a window less configuration as the ePHENIX one has to be confirmed.

So far, CsI is the only photoconverter that has been successfully used in gaseous detectors, although its usage is affected by some difficulties and limitations. In fact, its quantum efficiency is destroyed by the bombardment due to ions produced in the multiplication process when the integrated charge overcome a level of 1 mC/cm^2. Therefore, the detectors have to be used at limited gain that affects their overall efficiency. CsI is chemically fragile, in particular if exposed to water vapour and this feature imposes tedious

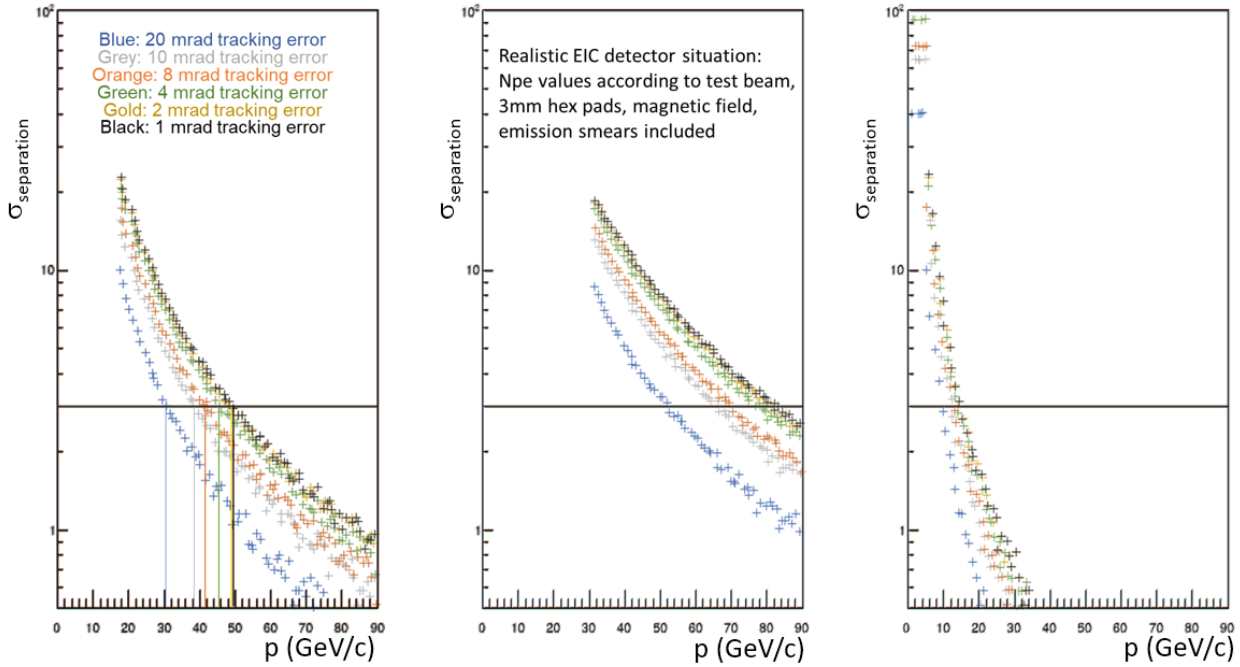

Figure 11.45: Simulation results for the GEM RICH.

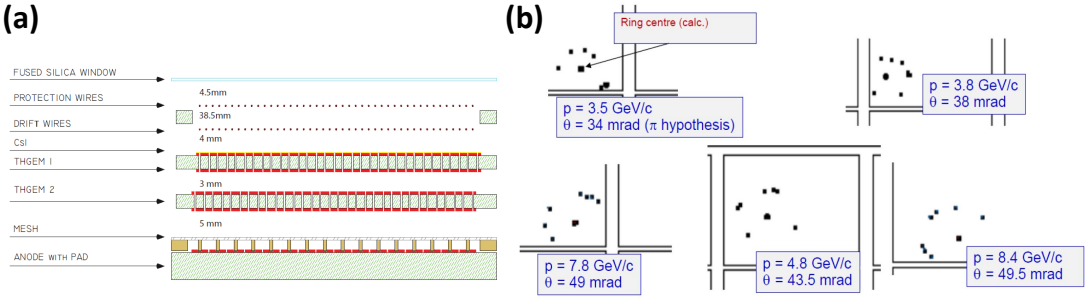

Figure 11.46: (a) Sketch of the hybrid single photon detector: two staggered THGEM layers are coupled to a resistive bulk MM; image not to scale. (b) Ring images detected with the hybrid single photon detector of COMPASS RICH; ring centres calculated from the reconstructed trajectory; no image filtering applied.

manipulation always in dry inert atmosphere. A novel, more robust option is offered by Hydrogenated Nano Diamond (HND) powder. It has sizeable quantum efficiency in the same UV domain as CsI with analogous values. Hydrogenation has to take place at high temperature. The powder hydrogenation before forming the converting coating makes this approach compatible with the components of gaseous detectors. HND exhibits good chemical stability and the coating layer is mechanically robust. The performance of THGEMs with HND coating is unchanged, when an appropriate post-coating heating protocol is applied (Fig. 11.48, (a)).The preservation of the quantum efficiency when the protocol is applied is under study Fig. 11.48, (b)); presently, the protocol is being optimized to obtain a complete preservation. The goal of these R&D is to obtain a valid alternative to CsI in order to empower the potentialities of single photon detection by gaseous detectors.

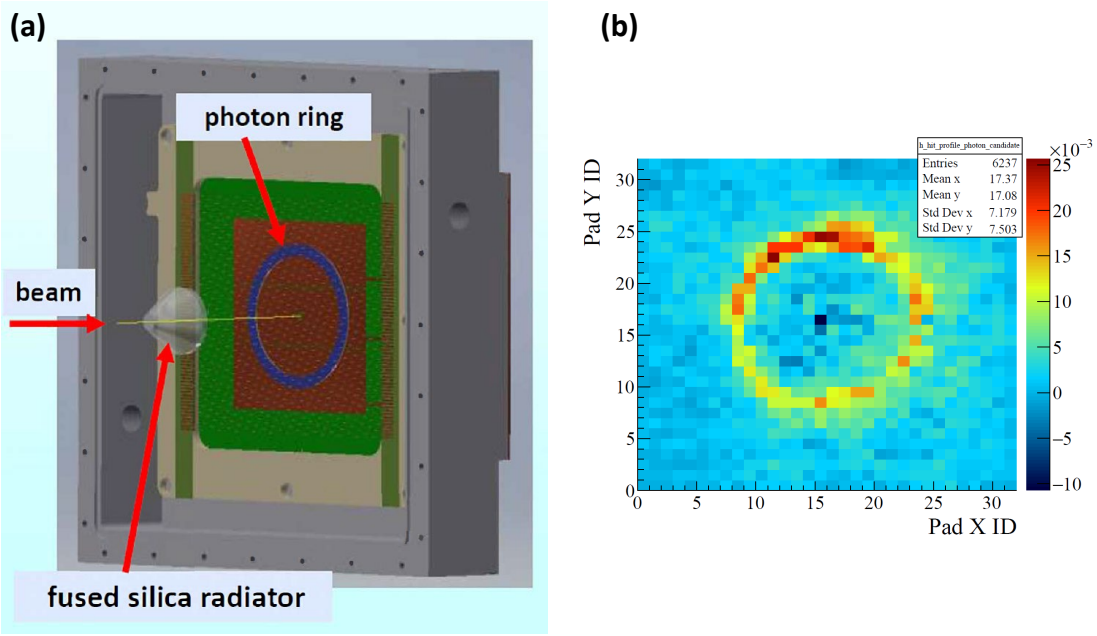

Figure 11.47: (a) The formation of the ring image on the photon detector prototype by Cherenkov photons generated in a quartz radiator crossed by beam particles (principle). (b) 2-D histogram of the hits produced by the Cherenkov photons in the small pad-size prototype

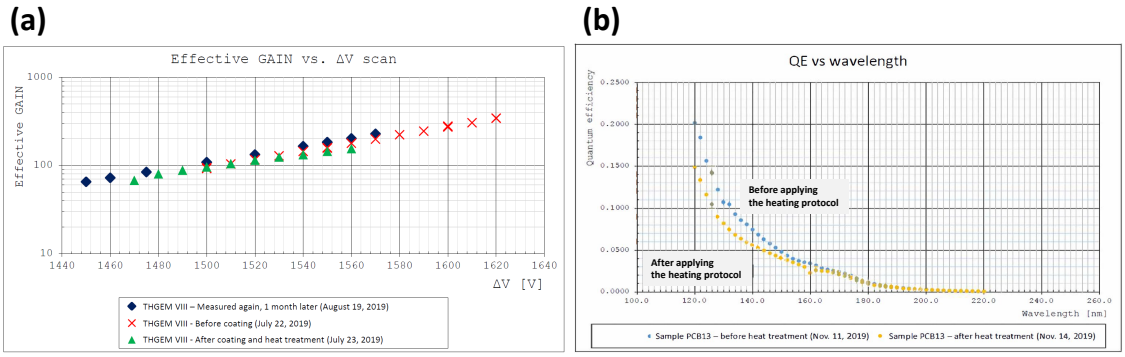

Figure 11.48: (a) Effective gain versus applied biasing voltage for a same THGEM measured with the bare device and with HND coating after applying the heating protocol; the measurement has also been repeated a month later. (b) QE versus wavelength of a NHD-coated sample measured before and after the heating protocol.

11.3.3.3 Dual RICH (dRICH)

A so-called "Dual RICH" utilizes two different radiator indices and thereby is able to cover the full momentum range without penalty owing to the Cerenkov threshold of the gas section. The design optimized for EIC is shown in Figure 11.49 and uses both an aerogel radiator and a gas radiator (C_2F_6) to cover the full momentum range in a single device. In the current design, it is assumed that the photon readout would use conventional technology (*e.g.* multi-anode phototubes) and therefore is is inappropriate to locate the focal plane directly in the path of the particles. This has multiple effects that drive the device performance:

- The optics is less ideal and therefore the emission term becomes dominant in the resolution.
- The focal plane is moved to a lower radiation zone. This helps not only in the level of background hits that can interfere with the photon ring, but also may allow the use of emerging technology such as SiPM detectors to be used for the readout.

Shifting the focal plane to one side widens and complicates the parameter space for detector design, making optimization a daunting task. The present design of the detector was optimized using neural network techniques to investigate a wide space of detector configurations. The design shown here is the result of that exhaustive investigation.

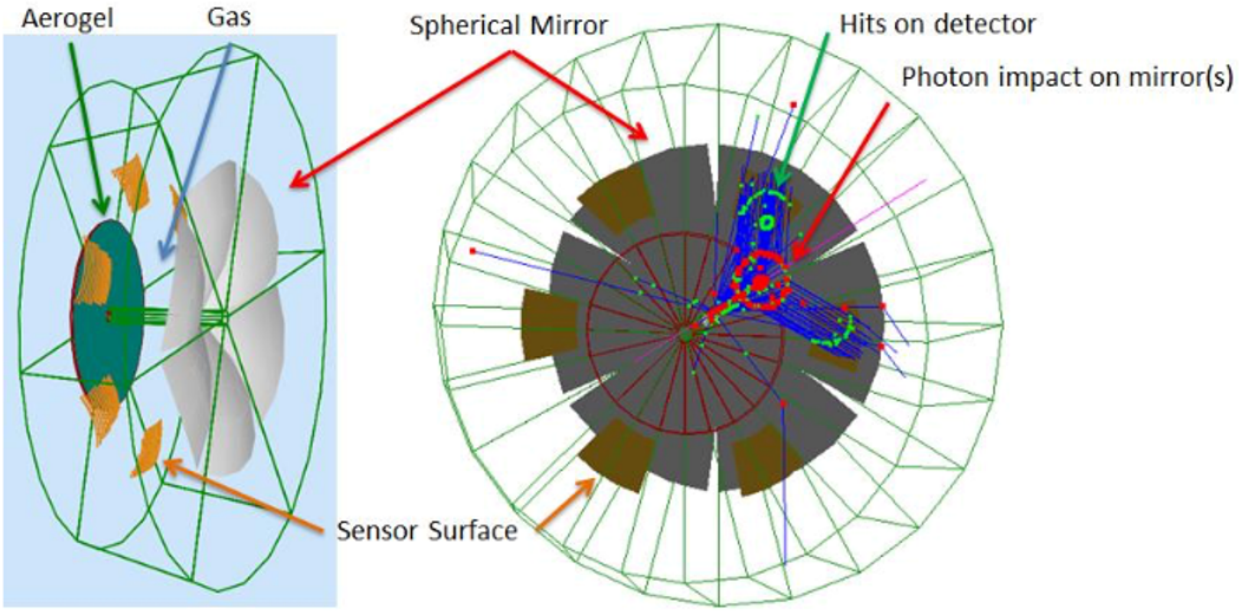

Figure 11.49: Dual RICH detector configuration.

Figure 11.50 shows the converged solution for the detector performance optimization in both the aerogel and the gas sections. Each term in the final resolution is isolated by its contribution of the Cerenkov angle resolution. The aerogel performance is dominated by the natural chromaticity of the radiator medium itself. All other contributing factors to the aerogel performance are negligible as compared to chromaticity which represents a fully optimal performance.

The angular resolution of the gas section is more complex. As referenced previously, emission terms (aberration) are dominant and peak at the edges of the segmented RICH mirrors. The optimization of this factor is evident by the fact that the Emission resolution term is of equal height at the two extremes of the polar angle acceptance.

Figure 11.51 indicates the calculated performance of the dRICH detector for e-π, π-K, and K-p separation. Several features are worth noting. First, the dRICH is not merely limited to PID application, but also provides excellent eID out to roughly 20 GeV/c momentum. Second, the dRICH does not have ”holes” in the performance either at low momentum (due to aerogel) nor at intermediate momentum due to the index match of the aerogel and gas radiator performance. Finally, the π-K performance achieves the full goals of the requirements matrix.

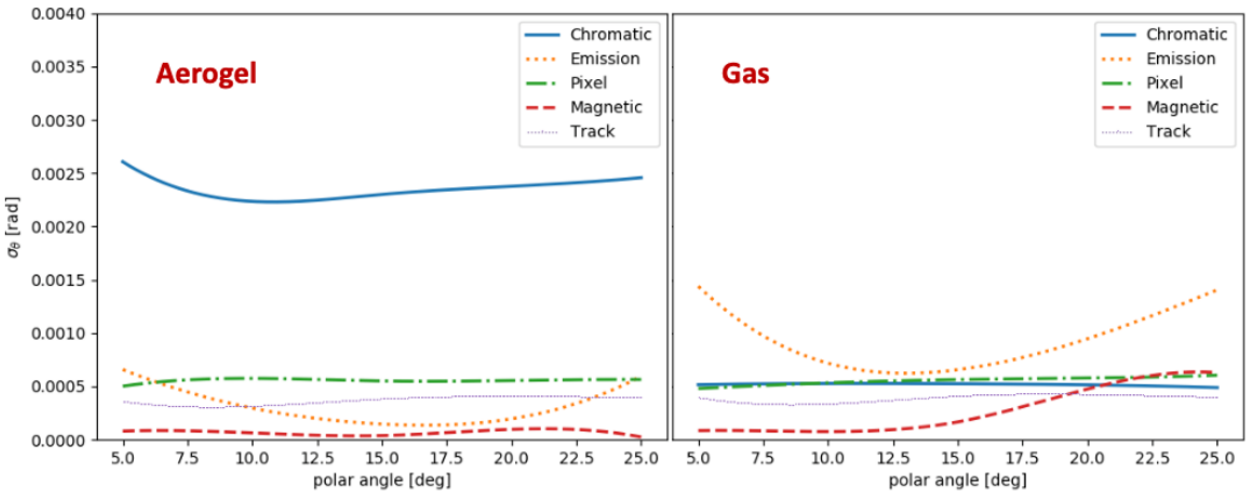

Figure 11.50: Resolution contributions for the Dual RICH.

As is true for most modern gas Cerenkov detectors, the dRICH design utilizes the superior performance of perfluorocarbon radiator gas (C_2F_6). Future environmental concerns can have two kinds of impact:

Current calculations demonstrate that these issues could be avoided by running an environmentally friendly gas at high pressure. Indeed, current calculations indicate that the dRICH performance would be insignificantly affected by a switch to Ar gas at 3 atm. This will nonetheless impose an engineering challenge to maintain a low material budget.

One final note is that the external requirement on the tracking systems was modeled to be a limiting resolution of 1 mrad on track inclination while the track passes through the whole length of the gas radiator. Due to the large lever arm (1.5 meters) and possible scattering internal to the detector itself (entrance window in the high pressure version), it is likely wise to supplement the tracking prior to the dRICH with a detector that provides an additional space point beyond the radiation volume. This latter point can be rather low resolution as compared to the rest of the tracking while still providing the necessary 1 mrad uncertainty in track direction.

- It may be required to recover and purify the radiator gas to avoid release to the environment, which is a significant cost and complexity.
- Environmental concerns in the worst case could drive the cost and availability of the gas beyond tolerable levels.

At the time of this writing, the dRICH is the best known approach to EIC particle at the highest possible momenta due to its full coverage of the dynamic range in momenta desired for the hadron arm.

11.3.3.4 Modular RICH (mRICH)

A so-called ”Modular RICH” is an aerogel-based RICH. A unique feature of this device is the use of a Fresnel lens to make a focused ring, thereby significantly improving the performance as compared to a

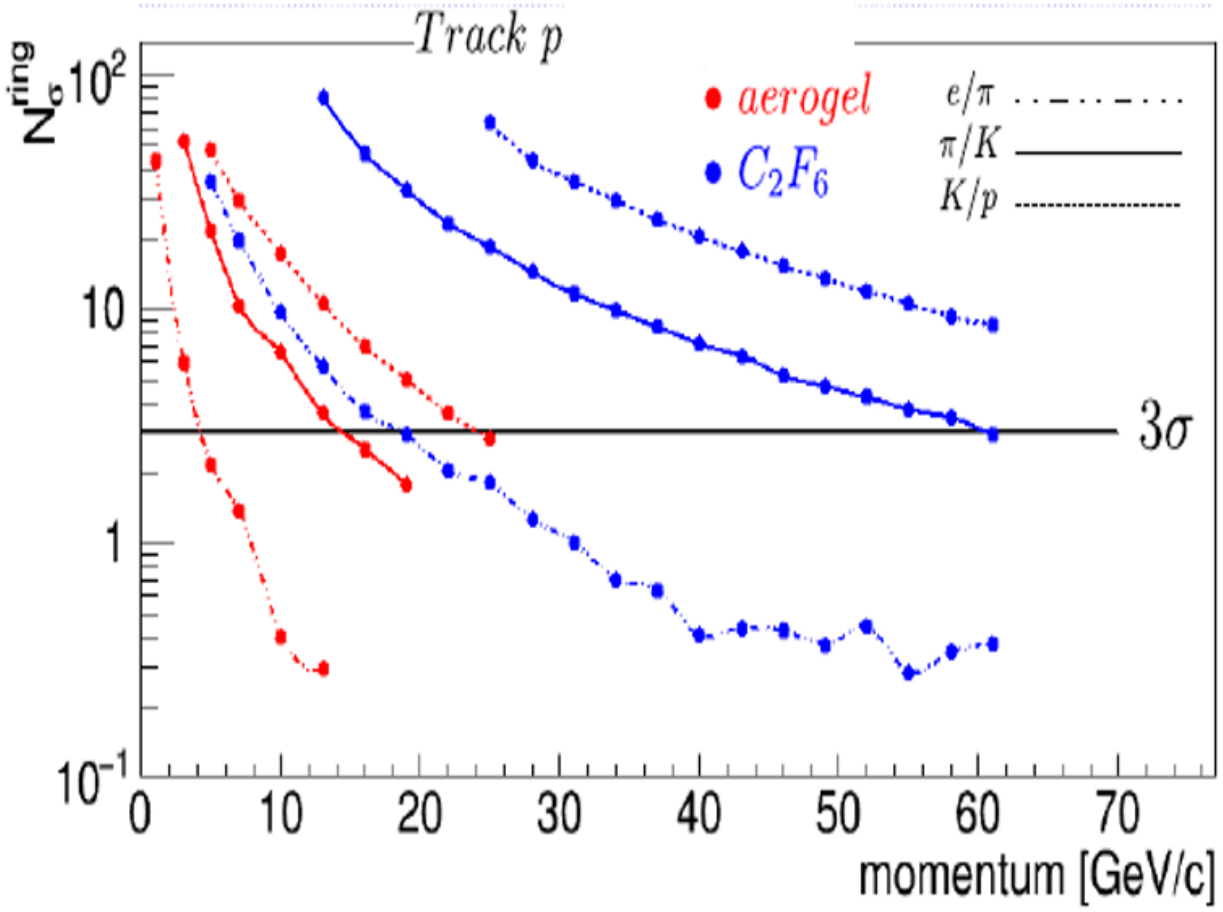

Figure 11.51: Performance of the Dual RICH.

"proximity focused" detector which is more common in aerogel applications. As shown in Figure 11.52, mirrors along the sides of the device allow it to collect light which is not initially directed to the photocathode found at the detector exit. Several aspects of the design of this device allow it to outperform conventional aerogel-based RICH detectors:

- The fresnel lens acts to generate a lens-focused rather than a proximity-focused ring.
- The fresnel lens imposes a wavelength cutoff on the transmitted light limiting the chromaticity effect.
- The focusing aspect somewhat relaxes the mechanical tolerances on the exit surface of the aerogel.
- The mRICH can possibly be configured with a photodetector that exhibits precision timing.

This device is useful both in the electron arm performing both eID and PID functions and also in the hadron arm (under the presumption of a gas RICH instead of a Dual RICH).

The limit to the resolution of the mRICH detector is the chromaticity term (as was trurn for the aerogel section of the dRICH), indicating the the design is presently optimal. The simulated performance of the mRICH is shown in Figure 11.53. The saturation yield of Cerenkov photons is 10 per ring and is shown as

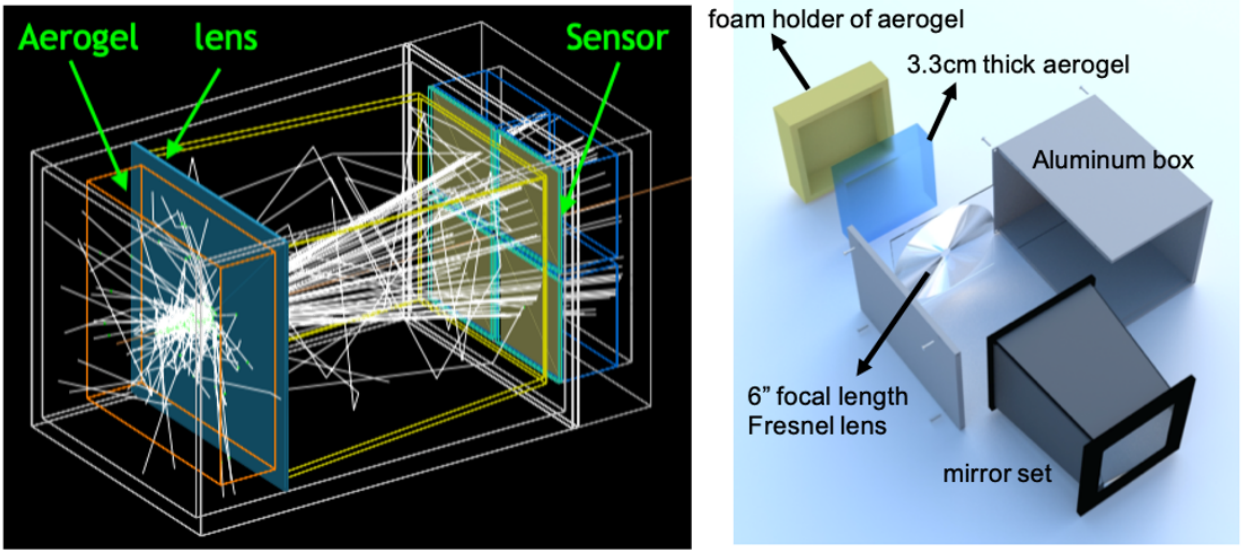

Figure 11.52: Configuration of the Modular RICH.

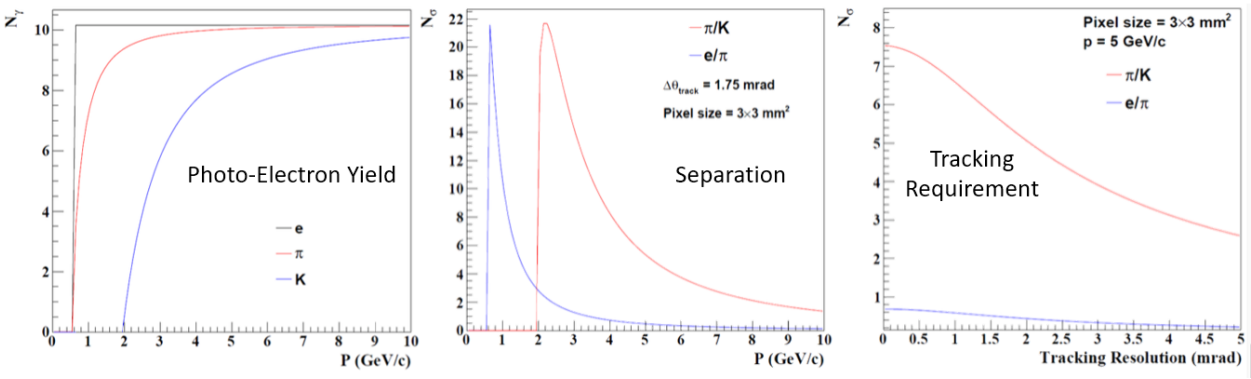

Figure 11.53: Performance of the Modular RICH.

a function of momentum for π and K. The center panel shows that the e-π rejection extends until roughly 2 GeV/c and π-K until roughly 6-7 GeV/c. These are well, but not perfectly matched to the requirements matrix in the electron arm. Finally, as with all precision Cerenkov devices, the mRICH has strict requirements on the tracking resolution provided. The third panel shows the degradation in separation as the tracking resolution worsens indicating a tolerance of roughly 1 mrad as supplied by the external system.

Finally, Figure 11.54 shows an option for configuring the output detection stage of the mRICH with a high precision timing detector so that it can additionally serve as a TOF tag, thereby improving its PID capability.

11.3.3.5 Detection of Internally Reflected Cerenkov (DIRC)

An interesting aspect of Cerenkov detectors emerges at high index. Since both the saturation Cerenkov angle ($\beta = 1$) and the angle for total internal reflection are solely dependent upon refractive index, one finds that at normal incidence, Cerenkov light will be totally internally reflected by any material whose index

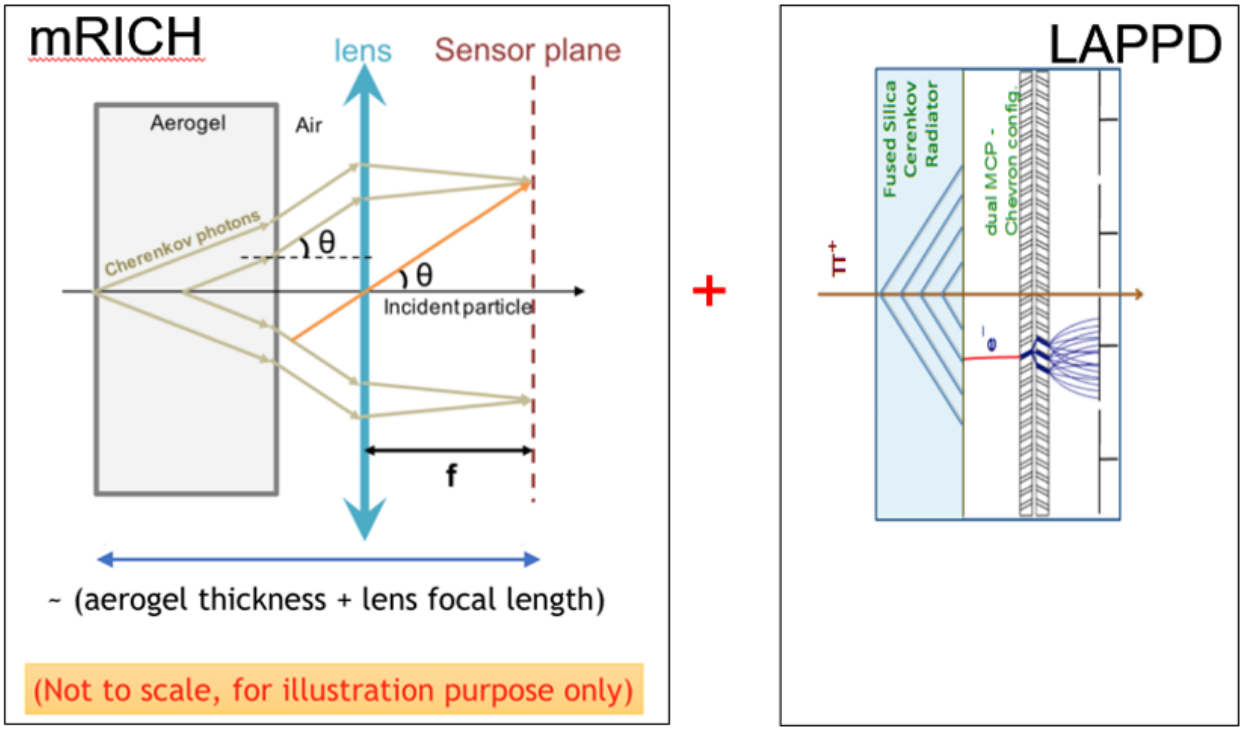

Figure 11.54: Timing Option for the Modular RICH.

satisfies the condition $n > \sqrt{2}$. This technique offers the unique advantage that, so long as the sides and corners of the radiator are made with high precision, the light can be propagated to the end of the radiator while preserving the Cerenkov angle. The result is a geometrically thin device that allows light detector detection only at the end(s). Furthermore, due to the in-medium light propagation length depending upon the Cerenkov angle, timing can also be used to aid the refining the Cerenkov angle determination.

The original application of DIRC was in the BaBar experiment at SLAC wherein the barrel section of the detector was surrounded by a series of quartz bars. Rings were imaged by a so-called ”expansion volume” that effectively made for a ”proximity focus”. In the years that followed many advances of DIRC technology have been accomplished to effectively replace the proximity focus with an actual focus. The result is that it is conservatively anticipated that an EIC application of DIRC technology can be made that far outperforms the Babar application while dramatically reducing the size of the expansion volume. A picture of this High Performance or hpDIRC is shown in Figure 11.55. The left panel shows the quartz bars and the expansion volume isolated from the rest of the EIC detector. The right panel shows one possible geometry by which the DIRC could be realized in an EIC detector. Here the expansion volume is terminated with the photon detectors as indicated in red. Because the photon detectors prefer to be normal to the spectrometer’s magnetic field, their explicit locations will be tightly coupled to the edge field orientation. It has been demonstrated that all plausible magnetic field orientations can be accommodated with little or no degradation in overall performance.

The DIRC application in many ways represents exquisite precision in all the geometric aspects of Cerenkov. As a result, the DIRC’s precision must be similarly reflected in the tracking. The contribution of tracking resolution falls into the category of ”correlated terms” in the analysis of the DIRC performance. It is deter-

mined through detailed simulation that the full contribution of all correlated terms must not exceed 0.8 mrad and that the tracking terms must not exceed 0.5 mrad. Fortunately, these strict requirements are able to be achieved with technologies discussed elsewhere in this report.

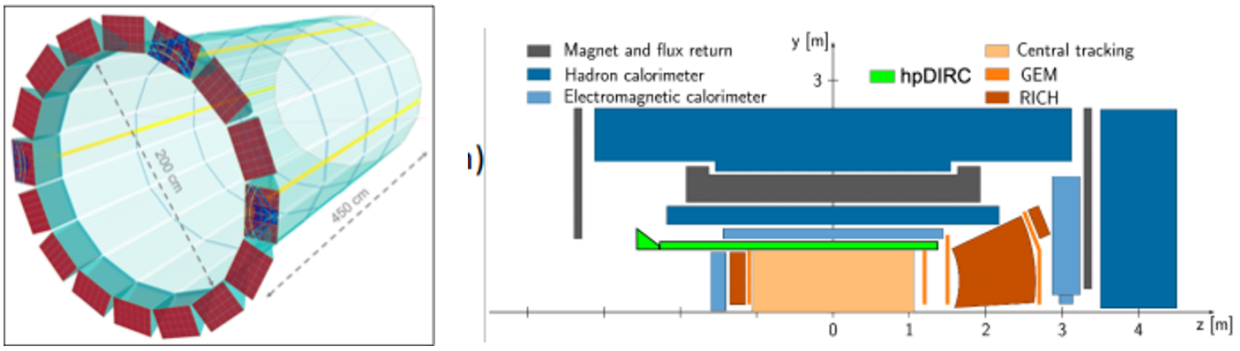

Figure 11.55: Configuration of the DIRC.

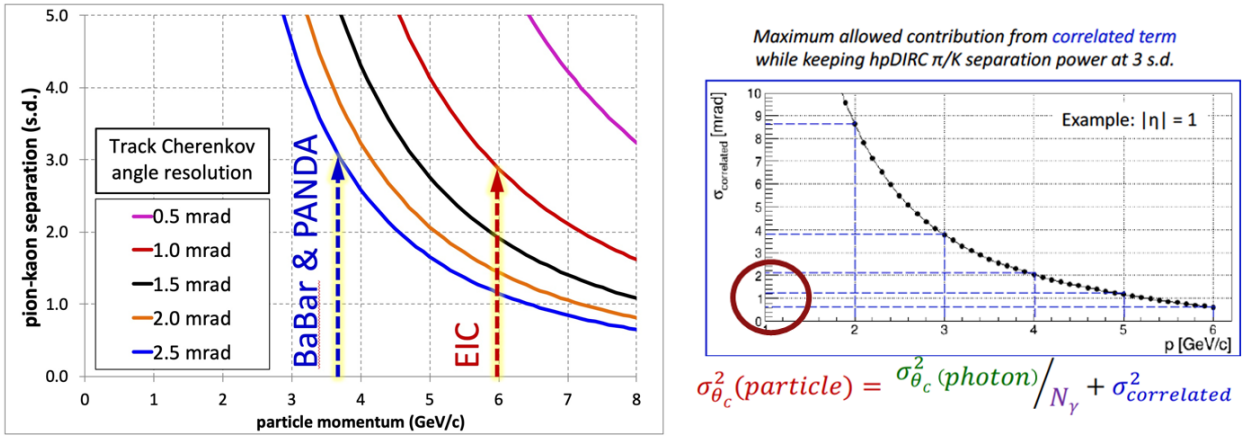

Figure 11.56: Performance of the DIRC in simulation.

Figure 11.56 summarizes the anticipated DIRC performance in the so-called ”hpDIRC” configuration and also compares the performance to the Babar and PANDA applications of this technology. The improvement in performance improvement is close to a factor of two in particle momentum for successful π-K separation and reaches 6 GeV/c. It is important to note that as with all PID detector technologies, various assumptions about the performance of other detector systems is vital to estimate the efficacy of the device. These factors can be combined into a single so-called ”correlated term”, the effect of which is indicated by the right half of Frigure 11.56. In particular, this figure denotes the limit applied to the convolution of all sources of correlated term as a function of desired 3-σ π-K separation goal. To reach the requried performance for EIC, it is clear that the correlated term must not exceed 0.8 mrad and this places a restriction on the tracking performance at the level of 0.5 rad.

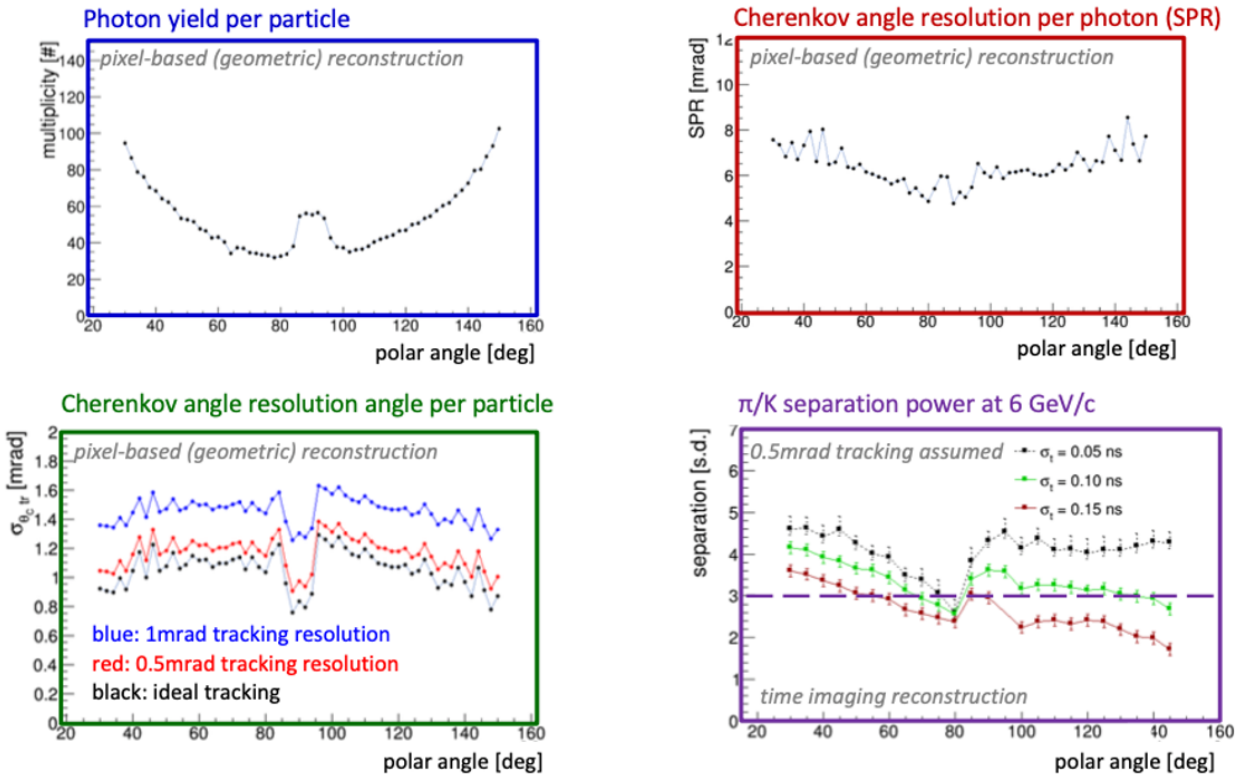

Figure 11.57: Dependence of the DIRC performance on η.

11.3.4 Time Of Flight (TOF)

Recent years have seen major advancements in the precision by which detector devices can measure the time of passage of a particle. Such time, whether compared to a reference time for the collision as a whole (aka "Start time") or whether measured at multiple points along the trajectory of a particle as it passes through the spectrometer allow for a direct measurement of the particle's velocity and hence are useful forms of particle identification. An intrinsic advantage of measurements is that they contain no limiting threshold in performance (*e.g.* Cerenkov radiation is only produced for $\beta > \frac{1}{n}$) and are thereby produce signals for charged particle of any momentum. These detectors are most often rather thin measured both by radiation length and by physical dimension.

One can divide modern TOF technologies into two categories depending upon whether the technology converts light into photo-electrons (which subsequently avalanche) or whether they produce and detect ionization directly. The former case (as discussed in more detail in Section 11.3.5) is most often sensitive both to the strength and orientation of the external magnetic field.

Figure 11.59 displays one possible configuration of TOF detectors as arrayed into the typical EIC detector geometry. This particular geometry makes the assumption that the ToF measurements would achieved with a silicon-based technology such as LGAD that is intrinsically insensitive to magnetic fields. The technology is layered in each direction so that several measurements of time are performed on every track and that these measurements additionally contribute to the tracking system by virtue of providing precision space points as well as precision timing ("4D" tracking).

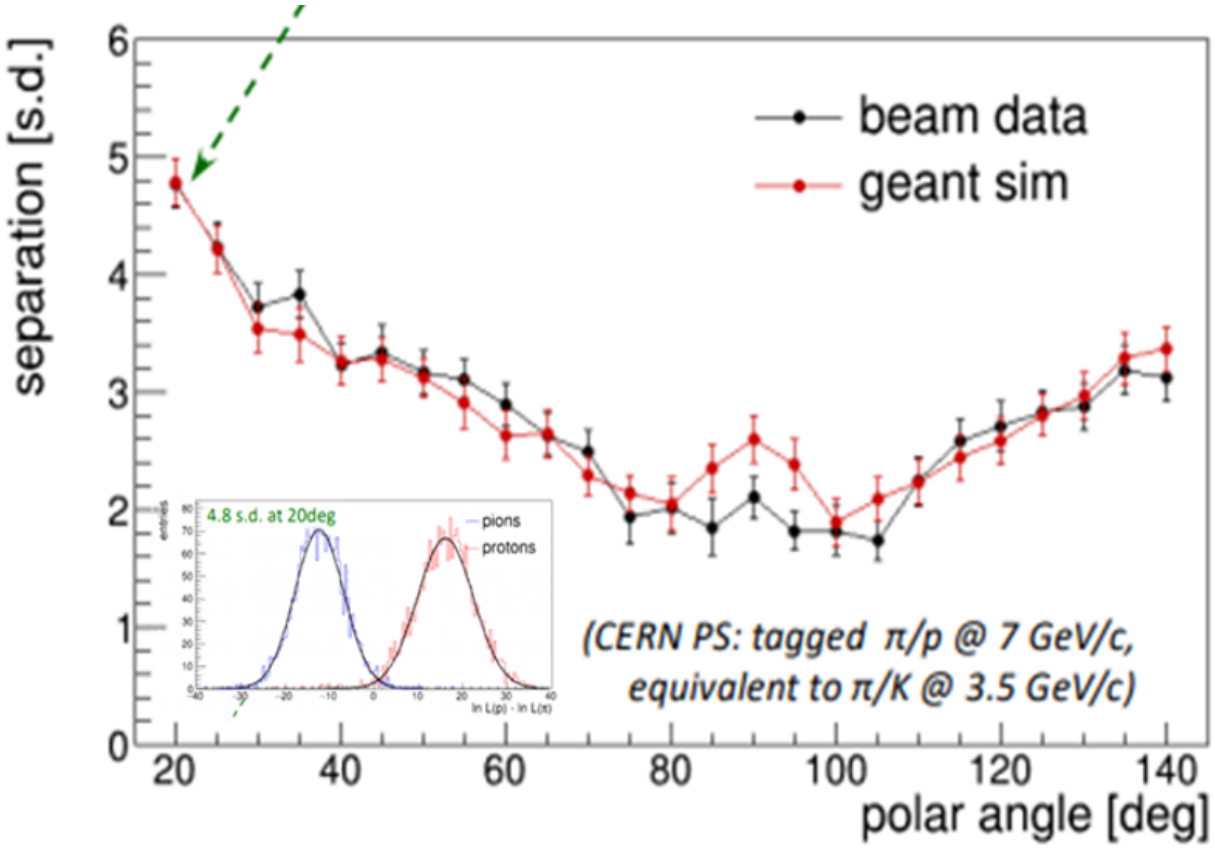

Figure 11.58: Comparison of the DIRC performance to test beam measurements.

The performance of the all-silicon TOF system shown previously is summarized in the left two panels of Figure 11.60. We note several aspects of this calculation. First, the calculation assumes that the overall time measurement scales with the number of measurements as $\frac{1}{\sqrt{N_{meas}}}$. This requires that common issues such as clock jitter are small compared to the intrinsic detector resolution. Appropriate R&D is ongoing to ensure that this will be the case by the time of EIC. Second, the calculation assumes the absence of HCAL detectors in the endcaps so that the flight path of the particles can be maximized. The existence or not of HCAL is thus one of the issues that can addressed in the design of complementary EIC designs.

At the time of this writing, the best TOF performance is supplied by LAPPD (Large Area Picosecond Photon Detector) devices at roughly 5 psec σ. The performance of that detector is summarized in eth right-most panel of Figure 11.60. Because these devices utilize the avalanche of photo-electrons to generate their signal they are sensitive to the magnetic field. The current implementations of the technology are therefore limited to end cap implementations.

11.3.4.0.1 MPGD-based-TRDs for Electron PID and Tracking in the End Caps

Identification of secondary electrons plays a very important role for physics at the Electron-Ion Collider (EIC). J/ψ has a significant branching ratio for decays into leptons (the branching ratio into electrons (e^+e^- pair) is 6%). The branching ratio of D-mesons is Br($D^+ \rightarrow e + X$) $\sim$ 16% and the branching ratio of

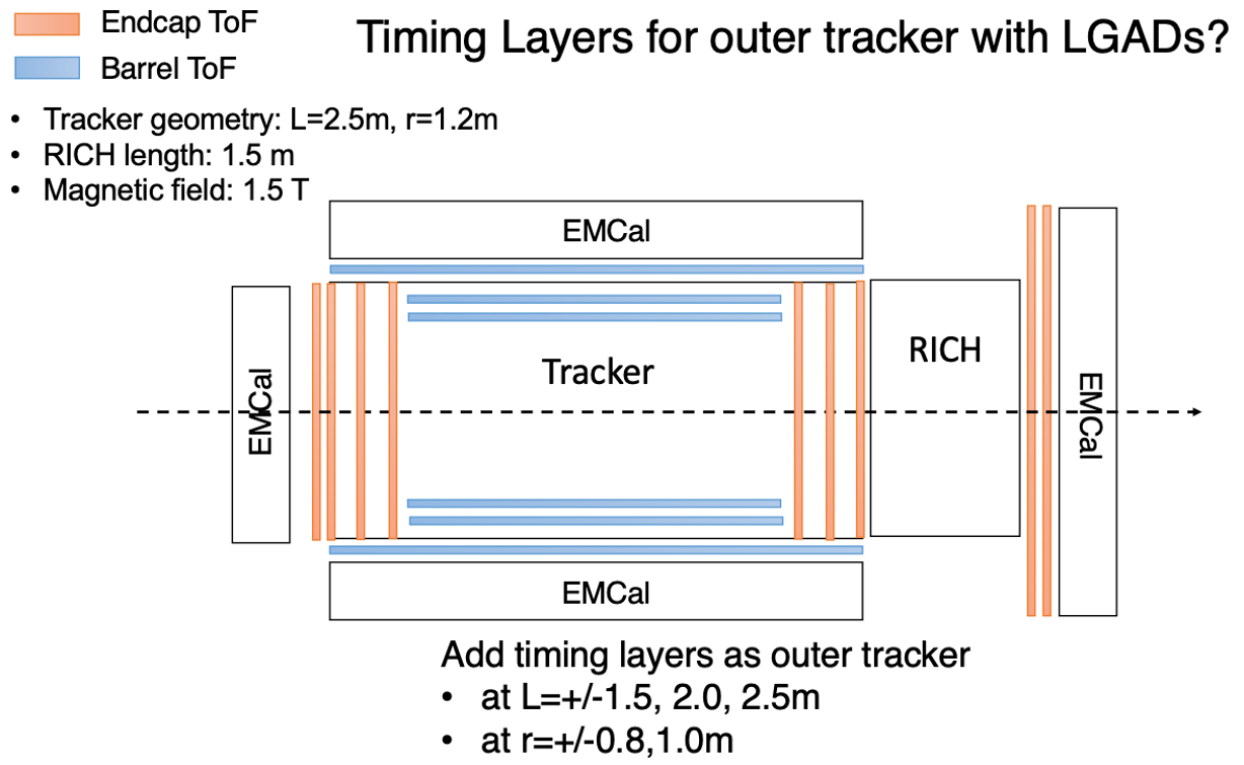

Figure 11.59: Configuration of Time of Flight for EIC.

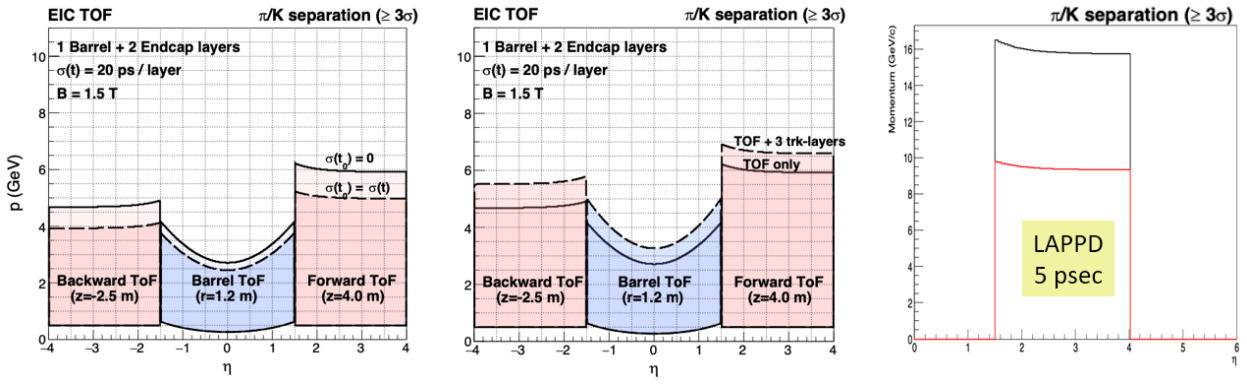

Figure 11.60: Performance of Time of Flight for EIC.

B-mesons is Br($B^{\pm} \rightarrow e + \nu + X_c$) $\sim$ 10%. Electron identification is also important for many other physics topics, such as spectroscopy, beyond the standard model physics, etc. By using more sophisticated electron identification an efficiency of those channels could be increased. A high granularity tracker combined with a transition radiation option for particle identification could provide additional information necessary for electron identification or hadron suppression. Due to asymmetric beam energies and boosted kinematics, it is important to provide such additional instrumentation in the hadron endcap. The basic concept of GEM-based TRD is shown on the Fig. 11.61. A standard triple-GEM detector [24] with high granularity strip pitch (400 μm) capable of providing high resolution space point position information was converted into a transition radiation detector and tracker (GEM-TRD/T) [54]. This was achieved by making several modifications

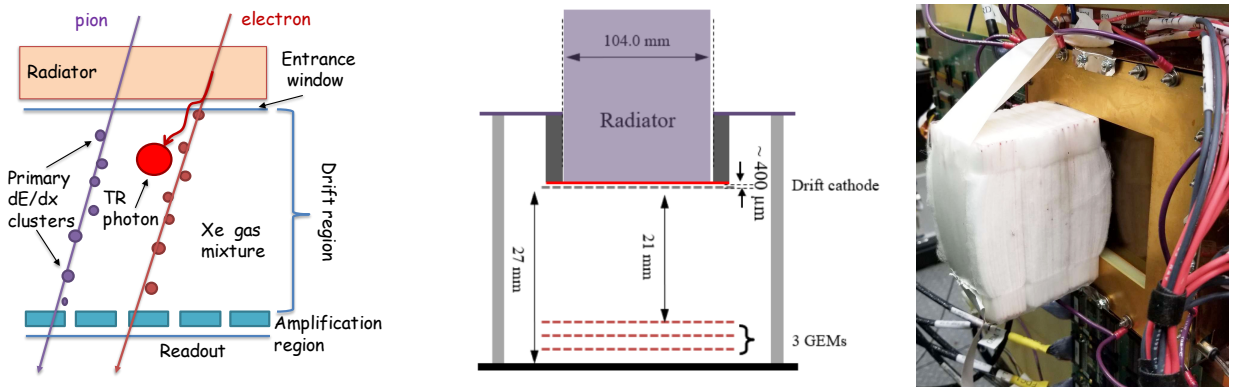

Figure 11.61: The concept of GEM-based TRD (left), the prototype scheme (middle), prototype in testbeam setup (right)

to the standard GEM tracker. First, since heavy gases are required for efficient absorption of X-rays, the operational gas mixture has been changed from an Argon based mixture to a Xenon based mixture. Secondly, the drift region also needed to be increased from ~3 mm to 20-30 mm in order to detect more energetic TR photons. Then to produce the TR photons, a TR radiator was installed in front of the GEM entrance window. Finally, the standard APV25 GEM readout electronics was replaced with faster electronics based on flash ADC (FADC) [55] and developed for JLab HallD GlueX Drift Chambers. A GEANT4 simulation and optimized the radiator and detector thicknesses for a single chamber (Fig. 11.61) has been performed. G4XTRGammaRadModel model was used for a fleece radiator, which could be simulated in GEANT4 as an irregular type of radiator with a certain density and two parameters (α_1, α_2), which define a spread of materials and air-gaps within a radiator. Due to the self-absorbing property of the radiator, soft photons (3-6 kEv) generated within first few centimeters of the TR-radiator will be absorbed, leading to an increase in the hard X-ray photon spectrum at the exit from a radiator. A thin layer of gas in Xe-based detector will not be effective at detecting hard X-ray photons. As one could see in Fig. 11.63 (left), rejection power is saturated after 22cm of radiator for our GEM detector with 21mm gas thickness, including 400μm of dead gas layer in front. Experimental data points (stars) shows a good agreement with MC projections. A TRD needs information about the ionization along the track, to discriminate TR photons from the ionization of the charged particle. The GEM-TRD/T prototype used a precise (125 MHz, 12 bit) FADC [55] coupled with fast shaper pre-amplifiers, developed at JLAB, with a VME-based readout. The FADCs have a pipeline readout window of up to 8 μs, which covers the entire drift time (500ns) of the GEM-TRD/T prototype and gives a room for HV scan. The pre-amplifiers used GAS-II ASIC chips to provide 2.6 mV/fC amplification with a peaking time of 10 ns. For the e/π rejection factor the amplitude and arrival time of each individual cluster along the drift time were analyzed. All this information (up to 20 variables) was used as input for likelihood and artificial neural network (ANN) programs, such as JETNET or ROOT-based (Multi-layer Perceptron). The ANN system was trained with MC or data samples of incident electron and pions. Then an independent sample was used to evaluate the performance. An example of such a training procedure is shown in Fig. 11.62. A 90% efficiency for our electron identification was required. The neural network output for e/π rejection is shown Fig 11.63. As one could see, with a 15cm radiator rejection factor ca. 9 could be achieved.

As for tracking aspects, a standard GEM plane can only provide the 2D X-Y position of a track, while the GEM-TRD/T with increased drift volume and with Flash ADC readout allows for 3D track segments to

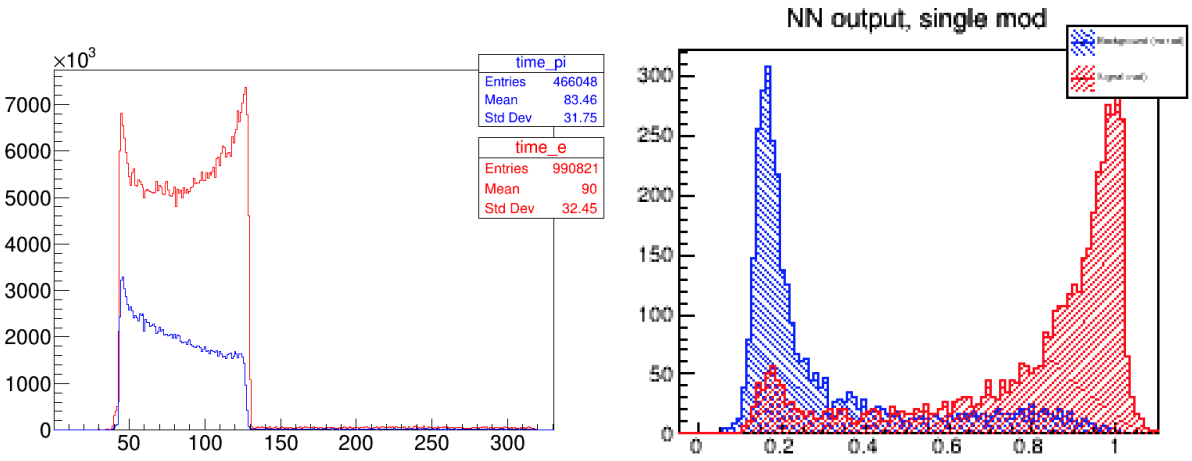

Figure 11.62: Left plot shows average energy deposition along the drift time (x-axis in fADC time-bins). Right plot is output from Neural Network, showing the separation between electrons and pions.

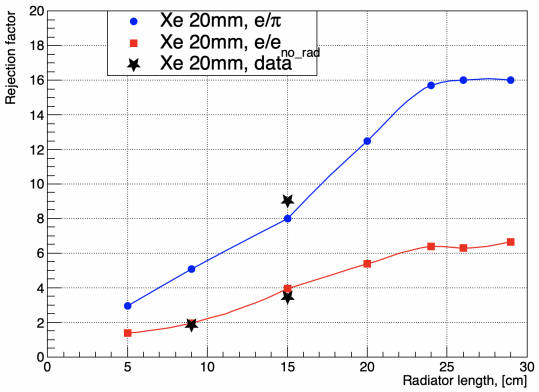

Figure 11.63: Rejection vs. TR-radiator thickness.

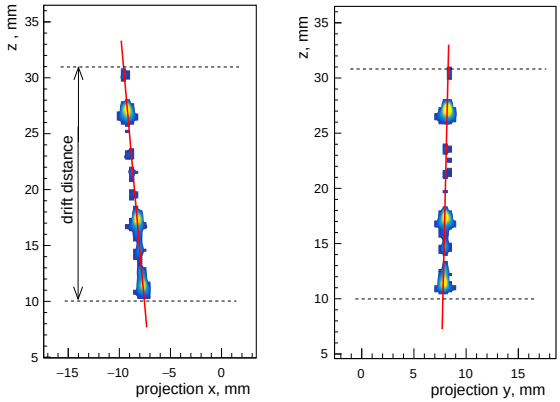

Figure 11.64: Single track reconstruction.

be reconstructed as in μTPC configuration. In the hadron end cap region, in addition to the e/π rejection capabilities, GEM-TRD track segment behind dRICH could be used to:

- measure a track angular resolution and therefore help to improve dRICH performance;
- correct for a multiple scattering before EMCAL and improve tracking performance for charged particles.
- improve pointing track resolution and cluster-seed position measurements for EMCAL
- could be used as a seed-element for a track finding algorithms.

Figure 11.64 shows projections of a typical 3D reconstructed track from the GEM-TRD/T prototype. The

left panel shows the track projection in XZ plane with Z the drift time as a function of the cluster position in the X direction. The right panel shows corresponding projection in YZ plane.

11.3.5 Photon Detection Technology Options

Many of the devices discussed previously involve the detection of visible and/or UV photons, frequently with an accompanying requirement of being able to discriminate between noise the signal resulting from a single photo-electron. Furthermore, the detection must maintain its quantum efficiency and much of its gain while immersed in the magnetic field of the spectrometer. Many traditional devices for single photo-electron detector fail the final criterion of operation when immersed in a magnetic field. Several suitable technologies exist or under development and have been studied in the context of EIC applicability.

The MCP PMT uses micro channel plate technology to replace the traditional dynode structure for achieving gain in a photomultiplier tube. These devices are intrinsically more tolerant to an external field, but are not entirely immune. Several options have been studied, one of which is summarized in Figure 11.65. Here the 10 μm Planacon device's performance is summarized in both quantum efficiency (dashed lines) and gain (solid lines) as a function of external magnetic field. At normal field incidence, and up to 1 Tesla, the device maintains sufficient gain (particularly at higher bias) and quantum efficiency to be suitable for use in a RICH detector. Further study is required to extend these studies to higher field since tracking considerations imagine central values of the field as high as 3 Tesla. At such a field it seems difficult to position photon detectors of the various Cerenkov detector devices (dRICH, mRICH, DIRC) in a manner such that they experience 1 Tesla or below. Conversely, it has been shown that for a 3 T central field, 1 T in the region of photon detection is plausible, but requires careful design. It should also be noted that the incident angle of the field to the PCM PMT is a critical parameter. By an incident angle of 20^o, the quantum efficiency of the device drops into the 20-40% range by roughly 1/2 Tesla. Typically a loss of 2X in photon statistics damages the performance of a Cerenkov device significantly and would require major changes in the device design.

Another developing photon detection technology is that of LAPPD. These devices also use micro channel plates as their basic of avalanche. These can be used both for Cerenkov readout (*e.g.* in an mRICH configuration to add timing) or directly as a TOF detector. As shown in Figure 11.66, these devices also suffer a significant loss in signal strength which is a combination of gain loss (somewhat tolerable) and quantum efficiency loss. The QE loss is a second order impact when the LAPPD is used as a TOF detector since the primary signal already consists of multiple photoelectrons. However, this loss is critical to the use of LAPPD as a Cerenkov detector readout.

Finally, we note the developments in recent years of silicon photo-multipliers or SiPMs. Initially, these devices (which operate on a Geiger avalanche mode in each pixel) were highly susceptible to radiation damage. Much work has been done to improve this performance intrinsically and it is now known as well that operation at cold temperatures and post-annealing processes have been effective means to maintain and restore operation. For this reason, SiPM technology seems a leading choice for readout of light signals from calorimeter devices at the EIC. That said, more work is required to demonstrate the efficacy and long term viability of SiPM technology for use in a Cerenkov detector. The basic distinction is signal size. A well designed and high performance calorimeter will deposit many photons into a single pixel, making the presence or absence of "several" photo-electrons a mere shift and widening of the pedestal. RICH detectors, on the other hand, must distinguish zero from one photo-electron and thereby are much more vulnerable to radiation damage of an SiPM. It is therefore a clear priority to continually develop and evaluate the

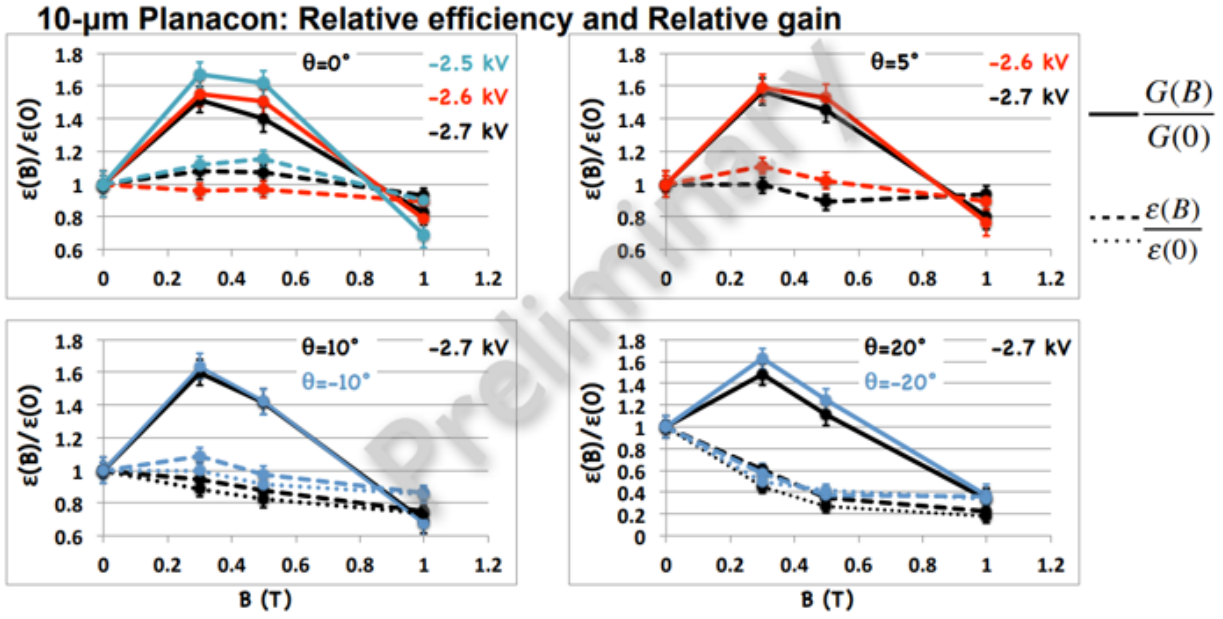

Figure 11.65: Magnetic Field Effects on MCP PMT Devices.

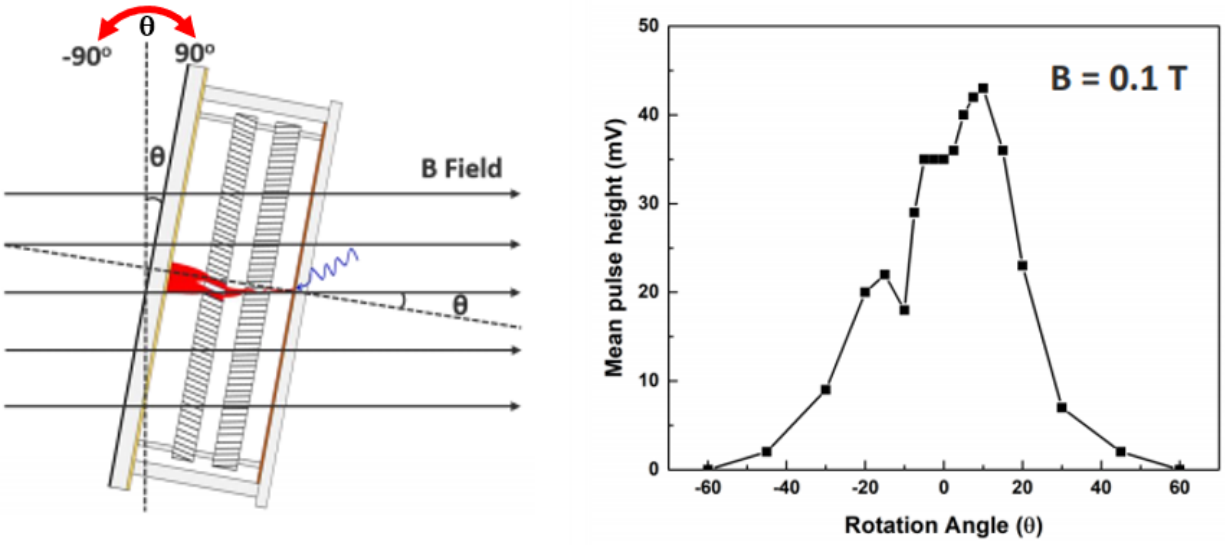

Figure 11.66: Magnetic Field Effects on LAPPD Devices.

performance of SiPM detectors for RICH applications in the coming years.

11.3.6 Configuration for EIC

Based upon the characteristics of known detector technologies as described above, it is possible to assert solutions for the detector performance matrix in each of the pseudo-rapidity regions. These possibilities are

outlines in the table below and discussed in more detail in the sections that follow.

Arm	eID-only Technologies	PID Technologies
Electron	HBD, TRD	mRICH, LAPPD, LGAD
Central	-	dE/dx, DIRC, LGAD
Hadron	TRD	dRICH, gRICH/LAPPD

Before we continue, it is necessary to establish simple criteria for what can be considered as acceptable performance and in particular the definition of dynamic range. The PID/eID task can be simplified to the identification of four particle species which in mass order are the electron, pion, kaon, and proton. For Cerenkov technologies, both the threshold and "imaged" mode of operation can be utilized as part of the ID process. Positive ID is defined as follows:

- Positive eID for a threshold device is valid up to the momentum at which the pion begins to radiate.
- Positive PID for an imaging device begins at the momentum where the kaon starts to radiate.

While careful analysis shifts these limits somewhat, they are nonetheless useful in comparison across detector technology comparisons. To this end, we list the Cerenkov thresholds for each radiator considered in any of our detector systems in Table 11.15.

These thresholds along with the detailed calculations shown in the prior sections can be summarized to form the following table of dynamic range summaries of each detector system discussed above:

11.3.6.1 Hadron Arm

The PID requirements in the hadron-going direction are naturally the most stringent in the spectrometer owing to the broad momentum range required for hadron identification. The various technologies considered have been accumulated into a table distinguishing their range in e-π separation and also in π-K separation. For Cerenkov devices, the lowest momentum for e-π is put at the Cerenkov threshold and the lowest momentum for π-K is placed at the kaon threshold. The results are summarized in Table 11.16.

Among the various options it becomes immediately clear that there is a clear need for gas-based Cerenkov to reach the high end momentum requirements of the EIC. Is also immediately clear that owing to the high

		Threshold (GeV/c)			
radiator	index	e	π	K	p
quartz (DIRC)	1.458	0.00048	0.13	0.47	0.88
aerogel (mRICH)	1.03	0.00207	0.57	2.00	3.80
aerogel (dRICH)	1.02	0.00245	0.69	2.46	4.67
C_2F_6 (dRICH)	1.0008	0.01277	3.49	12.34	23.45
CF_4 (gRICH)	1.00056	0.01527	4.17	14.75	28.03

Table 11.15: Table of Cerenkov thresholds for various media.

Hadron Arm Technology	Range (GeV/c)	
	e - π	π - K
CsI RICH	0.0150 - 20	14.75 - 50
dRICH (aerogel)	0.0025 - 5	2.46 - 16
dRICH (gas)	0.0127 - 18	12.34 - 60
dRICH (overall)	0.0025 - 18	2.46 - 60
TOF (LGAD)	0 - 1	0.00 - 5
TOF (LAPPD 4m 5psec)	0 - 2.5	0.00 - 16
TRD	1.0 – ∞	–

Table 11.16: Performance ranges for possible hadron arm detector technologies.

threshold imposed by a low-index radiator choice necessary to reach the high momentum range, there must be an additional technology. The dRICH presents an elegant solution to the issue by incorporating aerogel. The gRICH option must be augmented by the addition of technology like aerogel-base mRICH or by high resolution TOF in order to cover the full dynamic range.

11.3.6.2 Central Arm

The principle challenge of the central arm is the lack of space provided therein. As a result the DIRC technology and TOF technology become leading options in most designs. There exist, however, two significant issues with a DIRC-only solution. These are:

- The DIRC provides a threshold for kaon radiation at 0.47 GeV/c.
- There is a need for eID (e-π) that may not be fully met.

Central Arm Technology	Range (GeV/c)	
	e - π	π - K
$\frac{dE}{dx}$	0 - 2	0 - 3
$\frac{dE}{dx}$ (Cluster Count)	0 - 10 ??	0 - 15
DIRC	0.00048 - 1	0.47 - 6
TOF (LGAD)	0 - 1	0.00 - 5
HBD	0.0150 - 4.17	N/A

Table 11.17: Performance ranges for possible central barrel detector technologies.

It is therefore likely that a complementary technology in addition to the DIRC is required for the central barrel. The use of dE/dx follows naturally when one assumes that the tracking system would contain a hybrid of silicon and TPC. However, one much be cautious. Because of the so-called ”band crossings” in any dE/dx measurement, it is absolutely necessary to have a ”tag” of low velocity particles to eliminate these from any eID system (wherein the electron is well into the high beta plateau). TOF provided either by the DIRC system or by the inclusion of timing layers in the silicon tracker will be a must for such systems.

In a non-hybrid tracking system (internal silicon layers to 50 cm radius), one can imagine utilizing the additional space for a new PID device to complement the DIRC and TOF options. In this case, one can even imagine exceeding the TPC dE/dx performance by a significant factor utilizing cluster counting rather than merely energy loss measurements. Cluster counting devices require further R&D in the coming time to demonstrates that this capability can be reached. RICH systems modeled similar to the Delphi Barrel RICH can also be imagined, however the viability of SiPM devices as readouts for RICH detectors long term in the face of a high radiation environment must be demonstrated.

11.3.6.3 Electron Arm

In the direction of the electron arm, several possibilities exist. One of these possibilities is that despite the asymmetry of the collision itself, one could choose to place a device such as dRICH in the electron arm direction as well. This creates a challenge since the dRICH technology requires significant space. Nonetheless, dRICH in the electron arm would over-perform all the requirements of the electron ion collider and provide a singular solution for both endcaps.

More conventional thinking would attempt to fulfill the less stringent needs in the electron arm by instead using one or several layers of a more compact PID technology. The ideal requirement of 4 GeV/c eID capability is well matched to the HBD-style technology. In the sPHENIX application, a 50 cm radiation of gas with a 4.17 GeV/c pion threshold. A limitation of this technology is that its original design is optimized for separation of 2e from 1e and not for e-π. Calculations exist as shown above for a new avalanche stage that promises to produce a pion rejection of roughly 100X. An alternative, is to split the HBD volume into two halves and square a lesser pion rejection factor. Both these concepts are unproven at the time of the Yellow Report and would require further R&D to prove their validity.

Electron Arm	Range (GeV/c)	
Technology	e - π	π - K
dRICH (aerogel)	0.0025 - 5	2.46 - 16
dRICH (gas)	0.0127 - 18	12.34 - 60
dRICH (overall)	0.0025 - 18	2.46 - 60
HBD	0.0150 - 4.17	-
mRICH	0.0025 - 2	2.00 - 6
TOF (LAPPD 4m, 5psec)	0 - 3	0.00 - 16
TOF (LAPPD 3m, 10psec)	0 - 1.8	0.00 - 10
TRD	1.0 – ∞	–

Table 11.18: Performance ranges for possible electron arm detector technologies.

A more conventional approach is to use one or more compact PID technologies. The mRICH is reasonably well suited to the task for providing additional eID and also PID. An option is being considered for augmenting the readout of mRICH with LAPPD which adds high resolution TOF to the mix. Two improvements occur. First, the TOF tag does not need to exceed the Cerenkov threshold for aerogel (instead it need to exceed the threshold in the LAPPD window). This enhances the capability at the lowest momenta. Second, the TOF information will augment the performance so long as the mRICH would be placed with a long enough flight path (not a restriction for the ring-based mRICH mode of operation).

TRD is also a possibility in the electron arm. TRD, like HBD, can be thought of as a threshold technology in that only the electrons radiate while the pions do not. The threshold is at roughly 1 GeV which makes the TRD technology an excellent complement to the mRICH in providing the necessary eID in the electron arm.

11.4 Electromagnetic Calorimetry

11.4.1 Requirements and Overview

In EIC experiments the electromagnetic calorimeters (ECAL) are needed for their usual tasks:

- Detect the scattered electrons in order to separate them from pions and also improve the energy/momentum resolution at large $|\eta|$.
- Detect neutral particles - photons, and measure the energy and the coordinates of the impact.
- PID: separate secondary electrons and positrons from charged hadrons.
- Provide a spacial resolution of two photons sufficient to identify decays $\pi^0 \to \gamma\gamma$ at high energies.

The physics requirements for the EIC detector system including the calorimeters are specified in Chapter **??**. The kinematic range and the requirements for the electron detection in ECAL was discussed at length in presentations [59–63] (see Fig.11.67). The background to DIS electrons is shown in Fig.11.68.

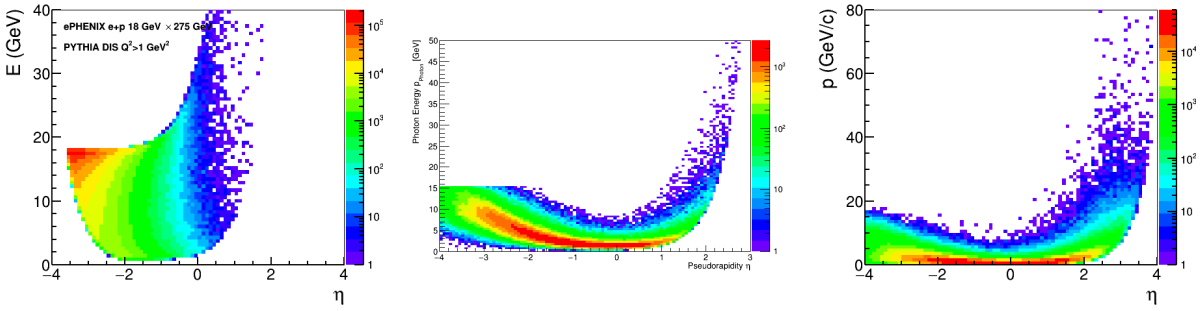

Figure 11.67: Calculated momentum spectra of particles in $e + p$ 18×275 GeV collisions [60]. Left: DIS e^- from PYTHIA [64]; Middle: DVCS γ from MILOU [65]; Right: π^0 from PYTHIA.

η	-4 to -2	-2 to -1	-1 to 1	1 to 4
$\sigma_E/E \cdot \sqrt{E/1\ \text{GeV}}$	2%	7%	10-12%	10-12%

Table 11.19: The initial requirements for the ECAL energy resolution [66, p. 25].

The initial requirements for ECAL are summarized in Table 11.19. The highest energy resolution is required at $\eta < -2$. Such a resolution can be achieved with heavy scintillating crystals. The best two-photon resolution is required at $\eta > 2$, which can be achieved with a fine granularity of a detector made of heavy materials, or by using a preshower detector with a fine granularity. The physics goals favor a reasonably hermetic detector, covering a range of about $-4 < \eta < 4$.

A practical limitation on possible choices of technologies comes from the space allocated for the EIC calorimeters. The tightness of the space in the endcaps is driven by the luminosity requirements. The

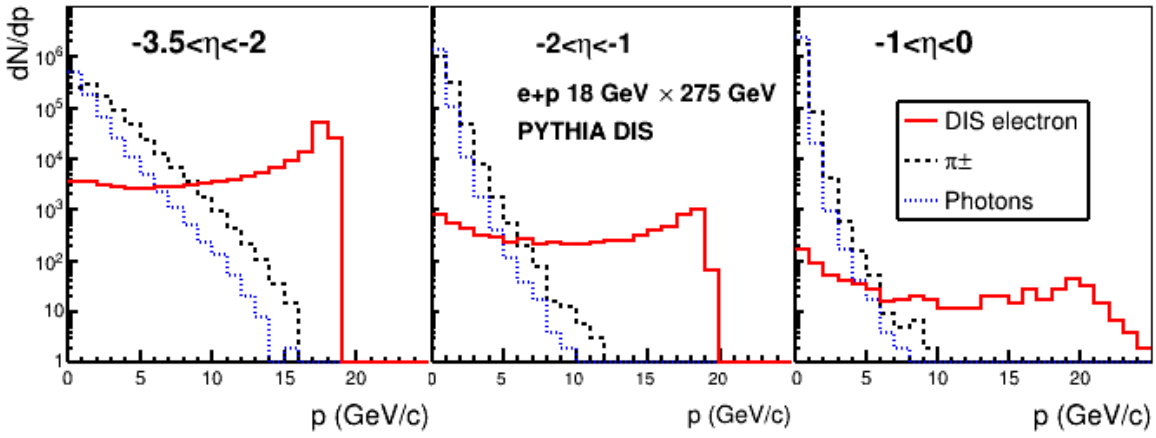

Figure 11.68: Calculated momentum spectra of DIS electrons, photons and pions in $e + p$ 18×275 GeV collisions [60].

barrel calorimeter depends on the magnet design. For the BaBar magnet the outer diameter of ECAL can go up to 140 cm, while the minimal radial thickness of ECAL is about 30 cm (based on the sPHENIX experience). The space in the magnet barrel is valuable for the momentum measurements, the PID etc. The tentative layout allocates:

- $\Delta Z < 50$ cm in the electron endcap;
- $\Delta R < 30$ cm in the barrel;
- $\Delta Z < 40$ cm in the hadron endcap;

Such a short space would favor calorimeter materials with a short radiation length (X_0).

The radiation environment at EIC is considered to be moderate at $|\eta| < 3$.

Only light-collecting calorimeters for the EIC have been considered in this report [1]. ECAL will be located in a strong magnetic field - in the bore of the solenoid, or in the stray field of > 0.1 T. Therefore, regular PMTs can not be used. Silicon photomultipliers (SiPM) are considered the most promising photosensor for ECAL. Compared to PMTs, SiPMs take much less longitudinal space, mostly for the readout electronics, which is an advantage at EIC. Based on the current experience the SiPM readout and the services (cables, cooling pipes etc) may take about 15 cm of the longitudinal space.

11.4.2 ECAL: Requirements, Options and Features

The important parameters of calorimeters are:

[1] An alternative approach to the EIC spectrometer - *TOPSiDE* [67] would require a separate consideration

- **Energy resolution**. The commonly used approximation for a particle of energy E is:

$$\sigma/E = \alpha \oplus \beta/\sqrt{E} \oplus \gamma/E. \tag{11.4}$$

The term γ depends on the noise level and is typically small for photosensors with high gains. The constant term α depends on a number of factors, including the calorimeter thickness (on the leakage of showers outside of the calorimeter active area), and also on the quality of the detector calibration. For ECALs with hundreds of channels or more, typically $\alpha > 1\%$ [68, 69]. The stochastic term β depends on the technology used (the sampling ratio, the size of the signal observed etc.).

- **Position resolution** of the particle impact. An approximation is used:

$$\sigma_X = \delta \oplus \epsilon/\sqrt{E} \oplus \Delta \cdot \sin\theta_I. \tag{11.5}$$

The resolution depends on the granularity (for ECAL limited by the Molière radius) and the energy resolution. The coefficients δ and ϵ are approximately proportional to the cell size. The third term describes the dependence on the angle θ_I between the incoming particle direction and the longitudinal axis of the calorimeter cell. The coefficient Δ is $d \approx X_0$, where X_0 is the average radiation length of the calorimeter material [70, p. 527].

- **Lowest detectable energy** depends on the signal size versus the noise and low-energy background.
- **Electron/pion separation** Mostly depends on the energy resolution and the longitudinal segmentation (if any).
- **Two-photon separation**. Two photon not hitting adjacent cells can be separated at the clustering level. An analysis of the shower profile allows to separate photons hitting adjacent cells, provided the hits are at least one cell-size apart.
- **Detector longitudinal size**. A denser material allows to make the detector shorter for the given thickness in radiation lengths. The resolution may depend on the thickness.
- **Signal timing**. A long signal may affect the signal/noise ratio and the pattern recognition.

The energy resolution of any calorimeter depends on:

- Uniformity of the measured response across the volume of the detector. The effect may be important both in high-resolution homogeneous calorimeters, in particular of a trapezoidal shape [71, 72], and in medium-resolution sampling calorimeters [73, 74].
- Shower containment. In a shorter calorimeter the fluctuations of the shower leakage lead to a higher constant term α and a worse resolution at high energies. The dependence of the energy resolution of the calorimeter on its depth in radiation length was calculated in Ref. [75]. For the expected energy range of $E < 20$ GeV the impact of the downstream leakage would not significantly change the resolution, for a thickness:

β	2.5%	7%	12%
thickness in X_0	>22	>20	> 18

The dependence of the constant term of a sampling calorimeter with a $0.25X_0$ layer thickness on the overall thickness $x = X/X_0$ has been calculated [76, p. 12] in a range of 18-24. The result is well fit using a polynomial $\alpha \approx 12.1 - 0.826x + 0.0144x^2$ and can be extrapolated to a wider range as 14-28.

- Signal size. More photoelectrons/GeV lead to smaller relative fluctuations and a lower impact of noise. A typical yield of a classic lead glass calorimeter is about 1000 p.e./GeV providing fluctuations of RMS=3% at 1 GeV, to be compared with the factor β. For high resolution calorimeters of $\beta < 3\%$ the yield should be higher.
- The readout threshold may be important since a shower splits between several cells. It is selected depending on the noise and background.

Numerous ECAL technologies have been developed for the field and the development is still ongoing. A number of technologies have been studied and developed in the framework of the EIC R&D, project eRD1 [76]. The results have been used in this report. The technologies considered are discussed in more details in in Section 11.4.3.

11.4.2.1 Homogeneous Calorimeters

Typically, the best energy resolution is obtained with homogeneous detectors not affected by the sampling fluctuations. Heavy scintillating materials produce large signals per MeV absorbed, leading to a good resolution. The best results have been achieved so far with scintillating crystals. Detectors using the Cherenkov light in heavy glass provide a medium resolution.

- **$PbWO_4$**. A combination of the requirements for the resolution, compactness, radiation hardness, the signal length, as well as the cost and availability considerations led to one candidate among the scintillating crystals: lead tungstate $PbWO_4$ (see Sec. 11.4.3.1) - a mature technology used in many experiments (Tab. 11.23). It typically provides $\beta \approx 2.5\%$.
- **Scintillating glass**. A search for a new, cheaper material - scintillating glass (see Sec. 11.4.3.2) - is being pursued in the framework of eRD1 [76]. Such a material may provide a resolution comparable with the lead tungstate. The material is less dense than lead tungstate and would require more space for the same thickness in X_0. A potential advantage with respect to lead tungstate would be a lower cost and higher availability.
- **Lead glass**. This technology uses the Cherenkov light produced in glass containing lead oxide (see Sec. 11.4.3.3) and provides a medium resolution of $\beta \approx 6\%$. Lead glass is less dense than lead tungstate and would require more space. It has been widely used in experiments since the 1960-s, and some of those detectors may become available for re-use at EIC.

11.4.2.2 Sampling Calorimeters

The resolution of sampling detectors may vary $\beta \sim 5 - 15\%$ depending on the sampling fraction and the granularity of the active and passive material:

- Sampling fraction f_{samp} is the fraction of the total energy released in the active material, evaluated typically for MIPs. For a better resolution one needs a larger sampling fraction, which typically increases the detector length for the same thickness in X_0.

- Sampling frequency is related to the thickness of one "layer" of the absorber and the active material (scintillator). This parameter is well defined for the "sandwich"-type geometry.

It has been argued [77, p. 119] that the stochastic coefficient is approximately proportional to $\sqrt{d[mm]/f_{samp}}$, where d is the thickness of the active material layer (or the fiber's diameter). This subject is discussed in Section 11.4.3.5 (*shashlyk* subsection), Figure 11.74 and Equation 11.6.

The requirements for the resolution and radiation hardness favor the absorber-scintillator combination. The popular technologies are:

- **Absorber/Scintillating Fibers: Pb/ScFi or W/ScFi**. The fibers are embedded into a heavy material as lead or tungsten (see Sec. 11.4.3.4). In one implementation the fibers are glued between lead sheets. Such *SPACAL-type* detectors have been used in a number of experiments [78–80]. In another implementation tungsten powder is used for the absorber. This technology [73] has been developed for the sPHENIX experiment. The resolution depends of the fiber density and the absorber material and may vary in a range of $\beta = 6 - 15\%$. A better resolution is provided by a less dense detector.
- **Shashlyk** - a stack of absorber and scintillator plates (see Sec. 11.4.3.5). The light is collected with the help of WLS fibers passing through the plates. For the absorber lead or tungsten are used. The technology is widely used and allows detectors of various resolutions and sizes (see Tab. 11.24). The resolution depends on the thickness of the plates and may vary between $\beta = 5 - 15\%$. Tungsten for the absorber material provides a high density and a short length of the calorimeter.

11.4.2.3 ECAL technologies considered for EIC

Technologies which may fit the EIC requirements are listed in Table 11.20.

Comments to Table 11.20:

1. Such a W/ScFi detector is being built for sPHENIX [73]. The properties have been measured in test beams.
2. $PbWO_4$ crystals have been used in a number of experiments (Tab. 11.23) and typically provide such properties.
3. Such a $20X_0$ calorimeter would fit into 40 cm space. The W/Sc sampling is similar to the Pb/Sc sampling of #5. The resolution coefficients α and β have been evaluated using Eq. 11.6. In order to account for calibration uncertainties 1% was added to the constant term: $\alpha \to \alpha \oplus 0.01$.
4. Such a W/ScFi prototype has been built and the properties measured in a test beam [82]. It used a long light guide and a PMT. The sampling can be adjusted to fit into a shorter space, as 40 cm.
5. Such a Pb/Sc *shashlyk* calorimeter (but $23X_0$) is used in the COMPASS experiment [83]. The constant term α is scaled to a shorter calorimeter of $20X_0$. See also Table 11.23.
6. TF1 glass has been used in many experiments (see Ref. [70, 83] for example). Cherenkov light is detected. For details see Section 11.4.3.3.

#	Type	samp-ling, mm	f_{samp}	X_0 mm	R_M mm	λ_I mm	cell mm^2	$\frac{X}{X_0}$	ΔZ cm	σ_E/E, % α	β
1	W/ScFi**	⌀0.47 ScFi W powd.	2%	7.0	19	200	25^2	20	30	2.5	13
2	$PbWO_4$***	-	-	8.9	19.6	203	20^2	22.5	35	1.0	2.5
3	Shashlyk***	0.75 W/Cu[a] 1.5 Sc	16%	12.4	26	250	25^2	20	40	1.6	6.3
4	W/ScFi** with PMT	0.59^2 ScFi W powd.	12%	13	28	280	25^2	20	43	1.7	7.1
5	Shashlyk***	0.8 Pb 1.55 Sc	20%	16.4	35	520	40^2	20	48	1.5	6
6	TF1 Pb glass***	-	-	28	37	380	40^2	20	71	1.0	5-6
7	Sc. glass*[b]	-	-	26	35	400	40^2	20	67	1.0	3-4

*** Mature technology, well understood. used in several experiments

** New technology, proven in test beams , in production for experiments

* Technology under development, not fully proven in test beams

a Material 80% W + 20% Cu by volume, X_0=4.1 mm

b The parameters of scintillating glass are tentative, see Section 11.4.3.2.

Table 11.20: The technologies promising for ECAL, ordered by the radiation length of the material. The Molière radius R_M is defined as $R_M = X_0 \cdot 21$ MeV$/E_{crit}$ and calculated for mixtures according to Ref. [81] (Eq. 34.37–34.38). X/X_0 is the thickness of the active area measured in radiation lengths, selected to provide the resolution presented in the table. A shorter active area would increase the constant term α. ΔZ denotes the full length of the module calculated as $X + 15$ cm, where 15 cm is reserved for everything but the active area and includes the photosensors, the readout electronics, the cables and services, and the support structure. The resolution is parametrized using Equation 11.4. The "noise" factor γ depends on the type of the photosensor, for SiPM $\gamma \approx 0.01$ GeV is expected.

7. Several types of Scintillating glass are being tested [76]. For details see Section 11.4.3.2.

The technologies listed can provide the energy resolution close to the initial requirements (Table 11.19). The $PbWO_4$ crystals nearly fit the requirements for the $-4 < \eta < -2$ area. The costs and manufacturing constraints will likely prevent its use in larger areas. The $1 < \eta < 4$ area requires a medium resolution, and a high granularity, which implies a dense material. The choice of the technologies for the $-2 < \eta < 4$ areas will depend on the geometrical constraints of the spectrometer and the space allocated.

All the described technologies are considered radiation hard for the radiation levels expected at the EIC.

11.4.2.4 Impact of the material in front of ECAL

A certain amount of material will be distributed along the path of particles from the interaction point to the face of ECAL. The electrons radiate and the photons convert to pairs. Because of the magnetic field the radiated photons may hit the calorimeter at a distance from the impact of the electron. Simulated signals are shown in Figure 11.69. The detected energy distribution has a tail to lower energies. A typical identification criteria for electrons $E/p > 1 - 2\sigma_E$ may lead to losses of 5-30%, in particular at low momenta (Fig. 11.69).

The losses can be partly recovered, since the material is expected to be concentrated at certain places, allowing to predict the impact position of radiated photons for a given particle trajectory. Still losses of 10-20% are expected for certain areas at $p < 10$ GeV.

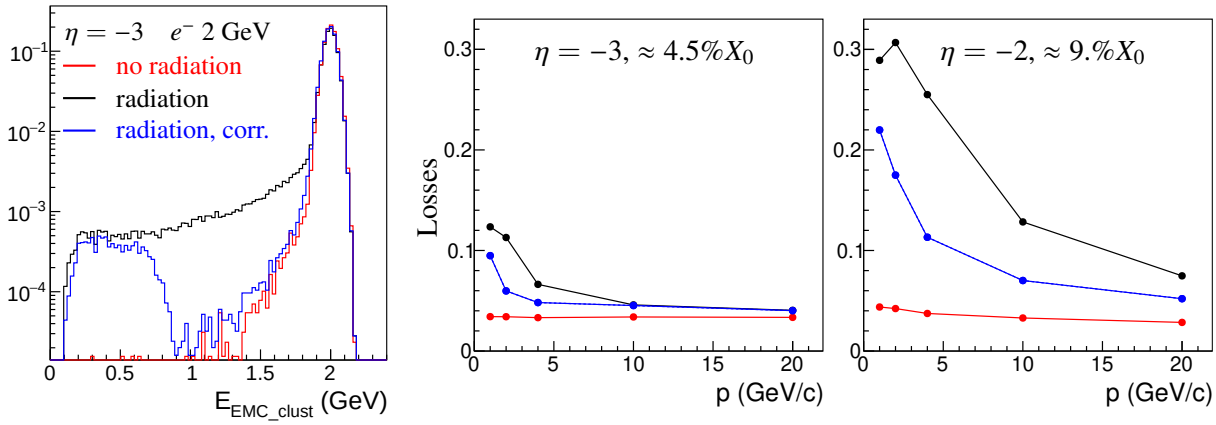

Figure 11.69: Simulated impact of material in front of ECAL on detection of 2 GeV electrons [63]. The amount of material depends on η. Three cases are considered: a) electron does not radiate in the material; b) electron radiates and only the cluster associated with electron track is considered; c) attempt made to recover the photons radiated in the thick objects upstream, whose positions can be predicted. Practically all the energy has been recovered up to a loss of a half of the initial energy, which was an arbitrary cutoff. The real cutoff will depend on the background, the tracking quality etc.
Left: The energy spectrum of the cluster in ECAL from GEANT4 [84] simulation.
Middle and **Right**: the losses of electrons, selected using $E/p > 1 - 2\sigma_E$.

11.4.2.5 Impact of the Cell Size and the Projective Geometry

In order to have the best coordinate resolution while minimizing the number of the readout channels the cell transverse size is usually selected close to the Molière radius of the calorimeter material. The coordinate resolution depends on the position of the hit and is the best at the boundary between two cell. The average resolution depends on the particle energy and the incident angle (see Equation 11.5). Based on experience (see Table 11.21) we may expect a resolution for the normal incident angle θ_I of about $(1 \oplus 3/\sqrt{E/1\text{GeV}})$ mm for the cell size 20-25 mm, and $(1 \oplus 6/\sqrt{E/1\text{GeV}})$ mm for the cell size of about 40 mm. Let us consider a dense detector with $X_0 \approx 10$ mm and the cell size of 25 mm. In the non-projective geometry, at $\theta_I = 45°$, the additional term $X_0 \sin\theta_I \approx 7$ mm will dominate the coordinate resolution. The relative deterioration of the resolution does not depend strongly on the density of the material.

Another important characteristics of ECAL is the ability to discriminate a single photon from a merged photon pair from a high momentum π^0 meson decay. For high momentum π^0 the minimal angle between two photons in the Lab frame is $\approx 2m_{\pi^0}/p_{\pi^0}$ and most of the decays produce two photons at angles close to the minimal angle. At high enough momentum two photons appear in the ECAL in a close proximity to each other, so that the ECAL response to a pair of decay photons becomes indistinguishable from the response to a single photon with the energy equal to a sum of decay photon energies. ECAL granularity defines the highest momentum at which ECAL can discriminate single photon from merged photons from π^0 meson decay. Usually, two photons are easily distinguishable in the ECAL when they are separated at least by a distance equal to twice of cell size. In this case two photons produce two clusters in ECAL, or a single

Type	R_M, mm	cell size, mm	σ_E/E at 1 GeV	δ mm	ϵ, mm GeV$^{0.5}$	Ref
$PbWO_4$	20	20	2.9%	0.4	2.6	[85]
$PbWO_4$	20	22	3.9%	0.3	2.6	[86]
TF1	37	38	5.7%	0.5	6.0	[87]
Shashlyk	41	55	8.4%	1.6	5.7	[70]
Shashlyk	59	110	4.7%	3.3	15.4	[88]

Table 11.21: The coordinate resolutions observed with several detectors for the normal incident angle θ_I. The resolution is parametrized using Equation 11.5. The stochastic factor ϵ appears to be approximately proportional to the cell size.

cluster with two distinct local maxima. With smaller distance between two photons, they produce a single cluster with one local maximum. Even in this case, different mathematical techniques to analyze the energy distribution among the cluster cells still can discriminate a single photon cluster from a merged photon cluster, down to a distance between two photons equal to the cell size, or even down to a half of the cell size, though with limited efficiency. Figure 11.70 illustrates such a capability for the hadron endcap ECAL with the cell transverse size of 2.5 cm, located at 3 m from the collision point. The performance deteriorates for a non-orthogonal impact (here at lower η), due to a wider shower profile and its larger fluctuations in the ECAL transverse plane. For a transverse size d and the distance to the collision point Z_{ECAL}, the momentum reach for π^0/γ discrimination scales roughly as Z_{ECAL}/d.

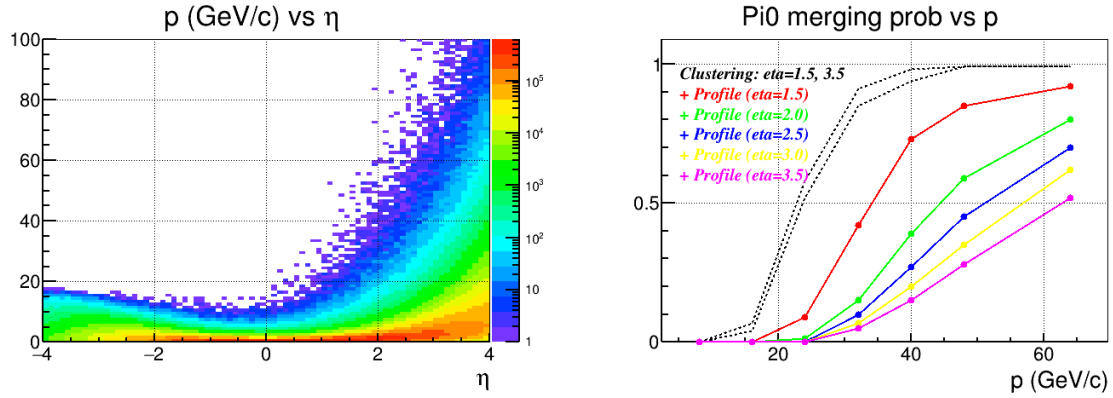

Figure 11.70: Left: The calculated π^0 momentum spectrum for SiDIS at $e+p$ 18×275 GeV collisions, using PYTHIA [64]. **Right**: The probability of two photons to merge, calculated [89] using GEANT4 [84] for the cell size of 25×25 mm^2 located at 3 m from the interaction point, for the non-projective geometry. For the projective geometry the results for $\eta > 3.5$ would be close to the non-projective curve at for η=3.5.

The requirements to the hadron endcap strongly favor a calorimeter material with a short radiation length and a small Molière radius, allowing a fine segmentation of ≤ 25 mm.

Using the projective geometry for ECAL in the barrel is standard for solenoid-based spectrometers. For the endcaps it is geometrically more complex. The projective geometry would provide a significantly better coordinate resolution at large radii.

11.4.2.6 Electron/pion separation

The DIS momentum spectra of the DIS electrons and pions are shown in Fig. 11.68. At lower momenta the pion flux dominates the flux of scattered electrons by orders of magnitudes. ECAL is expected to be the main tool for the electron identification. Pions produce smaller signals in ECAL than electrons of the same momentum (Fig. 11.71, left). Using the measured momentum of the charged track p and the energy deposited by this track in ECAL one can select electrons requiring $E/p > 1-\Delta$. The fluctuations of the E/p value are characterized by $\sigma(E/p) = E/p(\sigma_E/E \oplus \sigma_p/p)$, where σ_p/p are expected to be significant at $|\eta| > 2$. In this review we use typically $\Delta = 1.6\sigma_E/E$, using only the Gaussian width of the calorimeter signal. For the Gaussian calorimeter response the efficiency to electrons would be 95%. However, the response typically has a tail to lower energies, increased by material in front (Fig. 11.69), which reduces the efficiency for electrons. Larger σ_E and σ_p lead to a lower efficiency for electrons and a smaller rejection factor for pions for a given Δ.

In general, one expects a better electron-PID performance for a better energy resolution of the calorimeter and the momentum resolution of the spectrometer. Analysis of the shower profile can provide an additional pion suppression. However, the effect depends on the impact angles, and therefore, on the geometry of the calorimeter (projective or not).

The pion suppression performance of calorimeters has been measured in test beams and also evaluated using simulation. One should note that it is challenging to measure or calculate large rejection factors $R_\pi > 1000$ because of beam contamination, or uncertainties in simulation of hadronic processes. The pion rejection factor may be limited by charge exchange processes as $\pi^- + p \to \pi^0 + n$ that would produce signals similar to electrons at the same energy (noted in Ref. [90] for example). The cross section for such processes typically falls with energy.

Several examples of the measured pion suppression in various calorimeters are shown in Table 11.22. For the sampling calorimeters the largest reported rejection factor of R_π=2000, at the measured $\varepsilon_e = 90\%$, was obtained at 100 GeV, where the energy resolution was about 2%. A rejection of $R_\pi = 500$ was measured for a $PbWO_4$ calorimeter at 2.5 GeV, where the energy resolution was 2%. In this test a cut $\Delta > 2 \cdot \sigma_E$ was applied (98% "Gaussian" efficiency), which may translate to a $\varepsilon_e \approx 90\%$ of the real efficiency.

Figure 11.71 shows the calculated suppression dependence on energy, the calorimeter resolution and the track momentum resolution. The simulated pion-produced signals in $PbWO_4$ and in sampling detectors are compared - the former have a shorter tail to high values. A stronger response to neutrons by the plastic scintillator than by an inorganic one may contribute to the effect. While the results of calculations for sampling calorimeters are consistent with the measurements, the calculated R_π for $PbWO_4$ is more than an order of magnitude higher than a measurement at 2.5 GeV. It may be caused by systematic uncertainties of both the measurement and simulation. At this time we can not claim that a rejection power higher than 1000 is achievable at moderate energies even with the relatively high-resolution $PbWO_4$ detector.

Figure 11.71 (right) demonstrates how the momentum resolution affects the performance at small angles $|\eta| > 3$.

Calculations also show that taking the shower shape into account can improve the pion rejection by a factor of 2 even in non-projective geometry, or by a factor of 3-4 at small incident angles and in projective geometry.

In summary, in the energy range 4-20 GeV sampling calorimeters and lead glass calorimeters can provide

Type	Experiment	σ_E/E, %			E,	ε_e		par-	R_π	Ref
		α	β	γ	GeV	meas.	calc.	ticle		
$PbWO_4$	-	0.1	3.1		1.0-2.5		98%	π^-	500	[91]
$PbWO_4$	-	0.5	4.0		80.	90%		π^-	6000	[92]
TF1	PHENIX	0.8	6.0		1.5-4.0	80%	98%	π^-	250	[70]
						90%			160	
						95%			100	
					1.0	80%	98%		80	
					0.75	80%	98%		45	
					0.50	80%	98%		7	
TF1	Hall C	1.0	6.0		3.2	95%		π^-	*200	[93]
Pb/Sc	PHENIX	2.1	8.1		40	77%	84%	π^+	430	[94]
						88%	95%		350	
						92%	98%		300	
						95%	100%		200	
					4		95%		100	unpub
					3		95%		80	unpub
					2		95%		43	unpub
					1		95%		12	unpub
					0.5		95%		3.4	unpub
Pb/Sc	ALICE	1.7	11.1	5.0	100	90%		π^-	2000	[90]
					100	95%			1100	
					40	90%			700	
					40	95%			400	
W/ScFi	sPHENIX	2.8	15.5		8		50%	π^-	710	[95]
							84%		330	
							95%		210	
							98%		160	
							99.9%		90	

* The longitudinal segmentation not used

Table 11.22: The measured pion suppression factor R_π and the associated efficiency ε_e to electrons. The shower shape has not been taken into account, except for Ref. [92] ($PbWO_4$). In several studies the ε_e was measured and from the data reported it was possible to calculate the "Gaussian" efficiency, that is considerably higher than the measured one, as expected. For other studies only the calculated "Gaussian" efficiency is available. The measurements marked "unpub" come from the authors of the paper, but have not been included into the paper.

a pion rejection factor from a hundred to a thousand. $PbWO_4$ crystals may be able to provide factors 3-5 higher, but factors > 1000 need to be confirmed by measurements.

Figure 11.72 shows the calculated purity of electrons in the DIS sample, in 3 areas of η, each equipped with ECAL of a different resolution, close to the specifications in Table 11.19. The levels of the pion background are also different in these areas (Fig. 11.68). In all areas a >95% purity is reached at $p > 4$ GeV. The $-3.5 < \eta < 2$ area is supposed to be covered with a high-resolution ECAL ($\beta = 2.5\%$), and the purity >90%

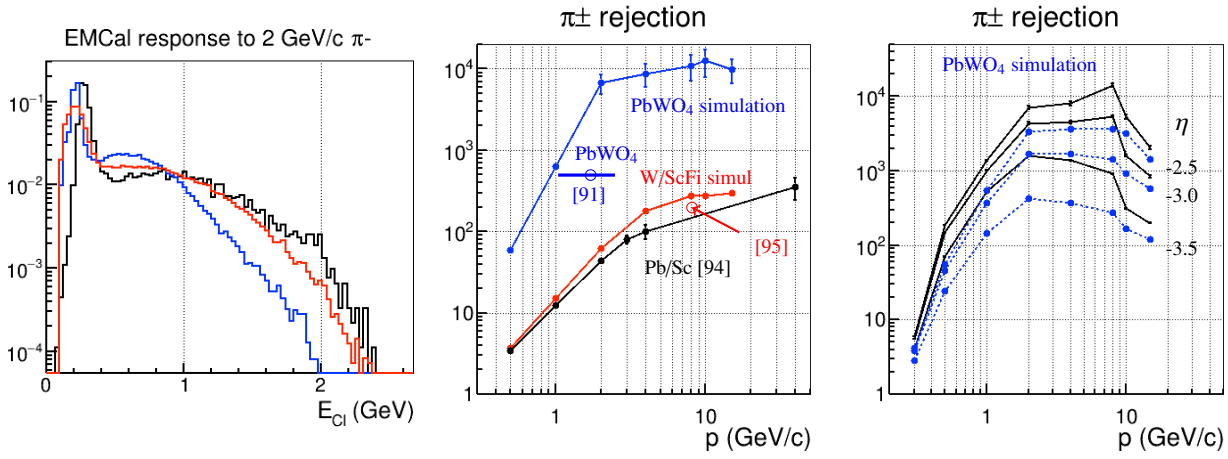

Figure 11.71: Measured and simulated (GEANT4 [84]) pion suppression [61, 62], evaluated with a $\Delta = 1.6 \cdot \sigma_E$ cut ("Gaussian" $\varepsilon_e = 95\%$).
Left: the response to 2 GeV pions for: black - measured for Pb/Sc $8\%/\sqrt{E} \oplus 2\%$ (PHENIX); red - simulated for W/ScFi $13\%/\sqrt{E} \oplus 3\%$; blue - simulated for $PbWO_4$ $2.5\%/\sqrt{E} \oplus 1\%$.
Middle: pion suppression, momentum resolution neglected; E/p cut only;
black - measured for Pb/Sc $8.1\%/\sqrt{E} \oplus 2.1\%$ (PHENIX [94], see also Table 11.22);
red - simulation for W/ScFi $12\%/\sqrt{E} \oplus 3\%$, calculation compared with a measurement at 8 GeV (Ref. [95] and Tab. 11.22);
blue - simulation for $PbWO_4$ $2.5\%/\sqrt{E} \oplus 1\%$. The calculation, exceeds a measurement at 1-2.5 GeV (Table. 11.22) by a factor of <10.
Right: simulated pion suppression for $PbWO_4$ $2.5\%/\sqrt{E} \oplus 1\%$, at $\eta = -3.5, -3.0, -2.5$, the momentum resolution taken into account. The dependence on η is caused by the momentum resolution.
blue - E/p cut, $\varepsilon_e = 95\%$;
black -E/p and shape cuts, $\varepsilon_e = 92\%$.

is reached at $E > 2$ GeV. The other areas are supposed to be covered with $\beta = 7\%$ and $\beta = 12\%$-resolution calorimeters and at $p < 4$ GeV the pion contamination remains high.

Pion rejection can be improved by using a "preshower" detector. Also, the calorimeter itself may be equipped with a second readout from the front part of the modules, which does not require an extra space for another detector. A factor of 2 improvement in e/π separation was achieved equipping a *shashlyk* detector with scintillator plates with different emission times [96].

Since X_0/λ_I is smaller for heavier materials, they should provide a better pion suppression. One should note that the material passed by the electron track in front of the calorimeter will reduce the energy reaching the calorimeter, affecting the E/p ratio and the e/π PID. For the same pion rejection factor the efficiency to electrons will be reduced. A lower efficiency typically causes a higher uncertainty of the measurement.

11.4.2.7 Lowest detectable energy

The lowest detectable energy depends on the amount of light detected versus noise of various origin and low-energy background. With $PbWO_4$ as low as 20 MeV photons can be detected, provided low-noise sensors and electronics, although with a 30-50% energy resolution. For sampling detectors one may expect

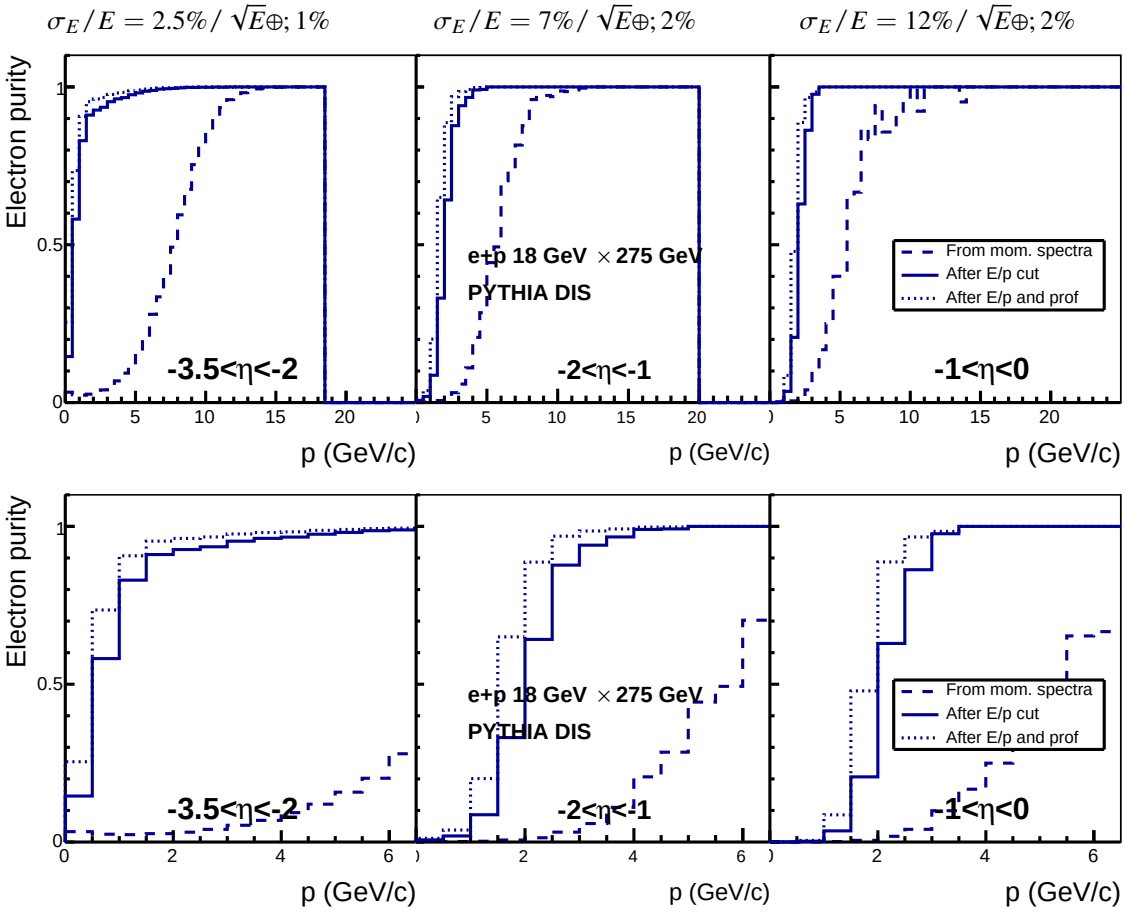

Figure 11.72: Calculated purity of the DIS electron sample and the effect of the pion suppression [62] for e+p 18×275 GeV. The pion suppression was evaluated using a $\Delta = 1.6 \cdot \sigma_E$ cut ("Gaussian" $\varepsilon_e = 95\%$). The columns present three areas of η with the assigned σ_E/E for each area. The bottom panel presents the zoomed in plots of the top panel. Dashed lines - no cuts, solid lines - E/p cut, dotted lines - E/p and shower shape cuts. A cap of 1000 on the calculated pion rejection was set in order to address the existing uncertainties.

the lowest detectable energy of 50-100 MeV.

11.4.2.8 Readout Considerations

Only detectors with optical readout have been considered. In the current scenarios the endcap ECAL photosensors will be located in a magnetic field of >0.1 T, which precludes the usage of regular PMTs. The barrel ECAL is located in a >1 T field. At the moment the sensor of choice is SiPM, which provides a high gain (about 10^6) and a medium photodetection efficiency of about 20%. The drawbacks are small surface, noise, susceptibility to radiation, in particular to neutron/proton radiation [97,98], sensitivity to temperature, a small dynamic range, and the intrinsic nonlinearity [99]. Radiation leads to a higher noise. Additionally, the performance degrades with the current flown [100]. For the same amount of light a SiPM can fire a number of pixels comparable to a PMT photoelectron count [101]. However, a fraction of the pixels fire due to the cross talk, not improving the statistical fluctuations. While a SiPM readout is natural for the fiber

technologies as *Shashlyk*, it does not look optimal for a large-surface - 16 cm^2 - glass blocks. Such a readout has not been tested yet with 4 cm^2 crystals.

The effect of non-linearity for SiPMs depends on the desired dynamic range and the calorimeter resolution. Let us consider the requirements of a 2% energy resolution at 1 GeV and the maximum energy of 20 GeV (at the center of the electron endcap), and find the total number of pixels needed for one calorimeter cell. With the optimal cell size about 80% of a shower energy on average goes to one cell, but with considerable fluctuations. The p.e. (or pixel) count at 1 GeV should be $\gtrsim$10k (1% statistical fluctuations). Then, at 20 GeV the pixel count with no saturation would be about 200k. The saturation effects for MPPC S12572-010P 90k-pixel, 3×3 mm^2 device have been shown to be as large [99] as would be expected for a 30k-pixel device. The correction to nonlinearity has to be calibrated rather than calculated, and may contain large uncertainties. This may require to limit the number of fired pixels to <20% of the total. Therefore, per one crystal one would need a device(s) with about 1M pixels in total. The technology of SiPM is still developing and the linearity might be improved in the future. Another factors to consider is the density of light coming from the crystal's face per GeV compared with the PDE and the density of pixels.

A *shashlyk* module made for MPD [102] has been tested with a Hamamatsu MPPC S13360-6025 which contains 57k pixels 25×25 μm^2. With the yield of about 5000 pxs/GeV the loss to non-linearity at 2 GeV was about 10%.

It is expected that for the electronics readout special ASIC chips will be developed (see Section **??**), which will provide the bias voltage to the SiPM, read out the signals using fADC, and process the signals producing the timing and the integral and/or maximum amplitude. Since both the detectors considered and the SiPM sensors are fast, one may expect a timing resolution of <1 ns. At least 12-bit fADCs are needed. It will be also important to be able to send out not only the processed, but also the raw signals as waveforms. Without an ASIC chip the power consumption of the on-detector electronics will be considerably higher and its functions may be limited.

ECAL must be equipped with a monitoring system, which distributes light flashes to the photosensors. The on-board electronics, additionally to the readout, must also operate the monitoring system.

11.4.2.9 Discussion

The EIC resolution requirements to the electromagnetic calorimetry system can be met or nearly met by using developed technologies. For the area $\eta < -2$ the $PbWO_4$ crystals appear to be the only practical choice providing a performance close to the required, and also being compact enough to meet the expected geometrical constraints. For the other areas several options exist. The choice strongly depends on the geometrical constraints. A better performance may be achieved with more space, which is a subject for a global optimization of the experiment. Other considerations to be mentioned:

- The area $\eta > 1$ requires a high granularity of ECAL in order to resolve photons from π^0 decays. It favors a small cell size and high-A materials, which would also allow a shorter space.
- The projective geometry allows a better coordinate resolution and e/π separation. The barrel part is supposed to be projective. A decision has to be made about the endcaps.
- The e/π separation provided by the "basic" ECAL with the required resolution will be sufficient to study the e+p 18×275 GeV DIS at $p > 4$ GeV. At $\eta < -2$ the high-resolution ECAL will extend the

coverage to about 2 GeV. With the electron beam energy of 10 GeV the signal to background ratio is different and a similar purity can be reached at momenta of about 1 GeV lower. The ePD can be improved either by using calorimeters with a much better resolution, or by providing a "preshower" capability, or by using different detectors as a Cherenkov or TRD.

- At this time a SiPM is the photosensor of choice. However, such a sensor may bring limitations to the performance of high-resolution detectors, as $PbWO_4$, that have to cover a relatively large dynamic range. Large-surface sensors with a high pixel density are needed for this application.

The eRD1 "EIC Calorimeter R&D Consortium" [76] is expected to continue the development of a number of technologies, including $PbWO_4$ crystals, scintillating glass, W/ScFi and *shashlyk* detectors.

11.4.3 ECAL: Appendix

11.4.3.1 $PbWO_4$ crystals

The EIC high-resolution EM Calorimeters have the following basic requirements:

- Interaction rate capability up to $0.5x10^6 Hz$ requiring reasonably fast scintillation kinetics
- Sufficient energy resolution and efficiency over a large dynamic range of photon energies, typically from order 50 MeV to 50 GeV
- Adapted geometrical dimensions to contain the major part of the EM shower
- Moderate radiation hardness up to 3 krad/year (30 Gy/year) electromagnetic and $10^{10} n/cm^2$ hadronic at the top luminosity.

This rules out most of the well-known scintillator materials. Finally, even a compact geometrical design requires, due to a minimum granularity, a large quantity of crystal modules, which rely on existing technology for mass production to guarantee the necessary homogeneity of the whole calorimeter.For hadron physics measurements with electromagnetic reactions, such as at multiple setups atJefferson Lab and also at PANDA/GSI, the most common precision calorimeter of choice has been lead tungstate, $PbWO_4$ (PWO). This is mostly driven by the requirement of good energy resolution and high granularity to detect and identify electrons, photons and pions. Good energy resolution aids in electron-pion separation and to determine the electron scattering kinematics, compactness and high granularity is driven by need for position resolution and separation of single-photons from neutral-pion decays. PWO meets the requirements of an extremely fast, compact, and radiation hard scintillator material providing sufficient luminescence yield to achieve good energy resolution. PWO is available from two commercial vendors with established mass production capability.

Parameters of $PbWO_4$ calorimeters used in various experiments and results of beam tests are summarized in Table 11.23.

11.4.3.2 Scintillating glass

A bridge between PWO and less stringent resolution requirements could be provided by SciGlass. Over the last year Scintilex, LLC has made tremendous improvements and progress in the formulation and production of transparent barium-silicate-based glass scintillators (SciGlass) using new formulation approaches that improve properties and solve the issue of macro defects that becomes even more acute upon scale-up. The properties of SciGlass in comparison to $PbWO_4$ are shown in Table 1. SciGlass has excellent radiation resistance - no damage up to 1000 Gy electromagnetic and $10^15 n/cm^2$ hadron irradiation, the highest doses tested to date. The SciGlass insensitivity to temperature is a clear advantage over $PbWO_4$, which has a dependence of about 2-3%/°C and has to be continuously monitored. Scintilex has demonstrated a successful scaleup method and can now reliably produce glass. samples of sizes up to 10 radiation lengths. Initial beam test results with particle energies of 4-5 GeV suggest that Scintilex glass samples have an energy resolution comparable to $PbWO_4$ crystals, if comparable radiation lengths are used, for higher light yield, which is important for low energy particle detection. Scale up to $\approx 15-20X_0$ long blocks is planned for late 2020. Additional beam tests are anticipated for 2021.

Experiment	Ref	#	cell size mm^3	$\frac{X}{X_0}$	Photosensor mm^2	Temperature °C	Test beam GeV	matrix	p.e./MeV E_{min}, MeV	σ_E/E[GeV],% α	β GeV$^{0.5}$	γ GeV^{-1}
GAMS	[103]	35	20^2	20	XP1911^b	14	10	5×5	6 p.e.	0.47	2.8	
1995			×180		176 mm^2	±0.2	70			±0.06	±0.2	
KEK	[85]	9	20^2	22.5	R4125^b	13	0.2	3×3		0.0	2.5	1.4
2000			×200		25 mm^2		1.0			±2.7	±0.1	±0.1
ALICE	[104]	18k^N	22^2	20	S8148^a	-25	0.6	3×3	7.5 p.e.	1.1	3.6	1.1
2005			×180		25 mm^2	±0.1	150			±0.3	±0.2	±0.3
CMS	[105]	76k^B	22^2–27^2	26	S8148^a	18	25	3×3	10 p.e.^{f}	0.4	2.9	12.9
2006			×230		2×25 mm^2	±0.1	100			±0.3	±0.2	±0.2
PRIMEX	[106]	1k^S	20.5^2	20	R4125A^b	14	25	5×5		0.9	2.5	1.0
2006			×180		176 mm^2	±0.1	100					
PANDA	[107]	11k^C	21^2 – 27^2	22.5	LAAPD^{ac}	-25	0.05	3×3	16 p.e.	0.5	2.3	0.27
2011	[108]	5k^B	×200		190 mm^2		0.75		10			
HPS	[109]	442^B	13.3^2 – 16^2	18	S8664-1010^a	-17	0.35	3×3		2.5	2.87	1.62
2017			×160		100 mm^2	±0.3	2.35					
CLAS12	[110]	332^S	15^2	22.5	S8664-1010^a	0.0	2.2	3×3	230 p.e.^{e}	3.3^d		
FT 2020			×200		100 mm^2	±0.1						
NPS	[111]	670^S	20.5^2	22.5	R4125^b	18.0	4.7	3×3	14 p.e.	1.6^d		
2019		350^C	×200		176 mm^2							
CCAL-NPSprot	[112]	140^S	20.5^2	22.5	R4125^b	17.0	4.7	3×3	14 p.e.	0.4	2.6	1.9
2019			×200		176 mm^2							

Manufacturer: **B** BTCP ; **N** NCC-RSS ; **S** SICCAS ; **C** CRYTUR.

a - APD; **b** - PMT; **c** - Signal shaping 1 μs. **d** - The full resolution at the given energy

e It is unclear why the yield is much higher than the yield from PANDA. **f** from Ref. [111].

Table 11.23: A list of parameters of $PbWO_4$ EM calorimeters.

11.4.3.3 Lead glass

The lead-glass electromagnetic calorimeters for EIC can be analogous to VENUS at Tristan [113], OPAL at LEP [114], JLab GlueX forward calorimeter [115]. Several types of lead glass, of different parameters have been used as radiator. The light generation mechanism for the lead-glass is dominantly Cherenkov radiation (scintillation is below 1-2%). The fraction of PbO in chemical composition may vary from 45% to 75% by weight, and density from 3.6 g/cm^3 to 5.5 g/cm^3 [93, 114, 115] . The radiation length is within 1.5 cm to 3.1 cm. The Moliere radius is 3.3 –3.7 cm, typically. In practice, homogeneous calorimeters must be 20 radiation length deep to contain electromagnetic shower. For the lead glass radiator this implies 30 – 50 cm length. For a hodoscopic construction, the optimal granularity size is $\approx 4cm$, which is conditioned by the Moliere radius. The refractive index ranges from 1.62 to 1.85 (1.65 typically) [93, 114, 115]. The transparency window starts from 350 nm, except for the Ce doped radiation resistant lead glass for which it starts from 400 nm [93]. PMT-s with bialcali photcathode (sensitivity range from 300 nm to 600 nm, peak quantum efficiency 20% at 400 nm) are well suited for Cherenkov light detection from electromagnetic showers in lead glasses. The lead glass calorimeters have modular construction. The glass blocks are wrapped in thin reflector (usually aluminized Mylar), then by light tight Tedlar film. It is important to have a thin layer of air between the block and Mylar, for full internal reflection of light at oblique incident angles.

The PMT-s are optically coupled to the blocks by means of optical glue or grease of suitable refractive index. In the moderate magnetic field the PMT-s can be shielded by layers of μ-metal. In stronger fields (10 – 100 G) additional shielding of photocathode by soft iron can be implemented. A light guide between the block and PMT, no shorter than diameter of photocathode shall be placed between the block and PMT. Such design of modules was effectively used in many lead glass calorimeters [113–116] . Radiation hardness of lead-glass crystals is ∼10 krad integral dose for TF-1, and 50 krad for F-101 type radiation hard crystals. The crystals recover from damage on their own within 1 to 3 months [93]. They can be cured in situ by exposing to UV radiation. A 30% reduction in transparency of 4 cm glass thickness can be recovered within 8 hours. Alternatively, off-line gradual heating, up to 260 ^{0}C and cooling may be implemented. Resolution of lead-glass calorimeters strongly depends on optical quality and light-yield of the crystals, light detection efficiency and electronic noise, and may vary from $\approx 5\%/\,sqrtE + 1\%$ [116] to $\approx 8\%/\,sqrtE + 3\%$ [93, 116, 117]. A coordinate resolution $6.4/\sqrt{E}(GeV)mm$ for incoming photons was obtained in a hodoscopic construction of $4x4cm^2$ granularity [115].

11.4.3.4 Scintillating fibers embedded in absorber

Scintillating fiber calorimeters (*SPACAL*s) have been built and used in many experiments in both High Energy and Nuclear Physics and have been used for both electromagnetic and hadronic calorimeters [78–80, 118, 119]. They consist of many scintillating fibers embedded in an absorber material which are then gathered at the front or the back (or both) and read out with photosensors. The sampling fraction and sampling frequency can be adjusted by changing the number of fibers and their spacing to provide a range of energy resolutions and other properties. In addition, the absorber material can be selected for a specific application in order to achieve a variety of requirements.

One of the requirements for any ECAL at EIC is that it be compact, i.e., that it has a short radiation length and small Molière radius so that the total length of the calorimeter can be minimized and that the lateral extent of the shower can be contained to provide good separation of neighboring showers. This can best be achieved with a high Z absorber such as tungsten. The sPHENIX barrel ECAL utilizes a tungsten *SPACAL* (W/SciFi) design where an array of scintillating fibers is embedded in a matrix of tungsten powder and epoxy. Some of the properties of this design are listed in Table 11.20. This design was originally developed at UCLA [120] and then later adopted by the sPHENIX Experiment [95] which then further developed the technology into an industrialized process to produce more than 6000 2D projective absorber blocks. These blocks are read out using SiPMs that are coupled to the blocks using short light guides, which keeps the total radial length of the calorimeter to 26 cm inside the BaBar solenoid magnet, including the readout and supporting structure. This calorimeter is currently under construction and is expected to be completed by the end of 2021.

One of the issues with the W/SciFi design is that the boundaries between the blocks and the light guides introduce certain non-uniformities in the energy response. These can be measured using the position information provided by the calorimeter itself and/or the tracking system and used to correct the energy response. For the sPHENIX design, this leads to an energy resolution $\sim 13\%/\sqrt{E} \oplus 2.5\%$.

For any future W/SciFi calorimeter for EIC, it would be advantageous to minimize the number of boundaries produced by the blocks and the light guides, which is possible by greatly reducing the length of the light guides to just a few mm (which is necessary to act as mixer for the light coming out of the fibers) and then covering nearly all of the readout area with SiPMs. This is now also possible with the availability of large area (6×6 mm^2) SiPMs at an affordable cost.

11.4.3.5 Shashlyk

Shashlik calorimeters have been used in many High Energy and Nuclear Physics experiments (Table 11.24). The light produced in an alternating stack of absorber plates and scintillating tiles is collected with the help of wavelength shifting (WLS) fibers passed through the stack and is detected on one or both of the fiber's ends. The outgoing light is concentrated on a surface much smaller than the cell size - an advantage for using the relatively small semiconductor photosensors.

The plate thickness can be selected in order to obtain the required sampling fraction and the sampling frequency. It should be noted that, as with other sampling calorimeters, a larger sampling fraction leads to a larger radiation length and the Molière radius, which then increases the length of the total stack and allows the shower to spread out more laterally.

Most of the *shashlyk* calorimeters to date have used lead for the absorber plates. Using tungsten helps to reduce the lateral overlap of showers (Table 11.24: HERA-B inner calorimeter), and to reduce the total length of the calorimeter.

Figure 11.73: Left: COMPASS Pb/Sc "spiral" 4×4 cm^2 modules [83]; Middle: LHC-B Pb/Sc 3 module types, with a single 12×12 cm^2 cell, with four 6×6 cm^2 cells, and with nine 4×4 cm^2 cells [121]; Right: eRD1 W/Sc prototype 4×4 cm^2 cell, readout: 16 small SiPM per cell [122, 123].

Figure 11.73 shows several examples of the *shashlyk* detector. Typically, the WLS fibers are 1 cm apart. In most *shashlyk* calorimeters, the WLS fibers are bundled at the back of the detector and read out with a single photosensor. In a new eRD1 W/Sc prototype (Fig. 11.73, right) each fiber is readout by a small SiPM. One module is often split into several readout cells in order to reduce the effect of the edges between cells (Fig. 11.73, middle). The grid of fibers leads to variations of the response across the cell surface. The best uniformity has been achieved with a "spiral" geometry of the fibers (Fig. 11.73, left). An example of a 3×3 module design is shown in Figure 11.74 (left).

The scintillator and WLS fibers are selected in order to match their spectral properties.

Table 11.24 shows the parameters of several large-scale *shashlyk* detectors as well as two prototypes. These detectors are built both in rectangular and trapezoidal shapes, the latter provides the projective geometry (ALICE [90] and MPD [126] for example). Various photosensors have been used: conventional PMTs, avalanche photodiods (APD), and SiPMs.

It has been argued [77, p. 119] that the stochastic coefficient is approximately proportional to $\sqrt{d/f_{samp}}$, where d is the thickness of the active material layer (or the fiber's diameter). For a number of sampling calorimeters of various types (LAr, LKr, Pb/Sc *shashlyk*, SPACAL etc) it was found that $\beta \approx$

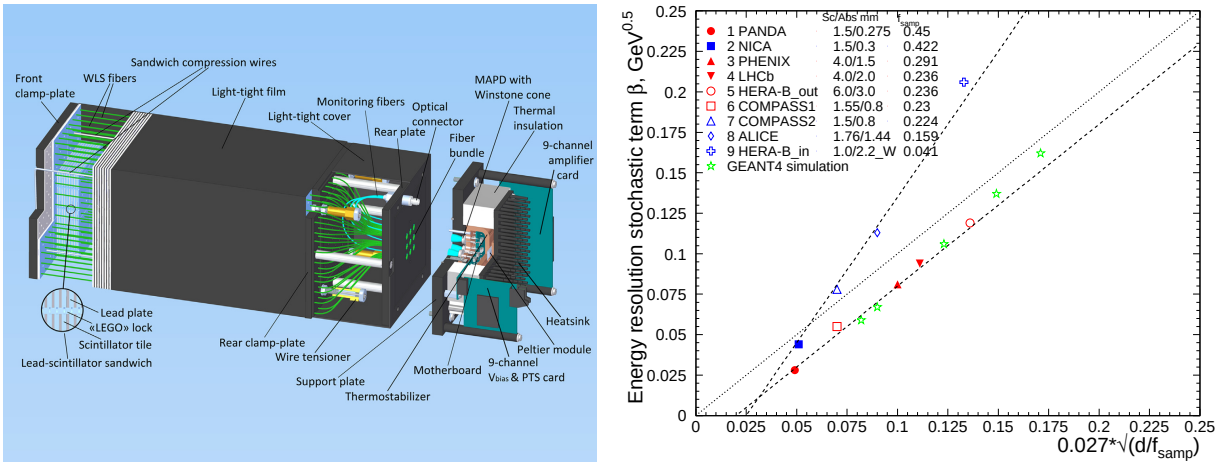

Figure 11.74: Left: A 3×3 module design [124] with a SiPM readout.
Right: The measured stochastic term β of the resolution of *shashlyk* calorimeters (Tab. 11.24) against a predicted value of $\beta = 0.027\sqrt{d/f_{samp}}$ [77, p. 119], where d is the thickness of the scintillator tile in mm. The "scaling variable" $\sqrt{d/f_{samp}}$ at the first order does not depend on the thickness of the scintillator tile. The plot indicates that the data can be split in two groups. In each group the dependence on the "scaling variable" is nearly linear: $\beta \approx 0.027(\sqrt{d/f_{samp}} - 0.74)$ and $\beta \approx 0.049(\sqrt{d/f_{samp}} - 0.92)$. The origin of the difference between the groups is unclear at this moment. The results of GEANT4 simulation (Fig. 11.75) match the lower curve well at moderate layer thickness.

$2.7\%\sqrt{(d/1\text{ mm})/f_{samp}}$. The data from Tab. 11.24 is shown in Fig. 11.74 (right). It is not clear what causes the data to split in two groups with different slopes. The lower group is described by the predicted slope of 0.027, while the higher group is described by a larger slope of 0.049. The offsets of the linear functions are not physical (β can not be negative at any layer thickness) but indicate that at a smaller layer thickness some other processes must dominate the resolution. Results of GEANT4 simulation of *shashlyk* calorimeters are shown in Fig. 11.75. The stochastic term describes the data well (Fig. 11.74). The constant term simulated for $0.25 \cdot X_0$ is well described by a parabolic function. In summary, the resolution of a *shashlyk* calorimeter can be approximated by:

$$\beta \approx 2.7 \cdot (\sqrt{d/f_{samp}} - 0.74)\% \tag{11.6}$$
$$\alpha \approx (1.31 - 0.251(x-20) + 0.144(x-20)^2)\%,$$

where d is the thickness of the scintillator tile in mm, f_{samp} is the sampling ratio; $x = X/X_0$ is the full thickness of the calorimeter. The constant term depends on the layer thickness as well. In a real experiment it also depends on the calibration quality and other factors.

The expected spacial constraints of the EIC favor the use of tungsten alloys for the absorber. One can select the sampling structure in order to be able to fit the detector into 40 cm of space (see Tab. 11.20). Assuming the approximation of Eq. 11.6 one may expect that such a structure of W/Sc 0.75/1.5 mm would provide a stochastic term of 6.3% $\text{GeV}^{0.5}$.

The eRD1 Consortium is planning to study in a test beam a 3×3 W/Sc detector prototype [122, 123] (see Fig. 11.73, right and Tab. 11.24). Instrumenting each individual fiber with its own small SiPM may provide more detailed information about the position of the shower inside the stack, thus providing better position

Experi-	Ref	sampling	f_{samp}	ρ	X_0	R_M	$\frac{X}{X_0}$	cell	read-	Yield/	Beam	σ_E / E[GeV]	
ment		mm	%	$\frac{g}{cm^3}$	mm	mm		mm	out	MeV	GeV	α %	β %
# ch		# layers	*2nd line: calculation*					WLSF	mm^2			γ %	
KOPIO	[125]	Pb/Sc 0.275/1.5		2.75	35.	60.	16.	110.	APD	50 p.e.	0.2-0.4	2.0	2.74
few		×300	45.	2.60	35.	57.		144	200.				
PANDA	[88]	Pb/Sc 0.275/1.5			34.	59.	20.	110.	PMT	5 p.e.	1-19	1.3	2.8
~ 2000		×380	45.	2.60	35.	57.		144	200.			3.5	
MPD NICA	[126]	Pb/Sc 0.3/1.5			32.	62.	12.	110.	SiPM		0.5-3.0	1.0	4.4
38000		×220	43.	2.70	32.	55.		144	36.				
PHENIX	[70]	Pb/Sc 1.5/4.0			20.		18.	55.	PMT	1.5 p.e.	5-80	2.1	8.1
15500		×66	29.	3.81	20.	42.		36	200.				
LHCb	[121]	Pb/Sc 2.0/4.0				37.	24.	40.	PMT	3.0 p.e.	5-100	0.8	9.4
6000		×66	24.	4.44	17.	35.	25.	16				14.	
HERA-B	[127]	Pb/Sc 3.0/6.0			17.	37.	20.	56.	PMT	0.8 p.e.	5-28	1.4	11.9
4000		×37	24.	4.45	17.	42.		36	490.				
COMPASS	[83]	Pb/Sc 0.8/1.55					23.	38.	PMT		1 - 7		5.5
888		spiral ×156	23.	4.50	16.	37.		16	490.				
COMPASS	[128]	Pb/Sc 0.8/1.5			16.4	35.	16.	40.	SiPM		1 - 7	2.3	7.8
≈2000	[129]	×109	22.	4.60	16.	36.		16	9.				
ALICE	[90]	Pb/Sc 1.44/1.76	9.5	5.68	12.3	32.	20.	60.	APD	4.4 p.e.	0.5-100	1.7	11.3
12288		×77	16.	5.63	12.4	30.		36	25.			5.	
HERA-B	[127]	W[a]/Sc 2.2/1.0			5.6	14.	23.	22.	PMT	0.13 p.e.	5-28	1.2	20.6
2100		×37	4.1	12.5	5.7	13.9		9	490.				
eRD1	[122]	W[b]/Sc 1.58/1.63					31.	38.	SiPM				
	[123]	×79	9	8.9	8.4	19.		16				1.	7.7 [c]

a - W/Fe alloy 90/10 % by volume; **b** - W/Cu alloy 80/20 % by volume

c - Results of GEANT simulation;

Table 11.24: A list of parameters of *shashlyk* EM calorimeters used in experiments. The values of the average properties of the calorimeter material (f_{samp}, ρ, X_0, and R_M), if published, are presented in the top lines of the proper cells. The values calculated using the published sampling structure are presented in the bottom line. The calculation is simplified, but done in a standard way for all the entries facilitating the comparison between the entries. The results of the calculations are usually close to the published values, except the only one published value of f_{samp}. The resolution is parametrized using Equation 11.4. The resolution was measured in test beams in the energy range specified. The size of the readout cell is shown, along with the number of WLS fibers per cell.

resolution, and also allowing this information to be used to correct for any non-uniformity in either the light collection or energy response. One may also consider adding the signals from several of those SiPMs electrically, reducing the number of readout channels. Such a design reduces the length of the module, saving a few cm of space needed for bundling of the fibers.

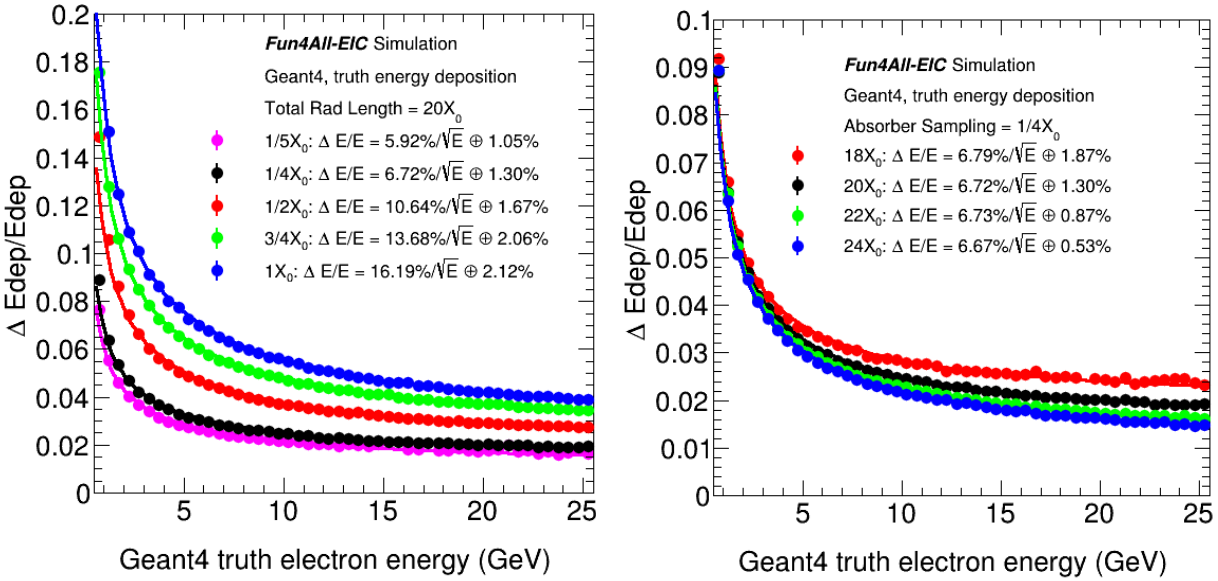

Figure 11.75: GEANT4 calculation of the *shashlyk* W/Sc detector resolution [123]. The scintillator tile is 1.5 mm (?) thick. Left: Dependence on the absorber plate thickness for $20X_0$ total thickness. The results are compared with data in Fig. 11.74. Right: Dependence on the total thickness $x = X/X_0$ for a $0.2X_0$ thick layer. The constant term is described by a polynomial: $\alpha = (1.31 - 0.251(x-20) + 0.144(x-20)^2)\%$.

11.5 Hadronic Calorimetry

11.5.1 General consideration for Hadron Calorimeters

The major point for the design of hadron calorimeters (HCAL) at the EIC is the capability of the whole detector to provide precise reconstruction of the jet energy. At EIC a particle flow-style approach is envisioned for jet reconstruction, unlike pure calorimetric methods used in the past. The calorimetry based jet reconstruction at HERA required very high resolution hadronic calorimetry systems [130]. Meanwhile at EIC tracker and EmCal will measure about 95% of jet energy with precision much higher than any hadron calorimeters built in the past, except may be for very forward region in the hadron endcap, where tracking performance starts to deteriorate (depends on magnet design). Particle flow-style methods rely on precision measurement of charged fragments of jets using the tracker instead of the calorimeters (ECal + HCal). However, calorimeter information is still needed to account for contributions from neutral particles for which a sufficient high granularity may be important to disentangle the different contributions, i.e. proper assignment of signal to the neutral components of the jet. These considerations lead to the set of parameters for hadron calorimeters of the EIC detectors shown in Table XX Energy resolution in the table is referred to a single particle resolution rather than jet.

At EIC all envisioned calorimetry systems are binary, i.e. EmCal followed by HCal. This is driven by the relatively high EM energy resolution requirement which will be difficult to achieve with a single device serving simultaneously as EmCal and HCal. A possible exception may be the very forward hadron endcap where the stochastic term for EM energy resolution might be relaxed due to the higher energy of incoming particles. Achieving high resolution for both EM particles and hadrons is a very difficult task, and there are no precedents from past experiments. For instance, the ZEUS collaboration at HERA operated a very high

resolution hadron calorimeter, but paid a price in the form of rather mediocre performance for EM shower detection $18\%/\sqrt{E}$ while the situation was vice versa for the H1 detector (ref H1). A common scenario is if one focuses on excellent EM resolution, one pays a heavy price when it comes to hadronic shower detection. As an example, as the pointed out in Ref. [131] once the choice is made for a crystal EM section, it essentially does does not matter what one installs behind it. The hadronic energy resolution will be poor. It will be completely determined by fluctuations in the energy sharing between the EM and hadronic calorimeter sections, which in this case have very different e/h values. This results in a typical hadronic resolution of approximately $100\%/\sqrt{E}$. Even the most sophisticated compensating hadronic sections cannot alter this conclusion. The challenge of balancing EM and hadronic calorimeter performance is a common problem for any calorimetry system, independent of other, detector/collider specific limitations such as available space, dead material between EM and hadronic sections, choice of readout and etc. These degrade the hadronic resolution of any system even more and will be discussed later in this section. To conclude this introduction, we will list some of the parameters of existing high-resolution hadronic calorimeters which will be referred to in subsequent subsections.

The total hadronic resolution of three high-resolution calorimeters (approximately compensated) and the various factors contributing to it are listed in the table below (where are σ_p, σ_s, σ_i the fluctuations in the number of signal quanta, sampling fluctuations and intrinsic fluctuations, respectively).

	ZEUS U^{238}	ZEUS Pb	SPACAL
σ_p	$6\%/\sqrt{E}$	$10\%/\sqrt{E}$	$5\%/\sqrt{E}$
σ_s	$31\%/\sqrt{E}$	$42\%/\sqrt{E}$	$27\%/\sqrt{E}$
σ_i	$19\%/\sqrt{E}$	$11\%/\sqrt{E}$	$11\%/\sqrt{E}$
σ_h	$37\%/\sqrt{E}$	$44\%/\sqrt{E}$	$30\%/\sqrt{E}$

Table 11.25: Hadronic energy resolution of different calorimeters. Data taken from [130, 132–134]

In all three detectors, the hadronic resolution is dominated by sampling fluctuations. This is a direct consequence of compensation (e/h=1), which requires small sampling fractions, for example, 2.3% for lead/plastic detectors and 5.1% for uranium/plastic devices.

Much effort went into understanding the mechanism of compensation in the past [135], upon which the high-resolution ZEUS calorimetry system was build. However, one aspect of compensation was not immediately clear at that time, namely, the energy dependence which affects the precision of jet reconstruction. Data from ZEUS, showed that, for particles below 10 GeV, the e/h ratio of the ZEUS calorimeter gradually decreases by 30% with decreasing energy (ref ZEUS,compensation). There is no known solution to this problem. For the EIC central detector, with exception of the very forward region in the hadron endcap (at $\eta > 2.5$), most hadrons will have energies below 10 GeV, and thus there is little value to pursue compensation (such as using depleted uranium) for the hadronic calorimeter section in these regions. In the very forward region of the hadron endcap the hadron energy will be above 10 GeV and the compensation technique is very relevant.

11.5.2 Central detector consideration

Precise measurements of the hadron energy with calorimeters requires sufficient containment of hadronic showers. Unlike the compact electromagnetic showers hadronic showers are very broad. The longitudinal

and radial containment $L_9 5\%$ and $R_9 5\%$, the required length and radius of the calorimeter for 95% hadronic energy deposition containment as given in [136], scales as:

$$L_{95\%} \approx t_{max} + 2.5\lambda_a, R_{95\%} \approx 1\lambda_{int} \tag{11.7}$$

, where $t_{max} \approx 0.2 \log[e] E(GeV) + 0.7$ is the shower maximum depth, and λ_a (in units of λ_{int}) describes the exponential decay of the cascade beyond t_{max} and varies with hadron energy as $\lambda_a = [E(GeV)]^{0.13}$. For the EIC central detector a calorimeter system of approximately 5 λ_{int} depth seems sufficient for most regions, except for the forward region of the hadron endcap where it should be of order 6-7 λ_{int}. Table 11.25 lists absorber materials typically used for HCals for 95% containment. (Absorber material - 95% containment). The choice of absorber material is often driven (apart from energy resolution) by cost, engineering constraints, magnet design, desire for a compensated calorimeter system, and, in case of readout with SiPM's, acceptable levels of neutron fluences. Low Z absorbers generates less neutron flux and in this regard steel absorbers are preferable.

11.5.3 HCal Energy resolution

Precise measurements of hadron energy with sampling calorimeters require sufficiently high sampling fraction and sampling frequency to keep sampling fluctuations and number of signal quanta fluctuations below the acceptable threshold (see Table 11.25). Increasing the sampling fraction leads to significant reduction of the final calorimeter density. In addition, calorimeters with large sampling fraction require significant additional space for mechanical stability, as they are usually not self supporting. For example, λ_{abs} for DU is 10.5 cm. However, the effective λ_{abs} of the ZEUS calorimeter is 24 cm, about a factor of two larger. Collider central detectors are generally large-volume detectors, and thus cost plays a non-negligible role in calorimeter, and in particular hadron calorimeter, design. As a consequence, compromises are usually necessary. As an example, the ZEUS and SPACAL HCAL systems listed in Table 11.25 can give an idea of the space requirement for high resolution calorimeters. The ZEUS calorimeter system (hadron endcap) extended over almost 4 meters, of which about half the space was occupied by the high resolution DU/Sc calorimeter. The remaining space was occupied by the backing calorimeter whose purpose was to control longitudinal leakages. The SPACAL system required about 2 meters for the Pb/ScFi structure and additional 0.7 meters for the readout, which is similar for the E864 calorimeter based on the SPACAL design).

The space available for all EIC detectors including the calorimeter systems is finite. Desired properties for the EIC calorimeters, beyond the requirement on energy resolution, are thus: compactness and mechanical sturdiness, which allow for building self-supporting structures and minimizing the space required for passive mechanical support structures. This for example, makes lead as a non-ideal choice for the HCAL absorber as it would require significant passive reinforcement to keep mechanical stability of detector plus additional space to support the Emcal section. Ideally, it would be preferable if the HCal structure serve as a support for the Emcal. This is possible to achieve with a steel absorber. This choice of material would also eliminate dead material between Emcal and HCal sections which degrades the overall system performance as the dead material sits almost in the shower maximum position. To control longitudinal leakage one usually employs tail catchers, or backing calorimeters, as in case of ZEUS. At the EIC a tail catcher would have to be integrated with the main calorimeter due to the lack of space for a separate device. Such an approach is described in Ref. XX, where the last few layers of the HCal section would have additional independent readout. The information from the tail catcher allows for clean identification of showers without longitudinal

leakage. There is a desire to have a higher resolution (better than $\approx 40\%/\sqrt{E}$ with a constant term of $\approx 5\%$) calorimeter in the forward hadron endcap ($\eta > 2.5$), i.e. the region where the calorimeter performance is anticipated to exceed that of the tracker. This interplay of calorimeter and tracker performance is similar to that in the electron endcap, where the inner part requires the highest resolution and the outer part has more relaxed requirements (see Table XXX). In the hadron endcap taking into account the limited available space, a very dense calorimeter that minimizes leakage and ideally serves as both Ecal and Hcal with a single readout would be preferable. Such a calorimeter should have a small sampling fraction and sufficiently high sampling frequency (to keep the Em energy resolution at an acceptable level), which is currently only possible with a fiber calorimeter technology.

11.5.4 eRD1 EIC R&D and STAR forward developments

To date R&D efforts towards high-resolution hadron calorimetry at the EIC have been limited as existing technologies have been considered sufficient. The very first eRD1 calorimetry consortium proposal aimed to develop new W powder ScFi technology for both EM and HCal sections to help balance the requirements of EM and hadron energy resolutions. In particular, the technique was aimed at simplifying the construction of EM calorimeters with high sampling frequency and small sampling fraction (approximately being compensated) and targeting about $12\%/\sqrt{E}$ resolution. With support from STAR Forward upgrade project the eRD1 consortium built a small prototype of a compensated calorimeter system with the new W/ScFi technology in the EM section and an HCal section copying the ZEUS Pb/Sc prototype, listed in 11.25. This system was tested at FNAL in 2014 and was modeled in the BEAST EIC detector model model as a hadron endcap. Such a compensated system can meet the requirements for EIC hadron calorimeters listed in Table XX. However the non-compensated variant was considered as well. This originated from a budgetary constraint for the STAR forward upgrade that eventually led to the development of a non-compensated calorimetry system consisting of Pb/Sc shashlik for the EM section (utilizing existing EM blocks from PHENIX experiment) and Fe/Sc for the hadronic section. A small prototype of this system was built and tested at FNAL in 2019. As expected, the compensated prototype had approximately 30% better hadronic energy resolution compare to the non-compensated one. Additional R&D efforts have been carried out to demonstrate a similar system with W/ScFi for the EmCal section that can meet the EIC physics requirements. [137].

11.5.5 Alternative methods for high resolution HCal

Over the past two decades there were attempts to significantly improve the energy resolution of hadron calorimeters using the dual readout method. This method uses an observable which correlates with the number of neutrons released in the hadronic shower, which correlates with "invisible" energy ($\approx 40\%$ in the hadronic shower By comparing the signals produced by Scintillation light and Cherenkov light in the same detector, including timing and spatial characteristics of the showers, the EM shower fraction, whose fluctuations are the main culprit for problems encountered with hadronic calorimetry, can be determined for individual events. The validity of this principle has been demonstrated with the DREAM fiber calorimeter. [138]. A realization of dual readout at EIC would have to take into account the relatively low energy of hadrons and the limit of available space. eRD1 took an opportunity to look at timing characteristic of showers using STAR Forward calorimeter prototype with steel absorber during the 2019 test run at FNAL and observed no meaningful correlations of fast component of hadronic shower with total energy, i.e. accounting for em fraction of the shower on event by event basis with this method did not look promising (at least with steel absorber).

At the end of this section we should also mention alternative concepts of designing the whole detector in which the role of calorimeters is quite different compared to what has been traditionally used. These concepts were initially driven by the HEP community for future linear collider development which require extremely high energy resolution for jets. Hadron calorimeters in these concepts are essentially digital devices with hundreds of millions of channels to track every single particle in hadronic showers, as required by particle flow algorithms. This approach requires significant space for the detector, appropriate design of the magnet, and perfect tracking performance over the entire rapidity. The TOPSIDE concept of the EIC detector is an example of such approach.

In summary, the set of parameters listed in Table XX should be achievable with existing technologies as demonstrated by the eRD1 consortium and STAR Forward upgrade with some additional R&D efforts to improve on the performance of a STAR-like forward calorimeter system. High resolution hadron calorimetry will require additional R&D efforts, e.g. to develop a high density fiber calorimeter with SiPM readout or another suitable technology.

11.6 Far-Forward Detectors

11.6.1 Introduction

The EIC physics program includes a very broad need for diffractive physics measurements. Experimentally, this means that robust far-forward ($\eta > 4.5$) hadron and photon detection, and far-rear electron detection ($\eta < -4.5$) is required. These regions of the IR require multiple detector concepts to meet the needs of the physics program, including calorimetry for electrons, neutrons, and photons, silicon sensors for charged particle tracking, and detector concepts such as Roman Pots for detecting protons or nuclear remnants that are very close to the central beam. The subsequent sections will introduce the various detectors and technologies, and discuss the results of simulations (including realistic acceptance, beam effects, and detector resolutions) and the associated impact on the physics.

11.6.1.1 General Layout of Far-Forward IR Region

The far-forward region of the interaction region at the baseline EIC detector is complex and requires novel ideas for covering a broad acceptance for charged and neutral particles from a long list of interactions. Fig. 11.76 shows a top-down sketch of the full baseline EIC IR region. Fig. 11.77 shows the layout of the far-forward region used in the GEANT4 simulations. The image shows the various magnets for the hadron beam that create a unique engineering problem for placement of particle detectors and for allowing passage of particles scattered away from the beam.

The various subsystems involved in the far-forward region are summarized in Table 11.26 and depict the challenge of building a suite of detectors to cover the full acceptance for the various interaction channels.

11.6.2 Roman Pots

Roman Pots (RP) are vessels with a thin window in which silicon detectors are placed. The pot vessel is inserted into the beam pipe vacuum, allowing detection of scattered charged particles that are very close

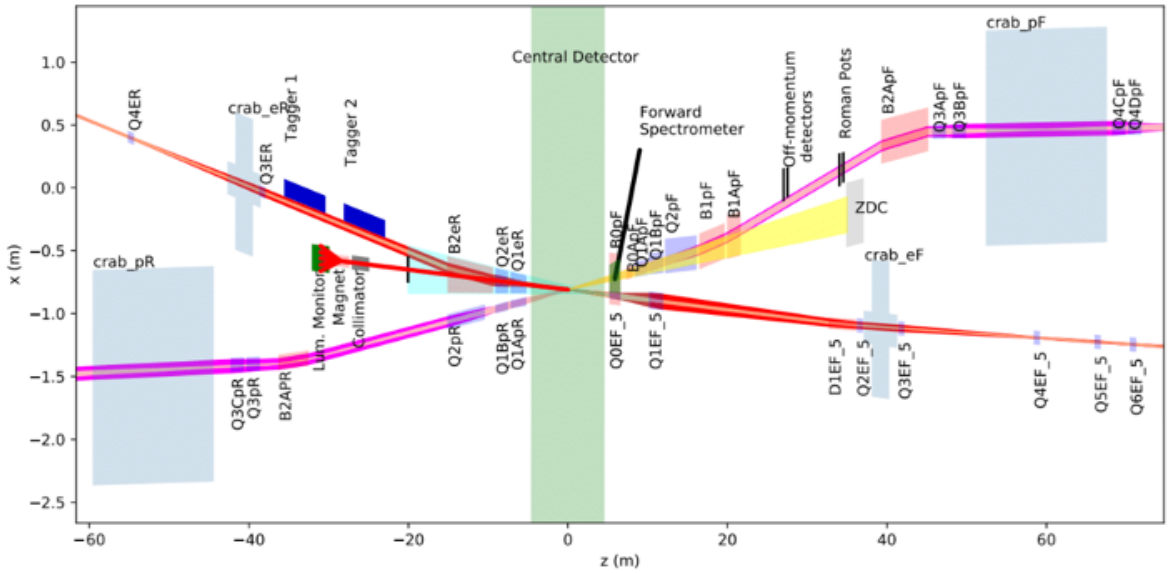

Figure 11.76: Image of the full EIC baseline IR layout.

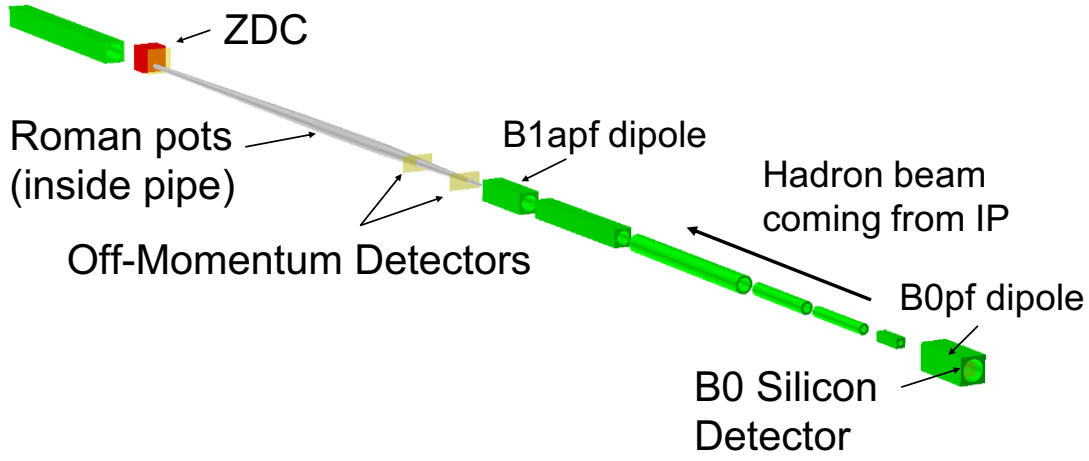

Figure 11.77: Image of the Far-Forward IR and the associated detector components. Image generated using Geant4+EicRoot.

to the beam, These detectors can measure scattered protons or light nuclei which are separated from the hadron beam by up to 5 mrad. The windows on the pots through which protons or light nuclei can enter to be measured by the silicon are generally placed within 1 mm or so of the beam (depending on the beam optics and transverse beam size at the RP location), with safe distance being defined as the "10 $\sigma_{x,y}$" region, where $\sigma_{x,y}$ is the transverse size of the beam in x and y. Fig. 11.78 shows a cartoon sketch of the basic concept begin considered, but note that the stainless steel pots themselves are not shown in the cartoon. In this section, basic requirements for the sensors will be discussed first, and technology appropriate for use in the EIC diffractive physics program will be discussed at the end.

Detector	(x,z) Position [m]	Dimensions	θ [mrad]	Notes
ZDC	(0.96, 37.5)	(60cm, 60cm, 2m)	$\theta < 5.5$	~4.0 mrad at $\phi = \pi$
Roman Pots (2 stations)	(0.85, 26.0) (0.94, 28.0)	(25cm, 10cm, n/a)	$0.0 < \theta < 5.5$	$10\,\sigma$ cut.
Off-Momentum Detector	(0.8, 22.5), (0.85, 24.5)	(30cm, 30cm, n/a)	$0.0 < \theta < 5.0$	$0.4 < x_L < 0.6$
B0 Spectrometer	(x = 0.19, 5.4 < z < 6.4)	(26cm, 27cm, n/a)	$5.5 < \theta < 13.0$	~20 mrad at ϕ=0

Table 11.26: Summary of far-forward detector locations and angular acceptances for charged hadrons, neutrons, photons, and light nuclei or nuclear fragments. In some cases, the angular acceptance is not uniform in ϕ, as noted in the table. For the three silicon detectors (Roman Pots, Off-Momentum Detectors, and B0 spectrometer) a depth is not given, just the 2D size of the silicon plane. For the Roman Pots and Off-Momentum Detectors, the simulations have two silicon planes spaced 2m apart, while the B0 detectors have four silicon planes evenly spaced along the 1.2m length of the B0pf dipole magnet bore. The planes have a "hole" for the passage of the hadron beam pipe that has a radius of 3.2cm.

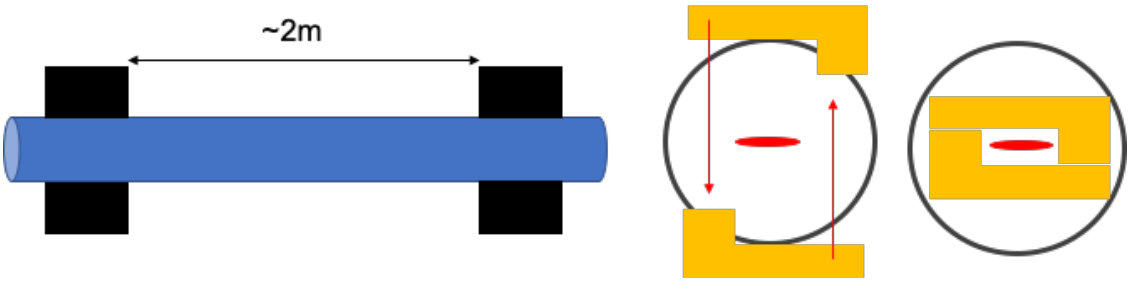

Figure 11.78: Cartoon sketch of the Roman Pots concept, without the stainless steel pots shown. This Yellow Report study assumes two Roman Pots stations, separated by 2 meters, for all of the simulations. The right side of the cartoon shows a potential shape of the sensors and how the pots could be inserted into the beam line. Given the small amount of space between the hadron and electron beams at this spot in the IR, horizontal movement of the pots could be challenging.

11.6.2.1 Basic Requirements for Roman Pots

In general, the Roman Pots need to have both the necessary acceptance and resolution to carry out the diffractive physics program at the EIC. The acceptance is driven by the machine optics (i.e. transverse beam size at RP location) and active sensitive region of the detector (sensor size). From studies of Deeply Virtual Compton Scattering in e+p collisions, the sensitive area of the sensors needs to be about 25cm x 10cm to capture the majority of the protons within the 5 mrad acceptance required. Protons at larger scattering angles can be measured with the B0 detector (see Sec. 11.6.4). At the highest proton beam energy (275 GeV), the protons are within the 5 mrad acceptance, with the lower cutoff of scattering angle acceptance being driven by the size of the beam at the RP. For protons at the lower beam energies (100 GeV and 41 GeV), the B0 and RP detectors are both required to cover the full acceptance range. Fig. 11.89, discussed in the physics impact from DVCS in Sec. 11.6.7.2 shows the p_T-acceptance of protons at various energies, and with two beam configurations.

The p_T resolution of the RP is dictated by both beam effects and detector effects. The effects are listed below in general order of the size of the effect, with the first being the largest contribution.

- Beam angular divergence

- Crab cavity rotation
- Silicon pixel pitch
- Transfer matrix uncertainty

The beam angular divergence sets the lower bound of the achievable resolution, so the goal is to mitigate the other effects such that they are less than the angular divergence contribution. The contribution from the crab cavity rotation manifests itself as an effective vertex smearing, since the crab cavity rotates the bunch horizontally such that the electron and hadron bunches arrive at the IP head-on. The effective vertex smearing is approximately $(.5 * \theta_{crossing} * L_{bunch})$. This contribution can be mitigated with fast timing (~35ps), allowing for precise measurement of the location of the collision within the bunch. Table 11.30 summarizes the smearing contributions with reference to the study that generated the quantitative assessment these values and relative impact.

11.6.2.2 Silicon Sensors for Roman Pots

The development of high spatial resolution pixel detectors with high per-pixel time resolution has been one of the major technological drivers in collider physics in recent years in order to meet some of the challenges posed by future collider experiments. Current particle trackers in collider experiments are based on silicon technology with a spatial resolution of few tens of microns, while novel silicon technologies have recently allowed timing resolution of few tens of ps, for instance with the Low Gain Avalanche Diodes (LGADs) [139, 140]. For example, the ATLAS and CMS experiments [141, 142] at the High Luminosity LHC (HL-LHC) [143, 144] have developed fast-timing detectors based on LGAD sensors.

The LGAD is based on a simple *p*–*n* diode concept, where the diode is fabricated on a thin high-resistivity *p*-type silicon substrate. A highly-doped *p*–layer (the "gain" layer) is implanted under the n^+: application of a reverse bias voltage creates an intense electric field in this superficial region of the sensor, able to start an avalanche multiplication for the electrons. The gain is limited to a factor of typically 10-100, such that the noise low compared to the case of avalanche photodiodes. The drift of the multiplied carriers through the thin substrate generates a fast signal with a time resolution of few tens of ps. However, there is a severe limit at the spatial resolution this detector can achieve. Important dead areas exist at the edges of the pixels and in-between the pixels, so that large-pitch pixel only are possible lest a low fill-factor is introduced. For example, the LGAD sensors developed for the ATLAS and the CMS timing-detectors have relatively large pads of about 1.3 x 1.3 mm^2 size.

Recent research has studied how to segment LGAD sensors [145], e.g. with pixels or strips with pitches in the tens of microns, in order to achieve fine spatial resolution while maintaining the fine LGAD time resolution. It was demonstrated [146, 147] that the new technology of AC-coupled LGADs (AC-LGADs [145]) is a good candidate for a 4-dimensional (4-D) silicon detector to provide time resolution in the few tens of ps and segmentation of few tens of microns. Figure 11.79 shows a schematic section of a segmented AC-LGAD sensor.

Differently from a standard DC-coupled LGAD, see Ref. [139], the n^+ layer is more resistive than in the standard LGAD. Above the active area, a thin dielectric layer is deposited and, on top of it, metal pads are placed to define the AC-couple electrodes of the structure. Signals are induced on these pads, which are connected to the read-out electronics. If the pads are close enough, there is an important cross-talk between

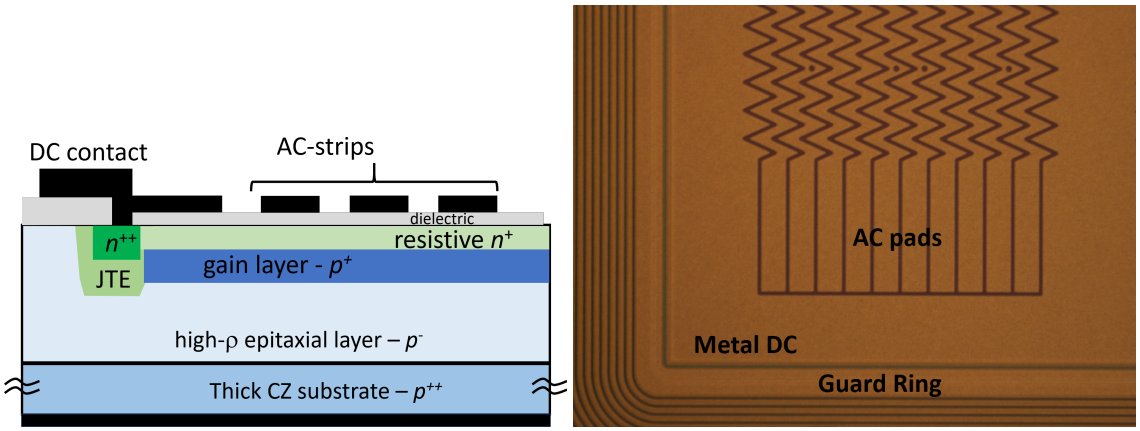

Figure 11.79: Left. sketch of the cross section of a segmented AC-LGAD (not to scale). For simplicity, only three AC electrodes are shown. Right: microscope image of an AC-LGAD, fabricated at BNL.

them that can be used for interpolation. Since the geometry of these pads can be arbitrary, by patterning the pads as zigzag (Figure 11.79) it is possible to use the cross-talk among strips to enhance the spatial resolution and, at the same time, to keep the number of the read-out channels low.

Since they are fabricated on thin substrates, the LGAD sensors,intrinsically have a very limited dead area external to the active region. One floating guard ring is sufficient to sustain the high voltage and scribelines at a distance smaller than 100 μm are possible.

Another sensor option for the Roman Pots is the 3D pixel technology that has been used, for example, in the ATLAS IBL. 3D sensors are intrinsically fast and are lacking of the ”landau” noise, which constitutes the ultimate limit of the timing resolution of the LGAD. On the other hand, 3D sensors do not have intrinsic gain and have a capacitance which is 4-5 times higher than that of an LGAD of the same area. Their fast timing properties cannot therefore be exploited by a power budget-limited readout electronics.

In fact, a critical aspect for the development of a Roman Pot pixel detector with fast-timing capabilities is the readout. The front-end electronics must have timing and feature size compatible with those of the sensor. Current ASICs for ATLAS (ALTIROC) and CMS (ETROC) are designed in the CMOS TSMC 130 nm and CMOS 65 nm technologies respectively, and they use TDCs to measure the Time of Arrival and Time over Threshold, as well as RAM for data buffering. In the ALTIROC, for example, the maximum jitter is of the order of 25 ps for 10 fC charge, and the ALTIROC and ETROC total power consumption per unit area is about 200-300 mW / cm^2. As a comparison, the RD53 readout chip for pixel detectors for tracking (i.e. no timing) at the HL-LHC with 50 x 50 μm^2 and 25 x 100 μm^2 feature sizes is estimated to have a power density of about 1 W / cm^2 or less. Small pixels complicate the design due to limited space to accommodate TDCs and RAM and increased preamp and TDC power density. However, it seems reasonable to reach 500 x 500 μm^2 feature size by rearranging blocks and removing components that are likely unnecessary in a Roman Pot detector (e.g. a large RAM), while maintaining the same timing performance. In addition, by using Time-Over-Threshold (TOT) features in the ASICs, the charge sensed by pixel can be measured and in turn the charge sharing among pixels estimated. Therefore, using the TOT information the spatial resolution may improve beyond the fixed pixel pitch.

11.6.2.3 Summary of the Current Design Constraints

Based on the requirements listed above, and the results of the studies detailed in Secs. 11.6.7.2 and 11.6.7.4, the overall optimized Roman Pots requirements can be summarized in the following way. In order to fully cover the p_t range of scattered protons and ions from the various physics channels covered by the Roman Pots, a total active sensor area of 25cm x 10cm will be required. This can be achieved with various different arrangements of the sensors, but the total area covered must be preserved in order to maximize the kinematic coverage.

The studies to date, along with the expected improvement of the proposed silicon sensor technology (AC-LGADs), indicate that a 500 μm x 500 μm pixel size will properly balance the smearing contribution and R&D efforts. The simulations detailed in Secs. 11.6.7.2 and 11.6.7.4 assumed two RP stations with one sensor plane each. However, in actual operation, anywhere from 2-5 sensor planes per station would likely be used for redundancy and background rejection. With the assumed active area per plane and pixel size, this leads to 100k channels (pixels) per plane.

Finally, in order to meet the needs of both background rejection and reduction of vertex smearing from the crab cavity rotation, a timing per plane of ~35ps will be required.

11.6.3 Off-Momentum Detectors

11.6.3.1 Basic Design Considerations

In any e+A collision event, protons and other charged particles can appear in the final state with very small scattering angles (e.g. proton spectators in nuclear breakup). In this scenario, the resulting charged particles will be directed toward the far forward (FF) detectors, but will have a significantly different magnetic rigidity compared to the nuclear beam in question. For example, a proton with 100 GeV/c of total momentum arising from an e+d collision where the deuteron beam has 200 GeV/n of energy would mean that the proton has an x_L ~0.5, and half the rigidity of the deuteron beam, causing it to experience more severe magnetic deflections in the lattice. In this case, the protons will not stay in the beam pipe all the way down to the Roman Pots, and will instead be bent out of the beam pipe after the B1apf dipole magnet, as shown in Fig. 11.80. Measuring these so-called "off-momentum" protons (or other charged particles) will require additional sensor planes outside the beam pipe - the so-called "off-momentum detectors" (OMD). These detectors will cover $0.25 < x_L < 0.6$ for protons, with the azimuthal symmetry of the acceptance degrading at $x_L < 0.4$ due to losses in the quadrupole magnets.

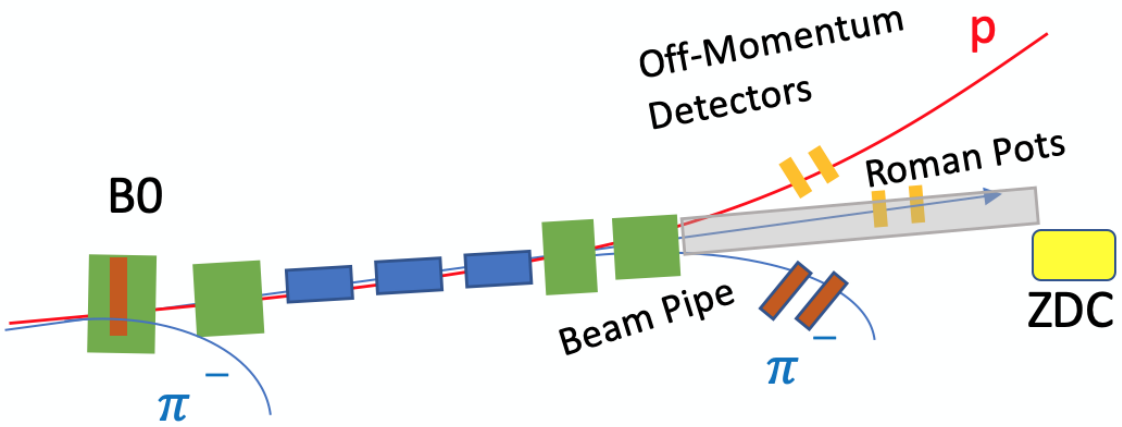

Figure 11.80: Cartoon schematic of the operation of the off-momentum detectors. In the schematic a nuclear beam is being used and the final state particles shown are from various potential collision events, such as from nuclear breakup or lambda decay.

The technology employed in these detectors can be the same used for the Roman Pots since the reconstruction approach using a transfer matrix will be similar. The main difference aside from the detection of off-momentum particles is that there will be no need for a 10σ cut that limits low-p_T acceptance since the detectors sit outside of the beam pipe.

The simulations using the OMD system are shown in Secs. 11.6.7.311.6.7.4, and 11.6.7.6. The spectator proton studies included only detectors on one side of the beam pipe, with two stations and the reconstruction approach as with the Roman Pots. The studies of lambda decay indicate the need for detectors on the other side as well for detection of negative pions, and also a more complicated reconstruction method to account for the highly displaced lambda decay vertex.

11.6.3.2 Summary of the Off-Momentum Detector Considerations

The Off-Momentum Detectors will be important tagging final state charged particles from nuclear breakup and lambda decay. The sensors used can be the same as for the Roman Pots. In the simulations, the sensors were assumed to be 30cm x 30cm, covering both sides of the beam pipe after the B1apf dipole magnet. This assumption will need to be refined when more up-to-date beam pipe designs are finalized. These detectors will use the same transfer matrix approach as is used for the Roman Pots, but it needs to be noted that the off-momentum particles will, in many case, not obey the linear optics assumption for the transfer matrix, and more advanced reconstruction methods will need to be employed.

11.6.4 B0-spectrometer

11.6.4.1 Basic requirements for B0

The B0 tracker can help provide very forward tracking capability for charged tracks. Such capability is important for forward ($\eta > 3$) particle measurements as well as event characterization and separation. Fig. 11.81 shows some conceptual drawings of the B0 bore with the sensors included. There has also been discussion of including electromagnetic calorimetry into the B0pf magnet bore, but simulations have not been carried out at this point.

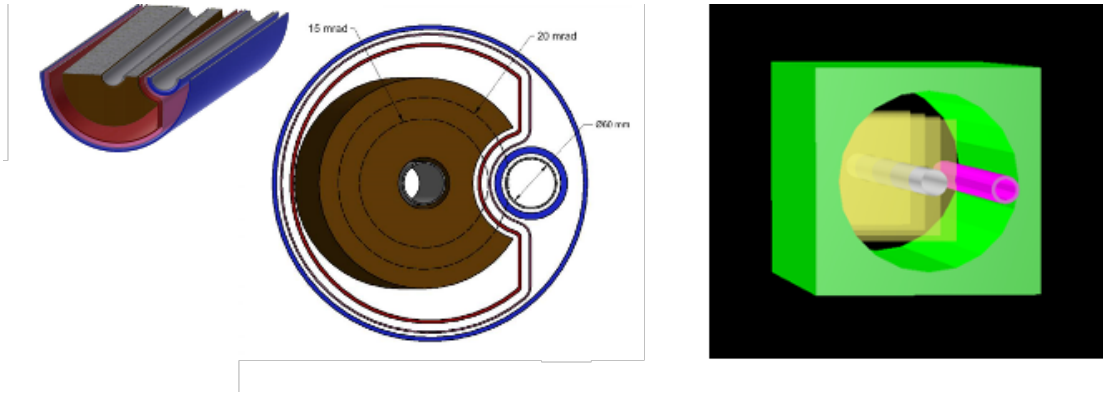

Figure 11.81: Conceptual drawings of the B0pf magnet showing the hadron and electron beam pipes going through the B0pf magnet bore (left side) and a basic set of silicon planes implemented in the EicRoot GEANT4 simulations (right side). Some other studies have assumed more conservative placement and shape of sensors, and this is still to be optimized and decided by a more mature design.

11.6.4.2 Silicon Sensors for B0-tracker

To meet the radiation tolerance, spatial and timing resolutions in this kinematic region, several silicon sensor candidates are considered.

One candidate is the Low Gain Avalanche Detector (LGAD) which has better than 30 ps timing resolution. Technical details are described in the previous chapter. Another top candidate is the radiation hard Monolithic Active Pixel Sensor technique: MALTA [20,21]. This technique utilize the Depleted Monolithic Active Pixel Sensor (or High Voltage Monolithic Active Pixel Sensor) to meet high granularity, low cost

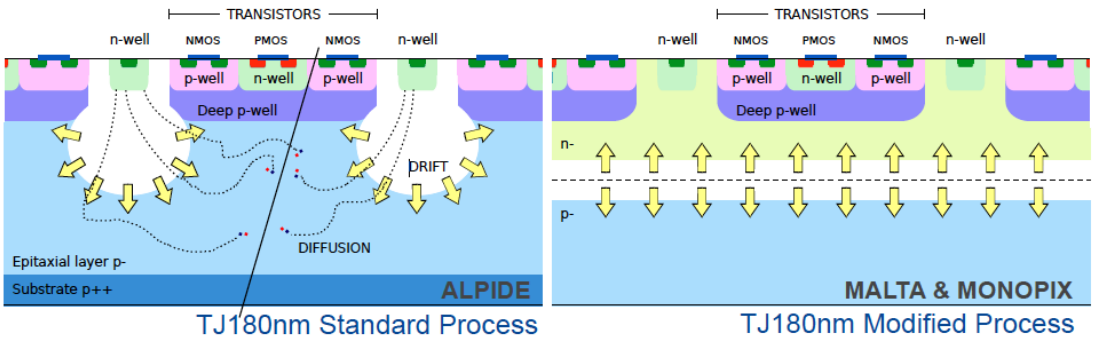

Figure 11.82: Comparison on charge ionization process between a normal Tower Jazz 180 nm Monolithic Active Pixel Sensor (left panel) and a depleted Tower Jazz 180 nm Monolithic Active Pixel Sensor (right panel). the Figure from H. Pernegger presentation in the HSTD2019 Hiroshima conference.

and low material budgets. The existing MALTA sensors based on the Tower Jazz 180 nm design, contain 36.4μm by 36.4μm pixels with the average silicon thickness at around 300 μm. Faster readout speed has been achieved for the MALTA sensor due to the charge ionization process is depleted (see Figure 11.82. High radiation tolerance ($> 10^{15} n_{eq}/cm^2$) has been demonstrated at shaping time at 25 ns [148]. Please see Table11.27 for the summarized performance of the LGAD and the MALTA technique. Ongoing R&D for different silicon sensor techniques will improve their radiation tolerance, achieve better timing and finer spatial resolution and get low material budgets.

Parameter	**LGAD or AC-LGAD**	**MALTA**
Technique	Low Gain Avalanche Diode	180 nm Tower Jazz HV-MAPS
Pixel size	current 1.3 mm×1.3 mm towards 100 μm × 100 μm	36.4 μm × 36.4 μm
Integration time	< 100 ps	< 5 ns
Thickness per layer	$< 1\% X_0$	$< 0.5\% X_0$
Radiation tolerance	$\sim 10^{14} n_{eq}/$ cm^2	$> 10^{15} n_{eq}/$cm^2

Table 11.27: Comparison of the LGAD and MALTA sensor performance

Some things that will need to be considered for the future design of the B0 detector system are listed below.

- Radiation background (in particular a synchrotron radiation and a radiation coming from the primary collisions) in the proposed very forward pseudorapidity region.
- The need for higher resolution sensors for reconstruction compared to the Roman Pots (pixels size ~50μm)
- Available space in bore for sensors, support structure, and cabling.

11.6.4.3 Pre-shower or EMCAL in the B0 spectrometer

In order to provide a detection of low-energy photons and to provide a coverage in the transition area between central detector and ZDC calorimeters, a pre-shower detector or electro-magnetic calorimeter might be considered in this area. Taking into account a limited amount of available along a Z-axis, and difficulties with integration a pre-shower might be a better option.

11.6.4.4 Summary of the Current Design Constraints

For the current design 26x27cm^2 planes were used with 50x50μm^2 pitch size. At least 4 layers will be needed, as a combination of high granularity and fast-timing detectors, to provide proper charged particle detection/tracking, momentum reconstruction and to deal with the high-background expected in this area.

11.6.5 Zero-Degree Calorimeter (ZDC)

11.6.5.1 Basic requirements for the ZDC

The Zero Degree Calorimeter (ZDC) will serve critical roles for a number of important physics topics at EIC, such as distinguishing between coherent diffractive scattering in which the nucleus remains intact, and incoherent scattering in which the nucleus breaks up; measuring geometry of $e + A$ collisions, spectator tagging in $e + d/^3He$, asymmetries of leading baryons, and spectroscopy. These physics goals require that the ZDCs have high efficiency for neutrons and for low-energy photons, excellent energy, p_T and position resolutions, large acceptance and sufficient radiation hardness.

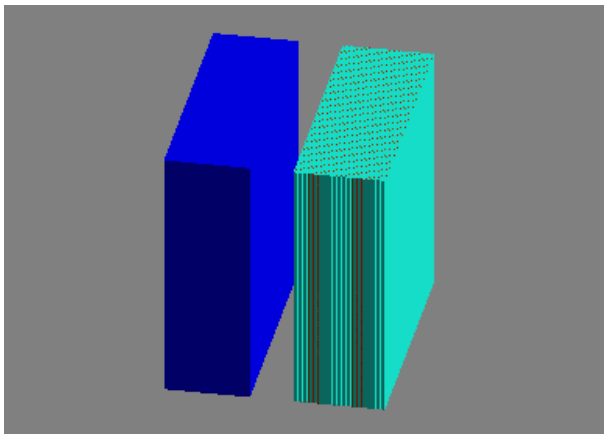

Figure 11.83: The schematic ZDC in Geant4 simulation.

The ZDC schematic plot is shown in Fig. 11.83. A 10 cm lead tungstate absorber is placed in front of 20 layers ALICE FoCal. Figure 11.84 shows events display for a 20 GeV neutron and a 500 MeV photon interacting with the ZDC.

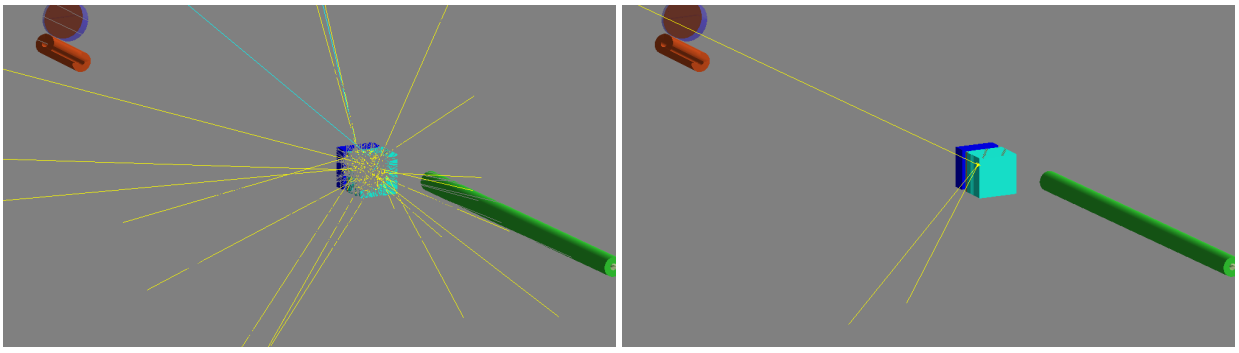

(a) ZDC 20 GeV neutron event display.

(b) ZDC 500 MeV photon event display

Figure 11.84: Event displays for (Left) a 20 GeV neutron and (Right) a 500 MeV photon interacting with the ZDC.

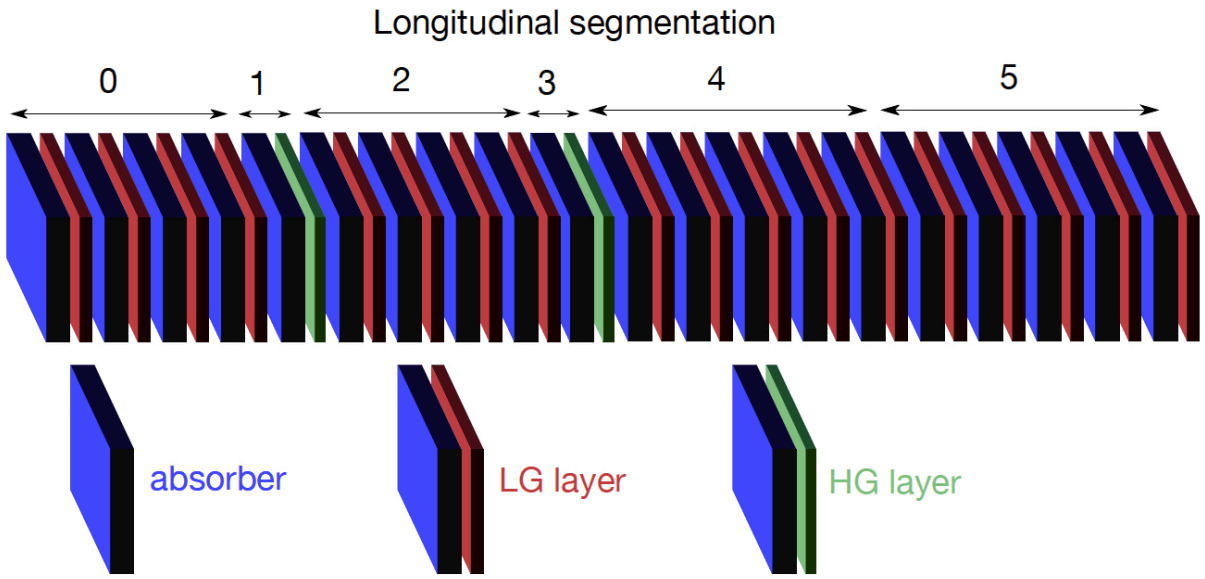

Figure 11.85: Schematic of the FoCal electromagnetic calorimeter. The blue absorber is tungsten, the red low granularity silicon layers are used for energy measurement while the green high granularity layers give precise position information [149].

11.6.5.2 EMCAL technologies for ZDC

There are several possible approaches to achieve high energy and position resolution in an electromagnetic calorimeter. As an example, the ALICE FoCal [149], is silicon-tungsten (Si+W) sampling calorimeter with longitudinal segmentation. Low granularity layers are used for the energy measurement while higher granularity layers provide accurate position information. A schematic of FoCal is shown in Fig. 11.85.

From simulations the photon energy resolution for FoCal is estimated to be $\sigma_E = 25\%/\sqrt{E} \oplus 2\%$. This is comparable to that expected for the sPHENIX W/SciFi calorimeter. Other technologies that would provide suitable resolution include crystals ($PbWO_4$, LYSO, GSO, LSO), DSB:Ce glass, and W/SciFi. $PbWO_4$ crystals and DSB:Ce glass have been developed and characterized by the eRD1 Consortium and the Neutral Particle Spectrometer project at Jefferson Lab. Tests have shown energy resolutions of $\sim 2\%/\sqrt{E}$ for photon energies $\sim$ 4 GeV [150]. The orbiting Fermi Gamma Ray Telescope uses a CsI crystal array and tracker to achieve very high spatial and energy resolution [151].

11.6.5.3 HCAL technologies for ZDC

The hadronic part of the ZDC is needed for neutron identification. An energy resolution of $\sigma_E < 50\%/\sqrt{E}$ with an angular resolution of at least 3 mrad / $\sqrt{E}$ is desired, especially for tagging spectator neutrons from light nuclei. Cerenkov calorimeters, which measure only the high energy component of the showers, give excellent position resolution and tight containment but are non-compensating and so somewhat non-linear. Sampling all charged particles produced gives better energy resolution at the cost of worse lateral containment. We seek to exploit both techniques to maximize both the energy and position resolution of the ZDC. This could be done by using the quartz fibers developed for the LHC ZDCs, [152], with traditional

scintillators.

11.6.5.4 Soft photon detection

In order to detect coherent collisions it is necessary to veto events in which soft photons are emmitted from an excited nucleus In general, the photon decay chain of a heavy nucleus is dominated by photons of energy of the order of 10 KeV. These photons may be indistinguishable from background. However, for a doubly magic nucleus such as ^{208}Pb, every bound-state decay sequence has at least one photon with an energy of at least 2.6 MeV. After accounting for the boost of the nucleus with momentum 275 GeV/c, 20% of these decay photons (with minimum energy 455 MeV) are detectable in the ZDC aperture of ~ 4.5 mrad. In order to detect such photons from nuclear excitation it is important that the ZDC have the largest possible aperture. It is possible that a 2nd IR design will allow a larger ZDC acceptance. Resolving nuclear decay photons from background will require a full absorption EM calorimeter with excellent energy resolution, e.g. made with crystal scintillator (LYSO, PWO, ...).

11.6.5.5 Scintillator Tracker Detector

The meson structure research for the EIC has shown the need of a tracker, in combination with the ZDC, to be used as a veto detector for π^- for an efficient measurement of the $\Lambda \rightarrow n + \pi^0$ channel (Section XXX Meson Structure WG). Besides this main purpose, adding a tracker could improve the reconstruction of charged particles in the ZDC for other different channels. A non-expensive and feasible option is the use of scintillating fibers (SciFi) as a tracker detector.

SciFi trackers combine the fast response of scintillator detectors with the flexibility and granularity that fibers can provide. A high efficiency fiber is made of a core of polystyrene-based scintillator surrounded by a cladding of PMMA, and some fibers by another cladding of fluorinated PMMA. A SciFi tracker can handle high rates and is highly tolerant to radiation [153], but in the other hand, the photon yield is quite low due to the small photon capture fraction, about 5% for the double cladding fibers[2]. Detection efficiency is increased adding extra fiber layers (Fig.11.86). Scintillating light can be read-out by several pixel devices like Avalanche Photo-diodes, Silicon photo-multipliers or multi-anode photo-multipliers. A SciFi tracker with a layout as figure 11.86 can achieve a spatial resolution of $\approx$ 300 μm and a time resolution of $\approx$ 500 – 220 ps [154] [155], but different fiber diameter and overlap between channels results in similar spatial resolutions [156].

11.6.5.6 Sumamry of the current design

The number of spectator neutrons is predicted to have somewhat correlation with the collision geometry. The required performance of the detector to identify the coherence of the collision is under development using the BeAGLE simulation [157]. Some of performance parameters are under ongoing study. The optimization of the performance requirements is included in the scope of the development based on the requirements known as of now as listed below.

[2] one side output of the fiber

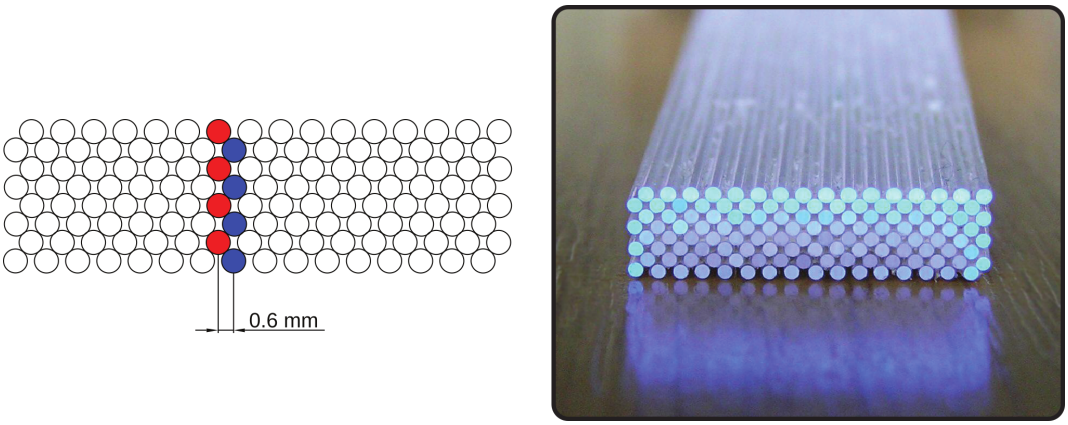

Figure 11.86: (Left) Schematic layout of a 4 layers SciFi bundle showing, in red and blue, two corresponding read-out channels for particles coming in the vertical direction. (Right) Picture of an assembled 4 layers, 32 channels SciFi bundle.

Acceptance A large acceptance (e.g. 60×60 cm^2) to establish good identification efficiency between coherent and incoherent collisions is necessary for vetoing spectator neutrons from nuclear breakup. This large acceptance is also required to determine the collision geometry [158] . For studying very forward production and asymmetry of hadrons and photons, a large acceptance is also important. The EIC aperture of ±4 mrad gives $p_T < 1\text{GeV}/c$ coverage for 275 GeV hadrons and photons, which covers the transition from elastic/diffraction to incoherent regime; for low-energy hadron beam the acceptance in terms of p_T is more limited e.g. $p_T < 0.4\text{GeV}/c$ coverage for 100 GeV beam.

Energy, position, and p_T resolutions Due to the strong β squeeze < 1 meter for the high luminosity, a beam spread of ∼20 MeV and ∼1 cm of the hadron beam angular divergence is induced. Thus the position resolution of neutron in sub cm won't help. 1 cm position resolution provides 300 μrad angular resolution, which can be translated to transverse momentum resolution $p_{\mathrm{T}} \sim 30$ MeV/c of 100 GeV spectator neutron.

The minimum energy resolution $\Delta E/E \sim 50\%/\sqrt{E(GeV)}$ to distinguish number of spectator neutrons from 20 to 30 for collision geometry determination. In order to accommodate a single MIP track to 30 spectator neutrons, wide dynamic energy range in the readout electronics is required.

It is anticipated to be a sampling type calorimeter with a sufficient longitudinal size of ∼10 interaction length [158]. It is also required to have a sufficient transverse size of ∼2 interaction length to avoid transverse leakage of the hadron shower and to achieve good hadron energy resolution.

11.6.6 Integration with accelerator

11.6.6.1 Beam parameters and lattice

The integration of Far-forward detector components with accelerator plays an important role for emerging EIC physic program. It is important to start at it at the earliest stage of the design, since it could have an impact on both parties: it could affect accelerator impedance, or, on the other hand, incorrect placement of accelerator elements could have an impact on the detector acceptance by blocking or obscuring incident

particles. The current studies were done with the accelerator lattices described in the Table(11.28 for an ion beam and Table(11.29 for an electron beam. Note, that sets of the quadrupoles will be placed in the common cryostat volume, therefore there will be no possibility to place any detecting elements there.

Name	Type	L [m]	R_{in} [m]	R_{out} [m]	Dipole [T]	Quadrupole [T/m]	X_c [m]	Y_c [m]	Z_c [m]	$Theta_c$ [rad]
Rear elements										
iYI6_HB2	SBEND	5.69	0.05	0.3	0 / -4.64	0	-1.18	0	-48.96	0.011
iYI6_HQ3	QUAD	1.2	0.05	0.3	0 / 0	47.8	-0.52	0	-20.7	0.025
iYI6_HQ2	QUAD	2.57	0.05	0.3	0 / 0	47.1	-0.323	0	-12.9	0.025
iYI6_HQ1	QUAD	3.42	0.05	0.3	0 / 0	-67.45	-0.2046	0	-8.18	0.025
Forward elements										
iB0PF	SBEND	1.2	0.2	0.5	0/-1.3	0	0.148	0	5.9	0.0259
iB0APF	SBEND	0.6	0.043	0.256	0/-3.47	0	0.2	0	7.7	0.0278
iQ1APF	QUAD	1.46	0.056	0.28	0/0	-72.61	0.24	0	9.23	0.0289
iQ1BPF	QUAD	1.61	0.078	0.34	0/0	-66.18	0.293	0	11.06	0.0289
iQ2PF	QUAD	3.8	0.131	0.58	0/0	39.45	0.383	0	14.16	0.0289
iB1PF	SBEND	2.99	0.135	0.5	0/-3.79	0	0.505	0	18.06	0.035
iB1APF	SBEND	1.5	0.168	0.4	0 /-2.70	0	0.6113	0	20.81	0.0436
iB2APF	SBEND	5.7	0.05	0.3	0 /6.00	0	1.5221	0	41.890	0.02713

Table 11.28: Ion beam lattice for 275 GeV

11.6.6.2 Beam pipe, vacuum, background

At this point we do not have a mature engineering design of the beampipe in the far-forward area. In this section we just formulate some requirements for it.

One of the important areas to pay attention an the material budget while designing the beampipe is the B0-dipole location. First of all we have to minimize amount of material at the exit window - this will be the area where common conical shape of the beampipe transfer to the two separate beampipes for the incoming electron and outgoing ion beams. Vacuum pumps, in front of the B0 dipole will be the sources of the background, where incident particles could start to develop showers, increasing an occupancy in the B0-tracker. Also shower-tails from the central detector HCAL or cryo-module around the B0- dipole could potentially give an additional source of background for the B0-tracker.

The exit window of the beampipe for Zero Degree Calorimeter needs to be properly designed, due to impact on the detection efficiency for low- energy photons in the forward direction.

Also the beampipe material around the off-momentum detectors needs to be minimized in order to minimize impact on the momentum resolution due to the multiple scattering.

The second vacuum chamber for the movable Roman-Pot sensors needs to be developed and impact on the accelerator impedance needs to be evaluated and minimized. In order to protect sensors from incident beam

Name	Type	L [m]	R_{in} [m]	R_{out} [m]	Dipole [T]	Quadrupole [T/m]	X_c [m]	Y_c [m]	Z_c [m]	$Theta_c$ [rad]
Rear elements										
eQ5ER	QUAD	1.2	0.05	0.3	0/0	7.481	0.4131	0	-46.8267	0
eQ4ER	QUAD	0.6	0.05	0.3	0/0	8.85796	0.4131	0	-37.99667	0
eDB3ER	RBEND	5.199	0.05	0.3	0/0.2115 0		0.39525	0	-34.79671	-0.00916
eQ3ER	QUAD	0.6	0.05	0.3	0/0	-22.7971	0.354	0	-31.597	-0.01832
eDB2ER	RBEND	5.5	0.05	0.3	0/-0.1999	0	0.01889	0	-12.249	-0.00916
eQ2ER	QUAD	1.4	0.05	0.3	0/0	14.1466	0	0	-8.3	0
eQ1ER	QUAD	1.8	0.05	0.3	0/0	-14.478	0	0	-6.2	0
Forward elements										
eQ0EF	QUAD	1.2	0.0031	0.007	0/0	-13.54	0	0	5.9	0
eQ1EF	QUAD	1.61	0.05	0.3	0/0	7.4612	0	0	11.065	0
eQ2EF	QUAD	3.8	0.05	0.3	0/0	0	0	0	14.17	0
eQ3EF	QUAD	1.2	0.05	0.3	0/0	-5.5461	0	0	20.82	0
eQ4EF	QUAD	1.2	0.05	0.3	0/0	5.85445	0	0	29.95	0

Table 11.29: Electron beam lattice for 18 GeV

losses, a proper collimation scheme needs to be designed together with a beam-loss monitor system.

At the backward direction a proper collimating scheme against the synchrotron radiation needs further development to protect low-Q2 tagger. The beampipe material needs to be optimized to minimize impact on the multiple scattering in this area.

An exit window for the bremsstrahlung photons is needed for the luminosity monitor.

11.6.7 Physics impact

11.6.7.1 Simulation Details

The simulations presented for the far-forward region of the IR were carried out using Geant4 implemented in either EicRoot or ESCalate. The simulations include the most-recently available layout of the IR magnets and engineering components (e.g. beampipe) and additionally include beam effects such as the smearing of the vertex due to rotation of the bunch by the crab cavity and beam angular divergence, unless noted otherwise for a particular study (e.g. studies of acceptance only). The parameters for the various beam effects can be found in the pre-CDR.

11.6.7.2 Deeply Virtual Compton Scattering (DVCS)

The initial proton is scattered by very small angles (~ few mrads), and therefore is within the far-forward acceptance - specifically in the Roman Pots or the B0 spectrometer. Using only the tagged final-state proton,

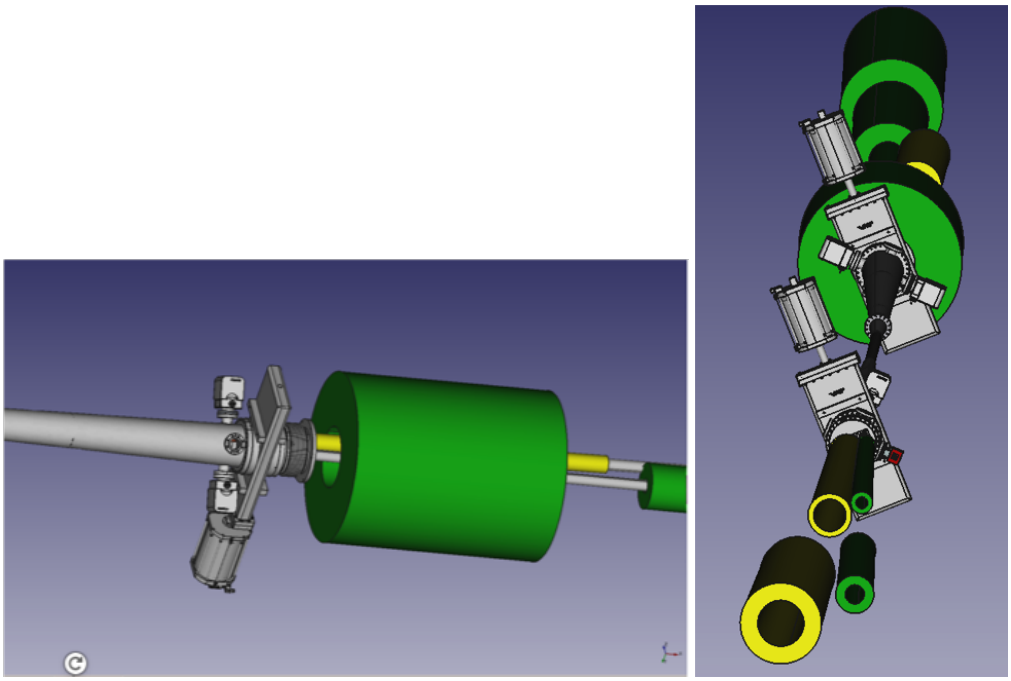

Figure 11.87: Beampipe at the B0 location

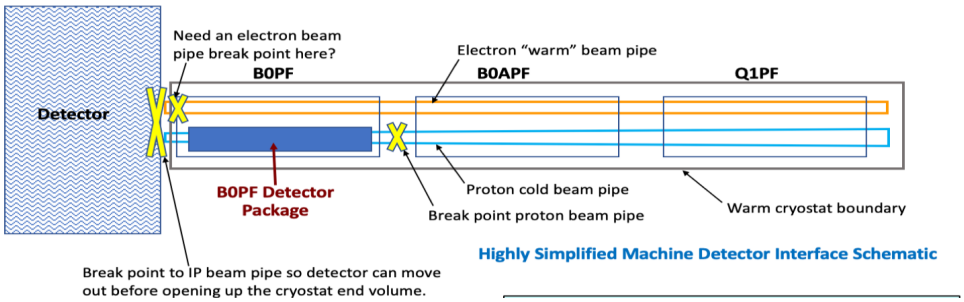

Figure 11.88: The integration of B0-dipole

one has access to the momentum transfer, t, in the interaction. The precise measurement of this t-distribution yields access to the impact parameter distribution related to the gluon GPD.

This simulation study was carried out using the MILOU MC generator to produce the simulated DVCS events, which were then passed through EicRoot and GEANT4 to simulate detector responses. These full simulations were then used to evaluate the DVCS proton acceptance and detector smearing. The study was conducted using three beam energy combinations, and included all of the smearing effects noted in Sec. 11.6.7.1. Fig. 11.89 shows the p_T-acceptance for the three different beam energy configurations.

The acceptance is driven by the aperture size (affected high p_T acceptance) and the beam optics choice, which determines the transverse beam size at the Roman Pots location, and provides the low pT acceptance cutoff. Fig. 11.90 shows the impact of the optics choices for the 10σ safe distance for two different beam energies.

Another important conclusion to be drawn from these acceptance plots is the need for a large active sensor

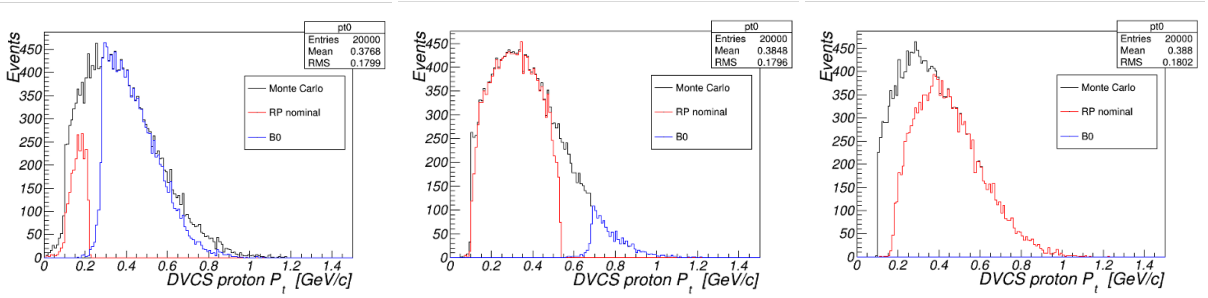

Figure 11.89: p_T acceptance for three different beam energy configurations: 5x41 GeV (left), 10x100 GeV (middle), 18x275 GeV (right). The black data in each figure represent the MC information from MILOU, the red data are the accepted particles in the Roman Pots, and the blue are particle accepted in the B0 sensors.

area to maximize the high-p_T acceptance. Fig. 11.90 implies the need for sensors to cover an active area of approximately 25cm $\times$ 10cm.

These simulations also included the effects of angular divergences, crab cavity rotation (which effectively smears the primary vertex), and detector reconstruction smearing. Table 11.30 summarizes the smearing contributions from this study. Based on this study and discussions ongoing in the EIC R&D effort, a 500 μm x 500 μm pixel size gives the necessary resolution while still keeping the cost and design constraints reasonable.

Δp_T	Ang. Div. (HD)	Ang. Div. (HA)	Crab Cavity	250 um	500 um	1.3 mm
18×275 GeV	40	28	20	6	11	26
10×100 GeV	22	11	9	9	11	16
5×41 GeV	14	-	10	9	10	12

Table 11.30: Summary of smearing contributions from angular divergence, crab cavity rotation, various pixel size choices (for the Roman Pots).

11.6.7.3 Spectator Tagging in e+D Interactions

In diffractive e+D interactions, either the proton or the neutron acts as a spectator, while the other nucleon is active. For this study, only the p+n final state for each spectator case was considered. The major difference here in proton detection is due to the proton having a different magnetic rigidity compared to the deuteron beam, requiring use of the off-momentum detector system for tagging these breakup protons.

Figs. 11.91 and 11.92 show the kinematic acceptances for the protons in neutrons for their respective spectator/active categories.

Figs. 11.93 and 11.94 show the kinematic acceptances for the protons in neutrons for their respective spectator/active categories.

From these figures it is clear that when a particle acts as a spectator, its acceptance is optimized because it's distribution of scattering angles is smaller. For the neutrons, this helps your acceptance because the aperture size limits your neutron acceptance to < 5 mrad. For the protons, larger scattering angles are okay in the case of angles > 5 mrad, since many of these enter the acceptance of the B0 spectrometer. However, the

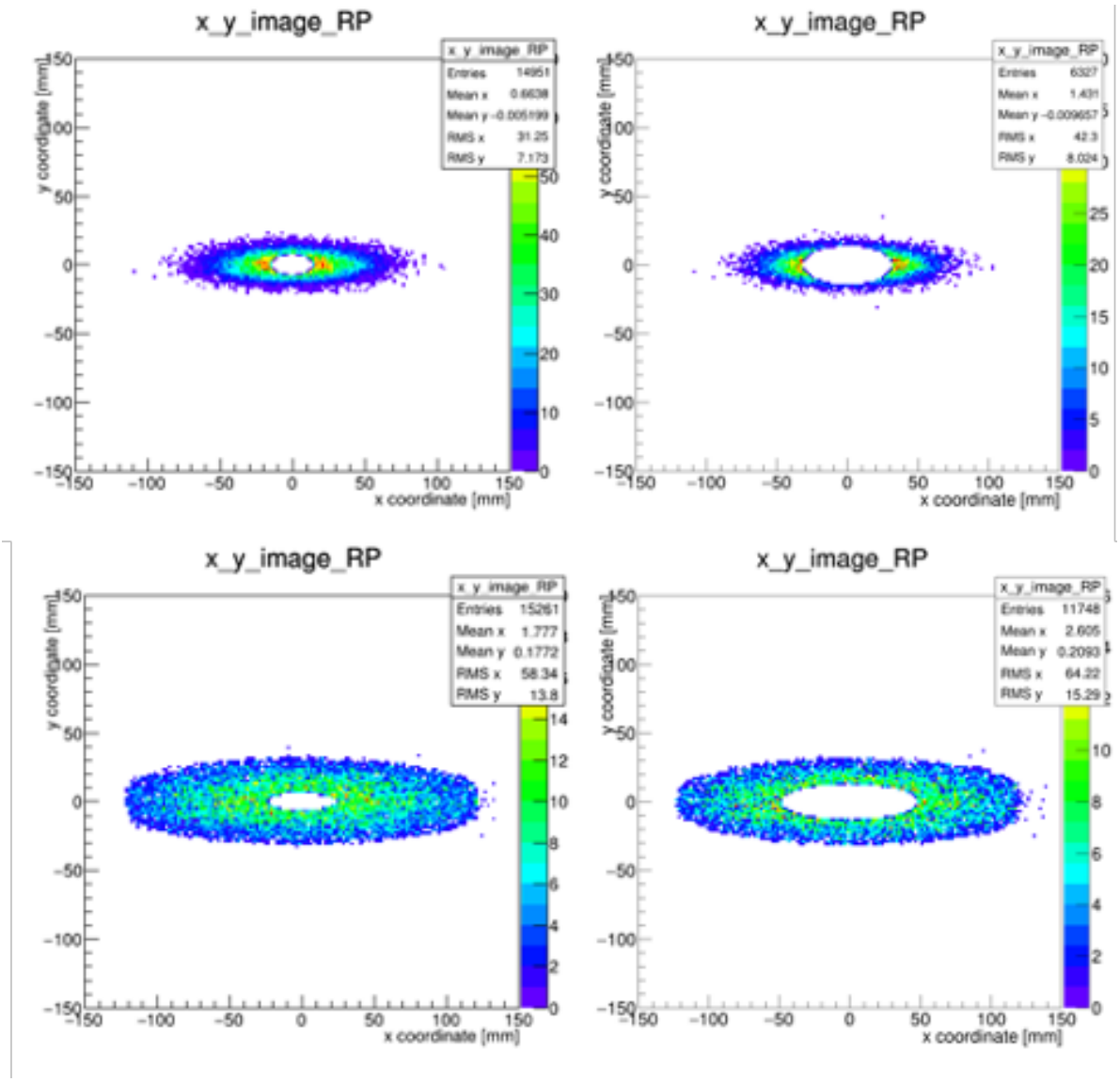

Figure 11.90: Acceptance images for protons incident on the first Roman Pots sensor plane. The top row is for the 18x275 GeV beam energy configuration, with the left plot and right plot being the high acceptance and high divergence optics configurations, respectively. The bottom row is for the 10x100 GeV beam energy configuration. Note the decrease in the size of the 10σ region (iris in the center of the plots) when we use the high acceptance optics, with left and right plots being the high acceptance and high divergence optics configurations, respectively. As noted previously, the trade off for more acceptance is a drop in luminosity at the IP.

larger spread in momenta imparted to the protons in the neutron spectator cases causes many protons to be lost in the lattice before making it to the off-momentum detectors.

In addition to the acceptances, the resolutions were studied in detail, and their effect on various physics observables evaluated. These results can be found in [159].

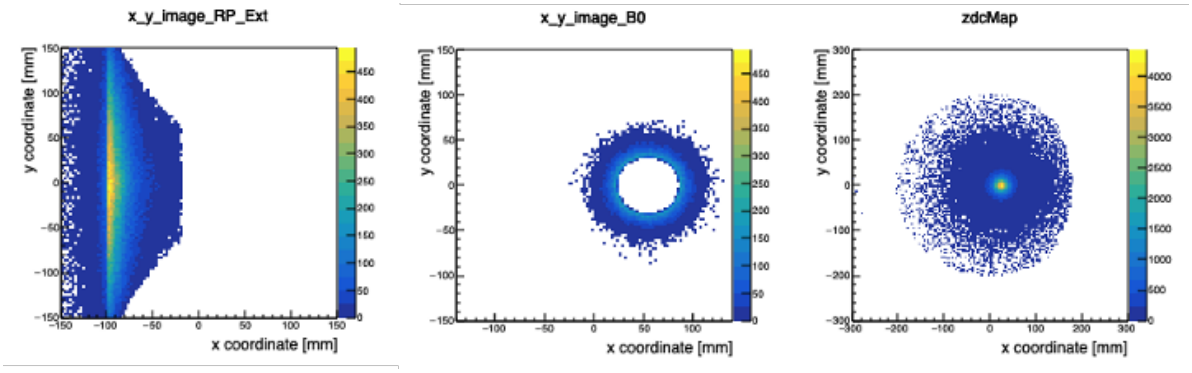

Figure 11.91: Acceptance images for protons and neutrons in the case where the neutron acts as a spectator. In this case, the protons have a larger range of scattering angles, and detection requires both the off-momentum detectors and the B0 detector. The plots show the protons incident on the off-momentum detectors (left), the B0 detector (middle), and the neutrons incident on the ZDC (right). All coordinates are local to the sensor plane.

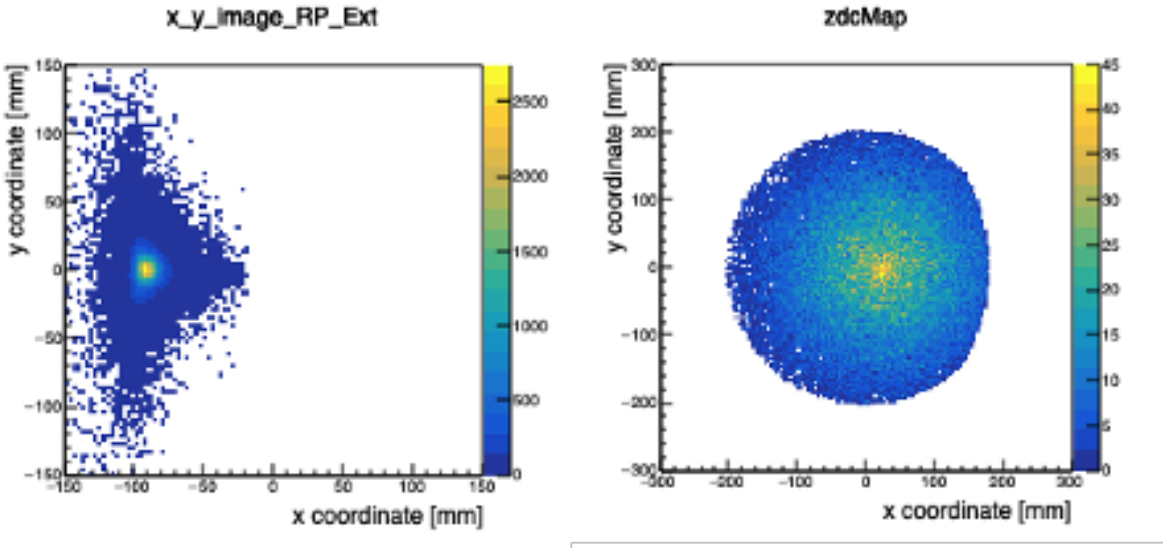

Figure 11.92: Acceptance images for protons and neutrons in the case where the proton acts as a spectator. The plots show the protons incident on the off-momentum detectors (left), and the neutrons incident on the ZDC (right). All coordinates are local to the sensor plane.

11.6.7.4 Spectator Proton and Neutron Tagging in e+^{3}He and e+^{3}H Collisions

Studying short-range correlations (SRC) and the polarized neutron structure can be accomplished by studying e+^{3}He (e+^{3}H) collision events in which the neutron (proton) is the active nucleon in the collision and the protons (neutrons) act as spectators. In order to do this type of study, the prospects of tagging both spectator protons or neutrons in the far-forward region needs to be assessed. A full-simulation study was carried out to this end using e+^{3}He DIS events from BeAGLE, as well as SRC events using a spectral function approach. These two paradigms allow for the study of the double-tagging of the final state spectator protons in two very different kinematic regimes. In the DIS case, the two protons end up with very similar final state kinematics, while in the SRC case, one of the protons is in an SRC pair with the active neutron and

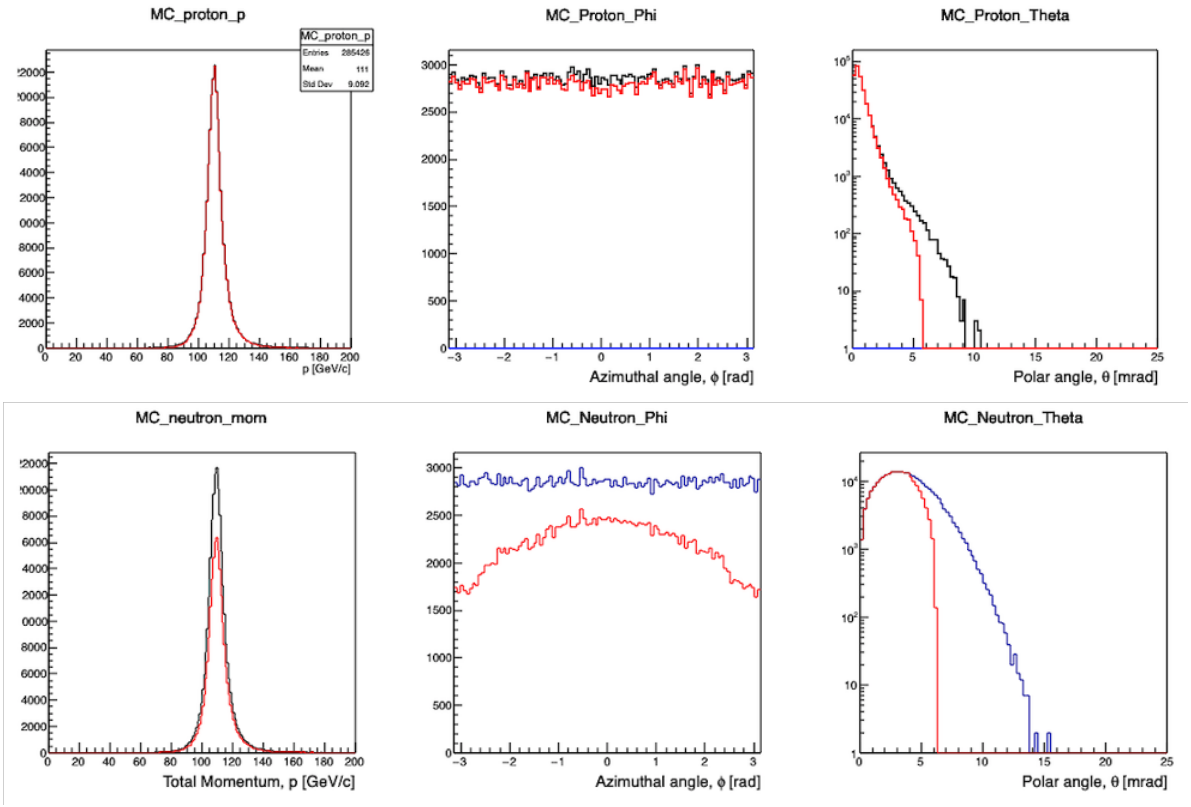

Figure 11.93: 3-momentum p, azimuthal angle (ϕ), and polar angle (θ) acceptance for protons (top) and neutrons (bottom) for the proton spectator case. The blue lines are from the BeAGLE MC, and the red are the accepted particles.

therefore has a very different initial p_T distribution than the other spectator proton. Fig. 11.95 shows the occupancy of protons incident on the various detector subsystems. These plots show the repeated need for multiple subsystems to cover the acceptance, as well as the need for a large active area for the Roman Pots subsystem. Fig. 11.95 only shows the lowest beam energy configuration since it is the most demanding on the acceptance.

Figs. 11.96 and 11.97 show the results of the study for two different energy configurations. The results indicate that the double-tagging efficiency for the spectator protons look very promising for the baseline interaction region, with most cases having a double-tagging efficiency above 85% (above 90% for the higher energy configuration), except for the lower energy SRC case which has an efficiency above 75%. Most of the losses in the double-tagging efficiency comes from a single proton being lost between the B0 detector and Roman Pots, or between the off-momentum detectors and Roman Pots. These acceptance gaps are to some point unavoidable do to the finite thickness of the beam pipe being the main driver of that gap between the detectors.

A study of the neutron double-tagging efficiency in e+^{3}H events was also carried out using fast simulations in eic-smear. The results indicate that the neutron double-tagging efficiency is also quite good, with most of the acceptance losses being in the SRC case when one of the neutrons has a larger scattering angle that may cause it to be lost in the 4.5 mrad aperture.

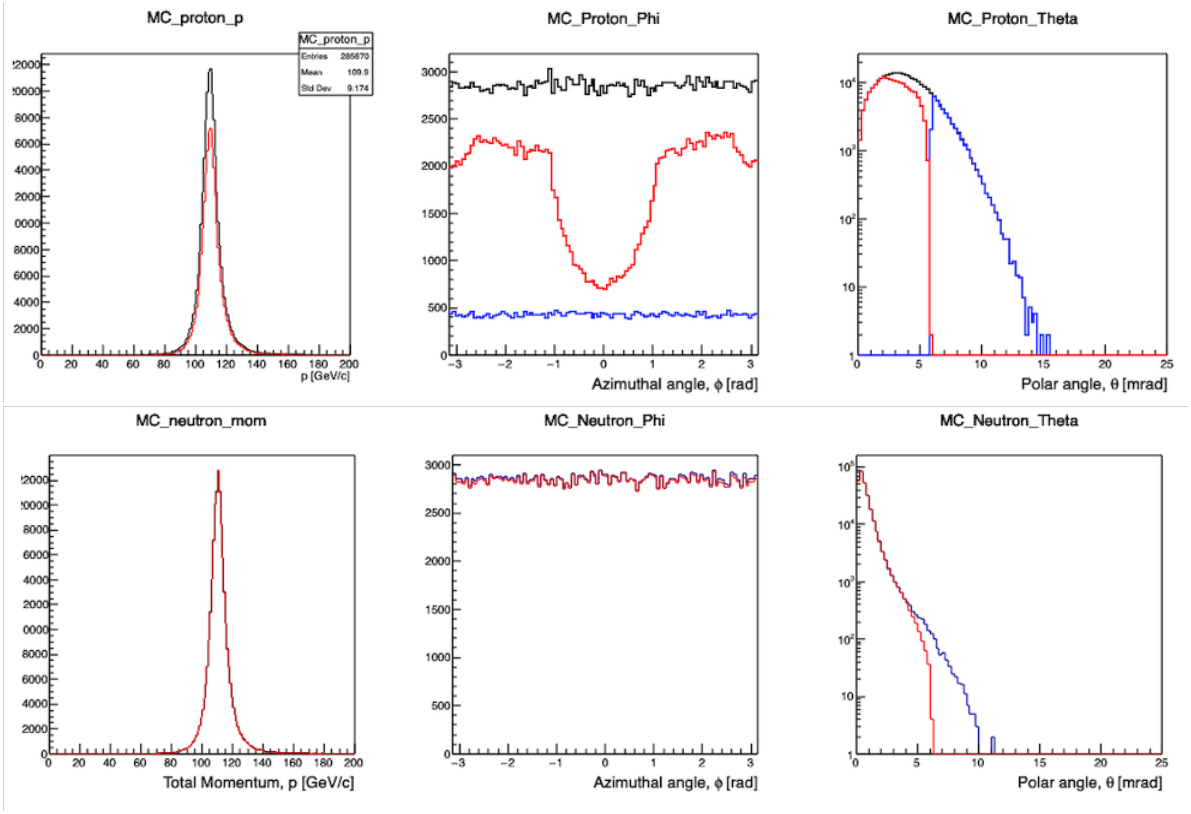

Figure 11.94: 3-momentum p, azimuthal angle (ϕ), and polar angle (θ) acceptance for protons (top) and neutrons (bottom) for the neutron spectator case. The blue lines are from the BeAGLE MC, and the red are the accepted particles.

11.6.7.5 Far-forward tagging ions

At the time of writing this document, no MC samples for light-nuclei tagging in the FF direction were available for validation in our simulation framework. However, based on the numerous other studies, some basic conclusions can be drawn. Light-ion tagging (e.g. ^{4}He) should have similar constraints as those seen for the tagging of protons in the FF direction (e.g. proton DVCS). The machine optics can be tuned similarly to maximize the low-p_T acceptance at the Roman Pots. From this, the main limitation will be the shape of the p_T distribution given by the coherent light nuclear scattering process. If the p_T distributions are similar as for the e+p case, than the acceptance of these light nuclei at the Roman Pots will also be similar. More studies should be carried out in the future to asses the impact of the various choices of machine optics on the FF light nuclei acceptance.

11.6.7.6 Meson Structure and FF Lambda Decay

The reconstruction of Lambda in the target fragmentation area is one of the most challenging tasks in the FF region of the IR. It comes from the fact that the decay vertex of such lambdas is spread by tens of meters along the Z-axis (along the beam-line) which makes detection of the decay products and mass reconstruction very difficult.

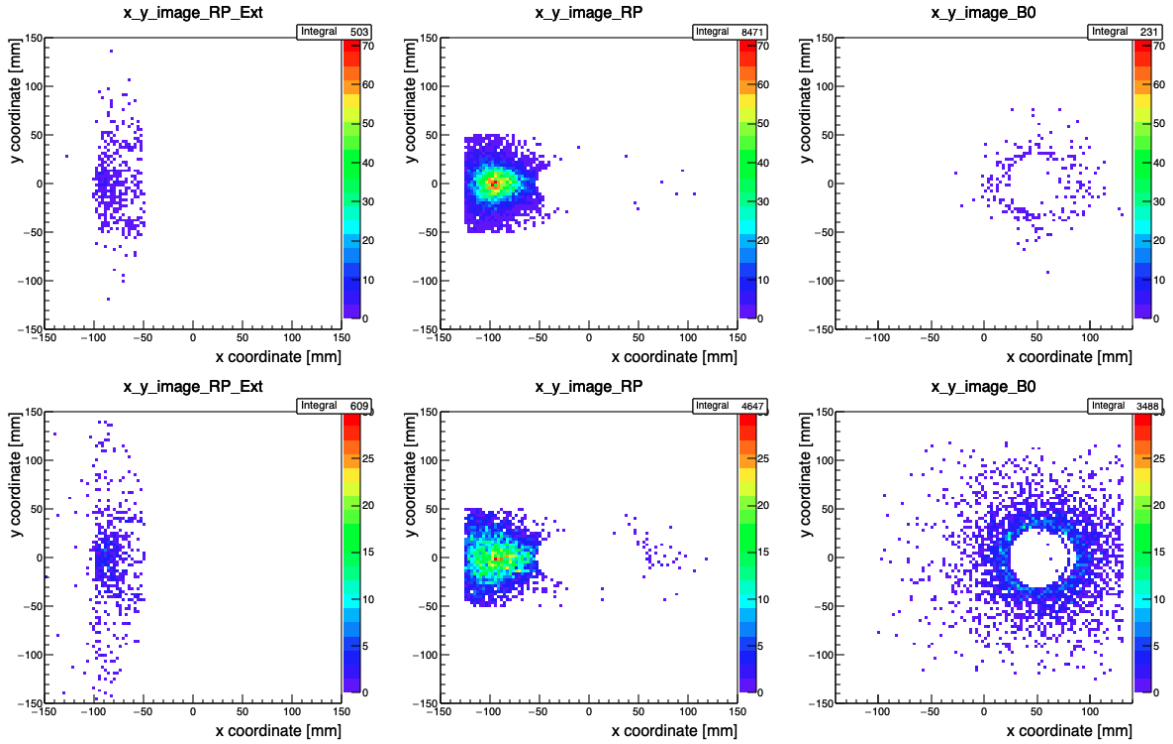

Figure 11.95: Occupancy plots of protons incident on the various FF detectors. The top row is 5x41 GeV BeAGLE DIS events, while the bottom row is 5x41 GeV SRC events. The left column is protons incident on the off-momentum detectors, the middle column is the Roman Pots, and the right column is the sum of the 4 individual planes of the B0 detector used in this simulation. All plots show the local coordinate system for the particular detector.

Occupancy plots for the beam energy setting of 5×41 GeV for pions and protons from Lambda decays is shown on Fig. 11.98. Since this is the lowest beam energy setting, most of the lambdas would decay in the first meter (before the B0 magnet), and the decay products of lambda are expected to have low momenta and larger theta. Therefore, as expected, protons coming from the Λ decays will mostly be detected, due to their lower rigidity, in the off-momentum detectors and partially in a B0 tracker, while the B0 tracker will be the only detecting element for pions (a). As one can also see from this Figure, the proton-beam-pipe aperture inside the B0-dipole plays an important role and sets the detection efficiency for pions. Also a full azimuthal angle ϕ-coverage of the detecting elements around the proton beam-pipe is important: outer radius of electron FFQ needs to be minimized to provide enough space for tracking detectors.

For another beam energy setting, for example 10 GeV×100 GeV (Fig. 11.99), one could clearly see, for charged pions, the "dead" area along the beamline, where the beam elements (focusing quadrupoles) are located. This comes from the fact that those pions have significantly lower momentum than the beam, and very small x_L, causing the pions to be lost in the lattice before they can be detected. It is also important to point out that negative charged particles (pions) will bend into opposite direction, compared to protons, as shown on the Fig. 11.80, therefore a proper coverage of off-momentum detectors would be required to to provide an efficient detection for those particles.

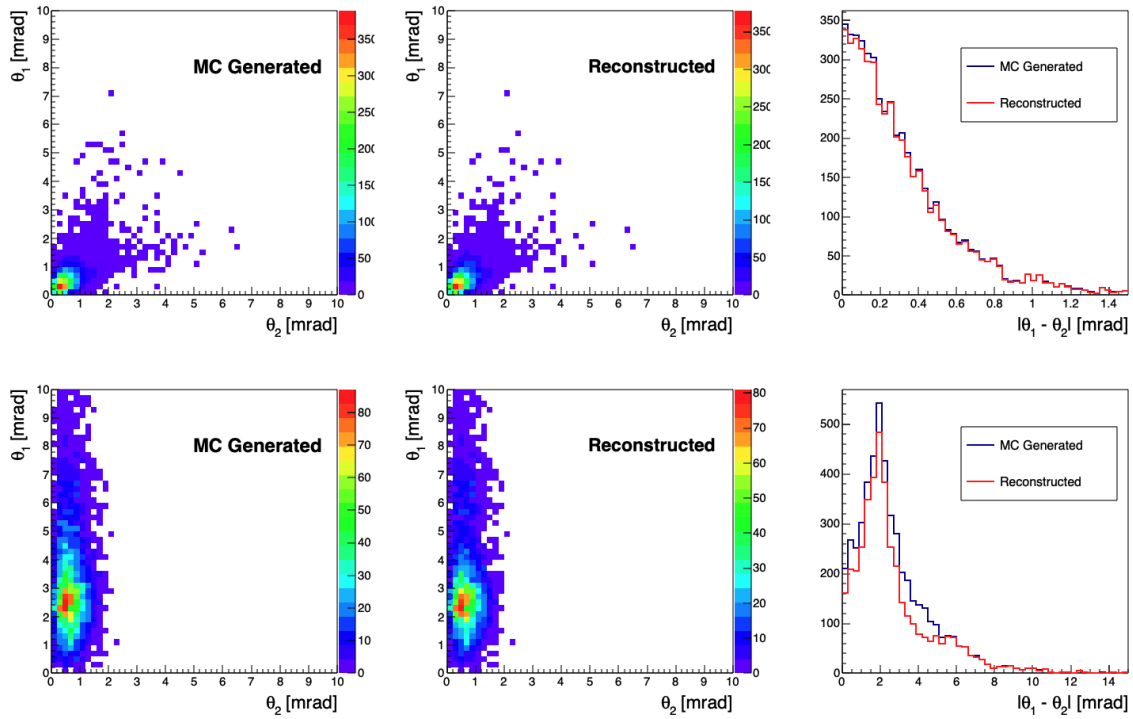

Figure 11.96: Scattering angle plots for spectator protons from e+^{3}He collisions using BeAGLE DIS events at 10x110 GeV (top row) and SRC events at 18x110 GeV (bottom row). The left panel in both rows shows the scattering angle of proton one vs. proton two from the MC generator, the middle plots shows what is reconstructed in the EicRoot GEANT simulation, and the right panel shows the absolute value of the difference between the angles, which tells us how close together they are when they arrive at the detector.

11.6.8 Conclusions

The far-forward region of the EIC baseline IR has been studied extensively throughout this entire Yellow Report process. The main conclusions from these studies are that several detector subsystems are needed to cover the entire far-forward region including Roman Pots, a high resolution zero-degree calorimeter, a silicon-based spectrometer in the first dipole magnet after the IP, and various planes of silicon on either side of the beam pipe after the B1apf dipole to capture charged particles with $x_L < 0.6$, so-called "off-momentum particles". The technology choices detailed in this chapter reflect the R&D efforts of numerous people and represent our recommendations to meet the needs of the FF physics programs at the EIC. As can be seen throughout the document, the IR design has undergone some revisions (especially the B0 magnet) that have led to different considerations for the detector geometry, as seen in the difference in the B0 coverage between the e+D study and the lambda study. These details are not yet final, and the different assumptions should make it clear what kinds of design difficulties could be faced in the B0 detector planning. As the IR design progresses and the community moves toward the formation of an experimental collaboration, more detailed simulations will need to be carried out in addition to what has been provided by these studies, and we hope these studies provide a strong foundation for validation of the future detector simulation and design efforts.

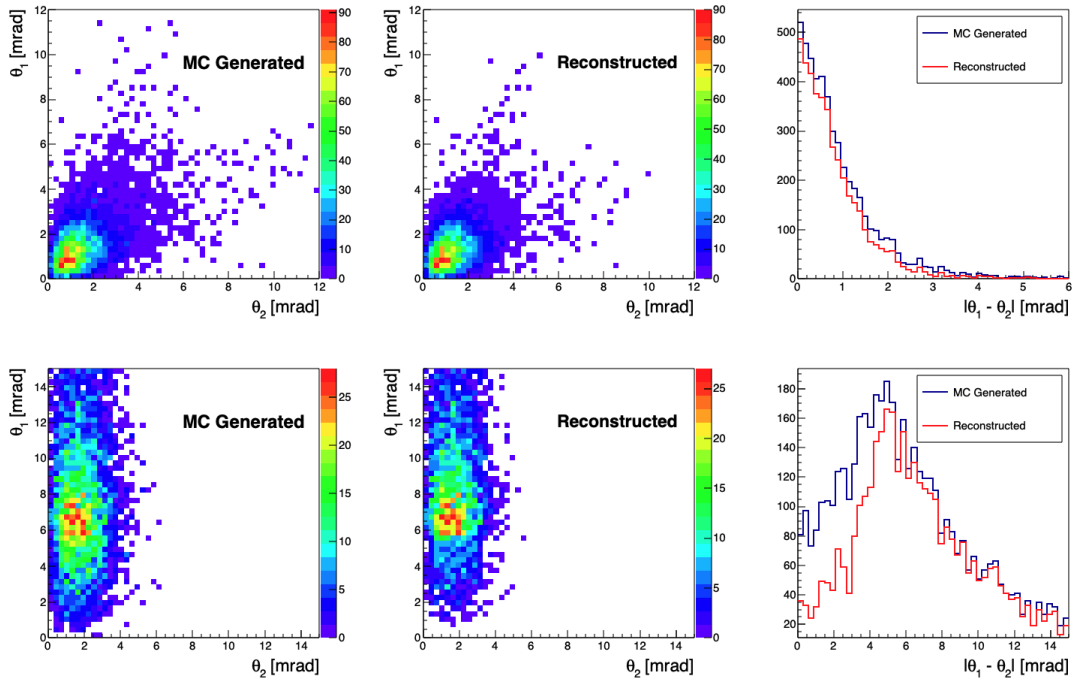

Figure 11.97: Scattering angle plots for spectator protons from e+^{3}He collisions at 5x41 GeV using BeAGLE DIS events (top row) and SRC events (bottom row). The left panel in both rows shows the scattering angle of proton one vs. proton two from the MC generator, the middle plots shows what is reconstructed in the EicRoot GEANT simulation, and the right panel shows the absolute value of the difference between the angles, which tells us how close together they are when they arrive at the detector.

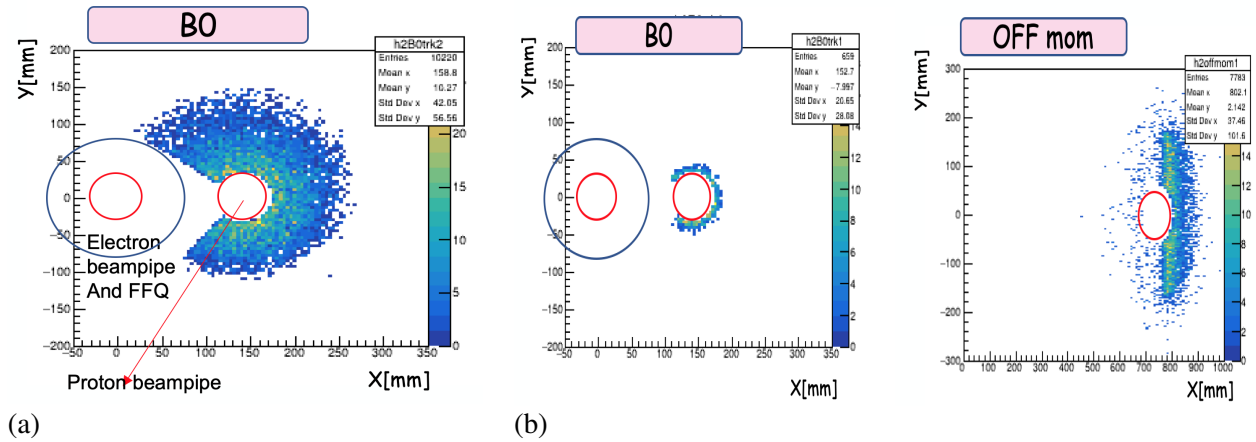

(a) (b)

Figure 11.98: Occupancy plots for energy setting 5x41 GeV (a) for π^- in B0 tracker (b) for protons in B0 and Off-Momentum detectors.The red circle shows the beampipe position and the blue circle shows electron FFQ aperture inside B0 dipole.

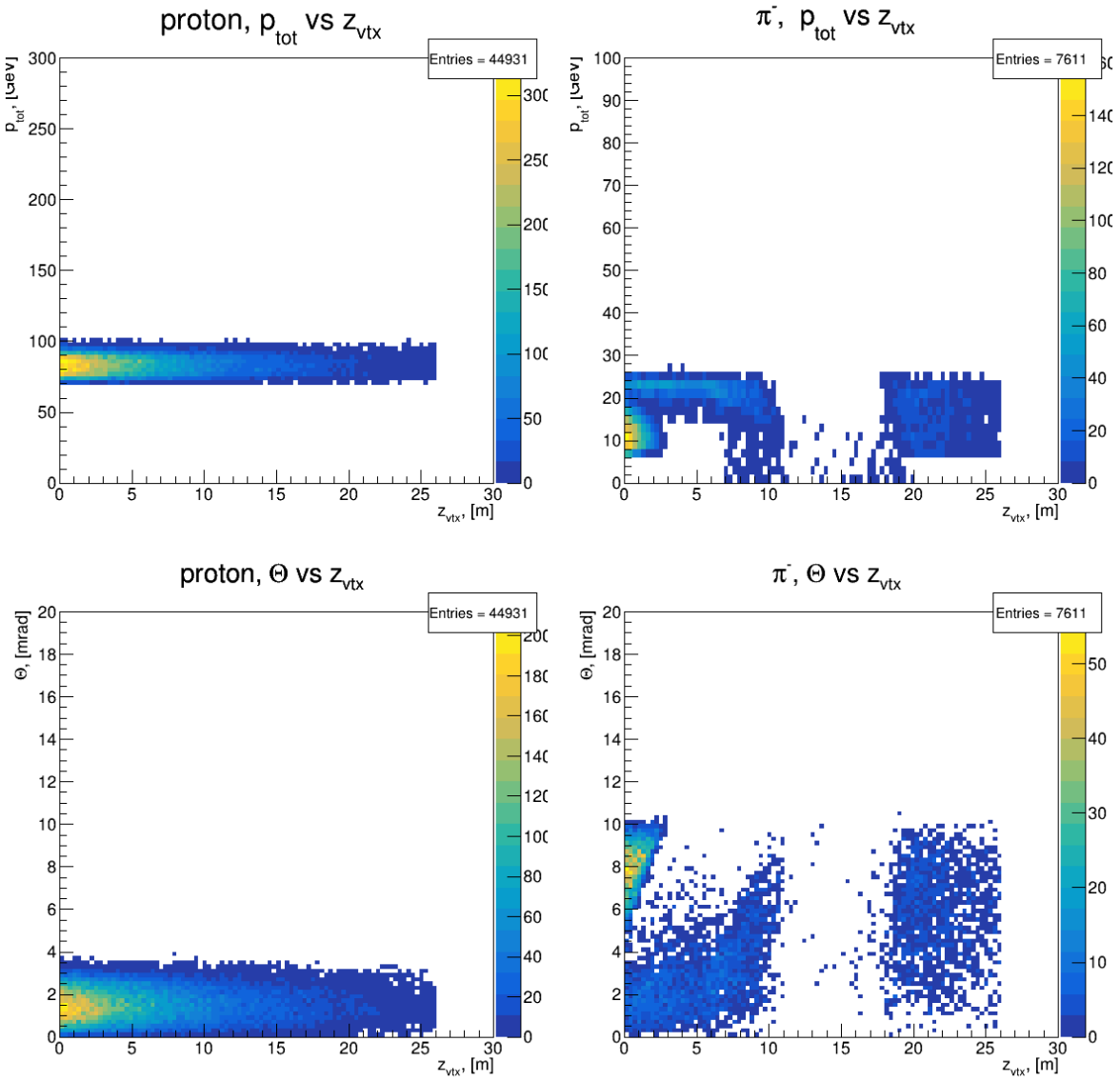

Figure 11.99: Beam energy 10x100 GeV. Momentum and Theta distributions for Lambda decay particles, protons (left) and π^-(right), registered in far-forward detectors vs their origination (decay vertex).

11.6.9 Appendix

[160]

Table 3.3: eRHIC beam parameters for different center-of-mass energies $\sqrt{s}$, with strong hadron cooling. High divergence configuration.

Species	proton	electron	proton	electron	proton	electron	proton	electron	proton	electron
Energy [GeV]	275	18	275	10	100	10	100	5	41	5
CM energy [GeV]	140.7		104.9		63.2		44.7		28.6	
Bunch intensity [10^{10}]	20.5	6.2	6.9	17.2	6.9	17.2	4.7	17.2	2.6	13.3
No. of bunches	290		1160		1160		1160		1160	
Beam current [A]	0.74	0.227	1	2.5	1	2.5	0.68	2.5	0.38	1.93
RMS norm. emit., h/v [μm]	4.6/0.75	845/72	2.8/0.45	391/24	4.0/0.22	391/25	2.7/0.27	196/20	1.9/0.45	196/34
RMS emittance, h/v [nm]	16/2.6	24/2.0	9.6/1.5	20/1.2	37/2.1	20/1.3	25/2.6	20/2.0	44/10	20/3.5
β^*, h/v [cm]]	90/4.0	59/5.0	90/4.0	43/5.0	90/4.0	167/6.4	90/4.0	113/5.0	90/7.1	196/21.0
IP RMS beam size, h/v [μm]	119/10		93/7.8		183/9.1		150/10		198/27	
K_x	11.8		11.9		20.0		14.9		7.3	
RMS $\Delta\theta$, h/v [μrad]	132/253	202/202	103/195	215/156	203/227	109/143	167/253	133/202	220/380	101/129
BB parameter, h/v [10^{-3}]	3/2	100/100	14/7	73/100	10/9	75/57	15/10	100/66	15/9	53/42
RMS long. emittance [10^{-3}, eV·sec]	36		36		21		21		11	
RMS bunch length [cm]	6	0.9	6	2	7	2	7	2	7.5	2
RMS $\Delta p/p$ [10^{-4}]	6.8	10.9	6.8	5.8	9.7	5.8	9.7	6.8	10.3	6.8
Max. space charge	0.006	neglig.	0.003	neglig.	0.028	neglig.	0.019	neglig.	0.05	neglig.
Piwinski angle [rad]	5.6	0.8	7.1	2.4	4.2	1.2	5.1	1.5	4.2	1.1
Long. IBS time [h]	2.1		3.4		2		2.6		3.8	
Transv. IBS time [h]	2		2		2.3/2.4		2/4.8		3.4/2.1	
Hourglass factor H	0.86		0.86		0.85		0.83		0.93	
Luminosity [10^{33}cm^{-2}sec^{-1}]	1.65		10.05		4.35		3.16		0.44	

Table 3.4: eRHIC beam parameters for different center-of-mass energies $\sqrt{s}$, with strong hadron cooling. High acceptance configuration.

Species	proton	electron	proton	electron	proton	electron	proton	electron	proton	electron
Energy [GeV]	275	18	275	10	100	10	100	5	41	5
CM energy [GeV]	140.7		104.9		63.2		44.7		28.6	
Bunch intensity [10^{10}]	19.53	6.248	6.9	17.2	6.9	17.2	4.7	17.2	2.6	13.3
No. of bunches	290		1160		1160		1160		1160	
Beam current [A]	0.71	0.227	1	2.5	1	2.5	0.68	2.5	0.38	1.93
RMS norm. emit., h/v [μm]	4.9/0.62	845/42.3	2.8/0.45	391/22	3.5/0.25	391/27	2.7/0.27	196/20	1.9/0.45	196/34
RMS emittance, h/v [nm]	16.7/2.1	24.0/1.2	9.6/1.5	20/1.1	33/2.4	20/1.4	25/2.6	20/2.0	44/10	20/3.5
β^*, h/v [cm]]	395/4.0	274/7.0	227/4.0	109/5.5	102/4.0	169/6.8	90/4.0	113/5.0	90/7.1	196/21
IP RMS beam size, h/v [μm]	256/9.2		148/7.8		184/9.7		150/10		198/27	
K_x	0.036		18.9		18.9		14.9		7.3	
RMS $\Delta\theta$, h/v [μrad]	65/229	94/131	65/196	135/143	180/243	109/143	167/253	133/202	220/380	101/129
BB parameter, h/v [10^{-3}]	3/1	100/71	14/5	75/71	11/8	75/57	15/10	100/66	15/9	53/42
RMS long. emittance [10^{-3}, eV·sec]	36		36		21		21		11	
RMS bunch length [cm]	6	0.9	6	2	7	2	7	2	7.5	2
RMS $\Delta p/p$ [10^{-4}]	6.8	10.9	6.8	5.8	9.7	5.8	9.7	6.8	10.3	6.8
Max. space charge	0.006	neglig.	0.003	neglig.	0.027	neglig.	0.019	neglig.	0.05	neglig.
Piwinski angle [rad]	2.6	0.4	4.5	1.5	4.2	1.2	5.1	1.5	4.2	1.1
Long. IBS time [h]	2		3.4		2		2.6		3.8	
Transv. IBS time [h]	2		2		2.0/3.0		2/4.8		3.4/2.1	
Hourglass factor H	0.88		0.87		0.85		0.83		0.93	
Luminosity [10^{33}cm^{-2}sec^{-1}]	0.83		6.4		4.07		3.16		0.44	

Figure 11.100: Parameters for eRHIC, ep operation

Table 3.5: eRHIC beam parameters for e-Au operation for different center-of-mass energies $\sqrt{s}$, with strong hadron cooling.

Species	Au ion	electron	Au ion	electron	Au ion	electron	Au ion	electron
Energy [GeV]	110	18	110	10	110	5	41	5
CM energy [GeV]	89.0		66.3		46.9		28.6	
Bunch intensity [10^{10}]	0.08	7.29	0.05	17.2	0.05	17.2	0.036	17.2
No. of bunches	290		1160		1160		1160	
Beam current [A]	0.23	0.26	0.57	2.50	0.57	2.50	0.41	2.50
RMS norm. emit., h/v [μm]	5.1/0.7	705/20	5.0/0.4	391/20	5.0/0.4	196/20	3.0/0.3	196/20
RMS emittance, h/v [nm]	43.2/5.8	20.0/0.6	42.3/3.0	20.0/1.0	42.3/3.0	20.0/2.0	68.1/5.7	20.0/2.0
β^*, h/v [cm]]	91/4	196/41	91/4	193/12	91/4	193/6	90/4	307/11
IP RMS beam size, h/v [μm]	198/15		196/11		197/11		248/15	
K_x	0.077		0.057		0.056		0.061	
RMS $\Delta\theta$, h/v [μrad]	218/379	101/37	216/274	102/92	215/275	102/185	275/377	81/136
BB parameter, h/v [10^{-3}]	1/1	37/100	3/3	43/47	3/2	86/47	5/4	61/37
RMS long. emittance [10^{-3}, eV·sec]	16		16		16		16	
RMS bunch length [cm]	7	0.9	7	2	7	2	11.6	2
RMS $\Delta p/p$ [10^{-4}]	6.2	10.9	6.2	5.8	6.2	6.8	10	6.8
Max. space charge	0.007	neglig.	0.008	neglig.	0.008	neglig.	0.038	neglig.
Piwinski angle [rad]	4.4	1.1	4.5	1.2	4.5	1.5	5.8	1.2
Long. IBS time [h]	0.33		0.36		0.36		0.85	
Transv. IBS time [h]	0.81		0.89		0.89		0.16	
Hourglass factor H	0.85		0.85		0.85		0.71	
Luminosity [10^{33}cm^{-2}sec^{-1}]	0.59		4.76		4.77		1.67	

Table 3.6: eRHIC beam parameters for e-Au operation for different center-of-mass energies $\sqrt{s}$, with stochastic cooling.

Species	Au ion	electron	Au ion	electron	Au ion	electron	Au ion	electron
Energy [GeV]	110	18	110	10	110	5	41	5
CM energy [GeV]	89.0		66.3		46.9		28.6	
Bunch intensity [10^{10}]	0.10	7.29	0.10	30	0.08	30	0.09	30
No. of bunches	290		580		580		580	
Beam current [A]	0.29	0.26	0.57	2.18	0.44	2.18	0.50	2.18
RMS norm. emit., h/v [μm]	2.0/2.0	845/60	2.0/2.0	391/102	2.0/2.0	196/63	2.0/2.0	196/113
RMS emittance, h/v [nm]	16.9/16.9	24.0/1.7	16.9/16.9	20.0/5.2	16.9/16.9	20.0/6.4	45.4/45.4	20.0/11.5
β^*, h/v [cm]]	288/12	203/116	91/12	77/39	146/12	113/31	149/50	339/196
IP RMS beam size, h/v [μm]	221/45		124/45		157/45		261/150	
K_x	0.202		0.363		0.284		0.577	
RMS $\Delta\theta$, h/v [μrad]	77/380	109/38	136/376	161/116	108/380	127/144	174/302	77/77
BB parameter, h/v [10^{-3}]	3/1	35/100	11/4	66/93	11/3	100/96	9/5	100/100
RMS long. emittance [10^{-3}, eV·sec]	64		64		64		64	
RMS bunch length [cm]	15	0.9	18	2	18	2	18	2
RMS $\Delta p/p$ [10^{-4}]	10	10.9	10	5.8	10	6.8	13	6.8
Max. space charge	0.001	neglig.	0.001	neglig.	0.001	neglig.	0.007	neglig.
Piwinski angle [rad]	8.5	0.5	18.1	2.0	14.3	1.6	8.6	1.0
Long. IBS time [h]	2.65		2.65		3.39		2.02	
Transv. IBS time [h]	1.02		0.80		1.32		0.93	
Hourglass factor H	0.54		0.54		0.54		0.65	
Luminosity [10^{33}cm^{-2}sec^{-1}]	0.14		2.06		1.27		0.31	

Figure 11.101: Parameters for eRHIC, eAu operation

Figure 11.102: IR

11.7 Far-Backward Detectors

The path of the electron beam downstream of the interaction point is shown in Fig. 11.103. Beam magnets are shown in full green, drift space in hatched green and detectors and components in red and yellow. The horizontal axis is aligned with the direction of the beam at the collision point, along which photons from e+p and e+A interactions will travel. These photons come predominantly from the bremsstrahlung process used for luminosity determination. The lower left of the figure shows possible instrumentation for the luminosity measurement. Bremsstrahlung and low-Q^2 processes also produce electrons with momenta slightly below the beam energy. After being bent out of the beam by lattice dipoles they may be measured by taggers as shown in the top left of the figure. This section will detail studies of a luminosity monitor as well a tagger for electrons from bremsstrahlung and low-Q^2 events. The technology considerations and machine-driven acceptances are both addressed as well.

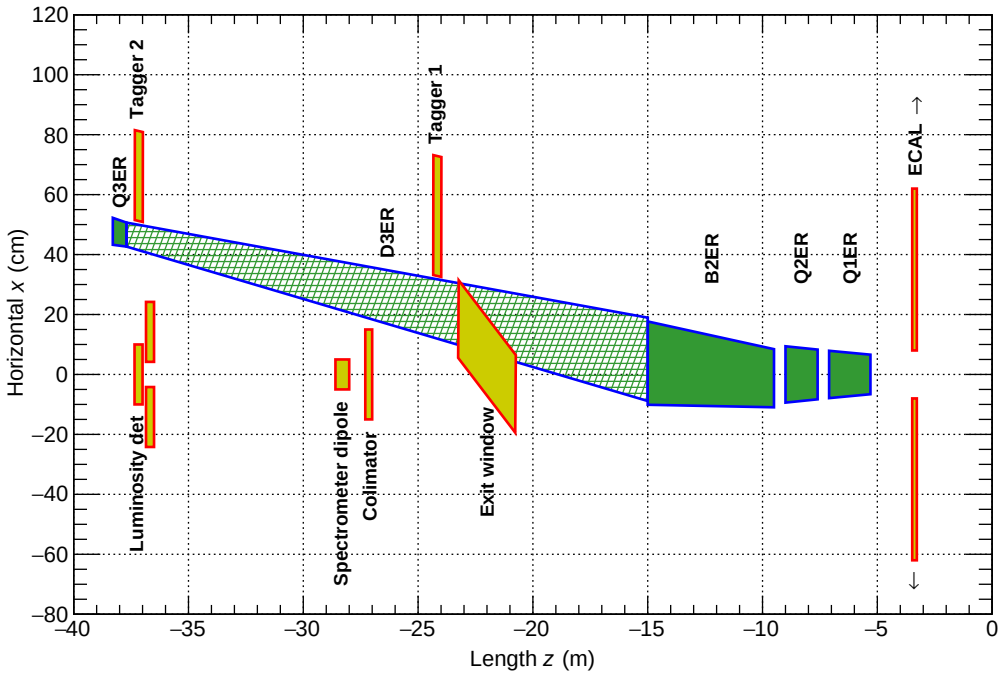

Figure 11.103: The region downstream of the interaction point in the electron direction.

11.7.1 Far-Backward Photons

11.7.1.1 Luminosity Measurement

The luminosity measurement provides the required normalization for all physics studies. At the broadest scale it determines absolute cross sections, such as needed for the structure function F_2 and derived PDFs. On an intermediate scale, it is also required to combine different running periods, such as runs with different beam energies needed to measure F_L, or runs with different beam species to study A dependencies. Asymmetry measurements are conducted using beams with bunches of both spin states. On the finest scale, the relative luminosity of the different bunch crossings is needed to normalize the event rates for the different

states; the uncertainty on the relative bunch luminosity is a limiting factor for asymmetry measurements.

The bremsstrahlung process $e + p \longrightarrow e + p + \gamma$ was used successfully for the measurement of luminosity by the HERA collider experiments [161–163]. It has a precisely known QED cross-section which is large, minimizing theoretical uncertainty and providing negligible statistical uncertainty. Thus the scale uncertainty of the luminosity is determined by the systematic uncertainties of the counting of bremsstrahlung events. The ZEUS collaboration at HERA measured luminosity with a 1.7% scale uncertainty; further improvements at the EIC should be able to reduce this to <1% as required by the physics program.

In contrast to HERA, where only the electron beam was polarized, both the electron and proton/light ion beams will be polarized in the EIC. In this case the bremsstrahlung rate is sensitive to the polarization dependent term $a(P_e, P_h)$ in the cross section $\sigma_{\text{brems}} = \sigma_0(1 + a(P_e, P_h))$. Thus, the polarizations P_e, P_h and luminosity measurements are coupled, and the precision of the luminosity measurement is limited by the precision of the polarization measurement. This is especially important for relative luminosities for asymmetry measurements, where the bremsstrahlung process used for normalization has different cross sections for different spin states. The precision needed for the relative luminosity measurement is driven by the magnitude of the physics asymmetries which can be as low as 10^{-4}; the uncertainty on relative bunch luminosities must reach this level of precision.

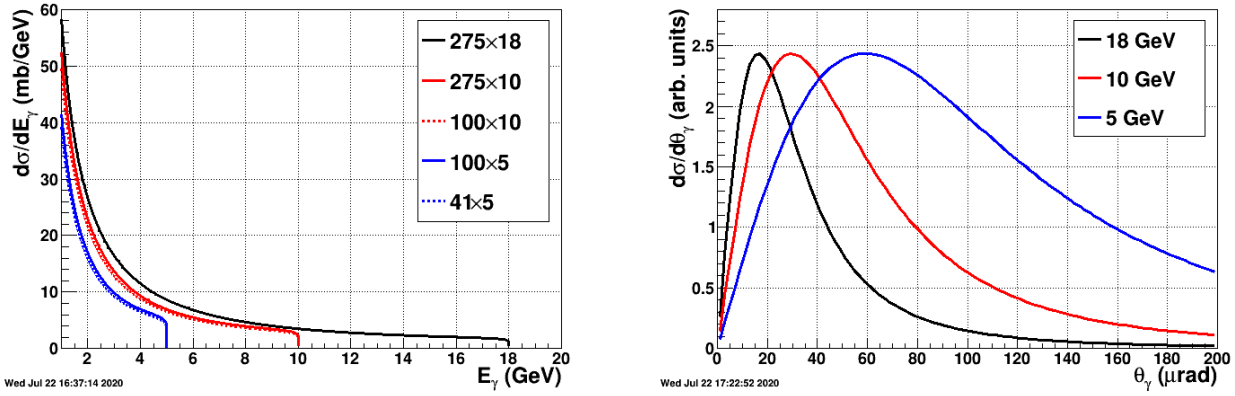

Figure 11.104: Bremsstrahlung photon energy (left) and angular (right) distributions for EIC beam energies.

The bremsstrahlung photon energy E_γ distributions for EIC beam energies are shown in left of Fig. 11.104. They diverge as $E_g \rightarrow 0$ and have sharp cutoffs at the electron beam energies. As shown in the right of Fig. 11.104, the bremsstrahlung photons are strongly peaked in the forward direction with typical values of $\theta_\gamma \approx m_e/E_e$, with values of 20-60 μrad at the EIC. The RMS angular divergence of the electron beam is significantly larger than these values and will dominate the angular distribution of bremsstrahlung photons as shown in Fig. 11.105.

11.7.1.2 Bremsstrahlung Photon Detection

Figure 11.108 shows a side view of detectors along the photon zero-degree line in the backward direction. The straightforward method for measuring bremsstrahlung situates a calorimeter at zero degrees in the electron direction counting the resulting photons, PHOT in the figure. The calorimeter is also exposed to the direct synchrotron radiation fan and must be shielded, thus degrading the energy resolution. This also

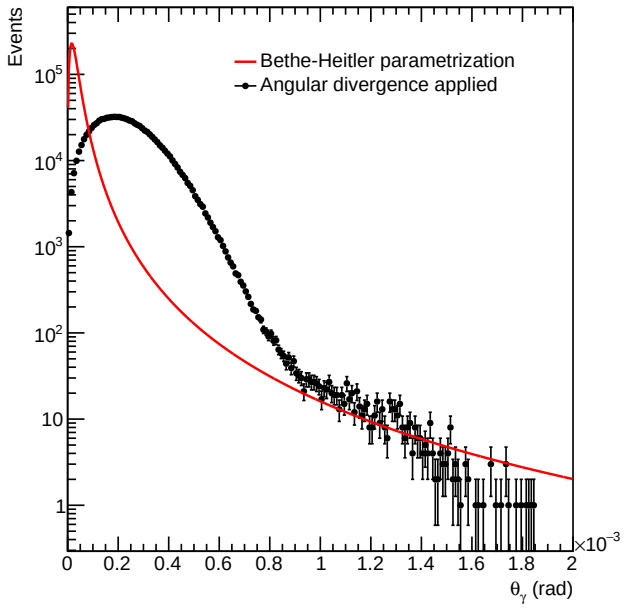

Figure 11.105: Angular dependence of bremsstrahlung cross section. The effect of beam angular divergence is shown.

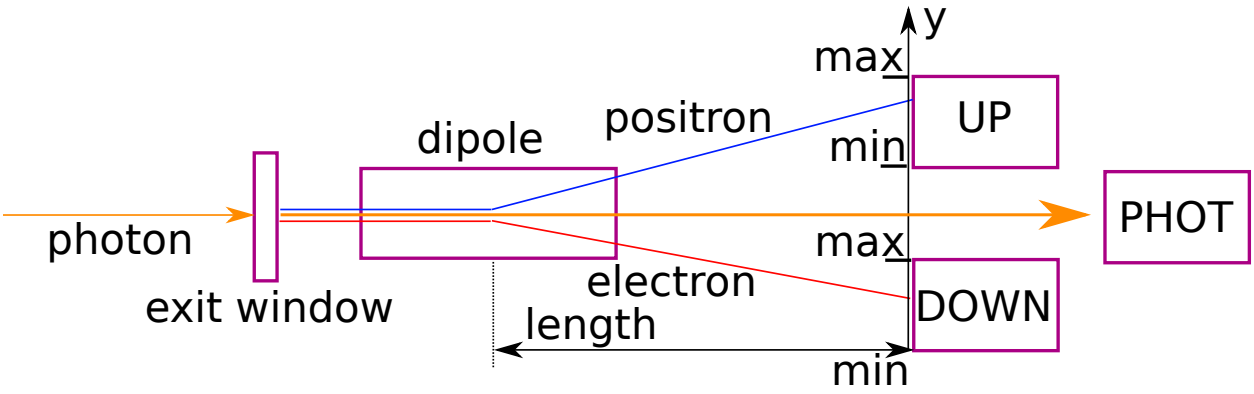

Figure 11.106: Principle of luminosity measurement. Bremsstrahlung photons are incident on aluminum exit window. Converted electron-positron pairs are split in spectrometer dipole magnet and detected in UP and DOWN detectors. Non-converted photons reach photon calorimeter PHOT.

imposes a rough low energy cutoff on photons typically $\approx$ 0.1-1 GeV below which the calorimeter is insensitive. At peak HERA luminosities, the photon calorimeters were sensitive to 1-2 photons per HERA bunch crossing. At an EIC luminosity of $10^{33}\,\mathrm{cm}^{-2}\,\mathrm{s}^{-1}$, the mean number of such photons per bunch crossing is over 20 for electron-proton scattering and increases with Z^2 of the target for nuclear beams. The per bunch energy distributions are broad, with a mean proportional to the number of photons per bunch crossing. The counting of bremsstrahlung photons thus is effectively an energy measurement in the photon calorimeter with all of the related systematic uncertainties (e.g. gain stability) of such a measurement.

An alternative method to counting bremsstrahlung photons, used effectively by the ZEUS collaboration at HERA, employs a pair spectrometer. A small fraction of photons is converted into e^+e^- pairs in the vacuum chamber exit window. A dipole magnet splits the pairs vertically and each particle hits a separate

calorimeter adjacent to the unconverted photon path. The relevant components are depicted in the lower left of Fig. 11.103. This has several advantages over a zero-degree photon calorimeter:

- The calorimeters are outside of the primary synchrotron radiation fan.
- The exit window conversion fraction reduces the overall rate.
- The spectrometer geometry imposes a low energy cutoff in the photon spectrum, which depends on the magnitude of the dipole field and the location of the calorimeters.

The variable parameters of the last two points (conversion fraction, dipole field and calorimeter locations) may be chosen to reduce the rate to less than or of order one e^+e^- coincidence per bunch crossing even at nominal EIC luminosities. Thus, counting of bremsstrahlung photons is simply counting of e^+e^- coincidences in a pair spectrometer with only small corrections for pileup effects.

The locations of a zero-degree calorimeter and pair spectrometer are shown in the bottom left of Fig. 11.103. Careful integration into the machine lattice is required, not only to allow for enough space for the detectors, but also to accommodate the angular distribution of the photons. This is dominated by the angular divergence of the electron beam, with RMS values as high 0.2 mrad. Thus a clear aperture up to a few mrad is required to measure the angular distribution and minimize the acceptance correction. The spectrometer rate is directly proportional to the fraction of photons which convert into e^+e^- pairs, placing stringent requirements on the photon exit window. It must have a precisely known material composition, and a precisely measured and uniform thickness along the photon direction.

Calorimeters are required for both luminosity devices, for triggering and energy measurements. The high rates dictate a radiation hard design, especially for the zero-degree calorimeter, which must also have shielding against synchrotron radiation. The spectrometer must also have precise position detectors to measure the $e^{\pm}$. Combined with the calorimeter energy measurement this allows reconstruction of the converted photon positions. The distribution of photon positions is required to correct for the lost photons falling outside the photon aperture and detector acceptances.

11.7.2 Luminosity detector

Luminosity measurement will be provided by detecting the bremsstrahlung photons. The advantage is in a relatively large cross section, driven only by QED, with no dependence on proton internal structure. The photons are emitted in a relatively narrow cone along direction of the electron beam.

Bremsstrahlung cross section is shown in Fig. 11.107. In Fig. 11.107a we can see it as a function of photon energy across all considered collider energies. Figure 11.107b gives angular dependence of the cross section, along with distribution of photon scattering angles θ_γ in presence of angular beam divergence.

Two independent methods to detect the bremsstrahlung photons are proposed, following a similar device from ZEUS experiment [164]. Principle is illustrated in Fig. 11.108. The photons are incident on aluminum exit window. Some of them get converted to e^+e^- pairs, traveling to pair spectrometer detectors UP and DOWN. Non-converted photons are detected in direct photon calorimeter PHOT. The spectrometer will provide precision luminosity measurement for physics results, the direct photons will be used to address instantaneous collider performance.

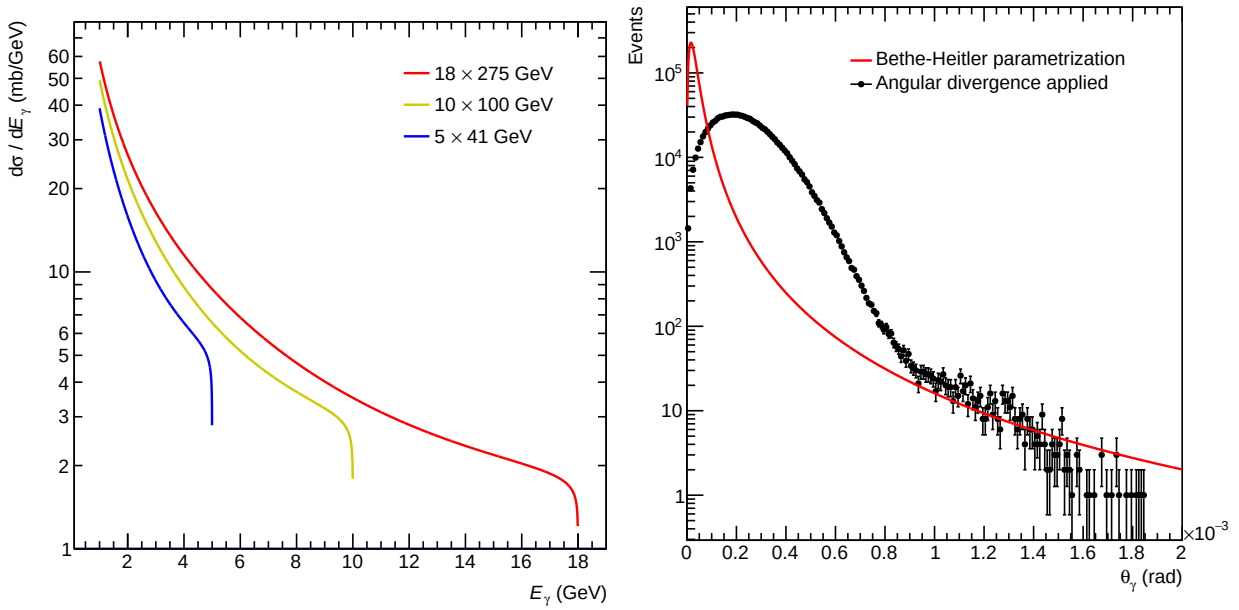

(a) Bremsstrahlung cross section as a function of photon energy.

(b) Angular dependence of bremsstrahlung cross section. Effect of beam angular divergence is shown.

Figure 11.107: Bremsstrahlung cross section as a function of photon energy E_γ and polar scattering angle θ_γ.

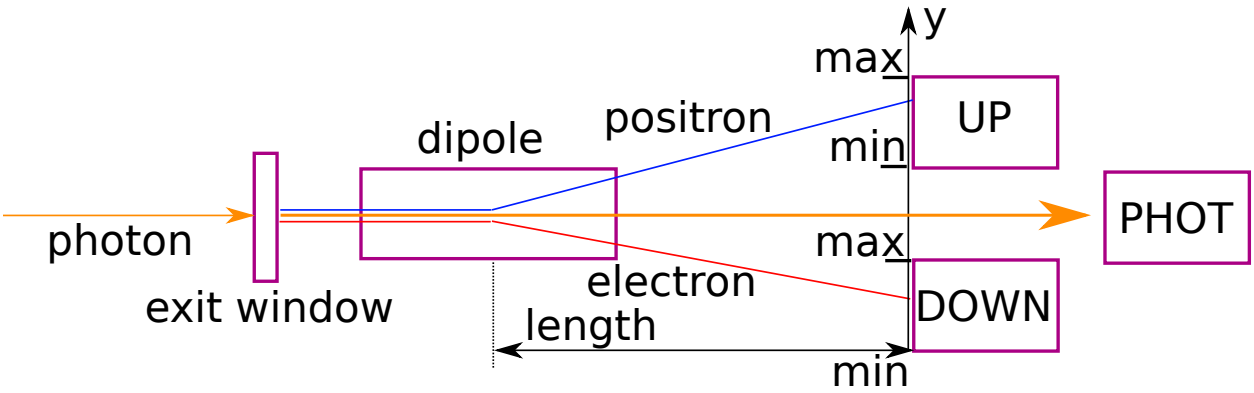

Figure 11.108: Principle of luminosity measurement. Bremsstrahlung photons are incident on aluminum exit window. Converted electron-positron pairs are split in spectrometer dipole magnet and detected in UP and DOWN detectors. Non-converted photons reach photon calorimeter PHOT.

Geant4 model of all essential components for luminosity measurement is shown in Fig. 11.109. Photon exit window is placed at z = -20.75 m. It is tilted by 100 mrad relative to axis of electron beam (and of the photons), to achieve an acceptable heat load from synchrotron radiation. Collimator at z = -27 m will prevent synchrotron radiation at larger angles to enter the luminosity system. Dipole spectrometer magnet at z = -28 m will split converted electron-positron pairs to spectrometer detectors. Direct photon detector is placed at z = -37.8 m, after a graphite filter of 5 X_0 length. The pair of spectrometer detectors is at z = -36.5 m. Vertical displacement (y axis) of spectrometer detectors is set for the edge of the detectors closest to $y = 0$ to be positioned at y = 42 mm. The detectors are implemented in the model as boxes which mark hits by all incoming particles.

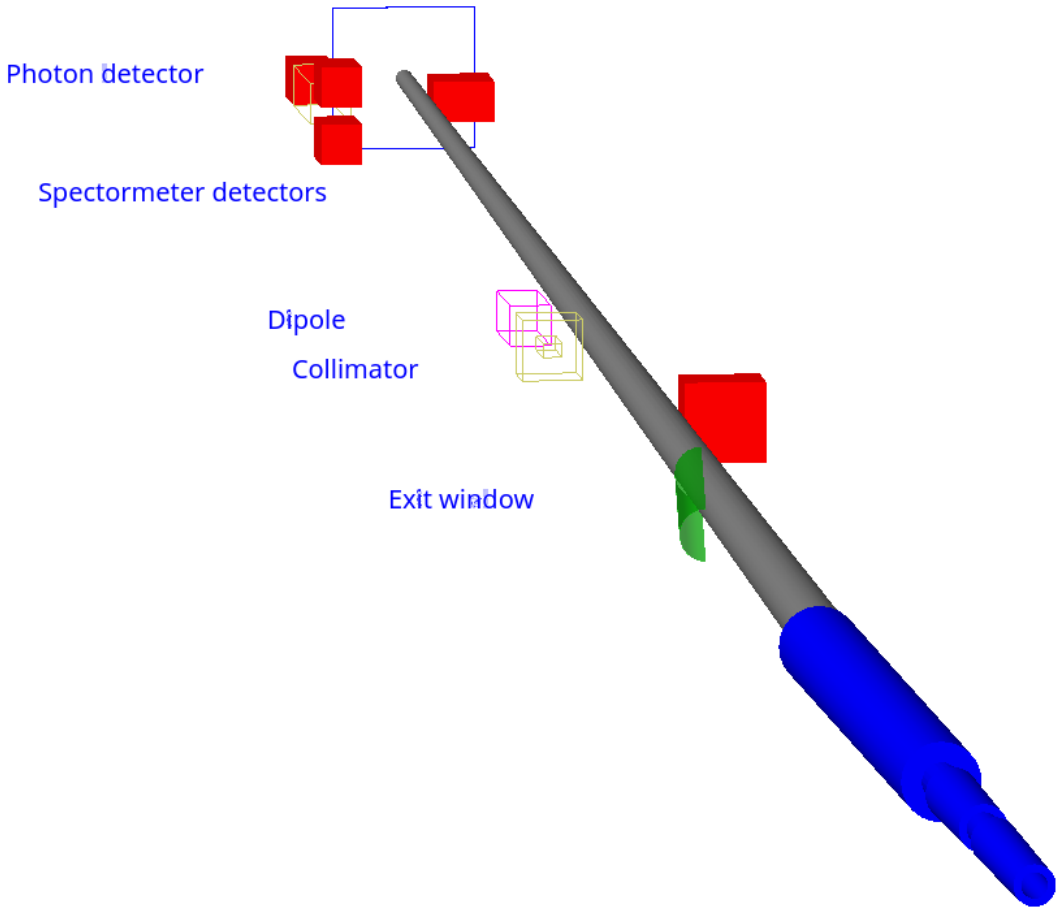

Figure 11.109: Geant4 model of luminosity detector.

Spectrometer acceptance as a function of bremsstrahlung photon energy depends on its layout as shown in Fig. 11.108. Namely it depends on distance *length* from the dipole magnet to spectrometer detectors, magnetic field of the dipole and positions *min* and *max* of UP and DOWN detectors along vertical y axis.

The acceptance is shown in Fig. 11.110 for the top energy of 18×275 GeV beams, as a function of generated bremsstrahlung photon energy E_γ. The Geant4 distribution is a result of simulation of 1M bremsstrahlung events generated by the eic-lgen event generator [165] and pasing the layout of Fig 11.109. The acceptance is constructed as a fraction of events with at least 1 GeV of energy coming into both UP and DOWN detectors.

Geometry model for the acceptance, shown in Fig. 11.110 as a solid line, is based on formula for deflection of a charged particle in a magnetic field and coincident requirement for both the detectors. Electron or positron passing along z direction through magnetic field B_x oriented along x axis gets a transverse momentum $p_T = \int B_x \mathrm{d}z$ along vertical y direction.

Position in y on UP or DOWN detectors of arriving electron or positron is given by the length l from magnet center to the detector and electron momentum p as

$$y = l\frac{p_T}{p}. \tag{11.8}$$

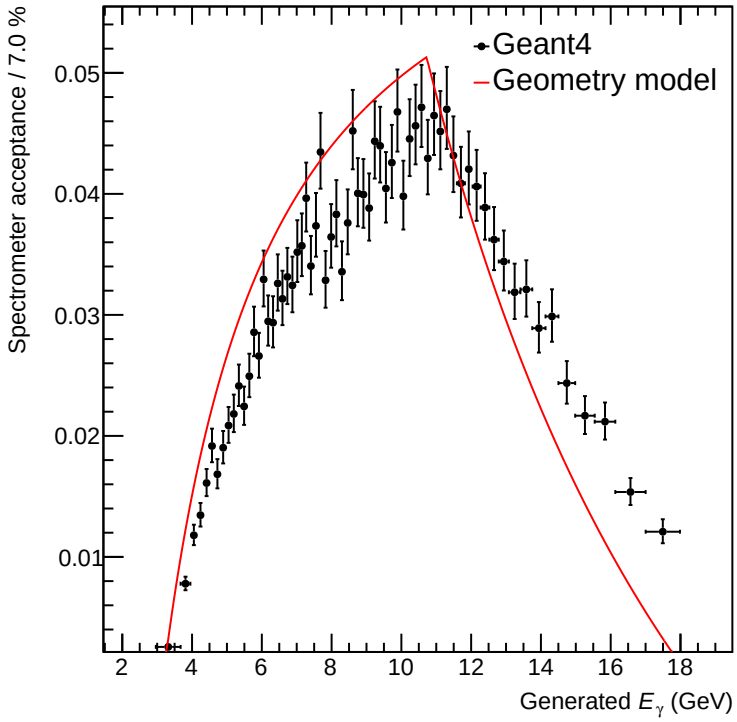

Figure 11.110: Luminosity spectrometer acceptance as a function bremsstrahlung photon energy E_γ.

Assuming that one electron in the pair has a fraction of photon energy $z = p/E_\gamma$, the other has a fraction $1-z$. Positions of the pair arriving on UP and DOWN detectors y_{up} and y_{down} are given by z and E_γ:

$$zE_\gamma = \frac{lp_T}{y_{\text{up}}}, \quad (1-z)E_\gamma = \frac{lp_T}{y_{\text{down}}} \tag{11.9}$$

Both spectrometer detectors cover a given minimal and maximal positions along y, as indicated in Fig. 11.110. Coincidence requirement for the detectors then limits the range in z for which the converted photon would be detected by the spectrometer. Result of the geometry model is the range of z for which the coincidence requirement is satisfied, calculated for each value of E_γ.

The geometry model has been used to obtain the magnetic field for the spectrometer dipole magnet as B_x = 0.26 T in order to get the most of the acceptance. Overall good agreement has been achieved with the full Geant4 simulation. A unique magnetic field will be required for each energy of electron beam.

11.7.3 Low-Q2 tagger

Bremsstrahlung and Low-Q^2 Electron Detectors: Downstream of the interaction point the electron beam is accompanied by a flux of electrons at small angles with respect to the beam direction and at slightly lower energy. They are predominantly final state electrons from the bremsstrahlung process $e + p \longrightarrow e + p + \gamma$, with an energy distribution the mirror image of the left of Fig. 11.104 with $E'_e = E_e - E_\gamma$. Also, a fraction of the electrons in this region are produced in quasi-real photoproduction with $Q^2 \approx 0$.

The final state bremsstrahlung electrons provide a powerful tool for calibrating and verifying the luminosity measurement with photons. Tagging bremsstrahlung electrons and counting corresponding photons in the photon detectors provides a direct measure of the luminosity detector acceptance in the tagged energy range. This is of paramount importance to precisely determine the pair conversion probability for the luminosity spectrometer, which depends on the exit window composition and thickness.

Tagging of low-Q^2 processes provides an extension of the kinematic range of DIS processes measured with electrons in the central detector. It crosses the transition from DIS to hadronic reactions with quasi-real photons. An example of acceptance as a function of Q^2 for measurements with the central detector and electron taggers as depicted in Fig. 11.103 is shown in Fig. 11.111. The electrons are generated by a simple model of quasi-real photoproduction [166] and Pythia. The taggers provide useful acceptance in the range $10^{-6} < Q^2 < 10^{-2}\,\mathrm{GeV}^2$. Application of the electron taggers for low-Q^2 physics will face a challenge from the high rate bremsstrahlung electrons, which can be addressed by tagger design and correlation with information from the central detector.

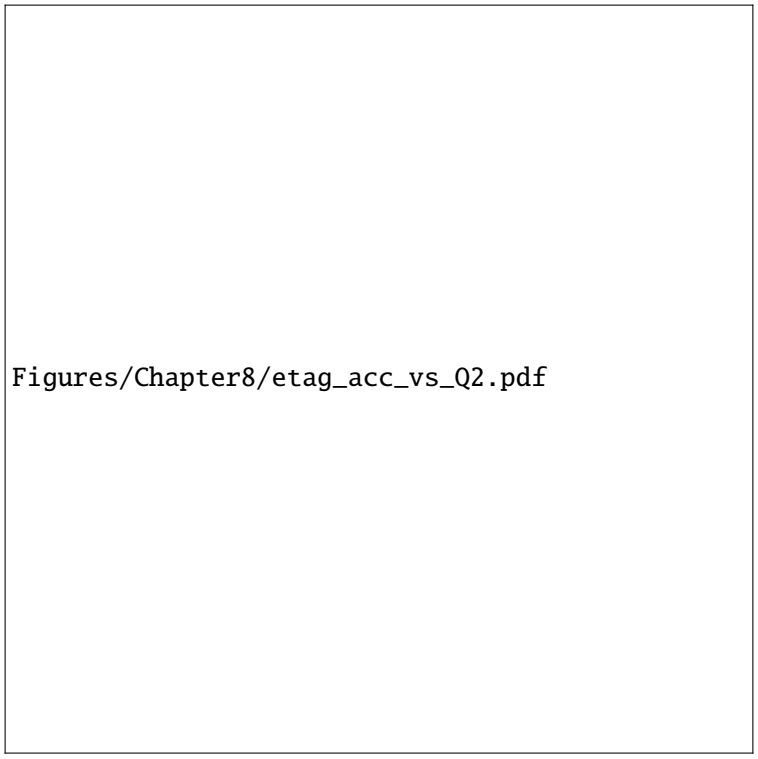

Figure 11.111: Acceptance as a function of Q^2 for electrons measured in the central detector (right plateau) and downstream taggers (left plateau). The electrons are generated by a simple model of quasi-real photoproduction and Pythia.

Possible locations of detectors for these electrons are shown in the top left of Fig. 11.103. Electrons with energies slightly below the beam are bent out of the beam by the first lattice dipole after the interaction point. The beam vacuum chamber must include exit windows for these electrons. The windows should be as thin as possible along the electron direction to minimize energy loss and multiple scattering before the detectors.

The taggers should include calorimeters for triggering and energy measurements. They should be finely segmented to disentangle the multiple electron hits per bunch crossing from the high rate bremsstrahlung

process. The taggers should also have position sensitive detectors to measure the vertical and horizontal coordinates of electrons. The combined energy and position measurements allow reconstruction of the kinematic variable Q^2 and x_{BJ}. If the position detectors have multiple layers and are able to reconstruct the electron direction this will overconstrain the variable reconstruction and improve their measurement; this may also provide some measure of background rejection. The beam angular divergence will introduce significant errors on the variable reconstruction. The reconstructed versus generated Q^2 is shown in Fig. 11.112 with smearing from beam divergence. There is reasonable resolution for Q^2 as low as $10^{-3}\,\mathrm{GeV}^2$; below $10^{-4}\,\mathrm{GeV}^2$ meaningful reconstruction of Q^2 based on the electron is not possible.

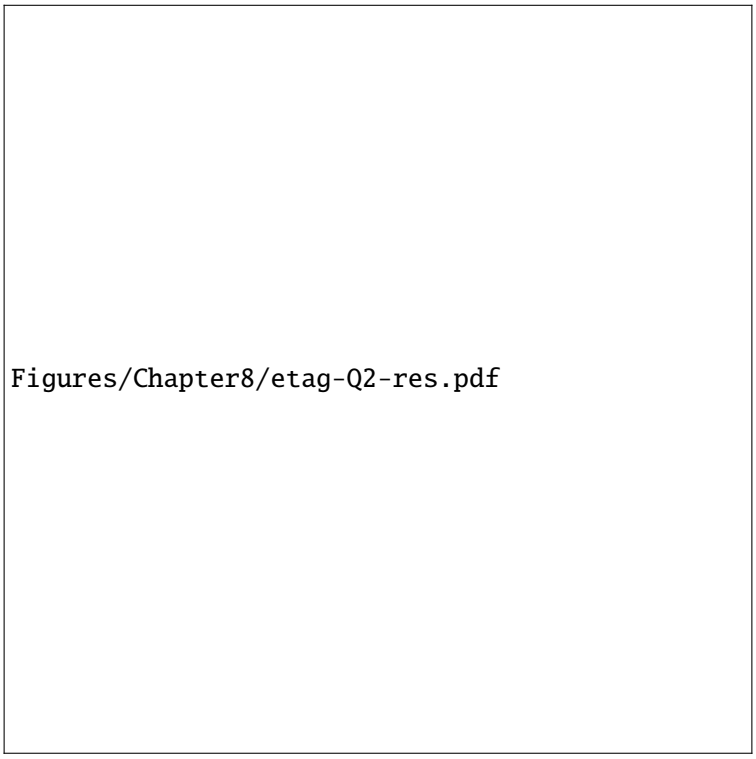

Figure 11.112: Comparison of reconstructed and reconstructed electron Q_e^2 with smearing for beam angular divergence.

Start old YR: The aim of the low-Q^2 tagger is to detect electrons scattered at very small angles, beyond coverage of central detector. Layout of backward (electron-outgoing) side of interaction region is shown in Fig. 11.113. Beam magnets are shown in full green, drift space in dashed green and detectors and components in red and yellow. Two tagger detectors are proposed, Tagger 1 at $z = -24$ m and Tagger 2 at $z = -37$ m respectively. Backward electromagnetic calorimeter ECAL is a part of central detector, located at $z = -3.28$ m. Rapidity coverage of ECAL as implemented in model for tagger studies is $-4.4 < \eta < -1.0$.

Geant4 model of backward side of interaction region is shown in Fig. 11.114. The tagger detectors Tagger 1 and 2 and backward electromagnetic calorimeter ECAL are implemented as boxes which mark hits by all incoming particles. Solenoid field of central detector is based in 3 T BeAST parametrization. Beam magnets eQ1ER, eQ2ER and eB2ER (11.29) are shown as blue cylinders. Drift spaces in gray are transparent to all particles. The layout ends with marker at position of Q3eR magnet.

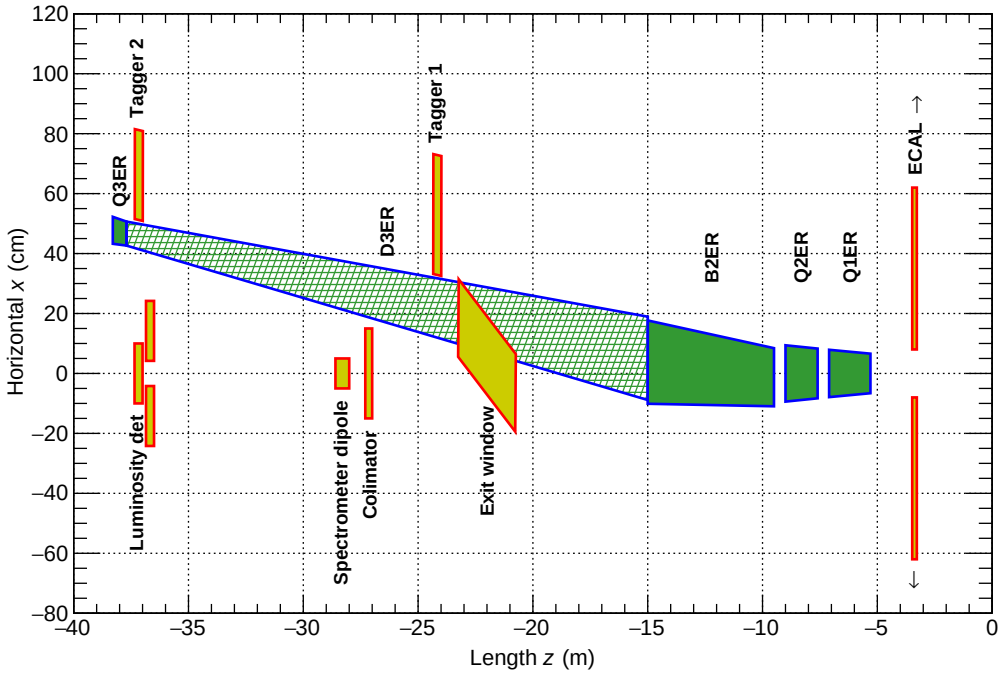

Figure 11.113: Layout of interaction region on backward side, showing electron taggers and components of luminosity monitor.

Two generated samples, Pythia 6 and quasi-real photoprotuction, were used to address acceptance of the taggers, both for the top energy 18×275 GeV for electron and proton beam respectively. Total cross section for both samples as a function of event true Q^2 is shown in Fig. 11.115.

Model of quasi-real photoproduction is based on approach used at HERA study [166] and implemented in eic-lgen event generator [165].

Angular and energy coverage for both tagger detectors is shown in Fig. 11.116. Energy of scattered electrons E_e and polar angle θ_e is shown for events where the scattered electron is incident on one of the tagger detectors. Energy and mainly angular coverage is complementary for both tagger detectors.

Coverage in Q^2 is shown in Fig. 11.117 for quasi-real photoproduction. Events with a hitin one of the taggers or in ECAL are shown along with all generated quasi-real events. Coverage in Q^2 for both of the taggers follows a similar interval, although as illustrated from Fig. 11.116, the coverage is achieved by different combinations of electron energies and angles. Transition of coverage takes place at lower reach of ECAL and upper reach of tagger detectors.

Combined acceptance of tagger detectors and ECAL is shown in Fig. 11.118 for both samples of Pythia 6 and quasi-real photoproduction. The acceptance is obtained as a fraction of all generated events with a hit in one of the tagger detectors or in ECAL. A dip takes place at a transition between ECAL and taggers acceptance, at Q^2 about 0.1 GeV^2. It was shown that magnitude and width of the dip strongly depends on available inner radius for ECAL. The acceptance is well compatible between the two event generators.

As main kinematics variables include Bjorken-x, inelasticity y and virtuality Q^2, coverage of both taggers is given in combinations of x, y and Q^2 in Fig. 11.119. Intervals of all generated events are shown as underlying red bands, box diagrams then give events with a hit in one of the taggers or in ECAL.

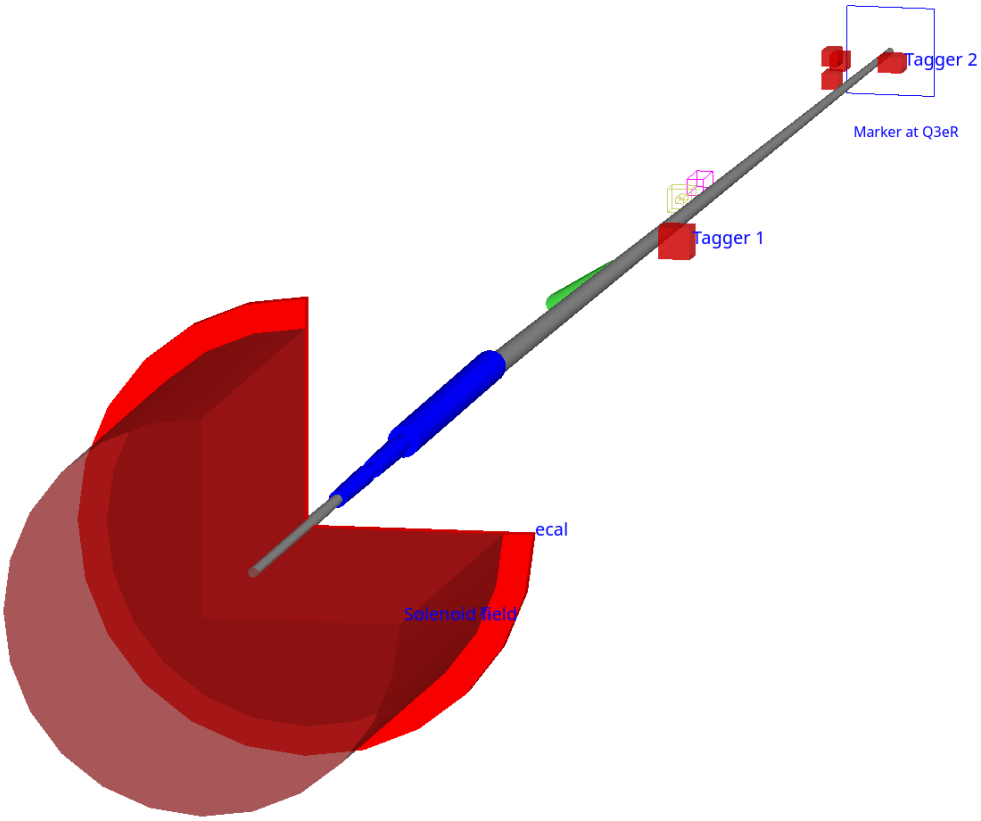

Figure 11.114: Geant4 model of backward interaction region, side of electron tagger detectors.

11.8 Polarimetry

Rapid, precise beam polarization measurements will be crucial for meeting the goals of the EIC physics program as the uncertainty in the polarization propagates directly into the uncertainty for relevant observables (asymmetries, etc.). In addition, polarimetry will play an important role in facilitating the setup of the accelerator.

The basic requirements for beam polarimetry are:

- Non-destructive with minimal impact on the beam lifetime
- Systematic uncertainty on the order $\frac{dP}{P} = 1\%$ or better
- Capable of measuring the beam polarization for each bunch in the ring - in particular, the statistical uncertainty of the measurement for a given bunch should be comparable to the systematic uncertainty
- Rapid, quasi-online analysis in order to provide timely feedback for accelerator setup

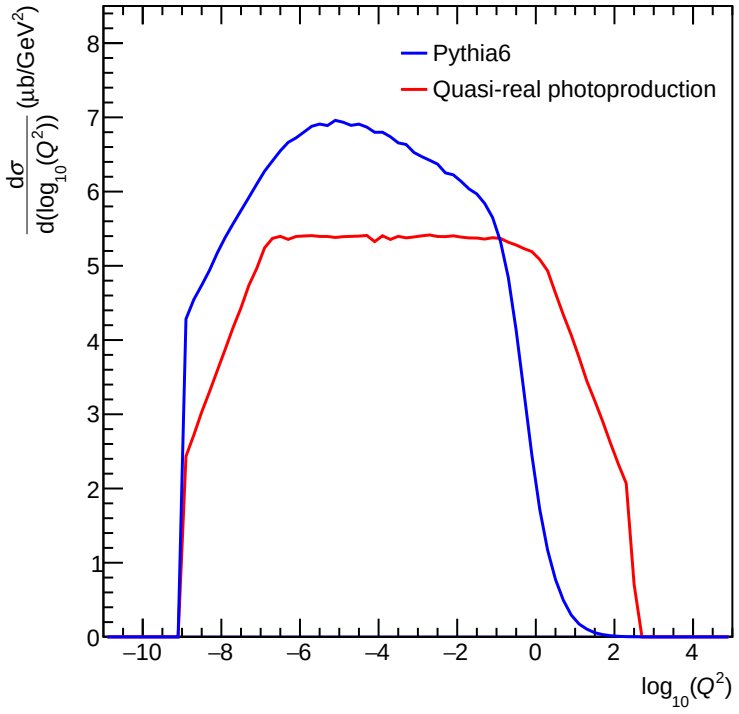

Figure 11.115: Total cross section as a function of event true Q^2 for Pythia 6 and quasi-real photoproduction.

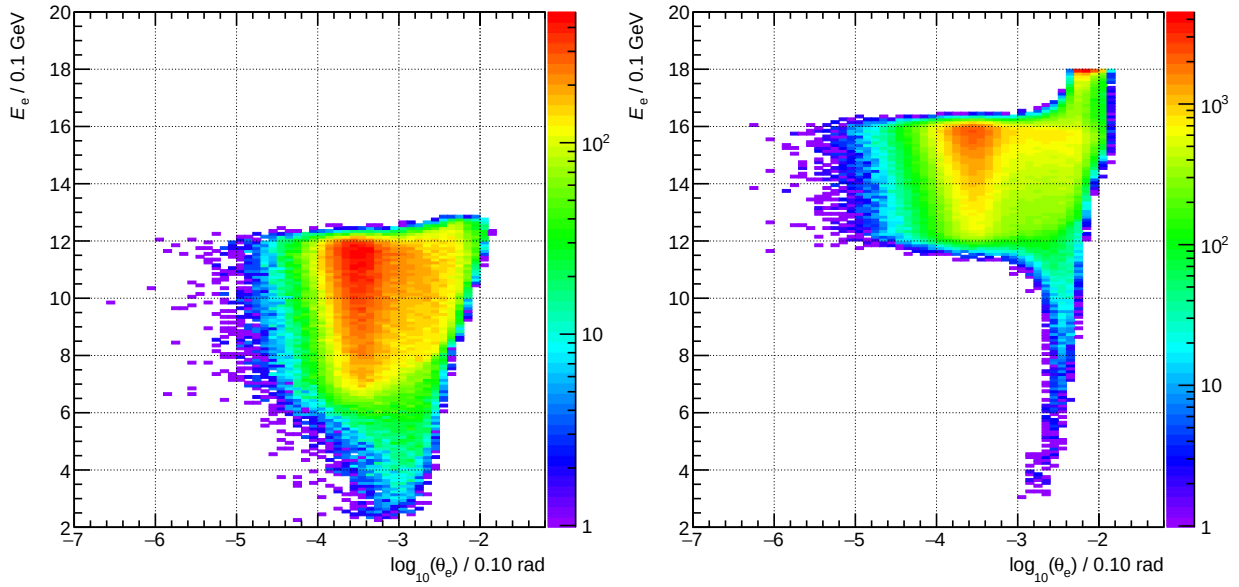

(a) Hit in Tagger 1

(b) Hit in Tagger 2

Figure 11.116: Scattered electron energy E_e and polar angle θ_e for events of quasi-real photoproduction with a hit in Tagger 1 or 2.

11.8.1 Electron Polarimetry

The most commonly used technique for measuring electron beam polarization in rings and colliders is Compton polarimetry, in which the polarized electrons scatter from 100% circularly polarized laser pho-

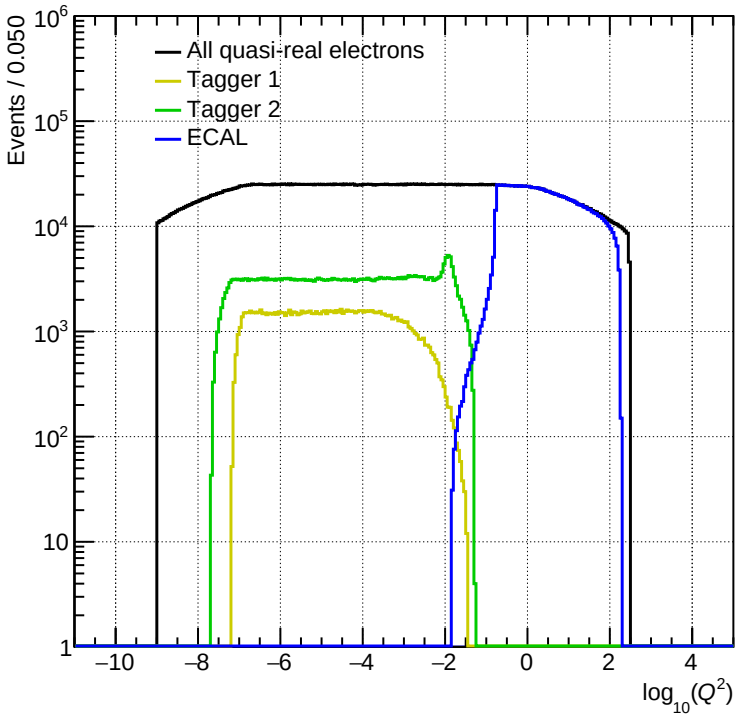

Figure 11.117: Coverage in Q^2 for tagger detectors and ECAL.

tons. The asymmetry from this reaction is measured via the scattered electrons or high energy backscattered photons. A brief review and description of several previous Compton polarimeters can be found in [167]. A particular advantage of Compton polarimetry is that it sensitive to both longitudinal and transverse polarization.

The longitudinal analyzing power depends only on the backscattered photon energy and is given by,

$$A_{\text{long}} = \frac{2\pi r_o^2 a}{(d\sigma/d\rho)}(1-\rho(1+a))\left[1-\frac{1}{(1-\rho(1-a))^2}\right], \tag{11.10}$$

where r_o is the classical electron radius, $a = (1+4\gamma E_{\text{laser}}/m_e)^{-1}$ (with the Lorentz factor $\gamma = E_e/m_e$), ρ is the backscattered photon energy divided by its kinematic maximum, E_γ/E_γ^{max}, and $d\sigma/d\rho$ is the unpolarized Compton cross section. In contrast, the transverse analyzing power depends both on the backscattered photon energy and the azimuthal angle (ϕ) of the photon (with respect to the transverse polarization direction);

$$A_{\text{tran}} = \frac{2\pi r_o^2 a}{(d\sigma/d\rho)}\cos\phi\left[\rho(1-a)\frac{\sqrt{4a\rho(1-\rho)}}{(1-\rho(1-a))}\right]. \tag{11.11}$$

This azimuthal dependence of the asymmetry results in an "up-down" asymmetry (assuming vertically polarized electrons) and requires a detector with spatial sensitivity. Both the longitudinal and transverse analyzing powers are shown in Fig. 11.120.

Plans for electron polarimetry at EIC include a Compton polarimeter at IP 12, where the electron beam is primarily vertically polarized. A Compton polarimeter near the primary detector in the vicinity of IP 6,

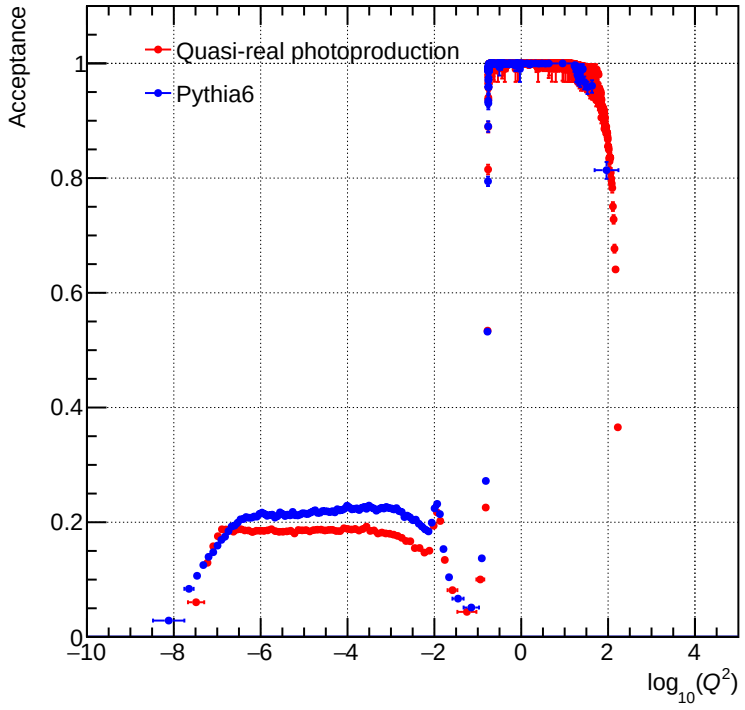

Figure 11.118: Acceptance in Q^2 for tagger detectors and ECAL as a fraction of events with a hit in one of the taggers or in ECAL

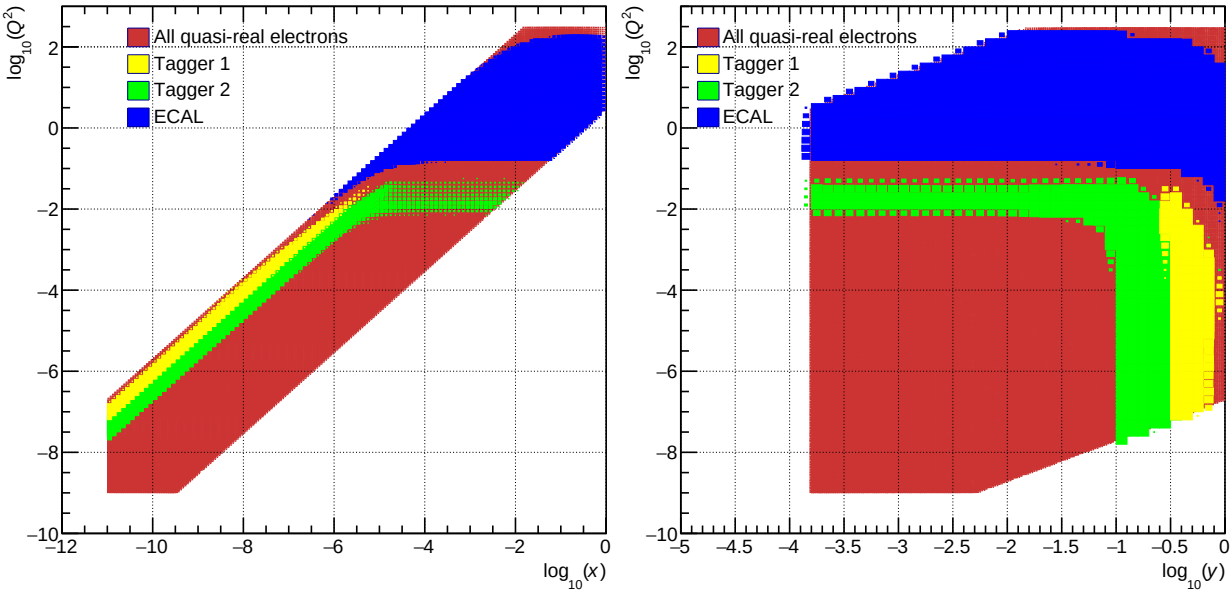

(a) Coverage in x and Q^2

(b) Coverage in y and Q^2

Figure 11.119: Coverage in x, y and Q^2 for tagger detectors and ECAL.

where the beam will be a mix of longitudinal and transverse polarization, is also under investigation; since that region of the ring is extremely crowded, care must be taken in the assessment of whether a polarimeter

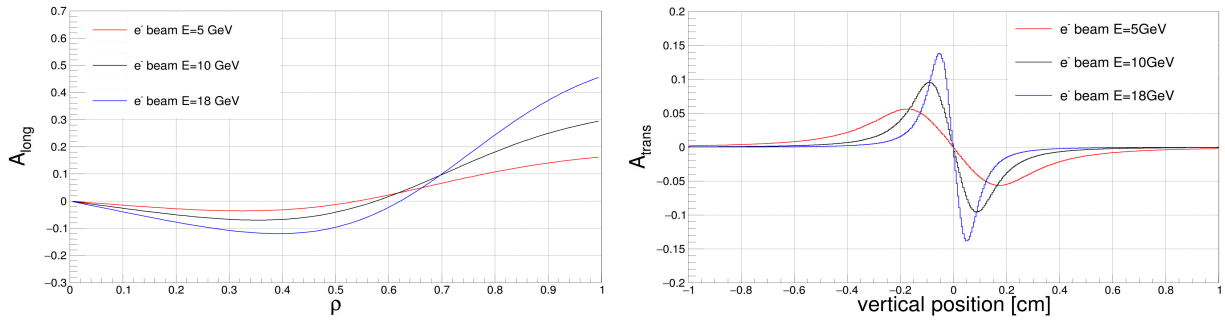

Figure 11.120: Longitudinal (left) and transverse (right) analyzing powers assuming a 532 nm wavelength laser colliding with an electron beam at 5 GeV, 10 GeV, and 18 GeV. The transverse analyzing power is shown for photons projected 25 m from the collision point and plotted vs. the vertical position.

can be accommodated. A schematic of the placement of the Compton polarimeter at IP 12 is shown in Fig. 11.121.

As noted above, a key requirement of the Compton polarimeter is the ability to make polarization measurements for an individual bunch. The measurement time to achieve a statistical precision dP/P is given by a combination of the luminosity, Compton cross section, and analyzing power:

$$t_{meth} = \left(\mathcal{L}\, \sigma_{\text{Compton}}\, P_e^2 P_\gamma^2 \left(\frac{dP_e}{P_e} \right)^2 \text{A}_{\text{eff}}^2 \right)^{-1} . \tag{11.12}$$

The effective Compton analyzing power, A_{eff}, depends on the measurement technique; in order of increasing effective analyzing power, these are integrated, energy-weighted integrated, and differential. For measurement time estimates here, we will use the smallest analyzing power (i.e., integrated) to be conservative.

Nominal electron beam parameters at IP 12 are provided in Table 11.31. Of particular note is the relatively short bunch lifetime at 18 GeV. Table 11.32 shows the average transverse analyzing power, luminosity, and time required to make a 1% (statistics) measurement of the beam polarization for an individual bunch, assuming a single Compton-scattered event per crossing. The constraint of having a single event per crossing is related to the need to make a position sensitive measurement at the photon and electron detectors. Note that even with this constraint, the measurement times are relatively short and, in particular, shorter than the bunch lifetime in the ring.

beam property	5 GeV	10 GeV	18 GeV
Bunch frequency	99 MHz	99 MHz	24.75 MHz
Beam size (x)	390 μm	470 μm	434 μm
Beam size (y)	390 μm	250 μm	332 μm
Pulse width (RMS)	63.3 ps	63.3 ps	30 ps
Intensity (avg.)	2.5 A	2.5 A	0.227 A
Bunch lifetime	>30 min	>30 min	6 min

Table 11.31: Beam parameters at IP12 for the EIC nominal electron beam energies.

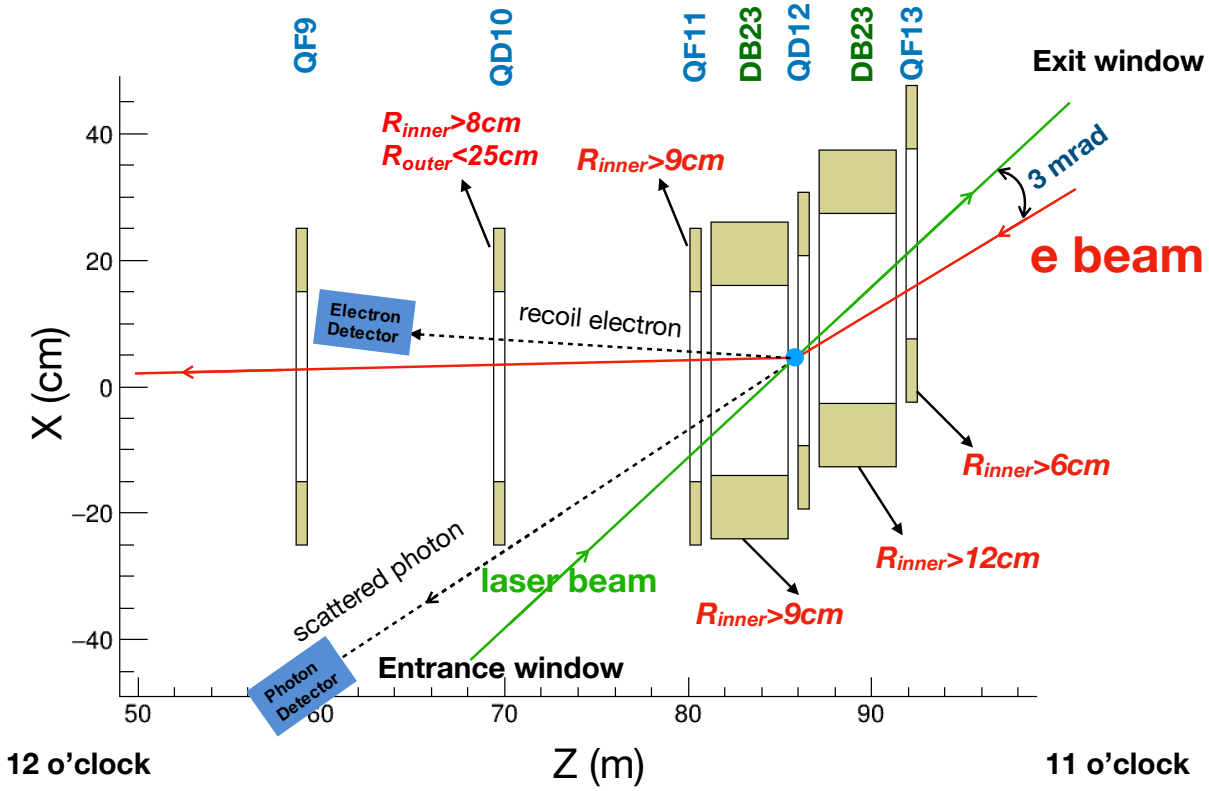

Figure 11.121: Layout of the Compton polarimeter at IP 12. In this figure the electron beam travels from right to left - the laser beam collides with the electrons just downstream of QD12. The dipole just downstream of the collision (DB12) steers the unscattered electrons allowing detection of the backscattered photons about 25 m downstream of the collision. DB12 also momentum-analyzes the scattered electrons, facilitating use of a position sensitive electron detector downstream of QD10. Also noted in the figure are constraints on required apertures of the magnets needed to allow transport of the laser beam, backscattered photons, and scattered electrons.

beam energy [GeV]	σ_{unpol} [barn]	$\langle A_\gamma \rangle$	t_γ[s]	$\langle A_e \rangle$	t_e[s]	L[1/(barn·s)]
5	0.569	0.031	184	0.029	210	1.37E+05
10	0.503	0.051	68	0.050	72	1.55E+05
18	0.432	0.072	34	0.075	31	1.81E+05

Table 11.32: Asymmetries, measurement times needed for a 1% statistical measurement for one bunch and needed luminosities for three different beam energies for a 532 nm laser.

Even for a single electron bunch (circulating through the ring at a frequency of ≈75 kHz), the luminosities provided in Table 11.32 can be readily achieved using a single-pass, pulsed laser. Since the electron beam frequency varies with energy, it would be useful to have a laser with variable pulse frequency. A laser system based on the gain-switched diode lasers used in the injector at Jefferson Lab [168] would provide both the power and flexible pulse frequency desired. Such a system would make use of a gain-switched diode laser

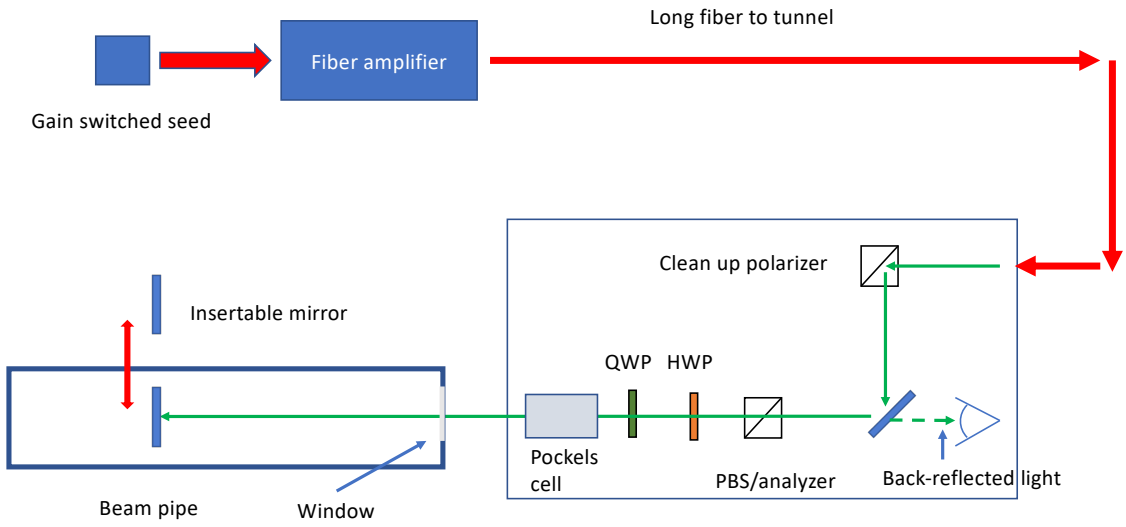

Figure 11.122: Layout of the Compton polarimeter laser system, including diagnostics to accurately determine the laser polarization at the interaction point.

at 1064 nm, amplified to high average power (10-20 W) via a fiber amplifier, and then frequency doubled to 532 nm using a PPLN or LBO crystal. The repetition rate is set by the applied RF frequency to the gain-switched seed laser.

A laser system based on the gain-switched diode lasers used in the injector at Jefferson Lab [168] can provide all of the requirements noted above. The proposed system will make use of a gain-switched diode laser at 1064 nm, amplified to high average power (10-20 W) via a fiber amplifier, and then frequency doubled to 532 nm using a PPLN or LBO crystal. The repetition rate of the laser is dictated by an applied RF signal and can be readily varied. In addition to the laser system itself, a system to set up and measure the laser polarization at the interaction point is required. Determination of the laser polarization in the beamline vacuum is non-trivial due to possible birefringence of the beamline window under mechanical and vacuum stress. We will employ a technique similar to that used at Jefferson Lab [169, 170] that makes use of optical reversibility theorems to determine the laser polarization inside the vacuum using light reflected backwards through the incident laser transport system. This polarization monitoring and setup system will require a remotely insertable mirror in the beamline vacuum so will need to be considered in the beamline design. A schematic of the proposed laser system is shown in Fig. 11.122.

The detector requirements for the EIC Compton polarimeters are dictated by the requirement to be able to measure the transverse and longitudinal polarization simultaneously. For longitudinal polarization, this means the detectors will require sensitivity to the backscattered photon and scattered electron energy. The photon detector can make use of a fast calorimeter, while the electron detector can take advantage of the dispersion introduced by the dipole after the collision point to infer the scattered electron energy from a detector with position sensitivity in the horizontal direction.

To measure transverse polarization, position sensitive detectors are required to measure the up-down asymmetry. This is particularly challenging given the very small backscattered photon cone at the highest EIC

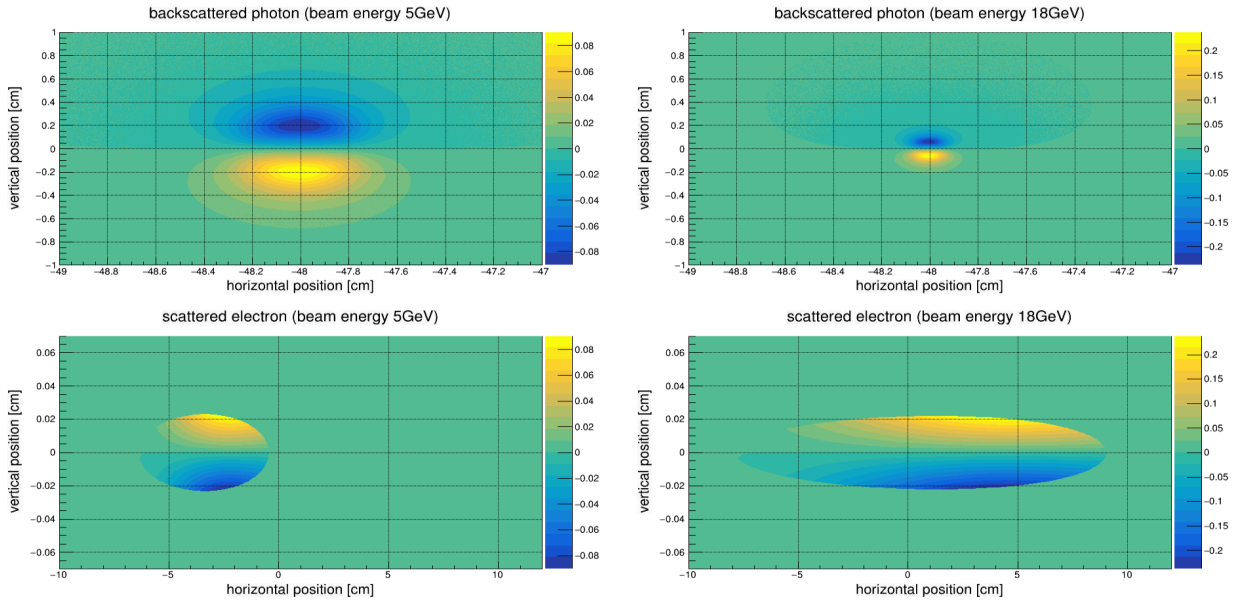

Figure 11.123: Compton (transverse) analyzing power at the nominal photon and electron detector positions for the IP 12 polarimeter.

beam energy. At HERA, the vertical position of the backscattered photon was inferred via shower-sharing between the optically isolated segments of a calorimeter [171]. Calibration of the non-linear transformation between the true vertical position and the energy-asymmetry in the calorimeter was a significant source of uncertainty. The proposed detector for the EIC Compton will measure the vertical position directly via segmented strip detectors, avoiding the calibration issues faced at HERA.

The transverse Compton analyzing power vs. position at the detector for the backscattered photons and scattered electrons at 5 and 18 GeV is shown in Fig. 11.123. The backscattered photon cone will be largest at the lowest energy (5 GeV) - this will determine the required size of the detector. The distribution at 18 GeV, where the cone is the smallest, sets the requirements for the detector segmentation. Note that the scattered electrons are significantly more focused than the photons. Monte Carlo studies indicate that the transverse polarization can be reliably extracted at 18 GeV with a vertical detector segmentation of 100 μm for the photon detector and 25 μm for the electron detector. The detector size should be at least 16 x 16 mm^2 for the photons and 10 cm x 1 mm for the scattered electrons. The horizontal segmentation for the electron detector can be much more coarse due to the large horizontal dispersion introduced by the dipole.

Diamond strip detectors are a feasible solution for both the photon and electron detectors. Diamond detectors are extremely radiation hard and are fast enough to have response times sufficient to resolve the minimum bunch spacing (10 ns) at EIC. Tests of CVD diamond with specialized electronics have shown pulse widths on the order of 8 ns [172]. For the photon detector, about 1 radiation length of lead will be placed in front of the strip detectors to convert the backscattered photons. As an alternative to diamond detectors, HVMAPS detectors are also under consideration. The radiation hardness and time response of HVMAPS will need to be assessed to determine their suitability for this application.

As noted earlier, the photon detector will also require a calorimeter to be sensitive to longitudinal components of the electron polarization. Only modest energy resolution is needed; radiation hardness and time response are more important requirements for this detector - a tungsten powder/scintillating fiber calorimeter

would meet these requirements.

Backgrounds are an important consideration for Compton polarimetry as well. The primary processes of interest are Bremsstrahlung and synchrotron radiation. Monte Carlo studies have shown that the contribution from Bremsstrahlung should be small for a beamline vacuum of 10^{-9} Torr. Synchrotron radiation, on the other hand, will be a significant concern. Careful design of the exit window for the backscattered photons will be required to mitigate backgrounds due to synchrotron. The electron detector is not in the direct synchrotron fan, but significant power can be deposited in the detector from one-bounce photons. This can be mitigated by incorporating tips or a special antechamber in the beampipe between the Compton IP and the detector [173]. The electron detector will also be subject to power deposited in the planned Roman Pot housing due to the beam Wakefield. Preliminary simulations indicate the Wakefield power should not be large enough to cause problems, but this will need to be considered in the detailed Roman Pot design.

In addition to measurements in the EIC electron ring, it is important to be able to determine the electron beam polarization in or just after the Rapid Cycling Synchrotron (RCS) in order to facilitate machine setup and troubleshoot possible issues with the electron beam polarization. In the RCS, electron bunches of approximately 10 nC are accelerated from 400 MeV to the nominal beam energy (5, 10, or 18 GeV) in about 100 ms. These bunches are then injected into the EIC electron ring at 1 Hz. The short amount of time each bunch spends in the RCS, combined with the large changes in energy (and hence polarimeter analyzing power and/or acceptance) make non-invasive polarization measurements, in which the the RCS operates in a mode completely transparent to beam operations, essentially impossible. However, there are at least two options for making intermittent, invasive polarization measurements.

The first, and perhaps simplest from a polarimetry perspective, would be to operate the RCS in a so-called "flat-top" mode [174]. In this case, an electron bunch in the RCS is accelerated to its full or some intermediate energy, and then stored in the RCS at that energy while a polarization measurement is made. In this scenario, a Compton polarimeter similar to that described above could be installed in one of the straight sections of the RCS. The measurement times would be equivalent to those noted in Table 11.32 (since those are for a single stored bunch), i.e., on the order of a few minutes.

Another option would be to make polarization measurements in the transfer line from the RCS to the EIC electron ring. In this case, one could only make polarization measurements averaged over several bunches. In addition, the measurement would be much more time consuming due to the low average beam current ($\approx$ 10 nA) since the 10 nC bunches are extracted at 1 Hz.

The measurement time at 10 nA using a Compton polarimeter similar to the one planned for IP12 would take on the order many days. The IP12 Compton limits the number of interactions to an average of one per crossing to be able to count and resolve the position of the backscattered photons. A position sensitive detector that could be operated in integrating mode, would allow more rapid measurements. However, the required position resolution (25-100 μm) would be very challenging for a detector operating in integrating mode. An alternative to Compton polarimetry would be the use of Møller polarimetry. Møller polarimeters can be used to measure both longitudinal and transverse polarization and can make measurements quickly at relatively low currents. The longitudinal and transverse Møller analyzing powers are shown in Fig. 11.124 and are given by,

$$A_{ZZ} = -\frac{\sin^2\theta^*(7+\cos^2\theta^*)}{(3+\cos^2\theta^*)^2}, \tag{11.13}$$

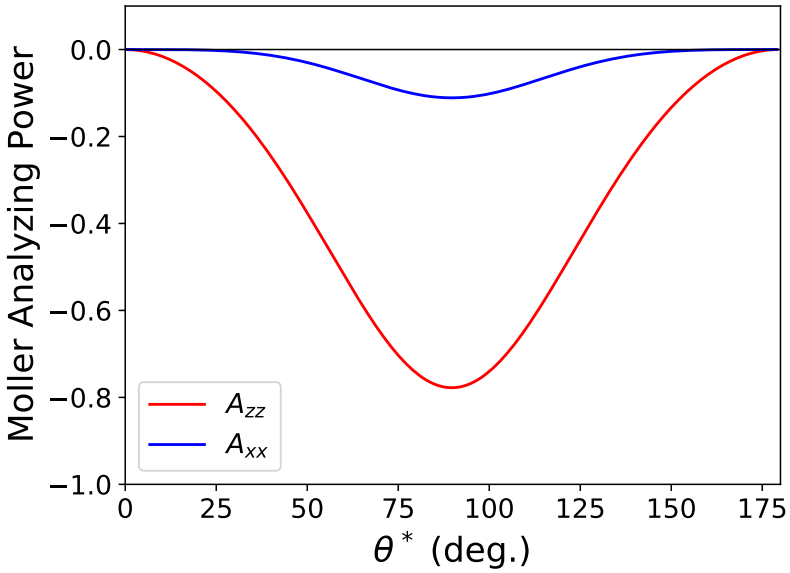

Figure 11.124: Analyzing power for longitudinally polarized beam and target electrons (A_{zz}) and transversely polarized beam and target electrons (A_{xx}) vs. center of mass scattering angle, θ^*. The magnitude for both is largest at θ^* = 90 degrees; $A_{ZZ} = -7/9$ and A_{XX}=-1/9.

$$A_{XX} = -\frac{\sin^4\theta^*}{(3+\cos^2\theta^*)^2}, \tag{11.14}$$

where A_{ZZ} is the analyzing power for longitudinally polarized beam and target electrons, A_{XX} for horizontally polarized beam and target electrons, and θ^* is the center-of-mass scattering angle. Note that $A_{YY} = -A_{XX}$. The magnitude of the analyzing power is maximized in both cases at $\theta^* = 90$ degrees, where $|A_{ZZ}| = 7/9$ and $|A_{XX}| = 1/9$.

Møller polarimeters at Jefferson Lab can make (longitudinal) polarization measurements with a statistical precision of 1% at average beam currents of 1 μA with a 4 μm iron foil target in about 15 minutes. Electrons from the RCS will be transversely polarized, and the analyzing power will be a factor of 7 smaller, which implies a factor of 50 increase in measurement time for the same precision. This smaller analyzing power combined with the low average beam current results in very long measurement times. These long measurements times can be partially mitigated through the use of thicker target foils. Even then, the measurements still take a significant amount of time - 1.5 hours for a 10% measurement of the polarization using a 30 μm target. While target foil thicknesses of 10-30 μm have routinely been employed in Møller polarimeters, it is possible that even thicker targets (perhaps a factor of 10 thicker) could also be used, reducing the measurement time further. The maximum useful target thickness would need to be investigated.

A key drawback of Møller polarimetry is that the solid foil targets are destructive to the beam, so cannot be carried out at the same time as normal beam operations. An additional complication is the requirement for a magneto-optical system to steer the Møller electrons to a detector system. In the experimental Hall A at Jefferson Lab, the Møller spectrometer employs several quadrupoles of modest length and aperture, combined with a dipole to deflect the Møller electrons into the detector system (see Fig. 11.125). The whole

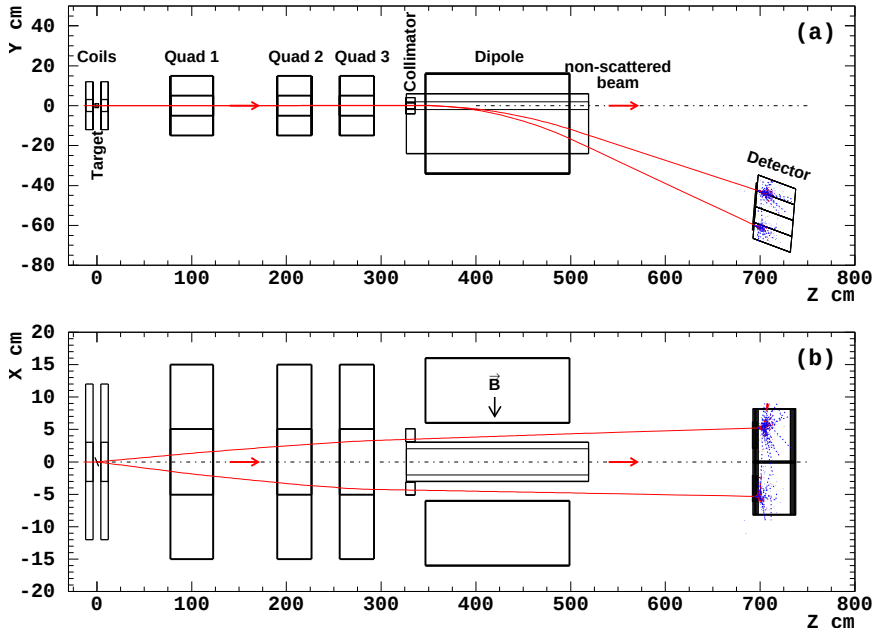

Figure 11.125: Layout of the Møller polarimeter in experimental Hall A at Jefferson Lab.

system occupies about 7 m of space along the beamline, but the space used by the quadrupoles can also be used for beam transport during normal operations (i.e., when Møller measurements are not underway).

The preferred choice for polarimetry at the RCS is a Compton polarimeter in the RCS ring, with measurements taking place during "flat-top" mode operation. However, if this "flat-top" mode is not practical, then a Møller polarimeter in the RCS transfer line could serve as a reasonable fallback, albeit with reduced precision and a larger impact on the beamline design.

11.8.2 Hadron Polarimetry

Hadron polarimetry has been successfully performed on RHIC polarized proton beams for nearly two decades. Through continual development a systematic uncertainty $\sigma_P^{\text{syst}}/P < 1.5\%$ [175] was achieved for the most recent RHIC polarized proton run. After improving data analysis, systematic uncertainties in measurement of the beam profile averaged polarization were reduced to $\sigma_P^{\text{syst}}/P \lesssim 0.5\%$ [176]. As the only hadron polarimeter system at a high energy collider it is the natural starting point for hadron polarimetry at the EIC.

Hadron polarization is typically measured via a transverse single spin left right asymmetry: $\epsilon = A_N P$. Unlike for polarized leptons, the proportionality constant is not precisely known from theory. The solution at RHIC employs an absolute polarimeter with a polarized atomic hydrogen jet target (HJET) [177], illustrated in Fig. 11.126. The hydrogen polarization vector is alternated between vertically up and down. The RHIC beam also has bunches with up and down polarization states. By averaging over the beam states the asymmetry with respect to the target polarization may be measured, and vice versa:

$$\epsilon_{\text{target}} = A_N P_{\text{target}} \quad \epsilon_{\text{beam}} = A_N P_{\text{beam}} \, . \tag{11.15}$$

The target polarization is precisely measured with a Breit-Rabi polarimeter. Combined with the measured asymmetries the beam polarization is determined:

$$P_{\text{beam}} = \frac{\epsilon_{\text{beam}}}{\epsilon_{\text{target}}} P_{\text{target}} \ . \tag{11.16}$$

The absolute polarization measurement is independent of the details of A_N.

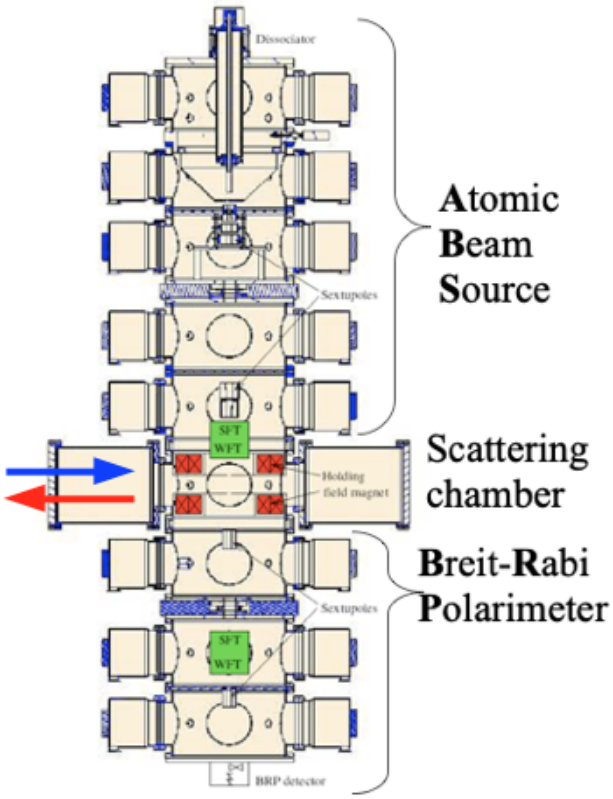

Figure 11.126: The RHIC polarized hydrogen jet polarimeter. The atomic beam source at the top passes polarized hydrogen across the beams (blue and read arrows) in the scattering chamber, with detectors left and right of the beams. The atomic hydrogen polarization is measured by the Breit-Rabi polarimeter at bottom.

Even though, the diffuse nature of the polarized jet target provides only a relatively low rate of interactions, continuous operation during the store resulted in statistical precision of the polarization measurement of about $\sigma_P^{\text{stat}} \sim 2\%$ per 8–hour RHIC fill (in Run 17). These measurements, however, are not sensitive to the inevitable decay of beam polarization throughout a fill. Also, the jet target is wider than the beam and measures only the average polarization across the beam. The beam polarization is larger at the center than the edges transversely; the polarization of colliding beams differs from the average polarization due to this effect [178]. The polarimeters must measure this transverse polarization profile to provide correct polarizations for use by collider experiments.

At RHIC the required finer grained polarization details are provided by the proton-carbon (pC) relative polarimeter, illustrated in Fig. 11.127. A thin carbon ribbon target is passed across the beam and scattered carbon nuclei are measured in detectors arrayed around the beam. The dense target provides a high interaction rate, allowing an asymmetry measurement with a few per cent statistical precision in less than 30

seconds. Such measurements are made periodically throughout a RHIC fill, providing a measurement of the beam polarization decay. The ribbon target is narrower than the beam; thus it is able to measure asymmetry as a function of position across the beam and determine the transverse polarization profile. The absolute polarization scale of the pC polarimeter is set by normalizing an ensemble of pC measurements to the results from the Hjet polarimeter for the corresponding RHIC fills.

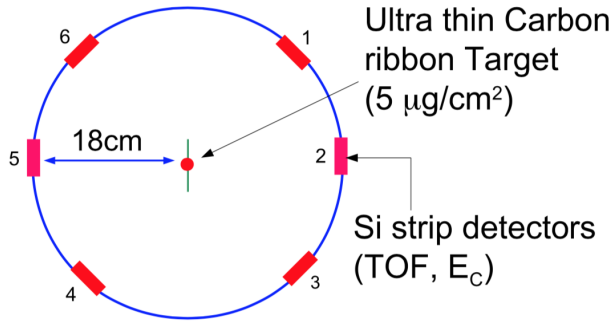

Figure 11.127: Cross section of the RHIC proton-carbon polarimeter. A thin carbon ribbon target is passed across the beam (into page) and scattered carbon nuclei are measured in the six detectors.

Both of the RHIC hadron polarimeters can in principle be used for proton polarimetry at the EIC. At present two significant difficulties are foreseen. First, backgrounds in both polarimeters are observed and lie partially beneath the signal events. They are distinguished by timing distributions different from the signal allowing separation or estimation of a subtraction from the signal. At the EIC with higher bunch crossing frequency, the backgrounds will lie under the signal events from adjacent bunches and separation or subtraction based on timing will not be possible. Studies are under way to determine the nature of the background and possibly find a rejection method. Second, materials analysis of the carbon ribbon targets indicates that the the higher proton beam currents and bunch crossing frequencies at the EIC will induce heating to temperatures causing the targets to break after only a few seconds in the beam. A search for alternative target materials has been initiated.

A possible alternative to the pC polarimeter has been proposed. It is based on the observation by the PHENIX collaboration of a large azimuthal asymmetry of forward neutrons in the proton direction in p+Au collisions [179]. This effect is well described by a process of the high Z Au nucleus emitting a photon, which produces neutrons off of the polarized proton [180]. A polarimeter based on this process would replace the Au beam with a high Z fixed target as a source of photons; a Xe gas jet may be a suitable target. Such a polarimeter could be tested at RHIC in the final years of operation.

For light ion polarimetry at the EIC, the following methods can be considered:
– Using a polarized light ion jet target. Similarly to the proton beam measurement with hydrogen jet target, the light ion beam polarization is given by Eq. (11.16). Tagging of breakup of beam nuclei may be necessary to isolate the elastic scattering signal required for an absolute polarization measurement. However, a preliminary evaluation, based on deuterium beam scattering at HJET, indicates that the breakup contamination of the elastic data is small, only few percent, and, thus, the correction to Eq. (11.16) is expected to be negligible.
– Using polarized hydrogen jet target to measure light ion, e.g. He-3 (h), beam polarization. Since the

beam and target particles are not identical, Eq. (11.16) should be corrected

$$P_{\text{beam}} = \frac{\epsilon_{\text{beam}}}{\epsilon_{\text{target}}} P_{\text{target}} \times \frac{\kappa_p - 2\text{Im}\, r_5^p - 2\text{Re}\, r_5^p\, T_R/T_c}{\kappa_h - 2\text{Im}\, r_5^h - 2\text{Re}\, r_5^h\, T_R/T_c} \tag{11.17}$$

where, $\kappa_p = \mu_p - 1 = 1.793$ and $\kappa_h = \mu_h/2 - 1/3 = -1.398$ are parameters derived from magnetic moments of proton and He-3, r_5^p and r_5^h are hadronic spin flip amplitudes [181] for $hp^\uparrow$ and $h^\uparrow p$ scattering, respectively, T_R is the recoil proton kinetic energy and $T_c = 4\pi\alpha Z_h/m_p\sigma_{\text{tot}}^{hp} \approx 0.7\,\text{MeV}$. Since $|r_5| = O(1\%)$ are small, such measured absolute He-3 beam polarization will meet the EIC requirement if r_5^p and r_5^h can be related, with theoretical uncertainties better than 30–50%, to the proton-proton r_5 experimentally determined at HJET [182].

– Using low energy technique, e.g. [183], determine absolute light ion polarization in source and, than, monitor beam polarization decay and profile with beam acceleration control tools. This method is expected to work well if the beam polarization losses will be small at EIC. However, for a precision calibration, alternative measurements of the absolute polarization may be needed.

The pC polarimeter or an alternative developed for protons at the EIC should also provide suitable relative polarimetry for light ions.

The main polarimeters may be situated anywhere in the EIC hadron ring. The Hjet and pC polarimeters each require 1-2 m space along and transverse to the beam. However, one relative polarimeter (pC or alternative) should be placed near the experimental interaction point between the hadron spin rotators. The hadron polarimeters are only sensitive to transverse spin polarization. During longitudinal spin runs asymmetry measurements near the interaction point are required to verify that the transverse component of the spin direction is zero.

11.9 Readout Electronics and Data Acquisition

11.9.1 Introduction

The Readout Electronics and Data Acquisition system is a key component for the future EIC detectors. The readout electronics is responsible of processing the electric signals from the various detector sensors and converting them into a numerical representation that can be handled by a digital system. The DAQ system, in an other hand, is responsible of collecting, filtering, and storing these data. The overall system must be designed keeping into account the constraints dictated both by the physics program and by the operation environment.

For these reasons, the architecture of the readout system has a very strong impact on the physics program that can be performed at the future EIC experiments. The front-end electronics have to be adapted to the characteristics of the sensors to be equipped, and to the measurements which have to be done with them. And in the same time the DAQ system must offer performance adapted to the data flow coming from these front-end electronics. Filtering features of the DAQ system could be required, in order to maintain the data flow at acceptable level, taken into account the limitation in term of bandwidth of this system. But such a feature would affect directly the EIC physics outcome, since any data discarded at the online level will be lost irretrievably - a careful design, construction, and validation of this system is thus necessary.

This section aims to review the possible solutions on which the readout and DAQ system for the EIC experiments could be built. Hypothesis in term of detector characteristics and data flux are considered, leading to a reflection on the possible architecture on which the DAQ system could be based. Efforts made to validate the proposed architectures are also described. At last a description of the state of the art of the detector front-end electronics is proposed, with a few hypothesis on what could be the possible evolution in this domain.

11.9.2 Glossary

Several terms used in the DAQ and readout electronics domains could be ambiguous or meant differently from one reader to the other. In order to lift up the ambiguities several of these terms are defined below. These definitions are the reference for the whole section.

11.9.2.1 Readout electronics terms

Front-end electronics (FEE): The electronics which amplify and put in shape the signals of the detector. After this stage the analog signals are generally digitized using analog-to-digital (ADC), charge-to-digital (QDC), or time-to-digital (TDC) converters [3]. FEE is typically associated to data treatment, data bufferization and logic for data transfer to the downstream element in the read-out and DAQ chain. Digitization and data treatment stages are often directly integrated in some of the existing front-end chips.

Amplification stage: groups the preamplifier + amplifier/shaper of the detector raw analog signals

Embedded amplification stage: preamplifier + amplifier/shaper directly integrated into the detector hardware

Digitization stage / Digitizer: transforms amplified signal into digital values (amplitudes, charges and/or times)

Bufferization / data concentration stage: setup which concentrates and stores temporarily digital values from several digitizers before to send them to the DAQ, could do data selection and/or reconstruction

Peaking time: time between the beginning of the pulse and its maximum after the amplification/shaping stage

Occupation time: time between the beginning and the end of the pulse after the amplification/shaping stage

Analog memory: temporary storage of samples of analog signals, generally made of capacitor arrays, before digitization. Allow to select the samples which will be digitized

Amplifier chip: ASIC which groups the preamplifier and the amplifier/shaper

Digitizing amplifier chip: ASIC which groups the amplification and the digitization stages

[3] TDC: digitizer which measures times of amplified signals going above a given threshold.

11.9.2.2 Data acquisition system terms

Triggered readout: A data acquisition system in which some data from a subset of detectors ("trigger data") is sent to a dedicated subsystem to produce a trigger decision. This is usually a hardware system, generally based on programmable devices such as FPGAs. The trigger decision is based on a partial elaboration of the "trigger data". "Trigger primitives" are reconstructed and analyzed to assess whenever all the data from the detector has to be stored for later analysis. In this case, a proper signal is sent back to all the readout elements to control the conversion of detector signals into the digital domain, or to trigger the read-out of a data-window from a continuously filled buffer. A key aspect of a triggered readout system is the fixed latency between the physical event time (FE → Trigger system) and the trigger time (Trigger system → FE) - in case of systems with multiple trigger levels, this is true for the first-level trigger.

Pipelined/buffered readout: A triggered readout system where event data is stored on the front ends and read out asynchronously by the backend when the trigger signal is received.

Second-level / high-level filtering: In triggered systems, higher-level triggers are often used to reduce deadtime (via a fast clear) or data amount (by dropping the so-far recorded data for that event). Each level in such a system typically has different time constraints and complexity limits. For example: a certain time frame could not be forwarded to the tracker if certain conditions are not met. In certain, complex, triggered setups, the later stages can resemble a streaming system, where a stream of events flows through a network of analysis nodes, and data selection criteria either accept or drop the event. The main remaining difference for this part is then that the data is organized and tagged by an event number instead of time stamps.

Streaming readout (SRO): A data acquisition system characterized by a unidirectional data flow from front-end electronics to the storage system. Each channel, independently, records data over a certain threshold and streams them to a CPU farm for further elaboration. In a streaming readout system there are no dedicated systems to control the conversion into the digital domain or readout of a buffer. Different implementations of streaming readout are possible, depending on the manipulations and filtering applied online to the data.

Unfiltered readout: A streaming data acquisition system without any system dedicated to event filtering / building. Only minimal zero suppression at the front-end level is adopted. Data is streamed directly from the front-end electronics to the storage system. Each detector hit is saved together with its time-stamp.

Zero suppression: Removal of data if close to the no-signal level of the detector. For example, in ADC data, removal of the signal digital values below a given threshold.

Noise suppression: Removal of data produced by intrinsic or extrinsic detector noise, for example by correlation with neighboring channels or shape analysis.

Feature extraction: Calculation of higher-level information. E.g. calculation of hit time and energy from ADC[4] samples, or calculation of track information from hits. Often, but not necessarily, accompanied with the removal of the underlying lower-level data.

[4] ADC: digitizer which measures the amplitude of one or several samples of the amplified signals.

Online Physics analysis: Analysis of the high-level information provided by the feature extraction steps to produce physics-relevant information (e.g. missing mass).

Data selection: In a SRO system, data can be algorithmically selected for further processing and long-term storage. Not selected data is dropped and not further processed. This is equivalent to the function of first and higher-level triggers in triggered systems but can make use of all detector information and results from further analysis steps including feature extraction and online physics analysis.

11.9.3 Overview on DAQ Structure

Most of the past and currently running particle-physics experiments adopt a DAQ system based on a triggered setup, usually with a multi-layer architecture. Usually the first data reduction is achieved by using dedicated boards where a significant filtering is applied by selection algorithms implemented on FPGAs, while the subsequent trigger layers are based on software components: a CPU farm reduces the data stream to a manageable size for storing and off-line processing and applies a second, more sophisticated, level of filtering. The main limitations of a FPGA-based trigger, where FPGAs are actively involved in the events-selection, reside in: the difficulty of implementing algorithms over a certain degree of complexity and sophistication; the difficulty of optimizing the selection criteria that requires reprogramming the boards each time a change is implemented; the partial information accessible at front-end level both in the term of quality (usually it incorporates only basic calibration) and quantity (trigger is usually performed using a limited subset of the full detector).

These limitations may directly affect the ultimate detector performances and the quality of recorded data since only partial information is available at trigger level, when the decision whether to write or not an event to tape has to be taken. Another drawback of this approach consists in the difficulty of changing the FPGA-board in case of unexpected experimental configuration changes or upgrades requiring more trigger resources.

At the same time, complicated hardware or firmware implementations of trigger logic are hard to characterize, for example via software simulations aimed to find their efficiencies and their intrinsic dead times. This can lead to significant challenges in controlling systematic uncertainties.

All these issues are largely solved when moving to a full (CPU) software-based system. The FPGA-based system may be replaced by a fully triggerless approach that removes the hardware trigger, performs the full on-line data reconstruction and provides precise selections of (complicated) final states for further high level physics analysis (a similar effort is currently faced at LHC in preparation for the high luminosity upgrade).

In a triggerless data acquisition scheme, each channel over a threshold implemented on the front-end electronics is transferred after being labeled with a time-stamp, disregarding the status of the other channels. A powerful station of CPUs (usually an on-line farm), connected by a fast network link (usually optical fibers) to the front-end electronic, receives all data from the detector, reorganizes the information ordering hits by time, includes calibration constants, and, at the end, applies algorithms to find specific correlations between reconstructed hits (online event reconstruction), eventually keeping and storing only filtered events. Advantages of this scheme rely in: making use of fully reconstructed (and corrected) hits to define a high-level events selection condition; online algorithms implementation in a high-level programming language; easy reprogramming to upgrade the system configuration and accommodate new requirement. Furthermore, the system can be scaled to match different experimental conditions (unexpected or foreseen in a planned upgrade) by simply adding more computing (CPUs) and/or data transfer (network switches) resources. We

underline that FPGAs are still used in a streaming-readout DAQ system, not to take decisions concerning events to select, but to make more "low-level" tasks such as adding the time-stamp to the data or canalize the data.

A triggerless option may result in: on-line implementation of calibration parameters, providing a more precise reconstruction of the kinematic quantities; implementation of more sophisticated reconstruction algorithms for a better reconstruction of close-by tracks; improvement in EM/hadron discrimination for a more efficient background rejection.

These considerations directly apply to the EIC. The EIC physics program will be carried out by measuring different reactions with at least one electron in the final state. Electromagnetic calorimeters will thus play a key role in the online events selection and filtering. For these sub-detectors, a triggerless option may result in: on-line implementation of calibration constants to compensate for longitudinal and transverse EM shower leakage and gain variation, providing a more precise reconstruction of the energy deposition (and therefore an improvement in the ultimate energy resolution); implementation of more sophisticated clustering algorithms for a better reconstruction of close-by tracks allowing to resolve gammas from π^0 in a wider kinematics; improvement in EM/hadron shower discrimination for a more efficient pion rejection.

A triggerless scheme will facilitate future extensions of the envisaged EIC physics program. For instance, hadron spectroscopy requires to identify rare exclusive finals states difficult to access experimentally (e.g. kaon-rich reactions). This would require to set and add multiple and sophisticated algorithms to select the physics of interest. Same rational is valid for other physics program that will be considered in the future.

The triggerless scheme is also an opportunity to extend the integrated IR-detector design to analysis to optimize physics reach as described above and to streamline workflows. A seamless data processing from DAQ to analysis would allow for a combined software effort for the triggerless scheme, online and offline analysis and to utilize emerging software technologies, e.g. AI / ML, at all levels of the data processing. A near real-time analysis at the EIC with auto-alignment and auto-calibration of the detectors and automated data-quality monitoring would enable significantly faster access to physics results and accelerate science.

For these reasons, we propose to design and develop a full streaming-readout DAQ system for the EIC detector, integrating all the sub-detector components.

11.9.4 Constraints and Environment

The EIC readout and DAQ system should be designed considering the following constraints, dictated both by the physics program (measurements to be performed) and by the experimental environment. The overall goal for the system, as an integrated component of the EIC detector, is to make it possible to complete the challenging EIC Science program, providing a seamless integration from the DAQ to the physics analysis.

The EIC detector will be made by many sub-components, based on different technologies and with different requirements concerning the values to be measured by them. This translates into specific constraints on each readout solution, in terms of needs and performances. In general, each sub-detectors will introduce its own requirements on the FEE parameters (shaping time, peaking time, gain, ...). For example, it is anticipated that one of the most realistic options to read out EIC calorimeters will be SiPM (or matrix of SiPM's) photosensors. It is expected that to realize the electronics readout chain a novel FE ASIC chip will be developed: the ADC board would provide the bias voltage to the SiPM and allow for signal amplification, processing and readout, including possibly the recording of the raw waveform. Similarly, each sub-detector

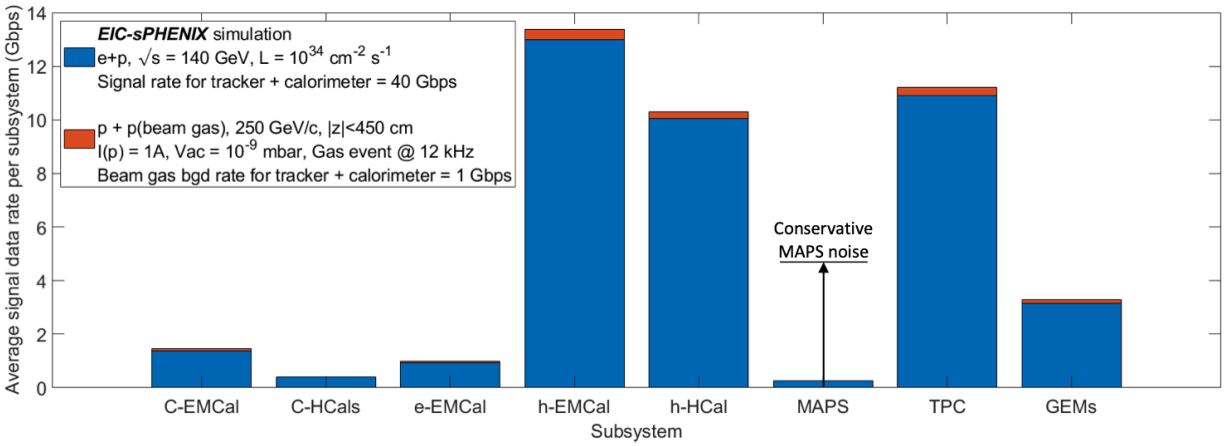

Figure 11.128: Collision data rate from each detector subsystem for the EIC sPHENIX detector model, at luminosity $\mathcal{L} = 10^{34}$ cm^{-2}s^{-1} [184, 185]. The total collision signal is approximately 100 Gbps, including a conservative estimate of the MAPS noise motivated by the recent ALICE ITS2 experience. We note this rate include collision signal only to record down all EIC physics events. In case excessive background rate, e.g. synchrotron photon hits, are observed, further noise and background filtering would be required.

will be characterized by different radiation levels, affecting the choice of the readout technology.

The number of channels anticipated for the EIC detector readout is shown in Fig. 11.129; a relatively small number of channels are not included. It is anticipated that three, and possibly four, different readout solutions will address the front-end readout needs of the various types of detectors.

The main constraint on the DAQ system is the total data rate to be processed, including both the signal (i.e. physics reaction of interest for the EIC physics program) and the background. A preliminary estimate of the total collision signal rate from the EIC detector was discussed in [186], assuming $e + p$ collisions at $\mathcal{L} = 10^{34}$ cm^{-2}s^{-1} and the sPHENIX-based detector concept [184, 185]. The calculation includes, for each component of this specific EIC detector model, the signal data rate from $e + p$ collisions and also from $p - p$ (beam-gas) interaction, and also considers a conservative estimate of the MAPS noise motivated by the recent ALICE ITS2 experience. The result is summarized in Fig. 11.128: a total collision signal rate from the EIC detector of approximately 100 Gb/s is expected.

Further constrains are introduced by the requirement of having, during EIC operations, an immediate online feedback concerning detector performance and data quality. Finally, the engineering requirements related the concrete EIC detector construction and assembly will introduce further constraints on the readout and DAQ system: available space, rating and standards to be satisfied, cooling power availability.

11.9.5 Readout Electronics: Present State of the Art

11.9.5.1 Introduction

The role of the readout electronics for an experiment like EIC is crucial. The quality of the data delivered by the data acquisition system will be directly dependent of the performance of each element of the readout chain. The characteristics of these elements should be in accordance with the characteristics of the detectors

Detector	Sub-system	Type	Sub-type	Channels
Tracking				
	Silicon Vertex Tracker	Si	Pixel	200M
	TPC	GEM	Pads	160K
	GEM	GEM	Strips	217K
	uRWELL	GEM	Strips/Pads	
	Cylindrical Micromegas	GEM	Strips	
	Drift Chambers	DWC	Wires	
	sTGC	GEM	Pad, Strip, Wire	
	Straw Tubes	Straw	Wires	
Calorimetry				
	e-EMCal	Cal	PMT/SiPM	5k
	C-EMCal	Cal	PMT/SiPM	24k
	h-EMCal	Cal	PMT/SiPM	26k
	h-Hcal	Cal	PMT/SiPM	3k
	c-Hcals	Cal	PMT/SiPM	2.8k

Detector	Sub-system	Type	Sub-type	Channels
PID				
	mRICH @ e-endcap	RICH	PMT/SiPM	
	dRICH @ h-endcap	RICH	PMT/SiPM	300k
	GEM RICH	GEM	Strips	220k
	hpDIRC @barrel	DIRC	PMT/SiPM	100k
	psTOF @barrel	TOF	PMT/SiPM	
	LGAD TOF	TOF	PMT/SiPM	
	LAPPD/MCP-PMT TOF	TOF	PMT/SiPM	
Far Forward Detectors				
	ZDC		PMT/SiPM	
	Low Q2 tagger		PMT/SiPM	
	Luminositymonitors		PMT/SiPM	
	Roman Pots	Si Strips	Si	
	Proton Spectrometer		PMT/SiPM	
	Lepton Polarimeter		PMT/SiPM	
	Hadron Polarimeter		PMT/SiPM	

Readout Variant	Channels (actual)	Channels w/+10% Spares	Type
V1	200M	220M	Si
V2	220k+	242k+	Straw/GEM - fADC
V3	377k+	415k+	GEM
V4	461k+	507k+	PMT/SiPM

Figure 11.129: Estimate of the number of different EIC Readout Channels.

which will be read by the electronics, as well as with the constraints which are described in the previous section.

The readout chain for a given detector is formed by electronics cards and chips with different functions: signal pre-amplification, amplification and shaping, digitization, data treatment like common mode noise reduction or zero suppression, data bufferization concentration, and transfer to the DAQ system. Side systems like readout trigger system can be also necessary to reduce the flux of data to be treated by the chain. At last several support systems are necessary in order for the readout electronics to work: clock signal distribution to synchronize all the electronics, slow-control to monitor the electronics behavior, power distribution, etc...

In this section a summary of the state of the art for the different elements of the electronics chain are given, with a few examples. Some of the chips described here regroup several functionalities listed above, for instance amplification and digitization.

11.9.5.2 Front-end electronics

The front-end electronics is there to amplify the signals from the detectors and to put them in a shape compatible with the digitization step. The amplification step is important in particular for detectors which deliver very low amplitude signals, like silicon detectors or gaseous detectors. Other detectors like photomultipliers used in some calorimeters deliver larger signals, so the electronics gain should be lower in order to avoid any saturation. Another important parameter is the shaping applied to the signal, which can be characterized by the ”peaking time”, which is the time taken by the shaped signal to reach its maximum. A short shaping,

for instance a few ns of peaking time, allows to get sharp output signals well adapted for fast detectors and fitted to time measurements, but may also induce a non-optimal noise figure. In an other hand slower shapes, in the order of a hundred of ns, are more adapted to slow detectors, for instance gaseous detectors, in order to integrate the totality of their signal and thus to get a more accurate amplitude measurement. A larger peaking time also induce a larger occupancy of the signal in the readout chain, which may limit the signal rate which can be read by the electronics.

In the current designs proposed for the future EIC experiments which are described in the sections XXX of this document, both silicon and gaseous detectors are considered to measure the trajectory of the secondary particles. However the silicon detectors presently considered, the Monolithic Active Pixel Sensors (MAPS) to be verified with tracking WG, references, integrate directly in the silicon die their own front-end electronics, signal processing and zero-suppression with adjustable threshold. These detectors return addresses of the hit pixels, with typically around 3 pixels per charged particle track. The thresholds are adjusted to give 99% efficiency and less than 10^{-9} fake hit rate.

Several existing chips are dedicated to the readout of small signals coming from gaseous detectors. A few examples of chips used in particle physics experiments are presented below. They are all based on pre-amplifier and amplifier/shaper stages. However the treatment of the signals after these stages vary from one chip to the other, depending on the purpose of these chips. Some of them are more focused on the measurement of the signal time, combining then a fast shaping with a TDC stage, while others are measuring the amplitudes with flash ADCs. 32 to 64 channels are usually read by these chips which are 5 to 15 mm large. Peaking times are usually tunable, with values from 25 ns to 1 μs. Maximum charges accepted by these chips, also usually tunable, cover a range from 50 fC to a few pC. The internal capacitance of the detector channels also play a role in the behavior of the pre-amplification stage. Depending on the design of this stage, a large capacitance, larger than 100 pF for instance, may alter the gain of the preamplifier and thus, of the whole chip. Some pre-amplification designs prevent this effect, allowing the chip to work with large detector capacitance at the level of several hundreds of pF. At last to keep the power consumption as low as possible is an important aspect for highly integrated detectors like the one foreseen for EIC, in order to limit the need of cooling. Power consumption values are typically around 10 to 30 mW/channel.

11.9.5.3 Digitization and data treatment

After amplification and shaping, detector signals are meant to be digitized before to be transmitted to the data acquisition system. Depending on the DAQ structure, signals may be continuously digitized, or the digitization can be triggered only when an interesting event happens. From one kind of chip to the other the digitization strategy can be different. Some chips, like the SAMPA chip (cf section XXX) are indeed able to continuously digitize the signal at a rate of several MHz and to transmit these data to the DAQ. But depending on the kind of detector to be read and the information to be extracted this may or may not an optimal strategy. That strategy is the most demanding in term of ADC performance and output data link bandwidth. Present ADC integrated in readout chips are able to read continuously signals with a sampling rate around 10 to 20 MHz, with a ADC dynamics of 10 bits. Data links of a few Gbit/s are also a common performance of the readout chips. Data treatment may be necessary to reduce the data flux to a scale compatible with the DAQ capacity. Several kinds of algorithms can be applied: common mode reduction which compensate the part of the electronic noise which is common to all channels of a chip, zero suppression which discards the sample measurements below a given thresholds, peak finding, correlation with other detectors which conditions the preservation of the data with data from an other detector, etc... Such data treatments can be

performed directly in the chip, for instance in an integrated DSP, or later by specific DSP electronics in the acquisition chain.

Another strategy which may be more adapted to detectors which do not require to store the full signal waveform, for instance trackers, would be to digitize only specific values like signal amplitude, using a sample & hold (S&H) circuit like in the VMM chip, or signal time. This strategy produces a much lower data flux. A last strategy is to not include any digitization of the signals in the readout chip, but rather to store them in analog memories which are arrays of capacitances, and to transmit in case of triggers the analog signals to commercial ADCs managed by a FPGA. This strategy is adopted by several chips like the AGET, the DREAM or the AFTER. However this strategy is largely incompatible with the streaming readout structure foreseen for the DAQ.

11.9.5.4 Examples of readout chips

Several chips representing the state of the art of the readout electronics are presented here. They concern mostly gaseous detectors and silicon detector front-end readout but their usage may be extended to other cases. The table 11.33 summarizes the characteristics of these chips.

ATLAS VMM and the CERN SRS Architecture: Building upon the highly successful APV25 architecture developed for the CMSexperiment, VMM was built for the ATLAS experiment upgrades, as part of CERN's implementation of the Scalable Readout System (SRS) for micropattern gaseous detectors developed by the RD51 Collaboration. Introduced in 2010 for ATLAS Micromegas and based on the APV25 chips, the SRS extended a modular architecture to integrate disparate ASIC chips to read-out electronics to select the most suitable front-end for the detector technology employed for a particular experiment. In short, SRS offered a modular and scalable architecture to act as a detector-dependent bridge between front-end and read-out sections of any HEP data acquisition architecture, where users could choose from a variety of front-end chips, readout by a central hub called a Scalable Readout Unit (SRU). The architecture is a bit complex, with ASIC-specific firmware modules residing in the FPGA chips on cards, however a large number of channels (maximum limit of up to 16000 channels) and up to 64 Front-end FPGA cards can be supported by the architecture.

The VMM chip was developed at Brookhaven (BNL) as a 64-channel mixed signal ASIC for readout from both the ATLAS Micromegas and sTGC detectors, specifically for the ATLAS Muon Spectrometer's New Small Wheel upgrade. Its first version, viz VMM1, was a bit primitive simple architecture chip, but a lot of functionality and features were added in the second version, known as VMM2. Another version, VMM3, and its revision VMM3a were also produced. The new versions were claimed to contain enhanced features such as deep readout buffer logic, longer TAC (Time-to-Amplitude Converted) ramps, SEU mitigation circuitry as well as handling of higher input capacitance of the order of 1.5 nF. The device (version 3) was fabricated at IBM's foundry with a 130nm MOSFET technology (die size 15.3 x 8.3mm), housing approximately 5.2 million transistors (with nearly 160 k MOSFETs per channel), and produced in a 1mm pitch 400-BGA (Ball Grid Array) package. It is indeed a state-of-the-art mixed signal ASIC device which was perhaps created to achieve the System on Chip (SoC) paradigm.

An excellent feature of the chip are having both time and amplitude (peak) detection circuitry on-board. For each of the 64 channels, a signal obtained from the input pads is amplified by a charge amplifier (CA) and after a shaping circuit (Shaper) is passed over to both a peak detector and time de-

tector working in tandem and giving their respective output to a digitization section. The digitization section is comprised of a novel three-ADC chain in a so-called "Domino Architecture". Output from the peak detector is given to both a 6-bit ADC for feed-thru synchronization/threshold and to a 10-bit ADC for precision read-out, whereas the time detector has its output passed over to an 8-bit ADC for TDC functionality. Outputs from both ADCs are read-out through a FIFO buffer, which is designed to accommodate 4 MHz data in 10μs latency windows. In addition, a 12-bit Gray code time-stamp is provided to facilitate time measurements, which incremented by an external clock provides a cumulative 20-bit timing information. The chip tests claim peak detection digitization process to complete in 25 ns. The chip also features a novel third-order filter and shaper architecture with a DDF (Delayed Dissipative Feedback) topology. This architecture results into a higher dynamic range, enabling the measurement to achieve a relatively high resolution at very low input capacitance ($\ll$200 pF). The architecture offers a variable gain in eight values (from 0.5, 1, 3, 4.5, 6, 9, 12, to 16 mV/fC) with four possible shaping time intervals, viz. 25, 50, 100, and 200 ns.

Two VMM chips are soldered on a FEC card in association with a Virtex-6 FPGA for a so far maximum streaming read-out rate of 1G-bit/s. However, theoretically, an ideal 9.7 Gbit/s should be achieved in principle by the ASIC, independent of FPGA and other logic. In short, the VMM chip's latest versions seem to achieve the promised sub-fC and sub-ns resolutions at 200 pF and 25 ns capacitance and time windows, respectively.

TIGER: TIGER is an acronym for the Torino Integrated GEM Electronics for Readout, a mixed signal ASIC chip first developed at INFN Torino. It is a general-purpose chip for readout from gaseous detectors with up to 64 channels, fabricated with a 110nm CMOS technology (fabricated on a die area of 5×5 mm2). While featuring a low-noise level of less than 2000 e^-, the chip offers a high input dynamic range of 2.0 to 50.0fC and gains of 12.4 mV/fC for time and 11.9 mV/fC for energy measurements, with time intervals of 60ns and 170ns, respectively. There is a provision of an on-chip calibration circuit which allows injected external pulses to calibrate the amplifiers and exploit the full input dynamic range. The signal conditioning circuitry in the time and energy measurement sections comprise both discriminator and pulse shaper in addition to a Time to Amplitude Converter which works in association with the ADC. A "Channel Controller", running at a clock speed of 200MHZ, supervises the operation and synchronization of the charge integration, quantization, and time to amplitude conversion sections. The data is readout from the chip using Low-Voltage Differential Signaling (LVDS) standard links. TIGER is a fine chip, with a simple yet elegant state-of-the-art architecture. Its major advantages include high input dynamic range, two high-resolution (10-bit) Wilkinson ADC's with very low non-linearity at each channel for both time and energy, and fast and a high-speed trigger-less readout, among other features, all offered with a reasonably low-power operation (less than 12 mW per channel while powered with 1.2 V). The limitations or drawbacks include a bit higher ENC noise, limited value of input capacitance range, no digital processing functions, and possible internal analog signal conditioning structure supporting negative polarity signals only.

SAMPA: The SAMPA chip has been designed as a 32-channel device with on-board pre-amplification (CSA with AGC), pulse shaping, quantization (digitizing) and DSP sections, including a high-bandwidth digital interface for computer readout. With the help of its eleven e-links with individual data transfer speed of 320 MB/s, it offers a sufficiently fast bandwidth (3.4 Gbit/s) to readout all 32 channels, at a sampling rate of 10 MSPS.

The chip is fabricated with 130 nm CMOS technology with a chip area of 9.6 x 9.0 mm^2 and offered in a 372 Ball Grid Array (BGA) package. A charge-sensitive amplifier amplifies the measured analog

signals, followed by a near-Gaussian pulse shaper, a novel element of the design. The 10-bit Successive Approximation ADC digitizes the amplified and shaped signals at a sampling rate of 10 MS/s (which can be configured to up to 20 MS/s), whereas the on-board DSP circuitry filters and carries out signal processing and compression operations on the digitized data. The chip offers a sufficiently high gain of 20-30 mV/fC with a low-noise performance (less than 1000 e^-).

SAMPA is a relatively modern chip suitable for high-performance applications. Its superior signal conditioning, digitization and on-board digital signal processing capabilities, as well as fast readout rates, are ideal for applications requiring a high-bandwidth, precision and versatile mixed signal data acquisition architecture.

AFTER (ASIC For TPC Electronic Readout): The AFTER chip is manufactured with AMS CMOS 0.35 μm technology. The die area is of 7.8 x 7.4 mm^2 (involving 500,000 transistors). The final chip is produced in a 160-pin LQFP package: (28 x 28 x 1.4 mm). It offers 72 channels which can be preset for a negative/positive polarity by resistor arrays, with a counting rate of up to 0.3 Hz/channel. The chip has a power consumption of less than 10 mW/channel while powered at 3.3 V. This chip has a dynamic range of 120 fC-600 fC with an integral non-linearity of less than 2% of LSB. However, it does not have an on-board ADC and requires an external ADC (with 20-25 MHz sampling rate). The specified peaking time range, as per the chip's technical sheet, is 100 ns to 2 μs (in 16 denominations). The sampling frequency range spans from 1 MHz to 50 MHz. Input signals sampled in circular analog memory buffers (in the form of a Switched Capacitor Array, SCA, with a depth of 511 time buckets). However, since the chip does not have an on-board ADC it needs an external one to digitize the SCA matrix signals. The SCA can be frozen by an external trigger. The minimum dead-time for the SCA is fixed at 79x40 ns*Number_Of_Time_Buckets (out of 511).

As AFTER chips do not include digitization stage, they should be associated to external ADC ASIC. A suitable commercial or custom low-latency 12-bit ADC ASIC can be employed to work with the chip. An hybrid ASIC chip built by Pacific Microchip Corp. PMCC ADC [187] is generally employed, as it presents interesting features like 12-bit digitization for up to 32 channels, a 8 ns latency, a 8 Gigabit/s transfer glue-logic on-chip. The company claims to have a fabrication facility down to 7 ns with both CMOS and BiCMOS processes, and have worked with DOE in recent past.

AGET (ASIC for General Electronics for TPC, GET system): The AGET chip is the very front-end of the GET system that performs the first concentration of the data from 64 input channels to one analog output connected to an external ADC. Each channel integrates a charge-sensitive pre-amplifier (CSA) with selectable signal polarity, a configurable shaper, a discriminator for multiplicity building and a 512-cell switch capacitor array (SCA). The gain and peaking times are tunable by slow control from 120 fC to 10 pC (4 values) and from 70 ns to 1 μs (16 values) respectively. The filtered signal is sent to an analog memory and discriminator inputs. The SCA for the analog memory is a 512-cell deep circular buffer in which the analog signal from the shaper is continuously sampled and stored. The sampling frequency is adjustable from 1 MHz to 100 MHz depending on the particular requirements of each detector. To process two consecutive events within a time window of 2 ms, such as the implantation of a radioactive ion followed by its decay, the SCA memory can be split into two halves using an adjustable parameter in slow control. The first signal that arrives is sampled and stored in the first half of the SCA memory. This is followed by a switch to the second half of the memory to sample and store the second signal. The system waits for this second signal to arrive for up to 2 ms. The switching from one half of the memory to the other corresponds to 2 sampling times. Sampling is stopped by a trigger decision. In the readout phase, the analog data from the different channels is

multiplexed towards a single output and sent to the external 12-bit ADC at a readout frequency of 25 MHz. It is possible to read only a user-defined fraction of the 512 analog cells (1 to 512) beginning from an index defined with a constant offset from the cell corresponding to the trigger arrival. In addition to the 64 input signal channels, the AGET chip has 4 channels that are called fixed-pattern noise (FPN) channels. The inputs of these channels are not connected to the detector but they are treated by the SCA in exactly the same way. The chip is fabricated with 0.35 μm AMS CMOS technology and is 8.5 x 7.6 mm^2 large. It is housed in a LQFP 160-pin package.

The placement scheme for the AGET ASIC is that an "AsAd (ASIC Support & Analog-Digital conversion)" card is formed with four AGET's soldered on it supported by four 4-channel 12-bit ADC's, one for each AGET. With the help of a glue-logic the digital outputs from ADCs are finally transmitted via 8 differential lines to a "CoBo (Concentration Board)" board, with a maximum speed of 1.2 Gbit/s. This board is responsible for functions such as applying time stamp, zero suppression and compression algorithms to the data. In addition, it serves as a communication intermediary between the AsAd boards and the outside world. The slow control signals and commands to the AsAds are transmitted via the CoBo (four AsAD per CoBo). MuTanT (Multiplicity Trigger And Time) card issues a three level trigger via the external trigger, multiplicity and the event pattern. It manages also the clock distribution over the whole system.

SAMPIC: The SAMPIC chip is a 16-channels low depth high-speed digitizer. Each of its 16 channels associates a DLL-based TDC providing a raw time with an ultra-fast analog memory (5 GHz sampling frequency) allowing fine timing extraction as well as other parameters of the pulse. Each channel also integrates a discriminator that can trigger itself independently or participate to a more complex trigger. After triggering, each sample is digitized by an on-chip ADC and only that corresponding to a region of interest is sent serially to the DAQ. The association of the raw and fine timings permits achieving timing resolutions of a few ps rms.

ALCOR (A Low power Chip for Optical sensor Readout): The ALCOR chip prototype is a first test vehicle for a high-rate digitization back-end for SiPM readout in fast timing applications. It is a 32-channel ASIC that features signal amplification, conditioning and digitization. It features low-power TDCs that provide single-photon tagging with time binning down to 50 ps and able to work down to cryogenic temperatures. The design of a system-grade ASIC targeting dRICH detector specifications is now being pursued at INFN. The ALCOR chip is based on a triggerless time-based (time-of-arrival and time-over-threshold) readout and features a SEU-protected logic. A dedicated design of the front-end shall allow for integrated cooling and customized decoupling circuits (high pass filter) for possible signal pre-conditioning and count rates well exceeding 500 kHz per channel. The chip architecture and matrix floor-plan will allow for a future version to be assembled chip-on-board with bump-bonding (the first prototype uses wire-bonding padframes), which will be an enabling factor for the design of very compact and robust front-end electronic board.

11.9.5.5 Support system

11.9.6 Possible Readout Chip Evolution and Future Technological Constraints

It seems that a mixed-signal multi-channel (greater than n=64) high-performance ASIC chip architecture is entailed with at least a 10-bit/12-bit resolution SAR ADC (offering a minimum sampling rate of 25MHz,

	SAMPA	VMM	TIGER	DREAM	AGET	AFTER
Architecture	Front-end + ADC + DSP	Front-end + S&H + discri + 3xADC	Front-end + S&H + discri + TDC + ADC	Front-end + analog memory		
	Analog characteristics					
Number of channels	32	64	64	64	64	72
Input dynamic range	66/500 fC	0.1-2.0pC	2.0-50 fC	50-600 fC	120 fC - 10 pC	120-600 fC
Peaking time range	160-300 ns	25, 50, 100 and 200 ns	60 ns (TDC), 170 ns (ADC)	50 ns - 1 μs	50 ns - 900 ns	100 ns - 2 μs
Full signal occupancy	550 ns					
Polarity	+/-	+/-		+/-	+/-	+/-
Detector capacitance range	18.5 pF/40-80 pF	200pF	up to 100pF	200 pF		¡30pF
Noise level	600/900 e^-	300 e^- at 9 mV/fC	up to 2000 e^-	610 e^- + 9 e^-/pF	580 e^- + 9 e^-/pF	370 e^- + 14.6 e^-
Sensitivity/Gain	4/20-30 mV/fC		12.4 mV/fC (TDC), 11.9 mV/fC (ADC)			120 fC/mV
Remarks			CR-RC shapers			
	Digital characteristics					
Sampling frequencies	10-20 MHz	200 MHz	1-40 MHz	1-50 MHz	1-100 MHz	1-100 MHz
ADC resolution	10-bit	10-bit	10-bit (Wilkinson)	No ADC	No ADC	No ADC
TDC time resolution		8-bit + 12 global	5 ns			
Remarks	10 MS/s			Internal trigger	Internal trigger	
Data treatment functions	On-board DSP	none	none			
Data bandwidth	11x320 Mbit/s	1 Gbit/s (ideal 9.7 Gbit/s)	1.28 Gbit/s (triggerless)			
Streaming readout capacity	3.4G bit/s		Readout on internal trigger, programmable threshold			
	Other information					
Die size	9.6x9.0 mm^2	15.3x8.3 mm^2	5×5 mm^2			7.8 x 7.4 mm
Package size	TFBGA 15x15 mm^2	400BGA				28 x 28 mm
Power consumption	20 mW/ch	10 mW/ch	12 mW/ch @ 3.3V	10 mW/ch	10 mW/ch	10 mW/ch
Technology	130 nm CMOS	130 nm MOSFET	110 nm CMOS			350 nm AMS CM
Remarks						

Table 11.33: Characteristics of different chips presently available for gaseous detector readout

very low non-linearity, INL <2.0%, and a low latency, <10.0 ns), working in tandem with a high-speed TDC (with excellent time resolution), preferably with buffer and glue-logic on-board, and a complementary FPGA with intelligent firmware designed, in the form of a total solution for readout. Additional features like an on-board DSP module (for baseline correction, zero suppression, anti-aliasing digital filtering etc.) would be added advantages. Other approaches such as companding ADC can also be explored to make a trade-off for low-resolution (6/8-bit ADC), if resources permit and substantial advantage is expected on the cost of chip component overhead.

There are certain other ASIC chips available in the HEP community, suitable for GEM and TPC applications etc., such as ALTRO and ALTRO-16 (CERN) with 12-bit ADC and digital processing etc on-board, and ALICE collaboration SDD chip. However, detailed evaluation is needed. So far, there seem to be not enough material available to evaluate them, or they seem to be in preliminary or unfinished stages. Necessary features and functionality are needed there perhaps, in addition to thorough radiation damage tests commensurate with the expected luminosity at the EIC.

Evaluation of radiation, thermal, and magnetic field effects needs to be carried out for all chips, although some of the chips discussed earlier have been through radiation damage tests and seemed to offer satisfactory performance in general, with very little damage.

So far, unfortunately, one single chip suitable for the prospective experiments at the EIC does not seem to exist. Every chip has some extremely vital feature or necessary benchmark missing.

The most promising places for development of future ASIC and mixed signal devices (and the supporting hardware and firmware/software) seem to be the CEA (France), INFN Torino (Italy) and Brookhaven National Laboratory (USA), etc., where excellent chips have been developed in past. However, more refinements are needed in existing chip architectures. A collaborative effort with these institutions could be a viable direction for fostering future front-end and readout technologies necessary for endeavors like the EIC.

11.9.7 Existing streaming readout DAQ Systems for particle physics experiments

In the following, we briefly present some existing data acquisition systems for particle physics experiments adopting, completely or in part, a streaming readout approach for data readout. Further examples not reported in this section are the ALICE experiment Online-Offline (O^2) system [188] and the new Compass data acquisition system [189].

11.9.7.1 LHCb streaming readout DAQ

The LHCb detector at CERN [190] is currently ongoing a major upgrade to replace the current trigger-based DAQ system to a fully streaming DAQ system (see [191] for a complete description). The new system will allow to acquire and select events at the full 30 MHz rate of proton-proton collisions at the interaction point[5]. To reach this goal, all front-end boards in the upgraded LHCb detector will be capable of acquiring signals at the full bunch-crossing frequency. The custom GBT protocol [192] will be used to transport data via optical fibers from the front-end boards to the readout system, with up to 4.5 Gb/s bandwidth per link. Data is then processed by the upgraded LHCb event builder system, capable of aggregating, analyzing, and filtering the events - considering the full 30 MHz collision rate and with a single event size up to 150 kB, the system was scaled to handle a total data rate up to 40 Tb/s. The main components of the event builder system are the readout units and the builder units. Each readout unit is responsible of collecting data from part of the readout board, using point-to-point links, and sends this to a builder unit. For each event, one builder unit receives all the fragments from all the readout units and aggregates them into the event. Each event is then passed to the online processing farm for reconstruction and filtering. A first level filter (HLT1) performs a fast reconstruction and events selection, reducing the input rate from 30 MHz to approximately 1 MHz. A second, more sophisticated, filtering level (HLT2) performs the final event selection, resulting to an output event rate of approximately 100 kHz to be written to the disk.

11.9.7.2 sPHENIX Hybrid DAQ

Construction is ongoing for the sPHENIX triggered-streaming Hybrid DAQ, which simultaneously reads out the conventionally triggered calorimeter subsystems and the streaming tracking subsystems [193]. Both the sPHENIX front-end readout and the back-end DAQ will also serve as an exercise of a large-scale streaming system that is applicable to future EIC experiments.

The tracking front-ends consist of the on-detector streaming ASICs for the readout of the MAPS pixel tracker (ALPIDE), a silicon strip tracker (PHFX), and GEM-based TPC read out with a new version (V5) of

[5]The nominal bunch-crossing frequency at the LHC is 40 MHz, corresponding to one interaction every 25 ns. At the LHCb interaction point, however, one every four collisions is empty, resulting to a 30 MHz physics events rate.

the ALICE SAMPA chip [194]. The streaming data are time-stamped with beam collision clock, aggregated in the front-end FPGAs, and transported to the back-end DAQ via O(1000) multi-Gbps fiber links providing O(10) Tbps overall readout bandwidth. A global timing system provides a low jitter collision clock, fixed-latency trigger signal, and time-stamp counter to all front end electronics, which are embedded in the data stream and serves as the basis for the streaming and hybrid synchronizations.

A fleet of O(50) Front-End Link eXchange (FELIX) [195] readout cards hosted in commodity Linux PCs is used to read out, buffer, and process these data streams. In the version used by sPHENIX, each FELIX is a PCI-express card carrying a large FPGA (Xilinx Kintex UltraScale KU115). It supports 48 bi-directional 10-Gbps optical links to the front-end and a 100-Gbps PCI-express Gen3 link with the hosting server's CPU. It is initially designed for the ATLAS Phase-I upgrade and continues to be developed to utilizing recent parts with a higher speed for future ATLAS upgrade towards the HL-LHC. The strategy of using PCIe FPGA cards to bridge the custom front-end and commodity computing is also used by the LHCb, ALICE, ATLAS, and CBM experiments. The overall peak disk data rate is designed to accommodate the RHIC Au+Au collision at the top luminosity that is orders of magnitude higher charged particle production rate when compared with the EIC.

While sPHENIX will have a trigger, the overall architecture is streaming-oriented and highly parallel. Individual substreams coming form the detector are written to different files directly, and synchronization will be performed via time stamps, not event numbers. The actual event building is moved to the offline analysis, removing the necessity to build a distributed, fault tolerant, reliable one-shot online event builder.

The FELIX system also provides the flexibility of throttling the recorded streaming data corresponding to the calorimeter triggers (i.e. global zero-suppression) or allows for triggerless recording of a fraction of or all of the tracker data. The streaming tracker data are demonstrated to enable a unique set of heavy flavor measurements that would be otherwise inaccessible, and this streaming DAQ development is recently commended by the RHIC Program Advisory Committee.

11.9.7.3 The RCDAQ Data Acquisition System

sPHENIX uses a powerful but lightweight data acquisition system called "RCDAQ" [196]. It is currently in use for virtually all sPHENIX R&D projects such as test beams, tests in labs, detector calibrations, and the like. RCDAQ supports all current sPHENIX front-ends and both triggered and streaming readout modes. It also supports, by way of plugins, a large variety of commercial or otherwise available readout electronics, such as the DRS4 Evaluation Board [197], the CERN SRS system [198], several CAEN modules such as the V1742 Waveform Digitizer, and many more.

RCDAQ has long been the de-facto standard data acquisition system for several EIC R&D groups, such as eRD1 (calorimetry), eRD6 [33] (tracking), eRD14 (time-of-flight), and eRD23 (streaming readout technologies). In addition, RCDAQ is used by dozens of external groups not connected to the EIC or RHIC R&D efforts because of the support for those common readout devices, its built-in support for ROOT-based online monitoring, comprehensive controls, and small footprint.

11.9.7.4 The ERSAP system

Development is underway for the Environment for Real-time Streaming, Acquisition and Processing (ERSAP) Streaming Data Readout System at JLab. ERSAP is a backend software system that combines com-

ponents to form a reactive data flow architecture. This combines software originally developed as part of the CODA data acquisition system and then advanced as part of the CLARA reactive microsevices framework [199] used by the CLAS12 experiment. The system encapsulates each component into a microservice with well defined inputs and outputs that allow for local or remote communications. This allows both horizontal and vertical scaling to make the system highly configurable. It also supports micro-services written in any language (C,C++, Python, Java, ...). Utilizing such a design helps ensure a level future-proofing since individual services can be easily replaced with ones using new syntax, languages, or technology (e.g. heterogeneous hardware components). A prototype of the system was tested successfully in summer 2020 using beam at the CLAS12 Forward Tagger. Also being developed as part of ERSAP is high performance tiered memory or "Data Lake" system that allows efficient data cooling (i.e. temporary buffering). The system is scalable enough to be used on a single desktop with other DAQ components in benchtop system or in a dedicated node with a large memory+disk. The Data Lake implements automatic fail-over to disk if its allotted memory resource becomes exhausted.

11.9.8 A Progressive Approach toward the EIC DAQ System

The final goal of the EIC streaming readout system is to reconstruct online all events, adding to the raw-data banks the high-level information from the reconstruction - ideally, four-vectors and PID assignment for all particles in a given interaction, and store all of them to the disk. Eventually, filtering algorithms can run online to tag events according to a certain condition (for example, events belonging to a certain exclusive channel), to speed-up the offline analysis.

Based on the preliminary estimates discussed before in Sec. 11.9.4, and considering the technologies that are available already today, the following key arguments concerning the EIC streaming DAQ system can be assessed (see also Fig. 11.130).

- In principle, it will be possible to write all raw data directly to the disk, without further online processing. However, unexpected large noise levels could exceed the system capacity, and the system must be prepared for such an event. This is particularly true during the initial phase of EIC operations, when unexpected backgrounds not predicted by simulations and not observed in the preliminary sub-detectors characterization phase could be present, and the machine still needs to be tuned.
- High-quality calibration constants are necessary for the online events reconstruction, analysis, and filtering. This requires a depth knowledge of the detector behavior, that may not be available at the beginning of the EIC operations.

The solution that we envisage is to design a modular system that will evolve with the experiment. During the first part of the EIC run, a hybrid streaming readout strategy will be adopted, using the so-called "cross-detector zero suppression technique". In this scheme, all hits from the detector are streamed to the online computing farm and stored to a temporary buffer. Only "interesting" portions of the data stream are further processed, while the others are discarded. Considering that most of the reactions measured to complete the EIC scientific program foresee the measurement of the scattered electron, we think that EIC calorimeter is an excellent candidate to provide the signal to identify the portions of the data stream to be further processed. Technically, this can be achieved both with a parallel hardware system, as in the sPHENIX case, or with a dedicated software component (the sPHENIX hardware-based cross-detector zero suppression system operation is illustrated in Fig. 11.130). Online filtering and online reconstruction will be then gradually introduced when the detector will be more under control.

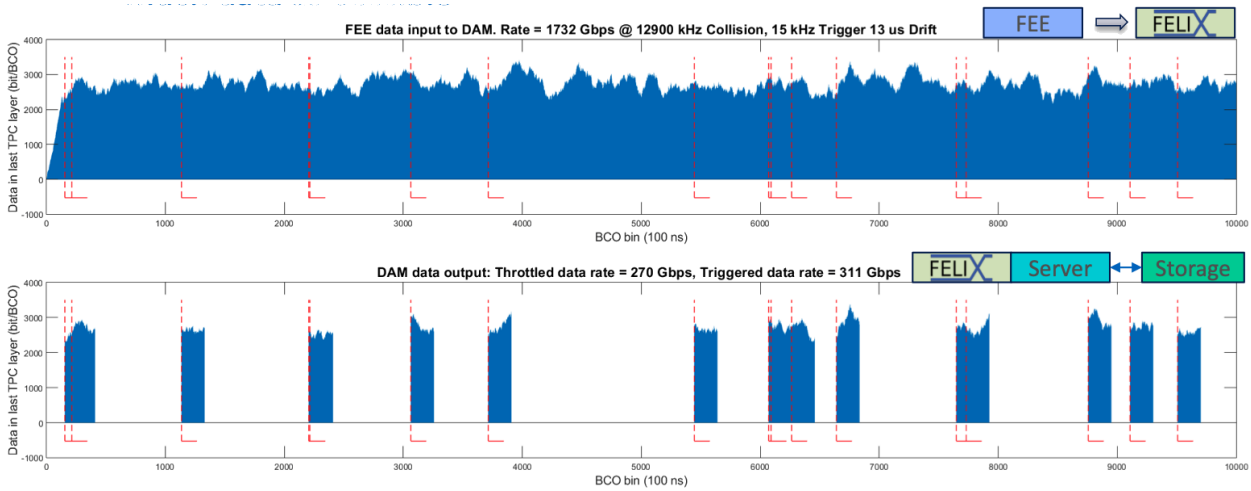

Figure 11.130: The sPHENIX hybrid DAQ system cross-detector zero suppression. The sPHENIX streaming tracker can use the calorimeter trigger as a data throttle for loss-less data reduction for triggered events + streaming as much data as possible [193]

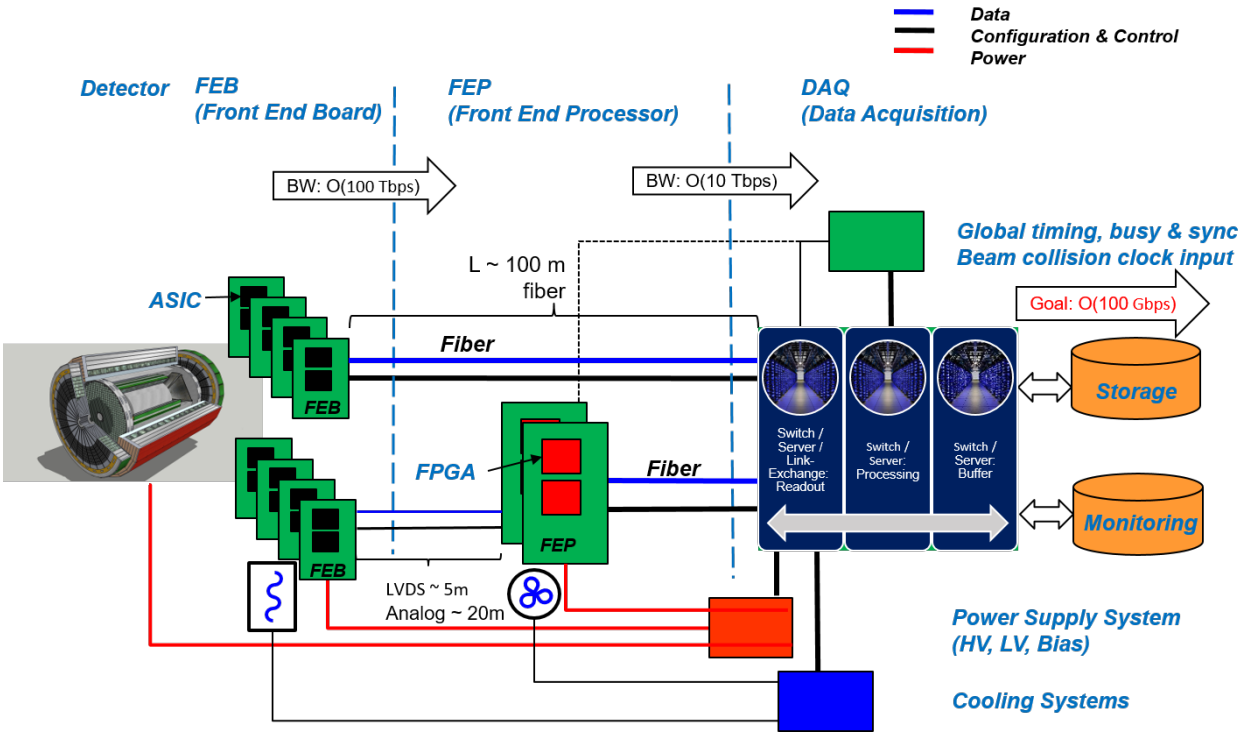

Figure 11.131: A possible scheme for the EIC Readout Architecture

A possible solution for the EIC readout architecture is shown in Fig. 11.131. Some front-end boards (FEB) containing ASICs and specific to different sub-detectors will likely require an intermediate stage of processing via FPGAs for data aggregation and reduction by employing front-end processors (FEP). Data transport to servers or link-exchange cards, such as FELIX, will be made via extensive use of optical fibers. Power supply and cooling systems are planned to be commercial-off-the-shelf (COTS) units.

An intense R&D program has already started to study and design the EIC readout system, covering all the technical aspects involved with it, including the different FE options compatible with a streaming readout system, the data transport system, the synchronization system, the back-end online processing software. Andrea: how to reference to this part in the Yellow Report document??

11.9.9 Experimental Validation of the Approach

Despite the conceptual simplicity of a triggerless DAQ, a realistic implementation with the specific detector readout is necessary to validate this solution and demonstrate the expected performances. The sophisticated combination of a suitable front-end electronics, network facilities and CPU algorithms requires a significant effort to identify, or develop in case they are not yet available, the best option for each element, set-up and test the whole scheme and compare results with more traditional approaches.

A dedicated test and validation program, with complementary experimental efforts, has already started in view of the EIC detector design and construction. In the following, we briefly present these efforts.

11.9.9.1 Jefferson Laboratory efforts

A first experimental characterization and validation campaign for the new DAQ approach has started at Jefferson Laboratory in 2020, using a streaming readout solution based on FA250+VTP / Waveboard digitizer boards [200, 201] for the front-end readout and on the TriDAS software [202] interfaced with the JANA2 data analysis framework for the back-end online data reconstruction and filtering [203].

Due to the comparable luminosity and detector complexity, **the CLAS12 detector in Hall B is an ideal study case to characterize and validate the streaming DAQ approach in view of its application for the EIC detector [204]**. A first measurement on beam was carried out using the CLAS12-Forward Tagger Calorimeter and Hodoscope detectors [110], with the CEBAF 10.6 GeV electron beam impinging on a lead (early 2020 run) / deuterium (summer 2020 run) target.

This represented the first attempt to acquire some CLAS12 sub-detectors using streaming readout: the growing interest for this approach is demonstrated by the plans of the CLAS Collaboration to extend it to the full detector in the near future. During the test, the single π^0 quasi-real photoproduction reaction was used as a benchmark to assess the performances of the streaming DAQ system. The π^0 was identified measuring the two photons from the decay in the Forward Tagger Calorimeter, whereas the scattered electron was identified by a combination of an electromagnetic cluster in the Forward Tagger Calorimeter and a geometrically matched signal in the Forward Tagger Hodoscope. Preliminary results show a good agreement between the measured data and the predictions from a Monte Carlo numerical estimate, in terms of the energy distribution and total yield of the measured π^0. The data analysis is currently in progress, and final results from the test are expected to be published in early 2021.

A pilot beam study was also conducted to test streaming data processing of the CLAS12 Forward Tagger

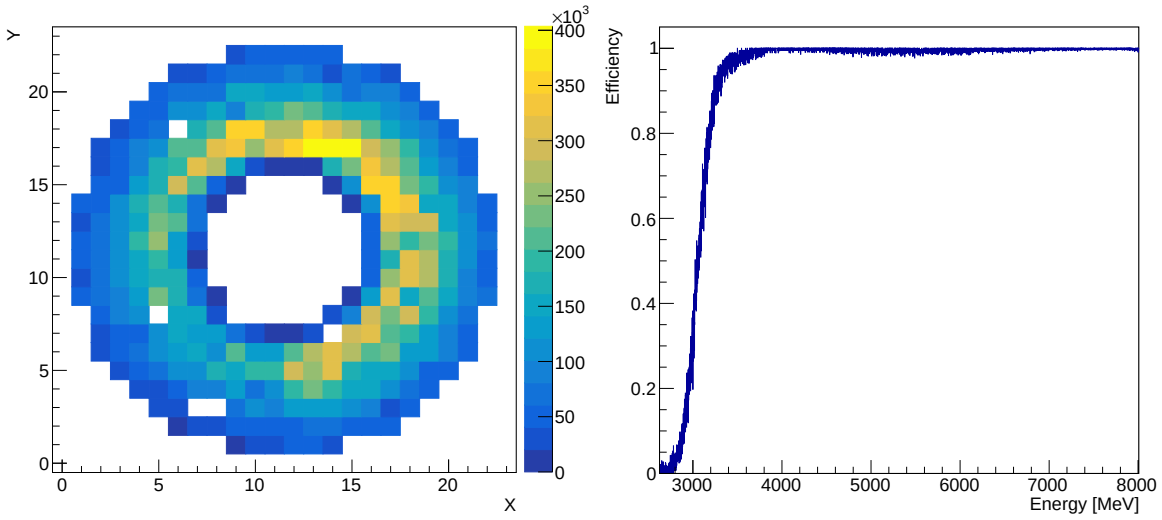

Figure 11.132: Left: measured FT-Cal hits during the early 2020 Hall-B streaming readout tests. Right: Efficiency of the online clustering algorithm, with a 3.0 GeV cluster threshold applied.

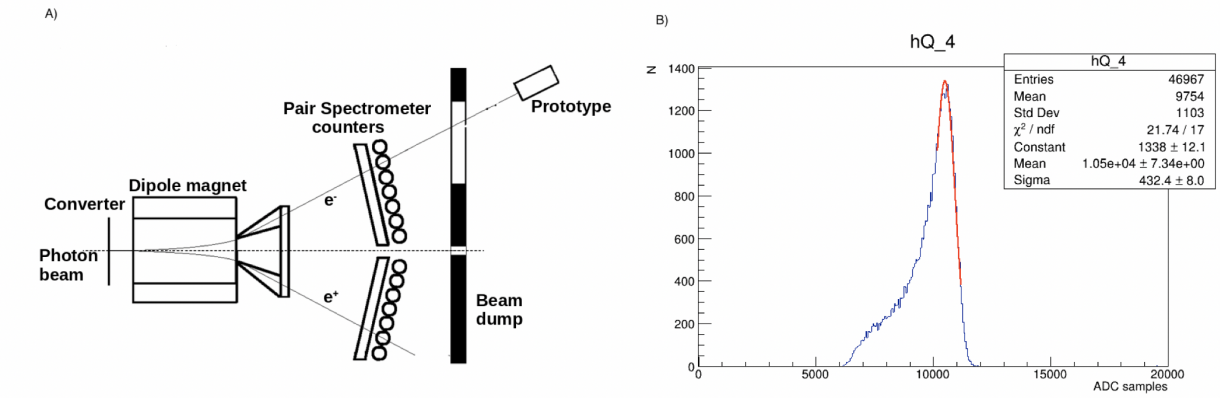

Figure 11.133: Left: Hall D PS beam test setup scheme; Right: Calorimeter central response (in arbitrary units) to 4.5 GeV impinging electrons.

Calorimeter and Hodoscope using ERSAP software package that includes JLAB data acquisition and data processing frameworks, such as CODA, CLARA and JANA. Specifically CODA VTP stream firmware was used to stream raw data to stream-aggregator, hit-finder, noise-reduction and event-building micro-services, followed by standard, Forward Tagger reconstruction micro-services from the CLAS12 reconstruction application. CLAS12 reconstruction application is based on the CLARA, which is a reactive micro-services orchestration framework for designing, deploying and scaling data stream processing applications [205] [206] . The goal of this study was to optimize (both performance and resource utilization) newly developed data-stream curation micro-services, and to estimate existing CLAS12 reconstruction micro-services scaling levels and resource requirements that will keep up with the VTP data stream. Preliminary results were reported at the 22nd IEEE Real Time Conference.

A complementary test was performed in Hall D, at the pair spectrometer (PS) facility [207]. The general purpose of the beam tests was to study the light yield and the energy resolution of glass-ceramic scintillator bars made in VSL/CUA/Scintilex and new produced $PbWO_4$ crystals made by CRYTUR/SICCAS. A glass-ceramic and a $PbWO_4$ prototype were installed behind the Hall D pair spectrometer and the response to the tagged electrons from the PS was measured. The prototypes were also used to test and optimize the entire readout chain: photosensorss (PMT vs SiPM), preamps, fADC or Waveboard digitizers in combination with streaming DAQ system. During the spring run 2020 at Jlab HallD a single prototype, assembled from nine scintillators coupled with R4125-01 Hamamatsu PMTs and active HV dividers with integrated preamplifier, was used. Signals were digitized using a Waveboard device. The SRO tests was performed parasitically during GlueX High Luminosity runs (350nA photon beam). The waveboard read-out nine calorimeter channels plus two scintillator pads mounted in front of the calorimeter, to tag the impinging electron. The system was operated with a rate up to 1.5kHz per channel. The full SRO chain (Waveboard+TriDAS+JANA2) was successfully tested, with data collected using different combination of software L2 triggers. The offline data analysis is currently ongoing, and final results from the test are expected to be published in early 2021.

11.9.9.2 BNL efforts

An example of a detector read out in streaming mode is a prototype of the sPHENIX TPC that was tested at the FermiLab Test Beam Facility (FTBF) in 2019. The TPC prototype, shown in Fig. 11.134, was moved perpendicular to the beam and rotated with respect to the beam to get particle tracks at different distances away from the pad plane, resulting in different drift lengths and angles.

At the test beam, we found that our event rate capability could be significantly increased by running the FELIX readout in "streaming mode". We still triggered the front-end card with signals from the FTBF beamline, however, the FELIX cards are oblivious to how the FEE actually arrived at the decision to send up the data. But by allowing the FELIX card to format the data as streaming data, one does not need to wait for all data from a particular beam event to be fully transmitted. In streaming mode, while data from trigger n are already arriving from one front-end, other parts can still be transmitting data from trigger $n-1$, or even $n-2$. In streaming mode, there is no need to wait for the completion of the data transmission from a given trigger, as the data parts are later re-assembled by their embedded clock information. That is what led to the increased event rate in streaming mode.

This also validated a running mode that sPHENIX is committed to in production running, combining the streaming data from the trcking system with triggered data from the calorimeters and the Minimum-Bias detector. During the test beam we achieved the simultaneous logging of data from the TPC prototype together with several channels worth of beamline instrumentation channels read out in "classic" triggered mode.

This also served as an early test of our timing system that provides a common clock to the various front-end cards, and can on demand also provide a standad trigger signal to legacy electronics.

11.10 Software, Data Analysis and Data Preservation

This section will describe the computing needs for the reference detector at the EIC and discuss the foreseen software developments.

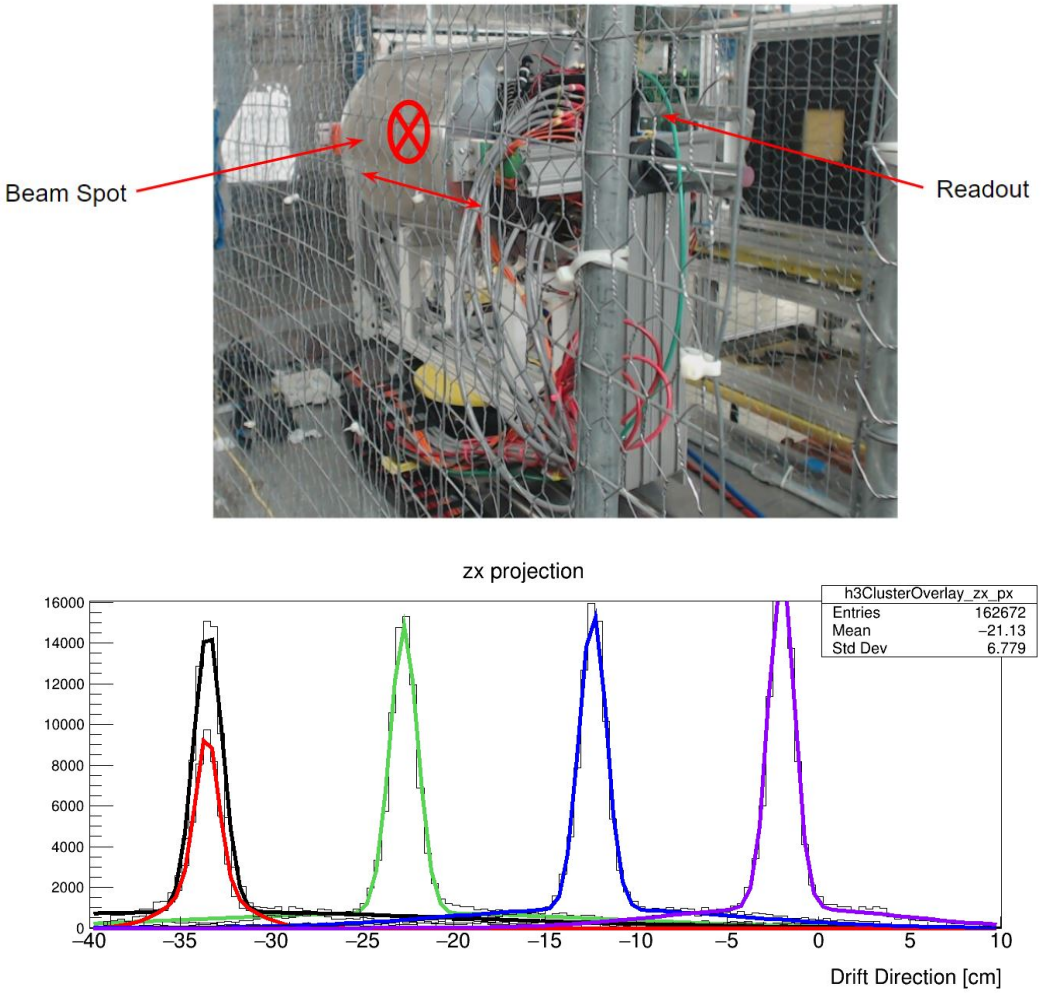

Figure 11.134: Left: The TPC prototype shown in the test beam which is read out with FELIX and the RCDAQ . The red cross-hair indicates the approximate beam position. Right: The reconstructed drift distance for 4 different positions of the TPC prototype relative to the beam.

Aside from possible contribution of machine backgrounds, the reconstruction of events at the EIC will be easier than the same task at present LHC or RHIC hadron machines, and, in perspective, much easier than for the high luminosity LHC (HL-LHC), which will start operating two years earlier than the EIC, when we may expect a gain in performance for CPUs of about a factor of 10 with respect to now.

Reconstruction time of DIS events at presently running experiments is around 0.35 s (or ∼ 5HS06 s) both at COMPASS and at CLAS12, with event sizes of 0.03 MB and 0.02 MB respectively. Filtering out machine background with high efficiency will allow to keep the reconstruction time at 5HS06 s also in 2030. Processing events at the same speed of acquisition, or 500 000 events per second, on today nodes will therefore require 200 000 cores or 1500 nodes, a computing farm well in the size of the EIC project. The expected gain in CPU power in the next 10 years, as well as the possible improvement in the reconstruction software from the use of machine learning techniques give a considerable margin to cope with higher event complexity

that may come by higher backgrounds rates.

Software design and development will constitute an important ingredient for the future success of the experimental program at the EIC. Moreover, the cost of the IT related components, from software development to storage systems and to distributed complex e-Infrastructures can be raised considerably if a proper understanding and planning is not taken into account from the beginning in the design of the experiment itself.

A growing group dedicated to this effort already exists. An important step in the clustering of a core group focusing on computational aspects at an EIC has been the approval by the EIC Generic R&D program of the eRD20 proposal, creating in 2016 the EIC Software Consortium or ESC. ESC has been the backbone to form in 2018 the Software Working Group within the EICUG. The Software Working Group has supported the Yellow Report initiative and provided the tools for simulations and helped in the creation of the infrastructure for storage and documentation.

The Software Working Group is starting in parallel a greenfield development that will focus on different aspects of future needs:

- Simulations for detector optimization, to cover the more immediate needs of the design and integration of the various sub detectors
- Help in the development of state of the art Monte Carlo event generators for the full spectrum of EIC physics. Validation of these generator will be possible by using data from running experiments.
- Development of a full simulation-reconstruction chain allowing to benchmark the performances of the reconstruction software.
- Development of modern "event reconstruction" schemes both using standard approaches but also exploring novel methods based on artificial intelligence machine learning techniques.

The reconstruction software will have to cope with the streaming read-out scheme adopted and will be design to match the chosen solution.

Software tools: While developing the software for simulation and reconstruction of events from a detector which will be up and running in 2030, we need to inquire ourselves about the long term perspective of software used in today HEP experiments and evaluate different options. Leaving aside for the moment both full purpose or dedicated Monte Carlo Event Generator discussed in a separate section, this means that we have to decide on: how to describe the detector; which program to use for particle transportation/interaction; reconstruction tools and the data model.

The choice of LHC experiments for the Run4 and after may guide us in this task.

DD4hep [208] is a toolkit for detector description developed within the AIDA2020 EU program (Advanced European Infrastructures for Detectors at Accelerators). It can be an interesting option for the EIC since recently the CMS collaboration announced that it plans to use it to provide the structure of the experiment to all their data processing applications.

It is worth considering it for the EIC since it is designed to answer a very common need of experiments, i.e. the development of a coherent set of software tools for the description of high-energy physics detectors from a single source of information. Detector description in general includes not only the geometry and the materials used in the apparatus, but all parameters describing, e.g., the detection techniques, constants required by alignment and calibration, description of the readout structures, conditions data and more.

Given it use withing CMS choice, it is expected that DD4hep will be supported over the entire experiment life-time.

DD4hep reuses existing software components, combines the functionalities and thus optimizes the flexibility, minimizing the efforts required by users to leverage the benefits. Reused components include elements of the ROOT geometry package [209] and the GEANT4 simulation toolkit [84].

GEANT4 [84] is the baseline for detector simulation on all LHC experiment and is a natural choice for the EIC. We have developed strong connections with the core developer team of GEANT4 and the improvements in physic list and in non standard geometries which may be needed for the EIC are being discussed with them. About one year ago, the core team of the Software Working Group organized together with the GEANT4 Collaboration a Technical Forum on the EIC. The Forum allowed to discuss both the information on recent updates on GEANT4, but also the physics list for the EIC as maintained by the EIC Software Consortium. The requested improvements on photo-nuclear and electro-nuclear reactions were included in GEANT4version 10.6, and this is under test right now. The study of vectorizing this transportation, as done withing the GEANT4, the vector transport R&D collaboration [210] will offer interesting improving options for GEANT4 itself and we will follow this activity closely.

ROOT [209] is by nowadays standards a fundamental ingredient of virtually all HEP workflows, being used for data persistency, modeling, graphics, and analysis. It is structured to have excellent, active connections with the experiments including, at least for LHC, direct investment by the experiments. The developing team is investing in future developments for HL-LHC, and is also assuming interesting approaches to machine learning tools. It pushes in fact the HEP community to not develop its own machine learning tools but, maybe in a more efficient way, to collaborate with other sciences on improving and growing tool-sets. For that they offer a Toolkit for Multi Variate Analysis TMVA to bridge between ROOT and external machine learning tools such as scikit-learn, XGBoost, TensorFlow, Keras, mxnet, or PyTorch.

ACTS [211] (A Common Tracking Software) is an experiment-independent toolkit for (charged) particle track reconstruction in (high energy) physics experiments, implemented in modern , with 2017 standards. It is being developed for the HL-LHC, but is also targeting sPHENIX. Adopts a highly-templated design allowing to avoid virtual lookup, and it is agnostic of detectors and magnetic fields for high portability. Another important aspects with respect to development is the designed rigorous unit tests, an essential aspect for the future EIC software. All these characteristics made this software an interesting option worth evaluation for the reconstruction software for the EIC reference detector.

Many others codes are under evaluation, like GENFIT [212], a generic track-fitting toolkit, GAUDI [213, 214], a software architecture and framework for building HEP data processing applications, JANA2 [203], a multi-threaded event reconstruction and others.

Finally, following the large worldwide spread, we are moving to the use of tools facilitating collaborative analysis and logbook as presently done at CERN with SWAN [215], as a Service for Web-based ANalysis, built upon the widely-used Jupyter notebooks.

Simulations for detector optimization: The tools developed for the Yellow Report initiative will be expanded and used for extensive full simulations of the reference detector. This is a short term goal for software developers in order to support with detailed simulation studies the finalization of the reference detector, thus allowing to move from the CDR stage toward the full technical design.

Monte Carlo event generators for the EIC: The EIC Software Working Group, and before the eRD20 Software Consortium have initiated a project with the Monte Carlo communities in the US and Europe

(MCnet) to work on MCEGs for the EIC, requiring MCEG for polarized e+p, , and ^{3}He as well as e+A measurements. The MCEG initiative is connecting the MCEG efforts in NP and HEP and is encouraging a strong interplay between experiment and theory already at an early stage of the EIC. As an initial step, we have started a workshop series on "MCEGs for future e+p and e+A facilities" where the third workshop was held in November 2019 at the Erwin Schrödinger International Institute for Mathematics and Physics in Vienna, Austria. During the workshop, we reviewed the theory for physics with light and heavy ions and discussed the modifications needed on the general-purpose MCEGs to simulate unpolarized observables also for e+A where a precise treatment of the nucleus and its breakup is needed. There were presentations about pioneering MCEG projects for e+A (BeAGLE, spectator tagging in , Sartre), as well as on the ongoing development of the e+A adaptation of JETSCAPE and the Mueller dipole formalism in Pythia8. We also summarized the status of MCEG-data comparisons in HZTool/Rivet that are critical to tune MCEGs to existing DIS and heavy ion data as well on the ongoing work of verifying MCEGs for TMDs with TMD theory/phenomenology. Our current focus is on benchmarks and validation. We are working with the EICUG on benchmark MC productions and the validation of MC results. This will facilitate the adaption of modern MCEGs that have been so far only used by the LHC community.

As a recent development, the DIRE authors [216, 217] introduced radiative effects in the simulation of the DIS. This is an important step, since a full multidimensional analysis will be needed in the study of TMDs and GPDs, given the dependence of the cross section over many kinematic variables. From the experimental point of view, and without entering to much in detail of the analysis, this means that detectors and RC effects will have to be accounted together at simulation level in order to derive matrices transforming from raw counts in the detector to Born cross sections.

The DIRE parton showers is a modern MCEG, usable as a extension of the general purpose event generation frameworks PYTHIA, and will be included as an option from the 8.3 release. This will allow to check the prediction of the Monte Carlo both using the data of running DIS experiments (at JLab and COMPASS at CERN) and with the outcome of the simulation of DJANGO [218, 219], the reference tool for the study of RC effects at HERA.

11.11 Artificial Intelligence for the EIC Detector

In the world of computing there is growing excitement for what is perceived as the revolution of the new millennium: artificial intelligence (AI). In particular the R&D program of the future EIC could be one of the first programs systematically exploiting AI. AI is becoming ubiquitous in nuclear physics [220]. According to a standard taxonomy [221], AI encompasses all the concepts related to the integration of human intelligence into machines; a subset of AI is machine learning (ML), which is usually grouped into supervised, unsupervised and reinforcement learning; deep learning (DL) is a particular subset of ML based on deep (*i.e.*, made by many hidden layers) neural networks, which is often considered the evolution of ML since it typically outperforms other methods when there is a large amount of data and features, provided sufficient computing resources. In the most frequent applications in our field, features are selected and a model is trained for classification or regression using signal and background examples.

Experimental particle and nuclear physics is big data [222]: the gigantic data volumes produced in modern experiments are typically handled with "triggers"—a combination of dedicated hardware and software—to decide near-real-time which data to keep for analysis and which to toss out. In this respect, AI plays already an important role in experiments like LHCb [223], where machine learning algorithms (see, *e.g.*,

topological trigger and ghost probability requirements) make almost 70% of these decisions, from triggers to higher level analysis of reconstructed data.

Supported by modern electronics able to continuously convert the analog detector signals, new approaches like Streaming Readout [224] could further the convergence of online and offline analysis: the incorporation of high level AI algorithms in the analysis pipeline can lead to better data quality control during data taking and shorter analysis cycles. Recently the Fast Machine Learning workshop [225] highlighted emerging methods and scientific applications for DL and inference acceleration, with emphasis on ultrafast on-detector inference and real-time systems, hardware platforms, co-processor technologies, and distributed learning. In this context, AI (used here in a broader sense to embrace different approaches) could foster in the next years significant advances in areas like anomaly detection (see, *e.g.*, [226]) and fast calibration/alignment of detectors.

For tracking detectors, particle tracking is always a computationally challenging step. Several approaches have been developed recently for tracking based on deep learning [227], but there are still open questions about the best way to incorporate such techniques. The problem in Nuclear Physics experiments is typically different, being characterized by most of the computing cycles spent in propagating the particles through inhomogeneous magnetic fields and material maps. Here AI can contribute to determine the optimal initial track parameters allowing to decrease the number of iterations needed by Kalman-Filter.

As for particle identification and event classification, we have witnessed in the last years a growth of applications based on machine learning both for global particle identification (see, *e.g.*, [228]) as well as custom novel solutions which combine different architectures for specific detectors (see, *e.g.*, [229] for imaging Cherenkov detectors).

The search for rare signatures in large acceptance detectors at high intensities necessitates advanced techniques to filter those events. The GlueX experiment at Jefferson Lab for example is searching for exotic hadrons and demonstrated the utility of machine learning techniques based on BDTs [230] to achieve the required performance in filtering events with rare reactions [231].

The utilization of jets at the future EIC can be beneficial for a variety of fundamental topics [232], including the gluon Wigner distribution, the gluon Sivers function, the (un)polarized hadronic structure of the photon, the (un)polarized quark and gluon PDFs at moderate to high momentum fraction (x) as well as studies of hadronization and cold nuclear matter properties. Machine Learning is having a major impact in jet physics, empowering powerful taggers for boosted jets as well as flavor tagging, and various deep learning applications like recursive neural network which leverage an analogy to natural language processing [233] have been developed. ML4Jets [234] is a series of workshop dedicated to these topics.

Another area where AI can significantly contribute is that of fast simulations. Simulating the detector response of large scale experiments like EIC is typically slow and requires immense computing power. One of the most computationally expensive step in the simulation pipeline of a typical experiment is the detailed modeling of the high multiplicity physics processes characterizing the evolution of particle showers inside calorimeters. AI, could speed up simulations and potentially complement the traditional approaches. Recent advances with generative networks (see, *e.g.*, GAN, VAE, Flow-based models [235–237]) look as a compelling alternative to standard methods with orders of magnitude increase in simulation speed [238] but so far usually at the cost of reduced accuracy.

Detector design is another fundamental area of research for EIC. Advanced detector design often implies performing computationally intensive simulations as part of the design optimization process. One of the

conclusions from the DOE Town Halls on AI for Science on 2019 [239] was that "*AI techniques that can optimize the design of complex, large-scale experiments have the potential to revolutionize the way experimental nuclear physics is currently done*". There are at present various AI-based optimization strategies based on, *e.g.*, reinforcement learning or evolutionary algorithm [240, 241]. Among these, Bayesian Optimization (BO) [242,243] has gained popularity for its ability of performing global optimization of black-box functions that are expensive to evaluate and that can be in addition noisy and non-differentiable. It consists in a surrogate modelling technique where the regression is typically done through Gaussian processes or decision trees depending on the dimensions of the problem, and a cheap acquisition function is used to suggest which design points to query next, overall minimizing the number of evaluations.

Recently, an automated, highly-parallelized, and self-consistent procedure has been developed [244] and tested for the dual-radiator Ring Imaging Cherenkov (dRICH) design, which has been considered as a case study. These studies not only showed a statistically significant improvement in performance compared to the existing baseline design but they also provided hints on the relevance of different features of the detector for the overall performance. This procedure can be applied to any detector R&D, provided that realistic simulations are available. One example is the optimization of detector materials, e.g. the optimization of large size aerogel composites for aerogel-based detectors in [245].

Beyond individual subdetectors AI can be also used to efficiently optimize the design of different subdetectors combined together, taking into account mechanical and geometrical constraints. An interesting approach consists in a multi-objective optimization (see, *e.g.*, [246–248]), which allows to encode the performance of the detectors as well as other aspects like costs in the design process, to determine the Pareto front [249]. Currently ongoing activities within the EIC R&D program which are leveraging AI for optimization include the EM/Hadronic Calorimetry, *e.g.*, optimizing the glass/crystal material selection in "shared rapidity regions" for best performance of the EM calorimeter.

Even more, AI has the ability to optimize the collection of all subdetectors of a large detector system, using more efficiently the figures of merit we use to evaluate the performance that drive the detector design. Remarkably, the design optimization of multiple subdetectors operating together has not been explored yet. This is a high dimensional combinatorial problem that can be solved with AI.

This is undoubtedly a strategic moment to discuss how to fully take advantage of the new opportunities offered by AI to advance research, design and operation of the future EIC. The interest of the community has been evidenced by the number of contributions and attendance of workshops dedicated to AI in Nuclear Physics, e.g. at the [220, 250], and the 2021 AI4EIC-exp workshop [251], which bring together the communities directly using AI technologies and provide a venue for discussion and identifying the specific needs and priorities for EIC.

Chapter 12

The Case for Two Detectors

Chapter 13

Integrated EIC Detector Concepts

13.1 General Purpose Detector Concept

13.1.1 Standard Layout

13.1.2 Detector technology description

13.1.3 Electronics, Data Acquisition and Computing technology description

13.1.4 Detector Integration

13.1.4.1 Central Detector

13.1.4.2 Forward and Backward Detector

13.1.5 Systematics Discussion

13.2 Second General Purpose Detector Concept

13.2.1 Standard Layout

13.2.2 Detector technology description

13.2.3 Electronics, Data Acquisition and Computing technology description

13.2.4 Detector Integration

13.2.4.1 Central Detector

13.2.4.2 Forward and Backward Detector

13.2.5 Systematics Discussion

Chapter 14

Detector Technology

14.1 Areas of Targeted R&D

14.2 Generic Detector R&D

References

[1] L. Gonella, "EIC Silicon Vertex and Tracking: Technology survey," *1st EIC Yellow Report Workshop at Temple University* (19 March 2020) .

[2] G. Contin *et al.*, "The STAR MAPS-based PiXeL detector," *Nucl. Instrum. Meth. A* **907** (2018) 60–80, arXiv:1710.02176 [physics.ins-det].

[3] **ALICE** Collaboration, B. Abelev *et al.*, "Technical Design Report for the Upgrade of the ALICE Inner Tracking System," *J. Phys. G* **41** (2014) 087002.

[4] **ALICE** Collaboration, G. Aglieri Rinella, "The ALPIDE pixel sensor chip for the upgrade of the ALICE Inner Tracking System," *Nucl. Instrum. Meth. A* **845** (2017) 583–587.

[5] R. Schimassek, A. Andreazza, H. Augustin, M. Barbero, M. Benoit, F. Ehrler, G. Iacobucci, A. Meneses, P. Pangaud, M. Prathapan, A. Schöning, E. Vilella, A. Weber, M. Weber, W. Wong, H. Zhang, and I. Perić, "Test results of atlaspix3 — a reticle size hvcmos pixel sensor designed for construction of multi chip modules," *Nuclear Instruments and Methods in Physics Research Section A: Accelerators, Spectrometers, Detectors and Associated Equipment* **986** (2021) 164812. http://www.sciencedirect.com/science/article/pii/S0168900220312092.

[6] K. Moustakas *et al.*, "CMOS Monolithic Pixel Sensors based on the Column-Drain Architecture for the HL-LHC Upgrade," *Nucl. Instrum. Meth. A* **936** (2019) 604–607, arXiv:1809.03434 [physics.ins-det].

[7] R. Cardella *et al.*, "MALTA: an asynchronous readout CMOS monolithic pixel detector for the ATLAS High-Luminosity upgrade," *JINST* **14** no. 06, (2019) C06019.

[8] M. Dyndal *et al.*, "Mini-MALTA: Radiation hard pixel designs for small-electrode monolithic CMOS sensors for the High Luminosity LHC," *JINST* **15** no. 02, (2020) P02005, arXiv:1909.11987 [physics.ins-det].

[9] W. Snoeys *et al.*, "A process modification for CMOS monolithic active pixel sensors for enhanced depletion, timing performance and radiation tolerance," *Nucl. Instrum. Meth. A* **871** (2017) 90–96.

[10] M. Munker, M. Benoit, D. Dannheim, A. Fenigstein, T. Kugathasan, T. Leitner, H. Pernegger, P. Riedler, and W. Snoeys, "Simulations of CMOS pixel sensors with a small collection electrode, improved for a faster charge collection and increased radiation tolerance," *JINST* **14** no. 05, (2019) C05013, arXiv:1903.10190 [physics.ins-det].

[11] P. Allport, L. Gonella, P. Jones, P. Newman, and H. Wennlöf, "eRD18 report and presentation," *EIC Generic Detector R&D Advisory Panel Meeting* (January 2020) .

[12] A. Collaboration, "Letter of Intent for an ALICE ITS Upgrade in LS3," *CERN-LHCC-2019-018. LHCC-I-034* (January 2020) .

[13] L. Gonella, L. Greiner, P. Jones, I. Sedgwick, E. Sichtermann, and H. Wennlöf, "eRD25 proposal," *EIC Generic Detector R&D Advisory Panel Meeting* (July 2020) .

[14] L. Greiner, "Silicon material projections," *2nd EIC Yellow Report Workshop at Pavia University* (21 May 2020) .

[15] G. Pellegrini *et al.*, "Technology developments and first measurements of low gain avalanche detectors (LGAD) for high energy physics applications," *Nuclear Instruments and Methods in Physics Research Section A: Accelerators, Spectrometers, Detectors and Associated Equipment* **765** (2014) 12 – 16. HSTD-9 2013 - Proceedings of the 9th International Hiroshima Symposium on Development and Application of Semiconductor Tracking Detectors.

[16] R. Padilla, C. Labitan, Z. Galloway, C. Gee, S. Mazza, F. McKinney-Martinez, H.-W. Sadrozinski, A. Seiden, B. Schumm, M. Wilder, Y. Zhao, H. Ren, Y. Jin, M. Lockerby, V. Cindro, G. Kramberger, I. Mandiz, M. Mikuz, M. Zavrtanik, R. Arcidiacono, N. Cartiglia, M. Ferrero, M. Mandurrino, V. Sola, and A. Staiano, "Effect of deep gain layer and carbon infusion on LGAD radiation hardness," *Journal of Instrumentation* **15** no. 10, (Oct, 2020) P10003–P10003.

[17] Y. Jin *et al.*, "Experimental study of acceptor removal in UFSD," *Nuclear Instruments and Methods in Physics Research Section A: Accelerators, Spectrometers, Detectors and Associated Equipment* **983** (Dec, 2020) 164611.

[18] N. Cartiglia, A. Staiano, V. Sola, R. Arcidiacono, R. Cirio, F. Cenna, M. Ferrero, V. Monaco, R. Mulargia, M. Obertino, F. Ravera, R. Sacchi, A. Bellora, S. Durando, M. Mandurrino, N. Minafra, V. Fadeyev, P. Freeman, Z. Galloway, E. Gkougkousis, H. Grabas, B. Gruey, C. Labitan, R. Losakul, Z. Luce, F. McKinney-Martinez, H.-W. Sadrozinski, A. Seiden, E. Spencer, M. Wilder, N. Woods, A. Zatserklyaniy, G. Pellegrini, S. Hidalgo, M. Carulla, D. Flores, A. Merlos, D. Quirion, V. Cindro, G. Kramberger, I. Mandić, M. Mikuž, and M. Zavrtanik, "Beam test results of a 16ps timing system based on ultra-fast silicon detectors," *Nuclear Instruments and Methods in Physics Research Section A: Accelerators, Spectrometers, Detectors and Associated Equipment* **850** (2017) 83 – 88.

[19] A. Apresyan, W. Chen, G. D'Amen, K. F. Di Petrillo, G. Giacomini, R. Heller, H. Lee, S. Los, C.-S. Moon, and A. Tricoli, "Measurements of an AC-LGAD strip sensor with a 120 GeV proton beam," *JINST* **15** no. 09, (2020) P09038, arXiv:2006.01999 [physics.ins-det].

[20] H. Pernegger, R. Bates, C. Buttar, M. Dalla, J. van Hoorne, T. Kugathasan, D. Maneuski, L. Musa, P. Riedler, C. Riegel, C. Sbarra, D. Schaefer, E. Schioppa, and W. Snoeys, "First tests of a novel radiation hard CMOS sensor process for depleted monolithic active pixel sensors," *Journal of Instrumentation* **12** no. 06, (Jun, 2017) P06008–P06008. https://doi.org/10.1088%2F1748-0221%2F12%2F06%2Fp06008.

[21] I. Berdalovic *et al.*, "Monolithic pixel development in towerjazz 180 nm cmos for the outer pixel layers in the atlas experiment," *JINST* **13** (2018) C C01023.

[22] B. Hiti *et al.*, "Development of the monolithic "MALTA" CMOS sensor for the ATLAS ITK outer pixel layer," *PoS* **TWEPP2018** (2019) 155.

[23] R. Schimassek, A. Andreazza, H. Augustin, M. Barbero, M. Benoit, F. Ehrler, G. Iacobucci, A. Meneses, P. Pangaud, M. Prathapan, A. Schöning, E. Vilella, A. Weber, M. Weber, W. Wong, H. Zhang, and I. Perić, "Test results of ATLASPIX3 — a reticle size HVCMOS pixel sensor designed for construction of multi chip modules," *Nuclear Instruments and Methods in Physics Research Section A: Accelerators, Spectrometers, Detectors and Associated Equipment* **986** (2021) 164812.

[24] F. Sauli, "GEM: A new concept for electron amplification in gas detectors," *Nucl. Instrum. Meth.* **A386** no. 2, (1997) 531–534. https://www.sciencedirect.com/science/article/pii/S0168900296011722.

[25] Y. Giomataris, P. Rebourgeard, J. Robert, and G. Charpak, "Micromegas: a high-granularity position-sensitive gaseous detector for high particle-flux environments," *Nuclear Instruments and Methods in Physics Research Section A: Accelerators, Spectrometers, Detectors and Associated Equipment* **376** no. 1, (1996) 29 – 35. http://www.sciencedirect.com/science/article/pii/0168900296001751.

[26] G. Bencivenni, R. D. Oliveira, G. Morello, and M. P. Lener, "The micro-resistive WELL detector: a compact spark-protected single amplification-stage MPGD," *Journal of Instrumentation* **10** no. 02, (Feb, 2015) P02008–P02008. https://doi.org/10.1088%2F1748-0221%2F10%2F02%2Fp02008.

[27] C. Altunbas, M. CapÃ©ans, K. Dehmelt, J. Ehlers, J. Friedrich, I. Konorov, A. Gandi, S. Kappler, B. Ketzer, R. D. Oliveira, S. Paul, A. Placci, L. Ropelewski, F. Sauli, F. Simon, and M. van Stenis, ""Construction, test and commissioning of the triple-gem tracking detector for compass"," *Nucl. Instrum. Meth.* **A490** no. 1, (2002) 177 – 203. http://www.sciencedirect.com/science/article/pii/S0168900202009105.

[28] K. Gnanvo, X. Bai, C. Gu, N. Liyanage, V. Nelyubin, and Y. Zhao, "Performance in test beam of a large-area and light-weight GEM detector with 2D stereo-angle (UV) strip readout," *Nucl. Instrum. Meth.* **A808** (2016) 83–92, arXiv:1509.03875 [physics.ins-det].

[29] A. A. et al., "The clas12 micromegas vertex tracker," *Nuclear Instruments and Methods in Physics Research Section A: Accelerators, Spectrometers, Detectors and Associated Equipment* **957** (2020) 163423. http://www.sciencedirect.com/science/article/pii/S0168900220300280.

[30] W. Xiong and et *al.*, "A small proton charge radius from an electron–proton scattering experiment," *Nature* **575** (2019) 147–150. https://www.nature.com/articles/s41586-019-1721-2.

[31] M. Collaboration, "The moller experiment: An ultra-precise measurement of the weak mixing angle using møller scattering," 2014.

[32] J. P. Chen, H. Gao, T. K. Hemmick, Z. E. Meziani, P. A. Souder, and the SoLID Collaboration, "A white paper on solid (solenoidal large intensity device)," 2014.

[33] E. Aschenauer, B. Azmoun, V.Bhopatkar, T. Burton, H. Caines, A. Camsonne, K. D. A. Deshpande, A. Drees, S. Fazio, A. Franz, C. Gal, H. Ge, K. Gnanvo, J. W. Harris, T. Hemmick, M. Hohlmann,

P. Kline, M. Lamont, A. Lebedev, B. Lewis, N. Liyanage, R. Majka, V. andR. Pak, R. Pisani, M. Purschke, M. Rosati, K.Saenboonruang, E. Sichtermann, N. Smirnov, M. Staib, S. Stoll, B. Surrow, S. Taneja, T. Ullrich, T. Videbaek, C. Woody, and S. Yalcin, "Proposal for detector R&D towards an EIC detector,". https://wiki.bnl.gov/conferences/images/9/95/RD2012-16_EIC-Tracking_proposal_April_2012.pdf.

[34] B. Stelzer, "The New Small Wheel Upgrade Project of the ATLAS Experiment," *Nuclear and Particle Physics Proceedings* **273-275** (Apr., 2016) 1160–1165.

[35] "The STAR Forward Calorimeter System and Forward Tracking System beyond BES-II." Https://drupal.star.bnl.gov/star/starnotes/public/sn0648.

[36] A. Abusleme, C. Bélanger-Champagne, A. Bellerive, Y. Benhammou, J. Botte, H. Cohen, M. Davies, Y. Du, L. Gauthier, T. Koffas, S. Kuleshov, B. Lefebvre, C. Li, N. Lupu, G. Mikenberg, D. Mori, J. P. Ochoa-Ricoux, E. P. Codina, S. Rettie, A. Robichaud-Véronneau, R. Rojas, M. Shoa, V. Smakhtin, B. Stelzer, O. Stelzer-Chilton, A. Toro, H. Torres, P. Ulloa, B. Vachon, G. Vasquez, A. Vdovin, S. Viel, P. Walker, S. Weber, and C. Zhu, "Performance of a full-size small-strip thin gap chamber prototype for the ATLAS new small wheel muon upgrade," *Nuclear Instruments and Methods in Physics Research Section A: Accelerators, Spectrometers, Detectors and Associated Equipment* **817** (May, 2016) 85–92.

[37] C. Yang and Q. Yang, "The STAR Detector Upgrades for the BES-II and at Forward Rapidity," *J. Inst.* **15** no. 07, (July, 2020) C07040–C07040.

[38] "Fun4All." HTTPS://WIKI.BNL.GOV/SPHENIX/INDEX.PHP/EIC_SPHENIX_FUN4ALL. Accessed: 2020-06-16.

[39] **PHENIX** Collaboration, C. Pinkenburg, "Analyzing ever growing datasets in PHENIX," *J. Phys. Conf. Ser.* **331** (2011) 072027.

[40] C. Pinkenburg, "Online Monitoring and online calibration/reconstruction for the PHENIX experiment," in *14th International Conference on Computing in High-Energy and Nuclear Physics*, pp. 127–129. 2005.

[41] "sPHENIX Technical Design Report." HTTPS://INDICO.BNL.GOV/EVENT/5905/CONTRIBUTIONS/32455/ATTACHMENTS/25084/37388/SPHENIX_TDR_20191015.PDF.

[42] "BeAST Magnetic Field." HTTPS://EIC.GITHUB.IO/SOFTWARE/BEAST_MAGNETIC_FIELD.HTML.

[43] "A dedicated eRHIC Detector Design ." HTTPS://INDICO.DESY.DE/INDICO/EVENT/12482/SESSION/7/CONTRIBUTION/259/MATERIAL/SLIDES/0.PPTX.

[44] "A. Y. Kiselev.". Private communication.

[45] "E. Cisbani.". Private communication.

[46] "erd25: "a compact all-silicon central tracker concept for eic"." HTTPS://INDICO.BNL.GOV/EVENT/8231/. open-mic session at the 2nd EIC Yellow Report Workshop at Pavia University.

[47] E. C. Aschenauer *et al.*, "eRHIC Design Study: An Electron-Ion Collider at BNL," *arXiv preprint arXiv:1409.1633* (2014) , arXiv:1409.1633 [physics.acc-ph].

[48] X. Li *et al.*, "A New Heavy Flavor Program for the Future Electron-Ion Collider," *EPJ Web Conf.* **235** (2020) 04002, arXiv:2002.05880 [nucl-ex].

[49] C.-P. Wong *et al.*, "A Proposed Forward Silicon Tracker for the Future Electron-Ion Collider and Associated Physics Studies," arXiv:2009.02888 [nucl-ex].

[50] B. Abelev *et al.*, "Technical design report for the upgrade of the ALICE inner tracking system," *Journal of Physics G: Nuclear and Particle Physics* **41** no. 8, (Jul, 2014) 087002.

[51] I. Berdalovic *et al.*, "Monolithic pixel development in towerjazz 180 nm cmos for the outer pixel layers in the atlas experiment," *JINST* **13** (2018) C C01023.

[52] **ALICE Collaboration** Collaboration, B. Abelev, J. Adam, D. Adamová, M. M. Aggarwal, G. Aglieri Rinella, M. Agnello, A. Agostinelli, N. Agrawal, Z. Ahammed, N. Ahmad, A. Ahmad Masoodi, I. Ahmed, S. U. Ahn, and M. More, "Technical Design Report for the Upgrade of the ALICE Inner Tracking System," Tech. Rep. CERN-LHCC-2013-024. ALICE-TDR-017, Nov, 2013. https://cds.cern.ch/record/1625842.

[53] eRD6, "eRD6 Progress Report," *EIC Generic Detector R&D Advisory Panel Meeting* (July 2020) .

[54] F. Barbosa, H. Fenker, S. Furletov, Y. Furletova, K. Gnanvo, N. Liyanage, L. Pentchev, M. Posik, C. Stanislav, B. Surrow, and B. Zihlmann, "A new Transition Radiation detector based on GEM technology," *Nuclear Instruments and Methods in Physics Research A* **942** (Oct., 2019) 162356.

[55] G. Visser, D. Abbot, F. Barbosa, C. Cuevas, H. Dong, E. Jastrzembski, B. Moffit, and B. Raydo, "A 72 channel 125 msps analog-to-digital converter module for drift chamber readout for the gluex detector," in *IEEE Nuclear Science Symposuim Medical Imaging Conference*, pp. 777–781. 2010.

[56] B. Azmoun, S. Aune, K. Dehmelt, A. Deshpande, W. Fan, P. Garg, T. K. Hemmick, M. Kebbiri, A. Kiselev, I. Mandjavidze, H. Pereira-Da-Costa, C. E. Perez-Lara, M. L. Purschke, M. Revolle, M. Vandenbroucke, and C. Woody, "Design Studies of High-Resolution Readout Planes Using Zigzags With GEM Detectors," *IEEE Transactions on Nuclear Science* **67** no. 8, (Aug, 2020) 1869–1876.

[57] B. Azmoun, P. Garg, T. K. Hemmick, M. Hohlmann, A. Kiselev, M. L. Purschke, C. Woody, and A. Zhang, "Design Studies for a TPC Readout Plane Using Zigzag Patterns With Multistage GEM Detectors," *IEEE Transactions on Nuclear Science* **65** no. 7, (2018) 1416–1423.

[58] L. Greiner, "https://www.jlab.org/indico/event/400/contribution/18/material/slides/0.pdf," *Silicon pixel-based particle vertex and tracking detectors towards the US Electron Ion Collider Workshop* (2 September 2020) .

[59] A. Bazilevsky, "Initial Considerations for EIC Detector EMCAL." https://indico.bnl.gov/event/7787/contributions/35311/attachments/26770/40728/EIC_EMCal_25feb20.pdf, Feb. 25, 2020. Presentation at a DWG Calorimetry meeting.

[60] A. Bazilevsky, "Initial Considerations for the EMCAL of the EIC Detector." https://indico.bnl.gov/event/7449/contributions/35965/attachments/27128/41350/EIC_EMCal_Temple_19mar20.pdf, Mar. 21, 2020. Presentation at EIC WG Workshop, Temple, March 2020.

[61] A. Bazilevsky, "EMCAL for eID." https://indico.bnl.gov/event/8231/contributions/37820/attachments/28257/43445/EIC_EMCal_Pavia_21may20_v2.pdf, May 21, 2020. Presentation at EIC WG Workshop, Pavia, May 2020.

[62] A. Bazilevsky, "EMCAL for eID: Shower Profile." https://indico.bnl.gov/event/8659/contributions/38247/attachments/28502/43931/EIC_EMCal_02jun20.pdf, June 2, 2020. Presentation at a DWG Calorimetry meeting.

[63] A. Bazilevsky, "EMCAL: Effect of Material." https://indico.bnl.gov/event/8933/contributions/39725/attachments/29364/45596/EIC_EMCal_14jul20.pdf, July 14, 2020. Presentation at a DWG Calorimetry meeting.

[64] T. Sjostrand, S. Mrenna, and P. Z. Skands, "A Brief Introduction to PYTHIA 8.1" *Comput. Phys. Commun.* **178** (2008) 852–867, arXiv:0710.3820 [hep-ph].

[65] E. Perez, L. Schoeffel, and L. Favart, "MILOU: A Monte-Carlo for deeply virtual Compton scattering," arXiv:hep-ph/0411389.

[66] E. Aschenauer, A. Kiselev, R. Petti, C. Ullrich, Thomas Woody, T. Horn, Y. Furletova, P. Nadel-Turonski, L. Gonella, Y. Ilieva, and K. Gnanvo, "Electron-Ion Collider Detector Requirements and R&D Handbook." http://www.eicug.org/web/sites/default/files/EIC_HANDBOOK_v1.2.pdf, Feb., 2020.

[67] **TOPSiDE concept group** Collaboration, J. Repond, "TOPSiDE: Concept of an EIC Detector," *PoS* **DIS2018** (2018) 179.

[68] **BaBar** Collaboration, B. Aubert *et al.*, "The BaBar detector," *Nucl. Instrum. Meth. A* **479** (2002) 1–116, arXiv:hep-ex/0105044.

[69] **BaBar** Collaboration, B. Aubert *et al.*, "The BABAR Detector: Upgrades, Operation and Performance," *Nucl. Instrum. Meth. A* **729** (2013) 615–701, arXiv:1305.3560 [physics.ins-det].

[70] **PHENIX** Collaboration, L. Aphecetche *et al.*, "PHENIX calorimeter," *Nucl. Instrum. Meth. A* **499** (2003) 521–536.

[71] D. Britton, M. Ryan, and X. Qu, "Light collection uniformity of lead tungstate crystals for the CMS electromagnetic calorimeter," *Nucl. Instrum. Meth. A* **540** (2005) 273–284.

[72] **PANDA** Collaboration, S. Diehl, D. Bremer, K.-T. Brinkmann, V. Dormenev, T. Eissner, R. W. Novotny, C. Rosenbaum, and H.-G. Zaunick, "Measurement and optimization of the light collection uniformity in strongly tapered PWO crystals of the PANDA detector," *Nucl. Instrum. Meth. A* **857** (2017) 1–6.

[73] C. Aidala *et al.*, "Design and Beam Test Results for the 2D Projective sPHENIX Electromagnetic Calorimeter Prototype," arXiv:2003.13685 [physics.ins-det].

[74] C. Woody, "W/ScFi and W/Shashlyk." https://indico.bnl.gov/event/9145/attachments/29919/46681/Wiki_Info_W-SciFi_W-Shashlik.pdf, July, 2020. Presentation at a DWG Calorimetry meeting.

[75] A. Bazilevsky, "EMCAL Depth." https://indico.bnl.gov/event/9145/contributions/40427/attachments/29891/46636/EIC_EMCal_depth_11aug20_.pdf, Aug. 11, 2020. Presentation at a DWG Calorimetry meeting.

[76] EIC Calorimeter R&D Consortium (eRD1), "eRD1 Report Jan-Jun 2020." https://wiki.bnl.gov/conferences/images/6/68/ERD1_EIC_Calorimetry_June-2020.pdf, July, 2020. EIC R&D WWW page https://wiki.bnl.gov/conferences/index.php/EIC_R%25D.

[77] R. Wigmans, "New developments in calorimetric particle detection," *Prog. Part. Nucl. Phys.* **103** (2018) 109–161, arXiv:1807.03853 [physics.ins-det].

[78] D. Acosta *et al.*, "Results of Prototype Studies for a Spaghetti Calorimeter," *Nucl. Instrum. Meth. A* **294** (1990) 193–210.

[79] A. Antonelli *et al.*, "Construction and performance of the lead scintillating fiber calorimeter prototypes for the KLOE detector," *Nucl. Instrum. Meth. A* **354** (1995) 352–363.

[80] T. D. Beattie *et al.*, "Construction and Performance of the Barrel Electromagnetic Calorimeter for the GlueX Experiment," *Nucl. Instrum. Meth. A* **896** (2018) 24–42, arXiv:1801.03088 [physics.ins-det].

[81] **Particle Data Group** Collaboration, P. Zyla *et al.*, "Review of Particle Physics," *PTEP* **2020** no. 8, (2020) 083C01.

[82] EIC Calorimeter R&D Consortium (eRD1), "eRD1 Report Jan-Jun 2016." https://wiki.bnl.gov/conferences/images/9/9e/ERD1_EIC_Calorimetry_Consortium_June-2016.pdf, July, 2016. EIC R&D WWW page https://wiki.bnl.gov/conferences/index.php/EIC_R%25D.

[83] **COMPASS** Collaboration, P. Abbon *et al.*, "The COMPASS Setup for Physics with Hadron Beams," *Nucl. Instrum. Meth. A* **779** (2015) 69–115, arXiv:1410.1797 [physics.ins-det].

[84] **GEANT4** Collaboration, S. Agostinelli *et al.*, "GEANT4: A Simulation toolkit," *Nucl. Instrum. Meth.* **A506** (2003) 250–303.

[85] H. Shimizu, Y. Sakamoto, T. Hashimoto, K. Abe, Y. Asano, T. Kinashi, T. Matsumoto, T. Matsumura, H. Yoshida, and H. Okuno, "Performance of a PbWO-4 crystal calorimeter for 0.2-GeV to 1.0-GeV electrons," *Nucl. Instrum. Meth. A* **447** (2000) 467–475.

[86] G. Conesa, H. Delagrange, J. Diaz, M. Ippolitov, Y. Kharlov, D. Peresunko, and Y. Schutz, "Performance of the ALICE photon spectrometer PHOS," *Nucl. Instrum. Meth. A* **537** (2005) 363–367.

[87] **COMPASS** Collaboration, P. Abbon *et al.*, "The COMPASS experiment at CERN," *Nucl. Instrum. Meth. A* **577** (2007) 455–518, arXiv:hep-ex/0703049.

[88] Y. Kharlov *et al.*, "Performance of a fine-sampling electromagnetic calorimeter prototype in the energy range from 1-GeV to 19-GeV," *Nucl. Instrum. Meth. A* **606** (2009) 432–438, arXiv:0809.3671 [physics.ins-det].

[89] A. Bazilevsky, "Need for a preshowerin h-endcup?" https://indico.bnl.gov/event/9197/contributions/40574/attachments/29996/46820/Preshower_18aug20.pdf, Aug. 18, 2020. Presentation at a DWG Calorimetry meeting.

[90] **ALICE EMCal** Collaboration, J. Allen *et al.*, "Performance of prototypes for the ALICE electromagnetic calorimeter," *Nucl. Instrum. Meth. A* **615** (2010) 6–13, arXiv:0912.2005 [physics.ins-det].

[91] S. Inaba, M. Kobayashi, M. Nakagawa, T. Nakagawa, H. Shimizu, K. Takamatsu, T. Tsuru, and Y. Yasu, "A Beam test of a calorimeter prototype of PWO crystals at energies between 0.5-GeV and 2.5-GeV," *Nucl. Instrum. Meth. A* **359** (1995) 485–491.

[92] G. Alexeev *et al.*, "Studies of lead tungstate crystal matrices in high-energy beams for the CMS electromagnetic calorimeter at the LHC," *Nucl. Instrum. Meth. A* **385** (1997) 425–434.

[93] H. Mkrtchyan *et al.*, "The lead-glass electromagnetic calorimeters for the magnetic spectrometers in Hall C at Jefferson Lab," *Nucl. Instrum. Meth. A* **719** (2013) 85–100, arXiv:1204.6413 [physics.ins-det].

[94] T. Awes *et al.*, "High-energy beam test of the PHENIX lead scintillator EM calorimeter," arXiv:nucl-ex/0202009.

[95] **sPHENIX** Collaboration, C. Aidala *et al.*, "Design and Beam Test Results for the sPHENIX Electromagnetic and Hadronic Calorimeter Prototypes," *IEEE Trans. Nucl. Sci.* **65** no. 12, (2018) 2901–2919, arXiv:1704.01461 [physics.ins-det].

[96] **CALEIDO** Collaboration, A. Benvenuti *et al.*, "A shashlik calorimeter with longitudinal segmentation for a linear collider," *Nucl. Instrum. Meth. A* **461** (2001) 373–375.

[97] Y. Qiang, C. Zorn, F. Barbosa, and E. Smith, "Radiation Hardness Tests of SiPMs for the JLab Hall D Barrel Calorimeter," *Nucl. Instrum. Meth. A* **698** (2013) 234–241, arXiv:1207.3743 [physics.ins-det].

[98] B. Biró *et al.*, "A Comparison of the Effects of Neutron and Gamma Radiation in Silicon Photomultipliers," *IEEE Trans. Nucl. Sci.* **66** no. 7, (2019) 1833–1839, arXiv:1809.04594 [physics.ins-det].

[99] I. Chirikov-Zorin *et al.*, "Performance of the COMPASS II shashlyk calorimeter ECAL0 read out by SiPMs," *Nucl. Instrum. Meth. A* **936** (2019) 141–143.

[100] O. Tsai, "Hadron Calorimetry for EIC." https://indico.bnl.gov/event/7449/contributions/35968/attachments/27163/41401/EIC_YR_Temple_OT.pdf, Mar. 21, 2020. Presentation at EIC WG Workshop, Temple, March 2020.

[101] N. Anfimov *et al.*, "Novel micropixel avalanche photodiodes (MAPD) with super high pixel density," *Nucl. Instrum. Meth. A* **628** (2011) 369–371.

[102] NICA MPD Collaboration, "MPD NICA TDR for ECal." http://mpd.jinr.ru/wp-content/uploads/2019/01/TDR_ECAL_v3.6_2019.pdf, Nov., 2018.

[103] G. Alexeev *et al.*, "Beam test results of a PbWO-4 crystal calorimeter prototype," *Nucl. Instrum. Meth. A* **364** (1995) 307–310.

[104] **ALICE PHOS calorimeter** Collaboration, D. Aleksandrov *et al.*, "A high resolution electromagnetic calorimeter based on lead-tungstate crystals," *Nucl. Instrum. Meth. A* **550** (2005) 169–184.

[105] **CMS** Collaboration, P. Adzic *et al.*, "Results of the first performance tests of the CMS electromagnetic calorimeter," *Eur. Phys. J. C* **44S1** (2006) 1–10.

[106] **PrimEx** Collaboration, M. Kubantsev, I. Larin, and A. Gasparian, "Performance of the PrimEx electromagnetic calorimeter," *AIP Conf. Proc.* **867** no. 1, (2006) 51–58, arXiv:physics/0609201.

[107] **PANDA** Collaboration, C. Rosenbaum *et al.*, "Performance of Prototypes for the Barrel Part of the ANDA Electromagnetic Calorimeter," *J. Phys. Conf. Ser.* **742** no. 1, (2016) 012015.

[108] **PANDA** Collaboration, M. Kavatsyuk *et al.*, "Performance of the prototype of the electromagnetic calorimeter for PANDA," *Nucl. Instrum. Meth. A* **648** (2011) 77–91.

[109] **HPS** Collaboration, I. Balossino *et al.*, "The HPS electromagnetic calorimeter," *Nucl. Instrum. Meth. A* **854** (2017) 89–99, arXiv:1610.04319 [physics.ins-det].

[110] A. Acker *et al.*, "The CLAS12 Forward Tagger," *Nucl. Instrum. Meth. A* **959** (2020) 163475.

[111] T. Horn *et al.*, "Scintillating crystals for the Neutral Particle Spectrometer in Hall C at JLab," *Nucl. Instrum. Meth. A* **956** (2020) 163375, arXiv:1911.11577 [physics.ins-det].

[112] "PrimEx η electromagnetic calorimeter, prototype for experiments at Jefferson Lab." https://halldweb.jlab.org/DocDB/0047/004784/001/ccal_nps.pdf, Dec., 2020.

[113] T. Sumiyoshi *et al.*, "Performance of the Venus Lead Glass Calorimeter at Tristan," *Nucl. Instrum. Meth. A* **271** (1988) 432.

[114] **OPAL** Collaboration, K. Ahmet *et al.*, "The OPAL detector at LEP," *Nucl. Instrum. Meth. A* **305** (1991) 275–319.

[115] GlueX Collaboration, "GlueX/HallD Calorimeter Final Design and Safety Review. Section 4:FCAL-The Forward Calorimeter." https://halldweb.jlab.org/DocDB/0009/000988/001/fcal.pdf, Feb., 2008.

[116] Y. Prokoshkin and A. Shtannikov, "Energy resolution calculation of the PWO calorimeter, comparison with the beam tests," *Nucl. Instrum. Meth. A* **362** (1995) 406–409.

[117] H. Avakian *et al.*, "Performance of F101 radiation resistant lead glass shower counters," *Nucl. Instrum. Meth. A* **378** (1996) 155–161.

[118] S. Sedykh *et al.*, "Electromagnetic calorimeters for the BNL muon (g-2) experiment," *Nucl. Instrum. Meth. A* **455** (2000) 346–360.

[119] T. Armstrong *et al.*, "The E864 lead-scintillating fiber hadronic calorimeter," *Nucl. Instrum. Meth. A* **406** (1998) 227–258.

[120] O. Tsai *et al.*, "Results of \& on a new construction technique for W/ScFi Calorimeters," *J. Phys. Conf. Ser.* **404** (2012) 012023.

[121] **LHCb** Collaboration, S. Barsuk, "The LHCb Calorimeter Performance and its Expected Radiation-Induced Degradation," *IEEE Trans. Nucl. Sci.* **57** no. 3, (2010) 1447–1453.

[122] S. Kuleshov, "Shashlyk calorimeter option for EIC detector." `https://indico.bnl.gov/event/8200/contributions/36406/attachments/27471/42023/shashlik_RD_compressed.pdf`, Mar. 30, 2020. Presentation at a DWG Calorimetry meeting.

[123] EIC Calorimeter R&D Consortium (eRD1), "eRD1 Presentation July 2020." `https://wiki.bnl.gov/conferences/images/1/1c/EIC_R%26D_eRD1_Report_7-24-20_complete.pptx`, July, 2020. EIC R&D WWW page `https://wiki.bnl.gov/conferences/index.php/EIC_R%25D`.

[124] I. Chirikov-Zorin, Z. Krumshtein, and A. Olchevski, "The design of a photodetector unit of a new Shashlyk EM calorimeter for COMPASS II," *Nucl. Instrum. Meth. A* **824** (2016) 674–677.

[125] G. Atoian *et al.*, "An Improved Shashlyk Calorimeter," *Nucl. Instrum. Meth. A* **584** (2008) 291–303, `arXiv:0709.4514 [physics.ins-det]`.

[126] A. Semenov *et al.*, "Electromagnetic Calorimeter for MPD Spectrometer at NICA Collider," *JINST* **15** no. 05, (2020) C05017, `arXiv:2002.07709 [physics.ins-det]`.

[127] G. Avoni *et al.*, "The electromagnetic calorimeter of the HERA-B experiment," *Nucl. Instrum. Meth. A* **580** (2007) 1209–1226.

[128] N. Anfimov *et al.*, "Shashlyk EM calorimeter prototype readout by MAPD with superhigh pixel density for COMPASS II," *Nucl. Instrum. Meth. A* **718** (2013) 75–77.

[129] N. Anfimov *et al.*, "Tests of the module array of the ECAL0 electromagnetic calorimeter for the COMPASS experiment with the electron beam at ELSA," *Phys. Part. Nucl. Lett.* **12** no. 4, (2015) 566–569.

[130] E. Bernardi *et al.*, "Performance of a Compensating Lead Scintillator Hadronic Calorimeter," *Nucl. Instrum. Meth. A* **262** (1987) 229.

[131] R. Wigmans, "Sampling calorimetry," *Nucl. Instrum. Meth. A* **494** (2002) 277–287.

[132] G. Drews *et al.*, "Experimental Determination of Sampling Fluctuations in Uranium and Lead Hadronic Calorimeters," *Nucl. Instrum. Meth. A* **290** (1990) 335.

[133] D. Acosta *et al.*, "Electron, pion and multiparticle detection with a lead / scintillating - fiber calorimeter," *Nucl. Instrum. Meth. A* **308** (1991) 481–508.

[134] R. Wigmans, "Quartz fibers and the prospects for hadron calorimetry at the 1% resolution level," in *7th International Conference on Calorimetry in High-Energy Physics (ICCHEP 97)*, pp. 182–193. 1997.

[135] R. Wigmans, *Calorimetry: Energy measurement in particle physics*, vol. 107. Oxford University Press, 2000. doi: 10.1093/oso/9780198786351.001.0001.

[136] C. Leroy and P. Rancoita, "Physics of cascading shower generation and propagation in matter: Principles of high-energy, ultrahigh-energy and compensating calorimetry," *Rept. Prog. Phys.* **63** (2000) 505–606.

[137] H. Huang, G. Igo, S. Trentalange, O. Tsai, C. Gagliardi, and S. Heppelmann, "Proposal. Development of a New Detector Technology for Fiber Sampling Calorimeters for EIC and STAR." https://wiki.bnl.gov/conferences/images/d/d4/RD-1_RDproposal_April-2011.pdf, Mar., 2011.

[138] A. Benaglia, E. Auffray, P. Lecoq, H. Wenzel, and A. Para, "Space-Time Development of Electromagnetic and Hadronic Showers and Perspectives for Novel Calorimetric Techniques," *IEEE Trans. Nucl. Sci.* **63** no. 2, (2016) 574–579.

[139] G. Giacomini, W. Chen, F. Lanni, and A. Tricoli, "Development of a technology for the fabrication of Low-Gain Avalanche Diodes at BNL," *Nucl. Instrum. And Meth. in Phys. Res. A* **934** (2019) 52–57. http://www.sciencedirect.com/science/article/pii/S0168900219305479.

[140] N. Moffat, R. B. ans M. Bullough, L. Flores, D. Maneuski, L. Simon, N. Tartoni, F. Dohertya, and J. Ashbya, "Low gain avalanche detectors (LGAD) for particle physics and synchrotron applications," *JINST* **13** (2018) C 03014.

[141] CMS Collaboration, "Technical Proposal for a MIP timing detector in the CMS experiment phase 2 upgrade," Tech. Rep. CERN-LHCC-2017-027. LHCC-P-009, CERN, Geneva, Dec, 2017. https://cds.cern.ch/record/2296612.

[142] ATLAS Collaboration, "Technical Proposal: A High-Granularity Timing Detector for the ATLAS Phase-II Upgrade," Tech. Rep. CERN-LHCC-2018-023. LHCC-P-012, CERN, Geneva, Jun, 2018. http://cds.cern.ch/record/2623663.

[143] I. Bejar Alonso and L. Rossi, "HiLumi LHC Technical Design Report: Deliverable: D1.10," Nov, 2015. https://cds.cern.ch/record/2069130.

[144] **The project is partially supported by the EC as FP7 HiLumi LHC Design Study under grant no. 284404 Collaboration** Collaboration, L. Rossi and O. Bruning, "High Luminosity Large Hadron Collider: A description for the European Strategy Preparatory Group," Geneva, Aug, 2012. https://cds.cern.ch/record/1471000.

[145] M. Mandurrino, R. Arcidiacono, M. Boscardin, N. Cartiglia, G. F. D. Betta, M. Ferrero, F. Ficorella, L. Pancheri, G. Paternoster, F. Siviero, V. Sola, A. Staiano, and A. Vignati, "Analysis and numerical design of resistive ac-coupled silicon detectors (rsd) for 4d particle tracking," *Nucl. Inst. Meth. A* **959** (2020) 163479.

[146] G. Giacomini, W. Chen, G. D'Amen, and A. Tricoli, "Fabrication and performance of ac-coupled lgads," *JINST* **14** (2019) P09004.

[147] M. Mandurrino, R. Arcidiacono, M. Boscardin, N. Cartiglia, G. F. Dalla Betta, M. Ferrero, F. Ficorella, L. Pancheri, G. Paternoster, F. Siviero, and M. Tornago, "Demonstration of 200-, 100-,

and 50- μ m pitch resistive ac-coupled silicon detectors (rsd) with 100% fill-factor for 4d particle tracking," *IEEE Electron Device Letters* **40** no. 11, (2019) .

[148] A. Sharma, I. A. Asensi, I. Berdalovic, D. Bortoletto, R. Cardella, F. Dachs, V. Dao, T. Hemperek, B. Hiti, T. Kugathasan, K. Moustakas, H. Pernegger, P. Riedler, C. Riegel, P. Rymaszewski, C. Solans Sanchez, E. J. Schioppa, W. Snoeys, C. A. M. Tobon, T. Wang, N. Wermes, and L. S. Argemi, "The MALTA CMOS pixel detector prototype for the ATLAS Pixel ITk," *PoS* **VERTEX2018** (2019) 014. 11 p. http://cds.cern.ch/record/2697097.

[149] **ALICE Collaboration** Collaboration, "A Forward Calorimeter (FoCal) in the ALICE experiment." https://cds.cern.ch/record/2696471, Oct, 2019.

[150] **JLab Neutral Particle Spectrometer** Collaboration, T. Horn, "A $PbWO_4$-based Neutral Particle Spectrometer in Hall C at 12 GeV JLab," *J. Phys. Conf. Ser.* **587** no. 1, (2015) 012048.

[151] W. B. Atwood, A. A. Abdo, M. Ackermann, W. Althouse, B. Anderson, M. Axelsson, L. Baldini, J. Ballet, D. L. Band, G. Barbiellini, and et al., "The large area telescope on the fermi gamma-ray space telescope mission," *The Astrophysical Journal* **697** no. 2, (May, 2009) 1071?1102. http://dx.doi.org/10.1088/0004-637X/697/2/1071.

[152] "Joint Zero Degree Calorimeter Project." http://jzcap.physics.illinois.edu/pages.html.

[153] Y. Kharzheev, "Radiation Hardness of Scintillation Detectors Based on Organic Plastic Scintillators and Optical Fibers," *Phys. Part. Nucl.* **50** no. 1, (2019) 42–76.

[154] P. Achenbach *et al.*, "In-beam tests of scintillating fibre detectors at MAMI and at GSI," *Nucl. Instrum. Meth. A* **593** (2008) 353–360, arXiv:0802.2830 [nucl-ex].

[155] C. Ayerbe Gayoso, *The scintillating fiber focal plane detector for the use of Kaos as a double arm spectrometer*. PhD thesis, Mainz U., Inst. Kernphys., 2012.

[156] F. Blanc, "Scintillating Fiber Trackers: recent developments and applications,". https://cds.cern.ch/record/1603129.

[157] Aschenauer, E.C. and Baker, M.D. and Lee, J.H. and Zheng, L., "EIC R&D Project eRD17 Progress Report." https://wiki.bnl.gov/conferences/index.php/EIC_R&D.

[158] "Electron-Ion Collider Detector Requirements and R&D Handbook (version 1.1)." http://eicug.org/web/sites/default/files/EIC_HANDBOOK_v1.1.pdf, Jan, 2019.

[159] Z. Tu, A. Jentsch, M. Baker, L. Zheng, J.-H. Lee, R. Venugopalan, O. Hen, D. Higinbotham, E.-C. Aschenauer, and T. Ullrich, "Probing short-range correlations in the deuteron via incoherent diffractive j/ψ production with spectator tagging at the eic," *Physics Letters B* (2020) . https://arxiv.org/abs/2005.14706.

[160] *U.S. Department of Energy Office of Science, Reaching for the horizon: The 2015 Long Range Plan for Nuclear Science*. http://science.energy.gov/np/nsac.

[161] H1 Luminosity Monitor, http://www-h1.desy.de/h1/www/h1det/lumi/.

[162] **H1** Collaboration, F. D. Aaron *et al.*, "Determination of the Integrated Luminosity at HERA using Elastic QED Compton Events," *Eur. Phys. J.* **C72** (2012) 2163, arXiv:1205.2448 [hep-ex]. [Erratum: Eur. Phys. J.C74,2733(2012)].

[163] Zeus Luminosity Monitor, http://www-zeus.desy.de/zeus_det_papers/zeus_det_papers.html.

[164] T. Haas and V. Makarenko, "Precision calculation of processes used for luminosity measurement at the ZEUS experiment," *Eur. Phys. J. C* **71** (2011) 1574, arXiv:1009.2451 [hep-ph].

[165] J. Adam, "eic-lgen event generator,". https://github.com/adamjaro/eic-lgen.

[166] U. Amaldi, ed., *Study of an ep Facility for Europe DESY, Hamburg, April 2-3, 1979.*, vol. 790402. Deutsches Electron Synchrotron / European Committee for Future Accelerators, Hamburg, Germany, 1979.

[167] K. Aulenbacher, E. Chudakov, D. Gaskell, J. Grames, and K. D. Paschke, "Precision electron beam polarimetry for next generation nuclear physics experiments," *Int. J. Mod. Phys. E* **27** no. 07, (2018) 1830004.

[168] J. Hansknecht and M. Poelker, "Synchronous photoinjection using a frequency-doubled gain-switched fiber-coupled seed laser and ErYb-doped fiber amplifier," *Phys. Rev. ST Accel. Beams* **9** (2006) 063501.

[169] A. Narayan *et al.*, "Precision Electron-Beam Polarimetry at 1 GeV Using Diamond Microstrip Detectors," *Phys. Rev. X* **6** no. 1, (2016) 011013, arXiv:1509.06642 [nucl-ex].

[170] N. Vansteenkiste, P. Vignolo, and A. Aspect, "Optical reversibility theorems for polarization: application to remote control of polarization," *J. Opt. Soc. Am. A* **10** no. 10, (Oct, 1993) 2240–2245. http://josaa.osa.org/abstract.cfm?URI=josaa-10-10-2240.

[171] B. Sobloher, R. Fabbri, T. Behnke, J. Olsson, D. Pitzl, S. Schmitt, and J. Tomaszewska, "Polarisation at HERA - Reanalysis of the HERA II Polarimeter Data -," *HERA Internal Note* (1, 2012) , arXiv:1201.2894 [physics.ins-det].

[172] A. Camsonne, J. Hoskins, *et al.*, "eRD15: R&D for a Compton Electron Detector," *EIC R&D Progress Report* (June, 2017) .

[173] A. Camsonne, J. Hoskins, *et al.*, "eRD15: R&D for a Compton Electron Detector," *EIC R&D Progress Report* (January, 2016) .

[174] F. Méot *et al.*, "eRHIC EIC: Plans for Rapid Acceleration of Polarized Electron Bunch at Cornell Synchrotron," in *9th International Particle Accelerator Conference*, p. MOPMF013. 2018.

[175] **The RHIC Polarimetry Group** Collaboration, W. B. Schmidke *et al.*, "Rhic polarization for runs 9-17," Tech. Rep. BNL-209057-2018-TECH, C-A/AP/609, Brookhaven National Laboratory, 2018. https://technotes.bnl.gov/PDF?publicationId=209057.

[176] A. A. Poblaguev, A. Zelenski, G. Atoian, Y. Makdisi, and J. Ritter, "Systematic error analysis in the absolute hydrogen gas jet polarimeter at RHIC," *Nucl. Instrum. Meth. A* **976** (2020) 164261, arXiv:2006.08393 [physics.ins-det].

[177] A. Zelenski *et al.*, "Absolute polarized H-jet polarimeter development, for RHIC," *Nucl. Instrum. Meth. A* **536** (2005) 248–254.

[178] W. Fischer and A. Bazilevsky *Phys. Rev. ST Accel. Beams* **15** (2012) 041001.

[179] **PHENIX Collaboration** Collaboration, C. Aidala *et al. Phys. Rev. Lett.* **120** (2018) 022001.

[180] G. Mitsuka *Phys. Rev.* **C95** (2017) 044908.

[181] N. H. Buttimore, B. Kopeliovich, E. Leader, J. Soffer, and T. Trueman, "The spin dependence of high-energy proton scattering," *Phys. Rev. D* **59** (1999) 114010, arXiv:hep-ph/9901339.

[182] A. A. Poblaguev *et al.*, "Precision Small Scattering Angle Measurements of Elastic Proton-Proton Single and Double Spin Analyzing Powers at the RHIC Hydrogen Jet Polarimeter," *Phys. Rev. Lett.* **123** no. 16, (2019) 162001, arXiv:1909.11135 [hep-ex].

[183] G. Atoian, A. Zelenski, and A. Poblaguev, "Precision absolute polarimeter development for the 3He++ ion beam at 5.0–6.0 MeV energy," *PoS* **PSTP2019** (2020) 045.

[184] **PHENIX** Collaboration, A. Adare *et al.*, "Concept for an Electron Ion Collider (EIC) detector built around the BaBar solenoid," arXiv:1402.1209 [nucl-ex].

[185] **sPHENIX** Collaboration, "An EIC Detector Built Around The sPHENIX Solenoid - A Detector Design Study," sPH-cQCD-2018-001. https://indico.bnl.gov/event/5283/.

[186] C. Aidala, A. Bazilevsky, G. Borca-Tasciuc, N. Feege, E. Gamez, Y. Goto, X. He, J. Huang, A. K. V, J. Lajoie, G. Matousek, K. Mattioli, P. Nadel-Turonski, C. Nunez, J. Osborn, C. Perez, R. Seidl, D. Shangase, P. Stankus, X. Sun, and J. Zhang, "An EIC Detector Built Around The sPHENIX Solenoid," 2018. sPHENIX-note sPH-cQCD-2018-001.

[187] "A 32 Ch low latency 12b 0.5 GS/s ADC." http://pacificmicrochip.com/wp-content/uploads/2019/11/PMCC_32chADC_500M_12b.pdf.

[188] P. Buncic, M. Krzewicki, and P. Vande Vyvre, "Technical Design Report for the Upgrade of the Online-Offline Computing System," Tech. Rep. CERN-LHCC-2015-006. ALICE-TDR-019, Apr, 2015. https://cds.cern.ch/record/2011297.

[189] M. Bodlak, V. Frolov, V. Jary, S. Huber, I. Konorov, D. Levit, J. Novy, R. Salac, M. Virius, and S. Paul, "FPGA based data acquisition system for COMPASS experiment," *J. Phys. Conf. Ser.* **513** (2014) 012029, arXiv:1310.1308 [physics.ins-det].

[190] **LHCb** Collaboration, J. Alves, A.Augusto *et al.*, "The LHCb Detector at the LHC," *JINST* **3** (2008) S08005.

[191] T. Colombo *et al.*, "The LHCb Online system in 2020: trigger-free read-out with (almost exclusively) off-the-shelf hardware," *J. Phys. Conf. Ser.* **1085** no. 3, (2018) 032041.

[192] P. Moreira *et al.*, "The GBT Project," in *Topical Workshop on Electronics for Particle Physics*. 2009.

[193] **sPHENIX** Collaboration, "Technical Design Report for sPHENIX experiment," sPHENIX-TDR. https://indico.bnl.gov/event/7081/.

[194] J. A. et. al, "SAMPA chip: the new 32 channels ASIC for the ALICE TPC and MCH upgrades," *Journal of Instrumentation* **12** no. 04, (2017) C04008. http://stacks.iop.org/1748-0221/12/i=04/a=C04008.

[195] J. Anderson, K. Bauer, A. Borga, H. Boterenbrood, H. Chen, K. Chen, G. Drake, M. Dönszelmann, D. Francis, D. Guest, B. Gorini, M. Joos, F. Lanni, G. L. Miotto, L. Levinson, J. Narevicius, W. P. Vazquez, A. Roich, S. Ryu, F. Schreuder, J. Schumacher, W. Vandelli, J. Vermeulen, D. Whiteson, W. Wu, and J. Zhang, "FELIX: a PCIe based high-throughput approach for interfacing front-end and trigger electronics in the ATLAS upgrade framework," *Journal of Instrumentation* **11** no. 12, (2016) C12023. http://stacks.iop.org/1748-0221/11/i=12/a=C12023.

[196] M. L. Purschke, "RCDAQ, a lightweight yet powerful data acquisition system." https://github.com/sPHENIX-Collaboration/rcdaq, 2012.

[197] S. Ritt, "The PSU+I DRS4 Evaluation Board." https://www.psi.ch/en/drs/evaluation-board.

[198] "CERN SRS Home Page." https://espace.cern.ch/rd51-wg5/srs/default.aspx.

[199] V. Gyurjyan *et al.*, "CLARA: A Contemporary Approach to Physics Data Processing," *J. Phys.: Conf. Ser. 331 032013 doi:10.1088/1742-6596/331/3/032013* (2011) .

[200] H. Dong, C. Cuevas, D. Curry, E. Jastrzembski, F. Barbosa, J. Wilson, M. Taylor, and B. Raydo, "Integrated tests of a high speed vxs switch card and 250 msps flash adcs," in *2007 IEEE Nuclear Science Symposium Conference Record*, vol. 1, pp. 831–833. 2007.

[201] F. Ameli, M. Battaglieri, M. Bondí, M. Capodiferro, A. Celentano, T. Chiarusi, G. Chiodi, M. De Napoli, R. Lunadei, L. Marsicano, P. Musico, F. Pratolongo, L. Recchia, D. Ruggieri, and L. Stellato, "A low cost, high speed, multichannel analog to digital converter board," *Nuclear Instruments and Methods in Physics Research Section A: Accelerators, Spectrometers, Detectors and Associated Equipment* **936** (2019) 286 – 287. http://www.sciencedirect.com/science/article/pii/S0168900218310684. Frontier Detectors for Frontier Physics: 14th Pisa Meeting on Advanced Detectors.

[202] M. Favaro, T. Chiarusi, F. Giacomini, M. Manzali, A. Margiotta, and C. Pellegrino, "The Trigger and Data Acquisition System for the KM3NeT-Italia towers," *EPJ Web Conf.* **116** (2016) 05009.

[203] D. Lawrence, A. Boehnlein, N. Brei, and D. Romanov, "JANA2: Multithreaded Event Reconstruction," *J. Phys. Conf. Ser.* **1525** no. 1, (2020) 012032.

[204] V. Burkert *et al.*, "The CLAS12 Spectrometer at Jefferson Laboratory," *Nucl. Instrum. Meth. A* **959** (2020) 163419.

[205] V. Gyurjyan *et al.*, "CLARA: The CLAS12 Reconstruction and Analysis framework," *J. Phys.: Conf. Ser. 762 012009 doi:10.1088/1742-6596/762/1/012009* (2016) .

[206] V. Ziegler *et al.*, "The CLAS12 software framework and event reconstruction," *Nuclear Instruments and Methods in Physics Research Section A: Accelerators, Spectrometers, Detectors and Associated Equipment, Volume 959* (2020) .

[207] F. Barbosa, C. Hutton, A. Sitnikov, A. Somov, S. Somov, and I. Tolstukhin, "Pair spectrometer hodoscope for Hall D at Jefferson Lab," *Nucl. Instrum. Meth. A* **795** (2015) 376–380.

[208] M. Frank, F. Gaede, C. Grefe, and P. Mato, "DD4hep: A Detector Description Toolkit for High Energy Physics Experiments," *J. Phys. Conf. Ser.* **513** (2014) 022010.

[209] R. Brun, A. Gheata, and M. Gheata, "The ROOT geometry package," *Nucl. Instrum. Meth. A* **502** (2003) 676–680.

[210] G. Amadio *et al.*, "GeantV Alpha Release," *J. Phys. Conf. Ser.* **1085** no. 3, (2018) 032037.

[211] X. Ai, "Acts: A common tracking software," *arXiv: Instrumentation and Detectors* (2019) .

[212] J. Rauch and T. Schlüter, "GENFIT — a Generic Track-Fitting Toolkit," *J. Phys. Conf. Ser.* **608** no. 1, (2015) 012042, arXiv:1410.3698 [physics.ins-det].

[213] G. Barrand *et al.*, "GAUDI - A software architecture and framework for building HEP data processing applications," *Comput. Phys. Commun.* **140** (2001) 45–55.

[214] M. Clemencic, H. Degaudenzi, P. Mato, S. Binet, W. Lavrijsen, C. Leggett, and I. Belyaev, "Recent developments in the LHCb software framework Gaudi," *J. Phys. Conf. Ser.* **219** (2010) 042006.

[215] E. Tejedor, E. Bocchi, D. Castro, H. Gonzalez, M. Lamanna, P. Mato, J. Moscicki, and D. Piparo, "Facilitating collaborative analysis in SWAN," *EPJ Web Conf.* **214** (2019) 07022.

[216] S. Höche and S. Prestel, "The midpoint between dipole and parton showers," *Eur. Phys. J. C* **75** no. 9, (2015) 461, arXiv:1506.05057 [hep-ph].

[217] F. Dulat, S. Höche, and S. Prestel, "Leading-Color Fully Differential Two-Loop Soft Corrections to QCD Dipole Showers," *Phys. Rev. D* **98** no. 7, (2018) 074013, arXiv:1805.03757 [hep-ph].

[218] G. Schuler and H. Spiesberger, "DJANGO: The Interface for the event generators HERACLES and LEPTO," in *Workshop on Physics at HERA*, pp. 1419–1432. 1991.

[219] E. C. Aschenauer, T. Burton, T. Martini, H. Spiesberger, and M. Stratmann, "Prospects for Charged Current Deep-Inelastic Scattering off Polarized Nucleons at a Future Electron-Ion Collider," *Phys. Rev.* **D88** (2013) 114025, arXiv:1309.5327 [hep-ph].

[220] P. Bedaque, A. Boehnlein, M. Cromaz, M. Diefenthaler, L. Elouadrhiri, T. Horn, M. Kuchera, D. Lawrence, D. Lee, S. Lidia, *et al.*, "Report from the AI For Nuclear Physics Workshop," *arXiv preprint arXiv:2006.05422* (2020) .

[221] P. Mehta, M. Bukov, C.-H. Wang, A. G. Day, C. Richardson, C. K. Fisher, and D. J. Schwab, "A high-bias, low-variance introduction to machine learning for physicists," *Physics reports* **810** (2019) 1–124.

[222] C. Lynch, "Big data: How do your data grow?," *Nature* **455** no. 7209, (2008) 28.

[223] Alves Jr, A Augusto and Andrade Filho, LM and Barbosa, AF and Bediaga, I and Cernicchiaro, G and Guerrer, G and Lima Jr, HP and Machado, AA and Magnin, J and Marujo, F and others, "The LHCb detector at the LHC," *Journal of Instrumentation* **3** no. 08, (2008) S08005.

[224] "Streaming Readout Workshop," 2020. https://www.bnl.gov/srvii2020/.

[225] "Fast Machine Learning Workshop," 2020. https://indico.cern.ch/event/924283/.

[226] R. Chalapathy and S. Chawla, "Deep learning for anomaly detection: A survey," *arXiv preprint arXiv:1901.03407* (2019) .

[227] S. Farrell, P. Calafiura, M. Mudigonda, D. Anderson, J.-R. Vlimant, S. Zheng, J. Bendavid, M. Spiropulu, G. Cerati, L. Gray, *et al.*, "Novel deep learning methods for track reconstruction," *arXiv preprint arXiv:1810.06111* (2018) .

[228] D. Derkach, M. Hushchyn, T. Likhomanenko, A. Rogozhnikov, N. Kazeev, V. Chekalina, R. Neychev, S. Kirillov, F. Ratnikov, L. collaboration, *et al.*, "Machine-Learning-based global particle-identification algorithms at the LHCb experiment," in *Journal of Physics: Conference Series*, vol. 1085, p. 042038, IOP Publishing. 2018.

[229] C. Fanelli and J. Pomponi, "DeepRICH: learning deeply Cherenkov detectors," *Machine Learning: Science and Technology* **1** no. 1, (2020) 015010.

[230] H. Drucker and C. Cortes, "Boosting decision trees," in *Advances in neural information processing systems*, pp. 479–485. 1996.

[231] M. Dugger, B. Ritchie, I. Senderovich, E. Anassontzis, P. Ioannou, C. Kourkoumeli, G. Vasileiadis, G. Voulgaris, N. Jarvis, W. Levine, *et al.*, "A study of decays to strange final states with GlueX in Hall D using components of the BaBar DIRC," *arXiv preprint arXiv:1408.0215* (2014) .

[232] B. Page, X. Chu, and E. Aschenauer, "Experimental aspects of jet physics at a future EIC," *Physical Review D* **101** no. 7, (2020) 072003.

[233] G. Louppe, K. Cho, C. Becot, and K. Cranmer, "QCD-aware recursive neural networks for jet physics," *Journal of High Energy Physics* **2019** no. 1, (2019) 57.

[234] "Ml4jets workshop," 2020. https://iris-hep.org/projects/ml4jets.html.

[235] I. Goodfellow, J. Pouget-Abadie, M. Mirza, B. Xu, D. Warde-Farley, S. Ozair, A. Courville, and Y. Bengio, "Generative adversarial nets," in *Advances in neural information processing systems*, pp. 2672–2680. 2014.

[236] C. Doersch, "Tutorial on variational autoencoders," *arXiv preprint arXiv:1606.05908* (2016) .

[237] D. J. Rezende and S. Mohamed, "Variational inference with normalizing flows," *arXiv preprint arXiv:1505.05770* (2015) .

[238] M. Paganini, L. de Oliveira, and B. Nachman, "Accelerating science with generative adversarial networks: an application to 3D particle showers in multilayer calorimeters," *Physical review letters* **120** no. 4, (2018) 042003.

[239] R. Stevens, V. Taylor, J. Nichols, A. B. Maccabe, K. Yelick, and D. Brown, "AI for Science," tech. rep., Argonne National Lab.(ANL), Argonne, IL (United States), 2020.

[240] K. Li and J. Malik, "Learning to optimize," *arXiv preprint arXiv:1606.01885* (2016) .

[241] D. Whitley, "A genetic algorithm tutorial," *Statistics and computing* **4** no. 2, (1994) 65–85.

[242] J. Snoek, H. Larochelle, and R. P. Adams, "Practical bayesian optimization of machine learning algorithms," in *Advances in neural information processing systems*, pp. 2951–2959. 2012.

[243] D. R. Jones, M. Schonlau, and W. J. Welch, "Efficient global optimization of expensive black-box functions," *Journal of Global optimization* **13** no. 4, (1998) 455–492.

[244] E. Cisbani, A. Del Dotto, C. Fanelli, M. Williams, M. Alfred, F. Barbosa, L. Barion, V. Berdnikov, W. Brooks, T. Cao, *et al.*, "AI-optimized detector design for the future Electron-Ion Collider: the dual-radiator RICH case," *Journal of Instrumentation* **15** no. 05, (2020) P05009.

[245] "Town Hall on A.I. Projects in the Experimental Physics Program," 2020. https://wiki.jlab.org/epsciwiki/index.php/Aug˙_28,_ENP_%2B_CST_AI/ML_Town_Hall.

[246] K. Deb, S. Agrawal, A. Pratap, and T. Meyarivan, "A fast elitist non-dominated sorting genetic algorithm for multi-objective optimization: NSGA-II," in *International conference on parallel problem solving from nature*, pp. 849–858, Springer. 2000.

[247] K. Deb, *Multi-objective optimization using evolutionary algorithms*, vol. 16. John Wiley & Sons, 2001.

[248] P. Feliot, J. Bect, and E. Vazquez, "A Bayesian approach to constrained single-and multi-objective optimization," *Journal of Global Optimization* **67** no. 1-2, (2017) 97–133.

[249] Y. Jin and B. Sendhoff, "Pareto-based multiobjective machine learning: An overview and case studies," *IEEE Transactions on Systems, Man, and Cybernetics, Part C (Applications and Reviews)* **38** no. 3, (2008) 397–415.

[250] "Joint Machine Learning Workshop, GlueX Panda EIC," 2020. https://indico.gsi.de/event/9244/.

[251] "AI4EIC-exp Workshop." Center for frontiers in nuclear science, stony brook, 2021. https://indico.bnl.gov/category/218/.